Contact mechanics of thin films, viscoelastic materials, and frictional interfaces via Green's function molecular dynamics

Dissertation

zur Erlangung des Grades des Doktors der Naturwissenschaften der Naturwissenschaftlich-Technischen Fakultäten der Universität des Saarlandes

von
Christian Müller

INM - Leibniz-Institut für Neue Materialien
LMS - Lehrstuhl für Materialsimulation

Saarbrücken 2024

Tag des Kolloquiums:	04.11.2024
Dekan:	Prof. Dr.-Ing. Dirk Bähre
Berichterstatter:	Prof. Dr. Martin H. Müser
	Prof. Dr. Eduard Arzt
	Prof. Dr. Lars Pastewka
Akad. Mitglied:	Dr.-Ing. Florian Schäfer
Vorsitz:	Prof. Dr. Roland Bennewitz

Abstract

The theoretical framework of conventional contact mechanics is based on idealized assumptions that have shaped the field for more than 140 years. Unfortunately, these assumptions do not lend themselves to the modelling of thin films, viscoelastic materials and frictional interfaces. Therefore, the present thesis is concerned with the systematic generalization of these assumptions and their GFMD implementation to simulate a variety of previously inaccessible, realistic contact problems.

First, finite material thickness is considered in the design of film-terminated fibril structures for skin adhesion. An elastic film resting on a hard foundation is effectively more stiff than its bulk counterpart, which reduces its ability to conform to counter-faces and therefore reduces the adhesion to roughness. Second, the velocity-dependence of soft, adhesive multi-asperity contacts is studied, revealing the importance of topographical saddle points and the initial configuration, from which detachment is initiated. Furthermore, we identify a scaling relation describing how short-ranged microscopic interactions slow down the macroscopic relaxation of a contact. Finally, we explore the influence of interfacial friction, showing that it increases local stress concentrations and impedes the fluid flow through the interface.

The reported results provide new insight into commonly neglected phenomena, whose practical significance is reinforced by direct comparisons to experiments.

Zusammenfassung

Der theoretische Rahmen der konventionellen Kontaktmechanik basiert auf idealisierten Annahmen, die das Fachgebiet seit über 140 Jahren prägen. Leider eignen sich diese nicht für die Modellierung von dünnen Filmen, viskoelastischen Materialien und reibungsbehafteten Oberflächen. Daher widmet sich die vorliegende Dissertation der systematischen Verallgemeinerung dieser Annahmen und ihrer Umsetzung in GFMD, um zuvor unzugängliche, realistische Kontaktprobleme zu simulieren.

Zuerst wird die endliche Materialdicke berücksichtigt bei der Modellierung von filmterminierten Fibrillenstrukturen für die Hautadhäsion. Ein dünner, eingeklemmter Film verhält sich effektiv steifer, was seine Anpassungsfähigkeit verringert und somit auch seine Haftung auf rauen Oberflächen. Anschließend wird die Zeitabhängigkeit von weichen, adhäsiven Multi-Asperitätskontakten untersucht, wobei topographische Sattelpunkte und die Anfangskonfiguration die Ablösung beeinflussen. Zudem identifizieren wir eine Skalierungsbeziehung für die Verlangsamung der makroskopischen Kontaktrelaxation durch kurzreichweitige mikroskopische Wechselwirkungen. Abschließend erforschen wir den Einfluss von Reibung, die lokale Spannungskonzentrationen erhöht und den Flüssigkeitsfluss durch die Grenzfläche beeinträchtigt.

Die Ergebnisse bieten neue Einblicke in oft vernachlässigte Phänomene, deren praktische Relevanz durch direkte Vergleiche mit Experimenten verdeutlicht wird.

Acknowledgements

First and foremost, I want to thank Prof. Eduard Arzt, the Leibniz Institute for New Materials (INM) and especially Prof. Martin Müser for the opportunity to work with them and write this thesis. Looking back at the last four years made me realize how much I have learned thanks to them. My first encounter with Prof. Arzt as a first-year student of micro- and nanotechnology was a big part of what inspired me to switch to studying materials science. It could not have been more fitting to then end up working as a PhD student in his group. Similarly, I remember sitting in Martin's lecture and getting a glimpse of how much knowledge can be uncovered by learning just a bit more about mathematics and theoretical physics than I had known thus far. After I started my PhD, I probably bothered him a lot with questions about concepts I did not (yet) understand, but he made sure to take time for me, no matter how busy he was. It is those discussions and the "learning by teaching" concept that prepared me for the challenges that would come up along the way. Before starting this thesis, I could have never imagined that I would soon develop simulation software myself rather than merely using one. But what really made the hard work pay off was the opportunity to directly apply the theoretical insights to practical applications, thanks to the collaboration between the Lehrstuhl für Materialsimulation (LMS) and INM. I used to be the kind of student who would make an experimental observation and helplessly consult the literature in the hope of finding a model that explains my findings. Nowadays, I finally feel confident enough as a scientist to look at results and come up with explanations myself. Hence, I am forever grateful to Martin for teaching me the theoretical background and process of critical thinking necessary to achieve that.

I also want to thank the small working group at LMS for providing a familiar-feeling environment, partaking in stimulating discussions, and providing advice, especially in the early stages of my thesis. Sergey Sukhomlinov, Anle Wang and Yunong Zhou instructed me on the previous versions of the GFMD code, without which I would have been lost immediately. I will miss some of the great conversations I had over lunch and coffee with Martin, Sergey and Joshua.

I also thoroughly enjoyed the time spent together with the functional materials group at INM. I will remember the regular group meetings and especially the workshop in Santa Barbara as one of the highlights of my time as a PhD student. I am especially indebted to Manar Samri, René Hensel and Gabriela Moreira-Lana, who never rejected any of my requests to run another experiment and made it a very enjoyable experience for me to

Contributions of Coauthors

Coauthor contributions to published research articles are detailed in front of each individual publication in the appendix of this thesis.

There are some bits of original unpublished research in this thesis, to which colleagues have contributed. Fabian Faller collected the experimental data in Fig. 2.3. Similarly, the data presented in Fig. 2.4 was acquired by Gabriela Moreira Lana. In both cases, the analysis and visualization was done by me.

The derivation procedure for App. C is based on an initial outline by Martin Müser. Although he tackled the inverse problem (deriving a compliance kernel rather than a stiffness kernel), the basic procedure was already there for me to repeat. Sergey Sukhomlinov helped me to find the final solution with a combination of analytical reformulation and *WolframAlpha*. Martin Müser is also responsible for a considerable part of the numerical implementation of Real-space GFMD used in App. C.

The Green's function molecular dynamics (GFMD) simulation code used throughout my work is continuously evolving with minor and major contributions from many colleagues. The reference for the original design by Campaña *et. al.* is cited in the text, as well as the works corresponding to the first implementations of particular features. The changes necessary for my own research were mostly implemented by myself under the supervision of Martin H. Müser, but some parts have included help from Yunong Zhou, Anle Wang and Sergey Sukhomlinov. Any major contributions of colleagues cite their respective publications in the text. During the first half of my PhD, almost all GFMD-related developments were conceptualized and supervised by Martin Müser, which later shifted to me working on the code independently and managing it via GitHub.

Abbreviations

BAM	bearing-area model
BC	boundary condition
BVP	boundary value problem
CFT	continuous Fourier transform
CG	conjugate gradient
COM	center of mass
CZM	cohesive-zone model
DFT	discrete Fourier transform
DMT	Derjaguin, Müller and Toporov
EOM	equation of motion
FEM	finite element method
FFT	fast Fourier transform
FIRE	fast inertial relaxation engine
FT	Fourier transform
GFMD	Green's function molecular dynamics
GW	Greenwood and Williamson
INM	Leibniz Institute for New Materials
JKR	Johnson, Kendall and Roberts
KV	Kelvin-Voigt
LJ	Lennard-Jones
LMS	Lehrstuhl für Materialsimulation
LPF	low-pass filter
MD	molecular dynamics
ODE	ordinary differential equation
PBC	periodic boundary conditions
PDMS	polydimethylsiloxane
PR	Pastewka and Robbins

PSD	power spectral density
PT	Persson and Tosatti
rms	root-mean-square
SLS	standard linear solid
SSA	soft skin adhesive
TTSP	time-temperature superposition
vdW	van-der-Waals
WLF	Williams, Landel and Ferry

Mathematical symbols

Γ surface interaction potential

$\Delta\gamma$ surface energy

$\Theta(t)$ Heaviside function

$\boldsymbol{\Phi}$ Fourier transform of the Green's stiffness tensor

γ surface energy

$\boldsymbol{\varepsilon}$ strain tensor

ζ magnification

η damping coefficient

κ_{pot} relative curvature of the interaction potential

λ wave length

λ_0 long wave length cut-off

λ_{r} roll-off wave length

λ_{s} short wave length cut-off

μ_{c} Coulomb friction coefficient

μ_{T} Tabor coefficient

ν Poisson's ratio

ρ range of adhesion

$\boldsymbol{\sigma}$ stress tensor

σ_{I} first eigenvalue of the stress tensor

σ_{II} second eigenvalue of the stress tensor

σ_{III} third eigenvalue of the stress tensor

σ_{vM} von Mises stress

σ_{po} pull-off stress

τ relaxation time

ω temporal frequency

a_{r} relative contact area

a_{T} Williams, Landel and Ferry (WLF) parameter

$C(\mathbf{q})$ power spectral density

E Young's modulus

$\bar{E}$ effective modulus

$E(\omega)$ viscoelastic Young's modulus

E_0 quasi-static Young's modulus

E_∞ high-frequency Young's modulus

E^* contact modulus, usually $E^* = E/(1 - \nu^2)$

F_{pl} preload force

F_{po} pull-off force

$\mathbf{G}$ Green's tensor

$G^{(\mathrm{n})}$ normal Green's function

H Hurst exponent

J_n Bessel function of the first kind of order n

L system size (usually periodic length)

R radius of curvature

R_{a} arithmetic average height of a surface topography

R_{q} root-mean-square height of a surface topography

R_{t} peak-to-valley height of a surface topography

R_{z} average maximum height of a surface topography

g interfacial gap

$\bar{g}$ root-mean-square gradient of a surface topography

h thickness of an elastic body

$h(\mathbf{r})$	local height of a surface topography
$\bar{h}$	root-mean-square height of a surface topography
m	mass
$\bar{p}$	mean normal pressure
$\mathbf{q}$	in-plane wave vector
q	absolute value of an in-plane wave vector $\mathbf{q}$
q_0	wave vector corresponding to λ_0
q_r	wave vector corresponding to λ_r
q_s	wave vector corresponding to λ_s
$\mathbf{r}$	in-plane coordinate
r	in-plane distance from origin
s	ratio between high- and low-frequency modulus $s = E_\infty/E_0$.
t	time
T_{kin}	kinetic energy
$\mathbf{u}(\mathbf{r})$	displacement field
$u_l(\mathbf{r})$	longitudinal displacement component (relative to sliding direction)
$u_t(\mathbf{r})$	transverse displacement component (relative to sliding direction)
v_0	center-of-mass velocity
v_c	velocity of an interfacial crack
$\mathbf{v}_{\mathrm{rel}}$	relative velocity between two surfaces
V_{pot}	potential energy

Contents

Chapter 1

Introduction

The relevance of studying adhesive contacts is best described by the "adhesion paradox", a term coined by Kendall [1] describing a surprising observation about the strength of attraction between surfaces: Although "all atoms adhere with considerable force", "common experience tells us that ordinary objects do not stick together easily" [2]. What makes this realization so intriguing is that we know for a fact that *in theory* nature provides us with almost arbitrarily strong adhesion. But in order to take advantage of this powerful force, we need to understand and control the phenomena which usually take it away from us.

The study of contact mechanics was pioneered by Heinrich Hertz [3] more than 140 years ago. Many scientists have since contributed to the field and shaped our current understanding of why and how surfaces adhere or not. Throughout this history, roughness has often been identified as one of the greatest challenges for the accurate description and prediction of adhesion in theoretical studies as well as practical applications. Roughness is the reason why the real microscopic area of contact between two surfaces is often considerably smaller than the apparent macroscopic contact area. The only type of adhesive interaction that is present between all surface pairs regardless of material properties is the van-der-Waals (vdW) force, which requires very close proximity to produce considerable attraction. Therefore, most materials that we generally perceive as adhesive are rather soft and consequently deformable enough to conform to the topography of counter-bodies, allowing the intermolecular forces to act across a large portion of the entire contact. This mechanism for improving adhesion had already been perfected by nature itself long before humans even started to study it. One of the most famous examples for this is the foot of the gecko [4], who is able to effortlessly climb up walls and even ceilings without falling off. This is achieved by a hierarchical structure of very fine hair-like setae that provide exceptional flexibility and a very large combined surface area to interact with counter-faces.

Multiple designs for adhesive gripping devices have been developed based on fibril or pillar patterns mimicing the setae of the gecko [5–14]. They provide a unique combination of advantages compared to conventional solutions for pick-and-place applications. First

of all, since their adhesion is based on vdW interactions, they work for almost all surfaces regardless of chemical or electrical properties and in many different environments, including vacuum, where suction-based gripping does not work at all. Second, they can safely handle sensitive or fragile parts, leaving no damage or residue on the surface. This makes them particularly useful for skin contacts in medical applications. Finally, due to their specific mechanical properties, they provide relatively good adhesion to rough interfaces, where suction cups are again likely to fail. To better understand the effect of roughness on adhesion, recent studies often observe the pillar array while in contact, e.g. by choice of transparent materials, and try to correlate the observed "contact signature" with the resulting pull-off force necessary to separate the surfaces. Such predictions have been based on the the first detached pillar [15], statistical considerations [16] or machine learning [17]. However, the data obtained for the adhesion on a single surface is not indicative of other surfaces with a considerably different topography and therefore does not translate to real-world performance. One of the original motivations of this thesis was assessing to what extent predictions from contact signatures can be improved by taking topographical information and contact mechanics into account. This, in turn, requires a good general understanding of how roughness affects adhesion and what parameters and phenomena need to be considered for a realistic model, which became the extended scope of my research.

Rough contact mechanics theories and corresponding numerical methods have improved significantly over the past decades. Nevertheless, they still mostly rely on the framework introduced by Hertz and Boussinesq [3,18], which makes three important assumptions: The elastic body is i) infinitely thick, ii) deformed quasi-statically and iii) its surface is free of in-plane stresses. The first condition, the "semi-infinite" geometry, is a very good approximation as long as the characteristic size of contact patches is much smaller than the material's thickness. Consequently, it took many years until thin elastic films received special attention [19,20], which eventually revealed that geometric confinement does not only affect adhesion quantitatively but completely changes the detachment mechanism [21,22]. In recent years, more attention was drawn to the time dependence associated with polymer contacts, so that the second assumption is often eliminated by the introduction of a simple viscoelastic material model [23–25]. In spite of this progress, theoretical as well as numerical models usually pick two out of three "ingredients", namely, realistic roughness, adhesion and viscoelasticity. This is because even in quasi-static systems, any change of contact area comes with an adhesive hysteresis between attachment and detachment, so that the microscopic state of a multi-asperity system already depends on its history. Adding viscoelasticity to the mix complicates this history-dependence to an extent that makes predictions based on macroscopically known properties almost impossible. Studies tackling the combined problem have recently started to emerge but are still relatively rare [26–28, **IV**]. Getting rid of the third assumption requires the incorporation of interfacial friction, which is important for virtually all interfaces between moving parts. For example, when a gecko climbs up a vertical wall, the gravitational force is directed parallel rather than normal to the interface, meaning that the successful ascension depends on static friction. Nevertheless,

the contribution of in-plane stresses to the elastic deformation is almost never taken into account in conventional contact mechanics. As recent studies have shown, transverse stresses can indeed be neglected in the semi-infinite limit if the deforming material is incompressible [29], which is a reasonable assumption for polymers. Many industrial applications, however, include frictional contacts between metals, which usually require lubrication and thin polymeric seals to prevent wear and maximize efficiency. Hence, the incorporation of lateral tractions as well as the fluid flow through the interface would greatly improve our ability to model such contacts.

With this history and recent developments in mind, the present study aims to bridge some of the gaps between theoretical/numerical modeling and reality. For this purpose, Green's function molecular dynamics (GFMD) [30] is chosen as a highly efficient state-of-the-art numerical solution technique, which is applicable to a wide range of linearly (visco-)elastic contact problems. To approach reality, the existing GFMD implementation had to be enhanced in a variety of ways: The loading conditions had to be refined to more closely resemble those of real experiments and a more general viscoelastic material model was introduced to better capture the mechanical properties of real polymers. Furthermore, to allow lateral elastic stresses and deformations to be taken into account, the Green's function approach had to be generalized to three dimensions and a model for interfacial friction had to be implemented. Supported by direct comparisons to experiments, these novel simulation capabilities are put to the test by analyzing the following phenomena affecting a wide variety of real-world contacts:

1. the influence of finite material thickness and compressibility on contact stiffness, work of adhesion and detachment mechanisms,

2. the improved adhesion performance of film-terminated fibrillar adhesives compared to polymer bulk or conventional fibrils,

3. the effect of the preload-force on the adhesion observed in industrial gripping applications to understand the importance of the specific configuration, from which detachment is initiated,

4. the dynamics of contact formation as well as rupture resulting from different viscoelastic material models and

5. the influence of lateral tractions and displacements on real contact area, effective friction force, eigenstress distributions and resistance to fluid flow through the interface.

The common aim of these studies is to understand what ingredients are necessary for analytical and numerical models to provide more reliable predictions of real-world contacts.

Chapter 2

Theory

2.1 Origins of adhesion

The potential for surfaces to adhere is described by the so-called (Young-Dupré) surface energy, typically denoted $\Delta\gamma$ (or just γ, for short) with the physical dimension of energy per area. Particles at an object's surface do not form bonds in the direction normal to the surface, putting them in an unfavorable state compared to those particles that reside in the bulk material surrounded by many of their kind. For this reason, all surfaces and interfaces "cost" energy. When two objects "1" and "2" come into contact, their two surfaces (i.e. interfaces with vacuum) with respective surface energies γ_1 and γ_2 are replaced by a single interface between them with energy γ_{12}. Therefore, the total energy per unit area is reduced by

$$\Delta\gamma = \gamma_1 + \gamma_2 - \gamma_{12}. \tag{2.1}$$

Although this makes $\Delta\gamma$ a characteristic property of the given material pair, its value turns out to be in the range of 0.03 to 0.06 J/m^2 for a surprisingly large range of different surface combinations [31, 32]. This generality suggests that adhesion is dominated by the omni-present van-der-Waals (vdW) type of interaction. In many cases, researchers have ruled out all other options by process of elimination, most notably for the feet of the gecko [4], whose capabilities have inspired countless designs in practical adhesive applications [5–14].

In the introduction, we have already established the adhesion paradox, which basically asks the question why most surfaces do not stick although local tractions can easily reach 100 MPa even for passivated surfaces. Although there are many factors that can play a role for specific surface pairings or applications, the two most universal ones are probably microscopic surface contamination and roughness.

Contamination: Contact theories have proven to provide exceptional quantitative predictions for contacts in the vacuum of space [33]. However, on Earth, surfaces are typically not microscopically clean but covered by contamination films, which are difficult to characterize and can play a crucial role for adhesion. In some cases, these films sub-

stantially decrease adhesion because they prohibit intimate contact between surfaces. For example, the stickiness of conventional fibrillar adhesives almost vanishes in underwater applications [13]. On the other hand, in the natural environment of the gecko, its strength of adhesion tends to increase with higher temperature and air humidity due to capillary effects and material softening [34, 35]. The underlying chemical reactions of these mechanisms are beyond the scope of this thesis but actively investigated in other theoretical and numerical studies [36–38].

Roughness: In most cases, roughness reduces the real contact area between two surfaces. Nevertheless, a certain degree of roughness sometimes seems beneficial for adhesion, because the total available surface area is larger than the projected one [39–42]. When trying to understand and predict the effect of roughness on adhesive contacts, the problem often starts with the mere characterization of the topography, as will be discussed in Sect. 2.2. Acquiring accurate information from the largest down to the smallest length scales requires a combination of multiple imaging techniques and very careful postprocessing of the accumulated data [43, 44]. Depending on the surface properties and experimental techniques, measurement artifacts further complicate the evaluation [45]. These realizations have spawned the *Topography Characterization Challenge* [46], the results of which have not been published at the time of writing of this thesis. It was inspired by the *Contact Mechanics Challenge* [47], which compared the contact predictions of several numerical and theoretical models for a well-defined computer-generated surface topography. For adhesive interactions to take effect, the two contacting surface topographies must conform as well as possible, which generally requires a certain amount of deformability. It is for this reason that most practical adhesive applications include soft polymer materials, whose mechanical properties are discussed in Sect. 2.3 and 2.4.2.

2.2 Surface topography

The crucial importance of surface topography for adhesive contacts is probably best illustrated by the simple calculation in the original "adhesion paradox" publication [1]: If two ideally flat, infinitely large surfaces with surface energy $\Delta\gamma$ were to be pulled apart, the Van-der-Waals adhesion would be overcome after a displacement less than a nanometer. This would mean that the pull-off stress σ_{po} can be estimated to be

$$\sigma_{po} \approx \Delta\gamma/0.3\,\text{nm}. \tag{2.2}$$

This result is approximately three orders of magnitude larger than anything observed in nature. To explain this discrepancy, it needs to be taken into account that surfaces are never infinitely large and the constituent materials are deformable. Since the edge of the contact constitutes a pre-existing defect in the otherwise flat contact, the detachment usually does not occur uniformly but rather by propagation of an interfacial crack. This process can be described by Griffith's fracture mechanics, where the driving force for crack opening is proportional to the derivative of the stored elastic energy with respect to the contact area. For a circular contact with radius a, the pull-off stress is then calculated to be [48]:

$$\sigma_{po} = \sqrt{\frac{8E\Delta\gamma}{(1-\nu^2)\pi a}}, \tag{2.3}$$

where the circular surface is rigid and the other is a flat, isotropic and semi-infinite material with Young's modulus E and Poisson's ratio ν. Contrary to the previous estimate, Eq. (2.3) can reach values observable in nature, perfectly highlighting that shape and deformability of the contacting surfaces cannot be neglected. However, Eq. (2.3) predicts a trend opposite of what we observe in our daily lives: It predicts a hard steel surface to be much more sticky than a soft polymer with substantially smaller Young's modulus. Conversely, the well-known empirical Dahlquist criterion states that materials only feel sticky if their Young's modulus is smaller than a threshold of approximately $1\,\text{MPa}$ [49], which was later rationalized theoretically [8, 50]. This stark contradiction can only be explained by a combination of two things: i) Almost all real surfaces are microscopically rough and ii) softer, more compliant materials can easily conform to such rough counter-faces and achieve a much larger real contact area than hard materials [1].

2.2.1 Self-affine random roughness

Unfortunately, closed-form solutions like Eq. (2.3) only exist for contacts with very simple mathematical shapes, usually axisymmetric ones. The situation becomes much more complicated once we have to describe systems of realistic roughness. To this end, the model of isotropic, statistically self-affine height fluctuations provides exceptional accuracy while still maintaining a certain level of simplicity. A wide range of different industrial processing methods (e.g. sand blasting [51] and chemical/physical vapor deposition [43, 52]) as well as natural phenomena like plastic deformation [53], fracture [54] and even plate tectonics [55] all tend to create surface profiles that look random and

self-affine within their respective ranges of length scales. Furthermore, the model can easily be implemented numerically [30,45,56] and sometimes even simplifies analytic expressions into small closed-form solutions [23,57–59]. Natural exceptions to this broad applicability of the self-affine model are highly correlated, textured surfaces, which contradict the inherent assumption of randomness [60]. However, in some cases, results obtained from the random-phase assumption can be systematically generalized to "less random" profiles, e.g. by evaluating certain properties only over the real contact area rather than the whole surface [61,62]. To discuss the properties of self-affine random surfaces, we choose the representation in Fourier space. For the reader's convenience, the most important properties of the Fourier transform (FT) can be looked up in App. A. A much more detailed overview of spectral surface analysis can be found in the literature, especially Ref. [44].
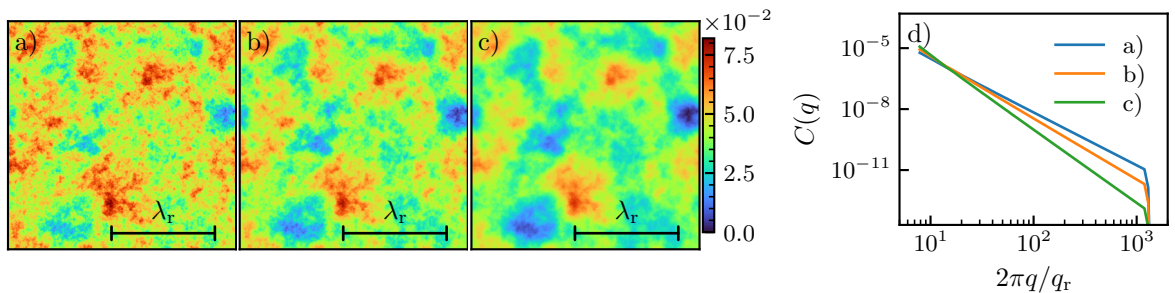
Figure 2.1: Comparison of different Hurst exponents. a) $H = 0.3$, b) $H = 0.5$ and c) $H = 0.8$. Panel d) shows the respective power spectral densities (PSDs). All surfaces have the same root-mean-square (rms) height of $\lambda_r/100$.

We assume that for every lateral coordinate $\mathbf{r} = (x, y)$, the height of a surface is given by a well-defined function $h(\mathbf{r})$ with the FT $\tilde{h}(\mathbf{q})$, where $\mathbf{q}$ is an in-plane wave vector. This allows us to define the so-called power spectral density (PSD) $C(\mathbf{q})$, which, for isotropic surfaces, only depends on the absolute value of the wave vector $q = |\mathbf{q}|$:

$$C(q) := \langle \tilde{h}(\mathbf{q}) \tilde{h}^*(\mathbf{q}) \rangle_{\{\mathbf{q} \,|\, |\mathbf{q}| = q\}}, \tag{2.4}$$

where $\tilde{h}^*$ is the complex conjugate of $\tilde{h}$. This is equivalent to defining the PSD as the FT of the height auto-correlation function in real space. An isotropic, self-affine random height profile is obtained when the PSD has the shape of a power law and the height coefficients have random phases, i.e. $U \in (0, 1)$ and

$$C(q) \propto q^{-2-2H}, \tag{2.5a}$$

$$\tilde{h}(\mathbf{q}) = \sqrt{C(q)} \exp(\mathrm{i}2\pi U(\mathbf{q})), \tag{2.5b}$$

where $H \in (0, 1)$ is the so-called Hurst exponent and related to the fractal dimension D via $H = 3 - D$. The above assumption of random phases automatically makes the resulting height values normally distributed. Since the real-space height $h(\mathbf{r})$ follows from adding up sinusoidal undulations with random phases, its value at each individual point $\mathbf{r}$ is just a sum of many independent random numbers. The results of such summations follow a Gaussian distribution according to the central limit theorem.

As hinted at near the start of this section, real surfaces only look self-affine within a certain range of length scales. The limits of this range are described by the roll-off wavelength λ_r and short-wavelength cut-off λ_s or their respective wave vectors $q_r = 2\pi/\lambda_r$ and $q_s = 2\pi/\lambda_s$. The name "roll-off" is chosen because to the left of q_r, the spectrum is not cut off abruptly but rather transitions (rolls off) into a constant value. This provides us with a more realistic model for rough surfaces given by

$$C(q) = C(q_r) \begin{cases} 1 & \text{if} \quad q_0 \leq q \leq q_r \\ \left(\frac{q_r}{q}\right)^{2+2H} & \text{if} \quad q_r < q < q_s \;, \\ 0 & \text{else} \end{cases} \tag{2.6}$$

where q_0 is the minimum wave vector and the phases of all $\tilde{h}(\mathbf{q})$ are still chosen randomly as in Eq. (2.5). Fig. 2.2 aims to show that a PSD with roll-off produces slightly more "natural" looking surfaces than an abrupt cut-off at $q_0 = q_r$. This subjective impression originates from the fact that natural surfaces usually are not ideally flat on long wavelengths (except maybe on length scales corresponding to the physical size of an object, which would be questionable to still consider as a component of roughness). The exact shape of the roll-off region only has a marginal influence, where the smoothened option has a lower intensity around the roll-off wavenumber but a slightly higher contribution everywhere else. In other words, from Fig. 2.2a to c, the relative significance of the roll-off wavelength λ_r is progressively reduced.
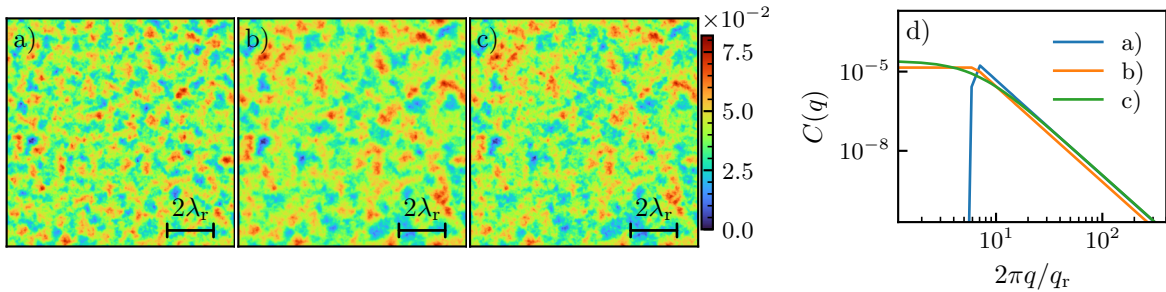
Figure 2.2: Comparison of different roll-off variants. a) is generated according to Eq. (2.5), b) with an abrupt roll-off as in Eq. (2.6) and c) with a smoothened roll-off. d) shows the respective PSDs. All surfaces have the same rms height of $\lambda_r/100$.

At this point, neither of the above equations have defined the proportionality factor in $C(\mathbf{q})$. This is because it unfortunately depends on the exact convention used for the normalization of the PSD and the underlying FT. For example, Persson [63] defines $C(\mathbf{q})$ so that its integration over all wave vectors is exactly the mean square height $\langle h^2 \rangle$:

$$\langle h^2 \rangle = \int d^2q \, C^{\text{Persson}}(\mathbf{q}) \overset{\text{(isotropy)}}{=} 2\pi \int dq \, q C^{\text{Persson}}(q). \tag{2.7}$$

On the other hand, Jacobs *et. al.* [44] use a different convention for the definition of the continuous FT,

$$C^{\text{Jacobs}}(q) = 4\pi^2 C^{\text{Persson}}(q). \tag{2.8}$$

Keeping that in mind, we can simply carry out the integral in Eq. (2.7) to express $C(q_r)$ in terms of $\langle h^2 \rangle$, H, q_0 and q_r, so for Eq. (2.6), we get the prefactor

$$C^{\text{Persson}}(q_r) = \frac{H}{\pi} \frac{\langle h^2 \rangle}{q_r^2(H+1) - q_0^2 H}. \qquad (2.9)$$

Similarly, Eq. (2.5a) becomes

$$C^{\text{Persson}}(q) = \frac{H}{\pi} \frac{\langle h^2 \rangle}{q_0^2} \left(\frac{q_0}{q} \right)^{2+2H}. \qquad (2.10)$$

This way, the properties of the self-affine surface are completely described by only a few scalar parameters with intuitive physical interpretations.

2.2.2 Roughness characterization

The previous section has introduced the PSD as a means of characterizing roughness, which is defined by at least three parameters: The roll-off q_r defines the lateral length scale, the exponent H contains the spectral properties and the third parameter, the root-mean-square (rms) height $\bar{h} = \sqrt{\langle h^2 \rangle}$, defines the proportionality factor, i.e. the magnitude in the normal direction. Thechnically, there is a fourth parameter, the high frequency limit q_s, which can, however, be considered a resolution limit characteristic of the numerical or instrumental technique rather than the surface topography.

In industrial/engineering applications, it is often preferred to characterize surface roughness using only a single representative value. Multiple conventions for these values have been standardized, which, in principle, makes it very easy to compare surfaces to each other, regardless of processing technique or manufacturer. Those parameters are typically determined for a single line scan $h(x)$ rather than the complete surface measurement $h(x,y)$, so the result generally depends on the rotation of the coordinate system and the y-position, from which the line is taken. Some of the most common conventions shall be discussed here for reference. The rms height R_q, the arithmetic average height R_a, Peak-to-valley height R_t and the average maximum height R_z are defined as [64]

$$R_q = \bar{h} = \sqrt{\langle h^2 \rangle_x - \langle h \rangle_x^2}, \qquad (2.11a)$$

$$R_a = \langle |h - \langle h \rangle_x| \rangle_x, \qquad (2.11b)$$

$$R_t = \max(h) - \min(h), \qquad (2.11c)$$

$$R_z = \frac{1}{5} \left(\sum_{i=1}^{5} \max(h_i) - \min(h_i) \right), \qquad (2.11d)$$

where the "measurement" $h(x)$ is divided into five partial measurements h_i, $i \in [1,5]$ to determine R_z. Consequently, R_z is simply an average of R_t over multiple sub-measurements. Compared to a characterization via PSD, all of these parameters lack any lateral or spectral information. [1] Furthermore, determining them from 1D line scans might be convenient, but fails to capture any potential anisotropy.

---

[1] There are many more roughness parameters, some of which neglect vertical information and use lateral information like the peak counts instead.

As mentioned in Sect. 2.2.1, many real surfaces have an approximately Gaussian distribution of height values. Under this assumption, the rms height $\bar{h} = R_q$ is the standard deviation of this distribution. It is not only used to define the PSD, but also often turns up in theoretical descriptions, most notably in Greenwood and Williamson (GW) theory [65] and other bearing-area models (BAMs) [66]. This arguably makes using R_q a strictly better alternative to the otherwise very similar R_a. The other parameters, which are based on maxima and minima, have the disadvantage that they depend on the scan length L_x and resolution Δx. For a set of $n = L_x/\Delta x \gg 1$ random numbers drawn from a normal distribution, the expectation value of the maximum is proportional to $\sqrt{\ln(n)}$ [67, p. 17f], which very slowly approaches infinity as n is increased. Based on a couple of computer-generated self-affine surfaces as in Eq. (2.6), increasing L_x from the roll-off wavelength λ_r to $10\lambda_r$ increases R_t and R_z by approximately 50% when the rms height and resolution are kept constant. Furthermore, maxima and minima in measurements often suffer from imaging artifacts.

In the scientific literature, it has also been suggested to describe the roughness based on the energy stored in the deformation of an elastic half-space in full contact with the given topography [68]. This is equivalent to evaluating a rms fractional derivative: It averages $(|\mathbf{q}|^n |\tilde{h}(\mathbf{q})|)^2$ over all $\mathbf{q}$ with $n = 1/2$, where $n = 0$ would correspond to the rms height and $n = 1$ the rms height gradient. We will refer to this parameter as R_{el} in Tab. 2.1. For a self-affine surface as in Eq. (2.6), reducing the Hurst exponent at constant rms height strongly increases the rms gradient $\bar{g}$, while R_z only increases moderately. R_a stays approximately constant, which is to be expected, given its mathematical similarity to $\bar{h}$. Some exemplary values are shown in Tab. 2.1, where the size-dependent parameter R_z was always evaluated over the same scan size.

	$R_a/\bar{h}$	$R_z/\bar{h}$	$R_{el}/\bar{h}$	$\bar{g}$
$H = 0.8$	0.0800 ± 0.0004	0.39 ± 0.01	0.27	0.031
$H = 0.5$	0.0797 ± 0.0002	0.50 ± 0.01	0.52	0.10
$H = 0.3$	0.0797 ± 0.0002	0.535 ± 0.003	0.72	0.16

Table 2.1: Roughness parameters averaged over five individual realizations of statistically identical self-affine surfaces with roll-off wavelength λ_r and shortest wavelength $\lambda_s = 0.004\lambda_r$. All profiles were generated with the same rms height of $\bar{h} = 0.01\lambda_r$. Data for R_{el} as well as $\bar{g}$ are exact within numerical precision.

The necessity to incorporate lateral information in roughness parameters is probably best highlighted by the examples in Figs. 2.1 and 2.2, where all surfaces have the same rms height and roll-off wavelength λ_r but clearly look different to each other, even to the naked eye. What is probably even more important in engineering applications is to account for potential anisotropy. Most industrial surfaces undergo directional treatments like, e.g., 3D printing, milling and grinding, which leave various sizes of patterns and/or microscopic scratches. To illustrate this, Fig. 2.3 summarizes the properties of an optical scan of a 3D-printed surface. Although optical scans are prone to image artifacts that undermine the quantitaive accuracy of the depicted PSDs, the qualitative differences in Fig. 2.3b clearly highlight the anisotropy of the surface. The spectrum measured parallel

to the printing motion is almost entirely below the PSD evaluated in the perpendicular direction. The pronounced peaks in the latter correspond to wavelengths that are integer multiples of the line spacing of the printing process.
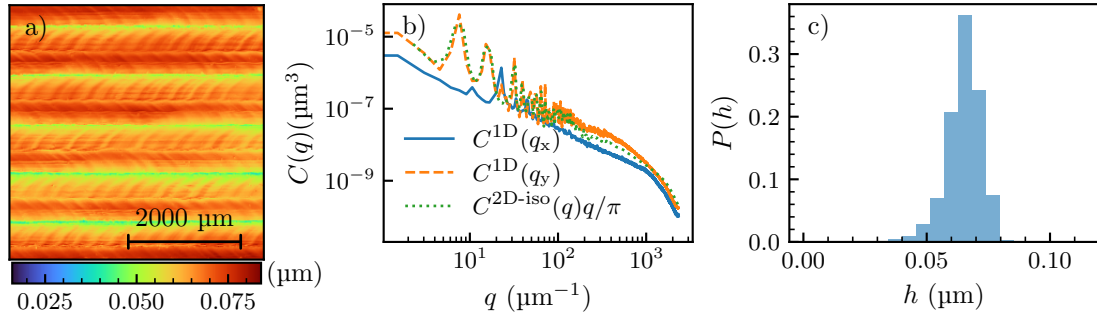
Figure 2.3: a) 2D height profile, b) PSDs and c) height histogram obtained from an optical image of a 3D-printed surface. The surface is clearly anisotropic and not ideally Gaussian.

The examples in this section should make it clear that the characterization via PSD is much more accurate than the scalar parameters discussed above, which do not capture lateral length scales or anisotropy. The PSD, on the other hand, only neglects the phase information for individual wavelengths. For example, flipping a topographical feature upside-down can be expressed as a phase shift of all Fourier coefficients, so both the original and the inverted profile would have the same PSD. More generally, the PSD misses information about the height histogram, which may be slightly skewed like the one in Fig. 2.3 with a few outliers at the extreme ends, which most likely correspond to bad data points.

To elaborate on the aforementioned optical artifacts and their effect on the PSD, Fig. 2.4 shows optical and tactile line profiles of the same surface side-by-side. The wild spikes are so dominant in the optical scan that the two measurements look nothing like each other and the optical PSD is completely wrong.
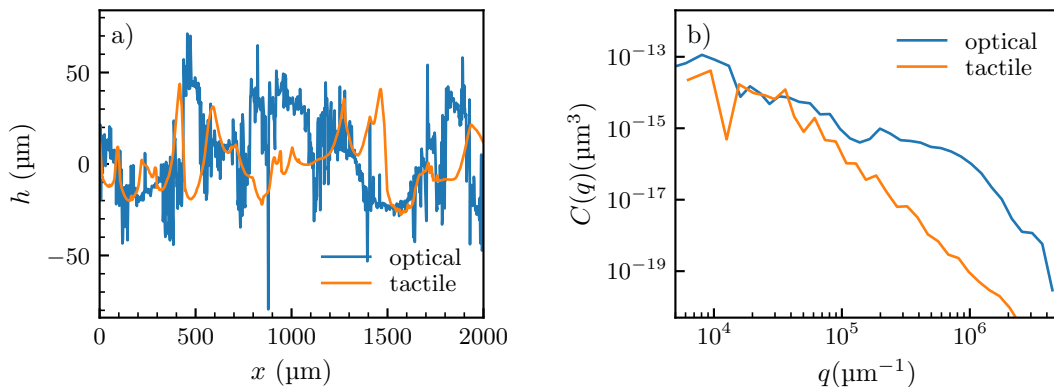
Figure 2.4: a) 1D height profile and b) corresponding 1D PSD obtained from an optical (blue line) and tactile (orange line) scan, evaluated through the *Contact.engineering* website [69]. The measurements were taken along two different lines of the same *Vitroskin* surface (IMS inc., Portland, ME). The optical scan shows a lot more spikes, corresponding to large wavenumbers.

2.3 The linearly (visco-)elastic contact problem

2.3.1 Constitutive equations

Describing the mechanical properties of materials first and foremost requires so-called constitutive equations, which define the relationship between their deformation state (usually given by a strain tensor $\boldsymbol{\varepsilon}$) and the corresponding stress tensor $\boldsymbol{\sigma}$. Both of these tensors are of rank 2 and can be represented by symmetric 3×3 matrices. The strain tensor follows from the partial derivatives of the 3-dimensional displacement field $\mathbf{u}(x_1, x_2, x_3)$ as

$$\varepsilon_{\alpha\beta} = \frac{1}{2}\left(\frac{\partial u_\alpha}{\partial x_\beta} + \frac{\partial u_\beta}{\partial x_\alpha}\right). \tag{2.12}$$

For small deformations, thanks to what is effectively a first-order Taylor expansion, the stress-strain relationship can be very closely approximated as linear, where the proportionality factors are given by the material-specific 4th rank stiffness tensor $\mathbf{C}$. This most universal form of the linearly elastic constitutive equation is known as generalized Hooke's law and can be written in index notation as

$$\sigma_{\alpha\beta} = C_{\alpha\beta\gamma\delta}\varepsilon_{\gamma\delta} \tag{2.13}$$

via Einstein summation convention. If the material is assumed to be mechanically isotropic, the number of independent degrees of freedom is significantly reduced, so all components of $\mathbf{C}$ can be expressed using only two independent parameters. We will use the representation of the Young's modulus E with the physical dimension of stress and the dimensionless Poisson's number $\nu \in (-1, 0.5)$, so we can simplify Eq. (2.13) into [70, p. 14]

$$\sigma_{\alpha\beta} = \frac{E}{1+\nu}\left(\varepsilon_{\alpha\beta} + \frac{\nu}{1-2\nu}\varepsilon_{\gamma\gamma}\delta_{\alpha\beta}\right). \tag{2.14}$$

This form of the equation helps to better understand the physical meanings of the two material parameters: While the Young's modulus is a global proportionality factor for the stiffness, the Poisson's ratio acts as a relative measure for the compressibility of the material. When it approaches 0.5, the prefactor of the volumetric strain $\varepsilon_{\gamma\gamma}$ diverges, meaning that an infinite stress would be necessary to change the volume of the body. The resulting material would still be deformable and stable, as long as the deformation is isochoric. When ν assumes negative values, said prefactor becomes negative, making it particularly easy to change the volume of the body. The lower limit for ν must be -1 because that is where the global prefactor diverges and the body would immediately become unstable once any deformation component is different from 0. Another interpretation for ν is the material's relative perpendicular contraction under a uni-axial tensile stress, which, however, is not directly obvious from the equations above.

The condition for equilibrium in the absence of body forces is

$$\frac{\partial \sigma_{\alpha\beta}}{\partial x_\beta} = 0, \quad \alpha \in \{1, 2, 3\}, \tag{2.15}$$

into which we can substitute Eqs. (2.12) and (2.14) to get [70, p. 18]

$$\frac{E}{2(1+\nu)}\frac{\partial^2 u_\alpha}{\partial x_\beta^2} + \frac{E}{2(1+\nu)(1-2\nu)}\frac{\partial^2 u_\gamma}{\partial x_\alpha \partial x_\gamma} = 0, \quad \alpha \in \{1,2,3\}, \tag{2.16}$$

which is known as the Navier(-Cauchy) equation of elasticity and usually given in a more concise vector notation after cancelling the factor $E/2(1+\nu)$ [23, 71–73]:

$$\nabla^2 \mathbf{u} + \frac{1}{1-2\nu}\nabla(\nabla \mathbf{u}) = 0. \tag{2.17}$$

Ref. [74] applies the same formalism for the more general case of cubic symmetry with three independent elastic parameters (C_{11}, C_{12} and C_{44}) rather than just two (E and ν). However, since the present work is mostly concerned with polymer materials below the glass transition, the isotropic description is completely sufficient.

As mentioned above, the postulated linearity between stress and strain only holds true in the limit of small stresses and deformations. What happens beyond the small-displacement limit heavily depends on the class of material in question. In the case of polymers, the linear behavior often crosses over into a non-linear elastic regime, while for metals, the stress-strain relationship often stays approximately linear until plasticity takes over. Contrary to elastic deformation, the plastic component is not reversible and therefore unavoidably dissipates energy. The onset of plasticity as a material property is usually characterized by the so-called yield stress σ_y, which is measured in a simple uni-axial tensile test. To predict the equivalent threshold for a more complicated stress field, σ_y can be compared to the von Mises stress σ_{vM}, which provides a general measure for the magnitude of stress irrespective of coordinate system [75]. It is defined from the stress tensor $\sigma_{\alpha\beta}$ via

$$\sigma_{vM}^2 := \frac{1}{2}\Big((\sigma_{11}-\sigma_{22})^2 + (\sigma_{11}-\sigma_{33})^2 + (\sigma_{22}-\sigma_{33})^2\Big) + 3\Big(\sigma_{12}^2 + \sigma_{13}^2 + \sigma_{23}^2\Big) \tag{2.18a}$$

$$= \frac{1}{2}\Big((\sigma_I - \sigma_{II})^2 + (\sigma_I - \sigma_{III})^2 + (\sigma_{II} - \sigma_{III})^2\Big), \tag{2.18b}$$

where σ_I, σ_{II} and σ_{III} are the eigenvalues of the stress tensor.

One of the central features of the research presented in this thesis is that viscoelastic rather than elastic material models were employed. According to the elastic-viscoelastic correspondence principle, all of the above equations still apply, except that E and ν are not considered constants but functions of time t (or excitation frequency ω, which is an inverse time) [76–78]. This is particularly important for polymers, where deformations are accommodated by the microscopic reordering of chain molecules, which are processes that are considerably slower than the speed of light [79]. The exact shape of this time-dependence is usually approximated in terms of a linear ordinary differential equation (ODE) depending on a displacement u and its time derivative $\dot{u}$. The standard linear solid (SLS) model, in particular, has been used extensively for contact mechanics in recent years [23, 25–27, 80–84]. The derivation procedure for the Kelvin-Voigt as well as Maxwell representation of the SLS is detailed in App. E, including all commonly used

parametrizations and transformations between them. The viscoelastic GFMD implementation represents a generalized Maxwell model, which can closely reproduce a wide range of experimentally observed response functions. It is described in Publ. **IV** and Sect. 2.4.2.

2.3.2 The Green's function method

We want to solve Eq. (2.17) under the assumption of certain boundary conditions (BCs) indicative of contact mechanics. For this purpose, we will transition to using the conventional names for Cartesian coordinates x, y, z in place of x_1, x_2 and x_3. The first BC is that the elastic body is periodic in the x-y plane, where the period may be arbitrarily large. Furthermore, the material has a flat top surface at $z = 0$ and bottom surface at $z = -h$, which is fixed to a rigid foundation, i.e. $\mathbf{u}(x, y, -h) = \mathbf{0} \; \forall \; x, y$. In this framework, the $z = 0$ surface will represent the one that can be brought into contact with a counter-body, as shown in Fig. 2.5a. If body forces (e.g. gravity) are neglected, the stress and displacement fields in the rest of the volume can only depend on the state of that one surface. What we want to find now is the law that relates the stress distribution $\sigma_{\alpha 3}(x, y, 0)$ with the displacement field $\mathbf{u}(x, y, 0)$, resulting from the elasticity of the material underneath.
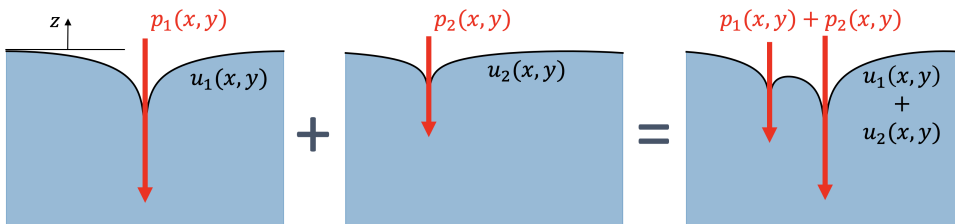
Figure 2.5: Illustration of the principle of superposition. The pressure distributions $p_1(\mathbf{r})$ and $p_2(\mathbf{r})$ both cause the respective displacement profiles $u_1(\mathbf{r})$ and $u_2(\mathbf{r})$. The resulting displacement of both pressures acting concurrently is therefore $u_1(\mathbf{r}) + u_2(\mathbf{r})$. This is only true under the assumption of small deformations, where all stresses can be assumed to be applied to the undeformed, flat body.

Instead of directly defining the Green's functions, the underlying idea will first be explained intuitively. For that purpose, we will focus on the simplest set of boundary conditions, where all in-plane stresses on the surface are 0 and only the normal stress and displacement are of interest. This essentially presents us with the task of relating the cause $\sigma_{33}(x, y, 0)$ with its effect $u_3(x, y, 0)$ across the whole surface. To break the areal problem down into a more local one, we ask the following question: *Given the stress state at a single in-plane position $\mathbf{r}'$, can we predict how this stress affects the displacement at a different point $\mathbf{r}$?* This simplification is thanks to the linear nature of the problem, as depicted in Fig. 2.5c. The effect of the entire areal stress distribution can always be formulated as a linear combination of contributions from arbitrary subdivisions of itself. In the case of a continuous surface, this "linear combination" becomes a two-dimensional integration. We also realize that applying a force F at location $\mathbf{r}' = (x_0, 0)$ will cause the exact same displacement field as an equally large force acting

at $\mathbf{r}' = (0,0)$, except that everything is shifted by $(x_0, 0)$. This means that the problem is translationally invariant, and the displacement at a point $\mathbf{r}$ can only depend on the distance $|\mathbf{r} - \mathbf{r}'|$ from the application point of the force. Consequently, if we call this cause-effect transmission function $G^{(\mathrm{n})}$, the mathematical solution of the problem must be of the form

$$u_3(x, y) = \int \mathrm{d}^2 r' \, G^{(\mathrm{n})}(\mathbf{r} - \mathbf{r}')\sigma_{33}(\mathbf{r}'). \qquad (2.19)$$

$G^{(\mathrm{n})}$ is what we call the Green's function (or fundamental solution) of this particular boundary value problem (BVP) and Eq. (2.19) represents the convolution of $G^{(\mathrm{n})}$ with σ_{33}. Although this is technically an answer to the question raised above, it still requires knowledge of the stress at infinitely many points in the surface, each of which affects the displacement at infinitely many other points. Based solely on this definition, it would still be an incredibly difficult task to determine $G^{(\mathrm{n})}$. However, thanks to the convolution theorem, this equation assumes the simplest imaginable form when it is transformed into Fourier space:

$$\text{Eq. (2.19)} \quad \Longleftrightarrow \quad \tilde{u}_3(\mathbf{q}) = \tilde{G}^{(\mathrm{n})}(\mathbf{q})\tilde{\sigma}_{33}(\mathbf{q}), \qquad (2.20)$$

where $\mathbf{q}$ is an in-plane wave vector and $\tilde{u}_3$, $\tilde{G}^{(\mathrm{n})}$ and $\tilde{\sigma}_{33}$ are the Fourier transforms of u_3, $G^{(\mathrm{n})}$ and σ_{33}, respectively. This has narrowed down the Green's function method into the much more manageable task of determining a proportionality factor in $\mathbf{q}$-space.

For the purely normal contact problem presented here, the solution for $\tilde{G}^{(\mathrm{n})}$ has been known for many years. It has been derived independently by many different authors [21, 71, 74]. In the form given by Carbone *et. al.* [56] and used in Publ. **I** and **II**, it reads

$$\tilde{G}^{(\mathrm{n})}(q, h) = \frac{2}{qE^*} \frac{(3 - 4\nu)\sinh(2qh) - 2qh}{(3 - 4\nu)\cosh(2qh) + 2(qh)^2 - 4\nu(3 - 2\nu) + 5}, \qquad (2.21)$$

where we have first introduced the contact modulus $E^* := E/(1 - \nu^2)$, which has become the de-facto standard measure of stiffness in the context of contact mechanics. For a detailed description of the derivation procedure, the reader is referred to Ref. [71]. An approximation to the real-space Green's function $G^{(\mathrm{n})}$ can be obtained by numerically evaluating the inverse Hankel transform (defined in App. A) of Eq. (2.21). This is illustrated in Fig. 2.6 to reveal the influence of the Poisson's ratio and thickness: If ν is close to 0.5, the volume of the material (almost) remains constant, so pushing down on the surface in the center inevitably makes it bulge up in the surrounding area. The thickness h, on the other hand, is a proportionality factor for the lateral spread of the displacement field, as indicated by the normalization on the x-axis. The case $h \to \infty$ is known as an "elastic half-space" or "semi-infinite" body. This is by far the best-known version and was first used around the same time by both Hertz [3] and Boussinesq [18]. Note that for large qh, i.e. for all wavelengths of deformation considerably smaller than the thickness of the elastic body, the right-most fraction in Eq. (2.21) quickly approaches 1. Therefore, Eq. (2.21) becomes $\tilde{G}^{(\mathrm{n})}(q, h \to \infty) = 2/qE^* \ \forall \ q$, for which the inverse Hankel transform results in a closed-form analytic expression given by [18]

$$G^{(\mathrm{n})}(\mathbf{r} - \mathbf{r}') = \frac{1}{\pi E^*|\mathbf{r} - \mathbf{r}'|}. \qquad (2.22)$$
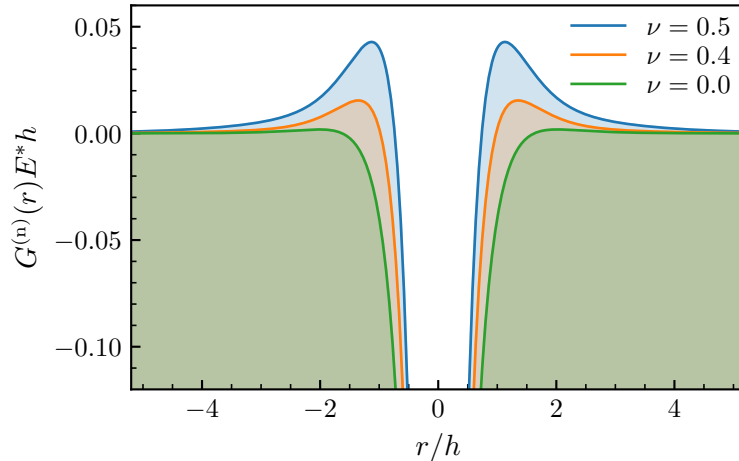
Figure 2.6: Graph of the normal Green's function, i.e. the displacement profile resulting from a concentrated force in the origin. The graphs represent the inverse Hankel transform of Eq. (2.21). In this case, they were approximated by GFMD simulations with linear system size $L \gg h$.

To derive the Green's function in Eq. (2.21), it was assumed that the lateral stresses in the surface vanish, i.e., at $z = 0$. This makes it inherently impossible for this model to accurately describe the deformation caused by interfacial friction. Relinquishing that boundary condition means that now all in-plane stresses and displacements need to be explicitly considered. Therefore, the previously one-dimensional Eq. (2.20) becomes a matrix equation defining the (Fourier transform of) the Green's tensor $\tilde{\mathbf{G}}$. What is used in GFMD, however, is not $\tilde{\mathbf{G}}$ but its inverse $\mathbf{\Phi} := \tilde{\mathbf{G}}^{-1}$:

$$\tilde{\boldsymbol{\sigma}}(\mathbf{q}) = \mathbf{\Phi}(\mathbf{q})\tilde{\mathbf{u}}(\mathbf{q}), \tag{2.23}$$

with $\tilde{\boldsymbol{\sigma}}$ being the FT of the in-plane stress vector $\boldsymbol{\sigma}(x, y) = (\sigma_{13}(x, y), \sigma_{23}(x, y), \sigma_{33}(x, y))$.

The components of the $\mathbf{\Phi}$ tensor, as well as its inverse $\tilde{\mathbf{G}}$ and all asymptotic limits and scaling relations as $h \to \infty$ or $q \to 0$, are given in App. B. A general solution method with which $\mathbf{\Phi}$ can be derived is described in the appendix of Ref. [72]. The authors implemented it in the form of a *Mathematica* notebook, which was made available to us in the context of Publication **V**.

2.4   Green's Function Molecular Dynamics (GFMD)

Almost all simulations reported in Chap. 4 were performed using some variation of the Green's function molecular dynamics (GFMD) technique. The source code containing all of the recent additions necessary to reproduce the obtained results can be found on GitHub [85]. GFMD is a boundary-value method allowing the numerical solution of linearly (visco-)elastic contact problems. It requires the fundamental solution (Green's function) $G(\mathbf{r})$ describing the relationship between displacements and stresses on the surface to be known. For a given surface stress distribution $\sigma(\mathbf{r})$, the resulting displacement distribution $u(\mathbf{r})$ can be calculated as the convolution of σ with G. Assuming periodic boundary conditions in the plane, this convolution equation can be transformed into Fourier space, where $\tilde{G}^{-1}$, the inverse of the FT of G, takes on the role of a stiffness:

$$\tilde{\sigma}(\mathbf{q}) = \tilde{G}^{-1}(\mathbf{q})\tilde{u}(\mathbf{q}). \tag{2.24}$$

This is an inverted (matrix) version of Eq. (2.20). The 3D version of GFMD, as developed for Publ. **V**, is described by the same equation, except that $\tilde{\sigma}$ and $\tilde{u}$ are vectors and $\tilde{G}$ is a tensor. The above notation makes this transition straight-forward so that the 3D version does not need to be introduced separately.

Nowadays, it is a simple task to numerically evaluate forward and backward Fourier transforms, so Eq. (2.24) allows us to compute the complete surface stress distribution resulting from an arbitrary displacement profile and vice versa. However, when solving a general contact problem, neither the correct displacement nor the correct stress distribution are usually known a priori. In order to determine these numerically, we also need a method prescribing how to iteratively update both of them until the correct configuration is reached. We realize that Eq. (2.24) describes an elastic stress response resulting solely from the constitutive equations of the material, which is only identical to the externally applied stress σ_{ext} if the system is in equilibrium. As long as $\tilde{u}(\mathbf{q})$ is still evolving, it must have a non-zero stress $\tilde{\sigma}_{\text{ext}}(\mathbf{q}) - \tilde{G}^{-1}(\mathbf{q})\tilde{u}(\mathbf{q})$ acting on it. Hence, solving the contact problem is equivalent to finding the root of this stress function, which, in turn, is equivalent to minimizing the underlying function for the potential energy of the system. Since the numerical minimization of a function is an omnipresent task in scientific applications, there are many available software packages that provide efficient algorithms dedicated to this purpose. For example, the *contact.engineering* website [69] as well as Bugnicourt *et. al.* [86] use a conjugate gradient (CG) algorithm to find the optimal configuration of a contact.

As the name suggests, GFMD follows the principles of molecular dynamics (MD) simulations to update the positional degrees of freedom, $\tilde{u}(\mathbf{q})$, according to the forces acting on them. For this purpose, we artificially introduce the mass $m(\mathbf{q})$ into Eq. (2.24) to obtain an equation of motion (EOM) that is isomorphic to that of the one-dimensional harmonic oscillator:

$$\tilde{\sigma}_{\text{ext}}(\mathbf{q}, t) = \tilde{G}^{-1}(\mathbf{q})\tilde{u}(\mathbf{q}, t) + m(\mathbf{q})\ddot{\tilde{u}}(\mathbf{q}, t). \tag{2.25}$$

Note that not only $\tilde{u}$, but also the external stress $\tilde{\sigma}_{\text{ext}}$ depends on the time t, because

the constantly varying displacement of the elastic body also changes where and how it interacts with the counter-surface. This interaction usually depends on the local distance between the surfaces according to a cohesive-zone model (CZM), which will be discussed in detail in Sect. 2.4.3. Finally, for the simulation to finish *in* the equilibrium configuration rather than oscillate around it, we also introduce a linear damping term and get the EOM of a damped harmonic oscillator

$$\tilde{\sigma}_{\text{ext}}(\mathbf{q}, t) = \tilde{G}^{-1}(\mathbf{q})\tilde{u}(\mathbf{q}, t) + \eta(\mathbf{q})\dot{\tilde{u}}(\mathbf{q}, t) + m(\mathbf{q})\ddot{\tilde{u}}(\mathbf{q}, t). \tag{2.26}$$

The choice of the introduced mass and damping terms will be discussed in the following Sections.

2.4.1 Conventional quasi-static GFMD

Since neither m nor η have any physical implication for the static contact problem to be solved, they can be arbitrarily adjusted to reach the equilibrium as fast as possible. If σ_{ext} were constant, the damped harmonic oscillator would relax fastest when it is near critically damped, i.e. $\eta^2 = 4m\tilde{G}^{-1} \ \forall \ \mathbf{q}$. This choice is usually referred to as mass-weighted GFMD (MW-GFMD). In principle, convergence can be improved by adjusting the masses or the damping over time, because σ_{ext} is, in fact, *not* constant. Such "dynamic mass-weighting" concepts have been tested in the past, but none of the implementations made it into the next "official" version of the GFMD code. The more robust approach would probably be to keep the masses constant and dynamically adjust the damping of each mode instead. This is because $\tilde{G}^{-1}$ is not a free parameter and the characteristic frequency $\omega_{\text{GFMD}} = \sqrt{\tilde{G}^{-1}/m}$ is used to determine the optimal time step size. Consequently, keeping the masses constant makes it easier to ensure the stability and efficiency of the algorithm, because only changing η does not affect ω_{GFMD}.

One presently available option in GFMD to further speed up the convergence is the fast inertial relaxation engine (FIRE) algorithm [87, 88]. This option switches off the damping term in Eq. (2.26) and increases the time step size for as long as the continuously measured potential energy in the system is decreasing. As soon as this trend turns around, the program stops the motion of all displacements and restarts with a smaller time step to more precisely probe the energetic minimum that has just been passed. By repeating this process and iteratively increasing the temporal resolution, FIRE typically does not only speed up the convergence but also improves the accuracy of the final configuration. However, since the global energy is used as a criterion, FIRE may not provide much benefit over conventional mass-weighting if there are only a few dominant $\mathbf{q}$ vectors in a given contact problem. This is where the aforementioned dynamic adjustment of mass or damping values for each individual $\tilde{u}(\mathbf{q})$ could potentially provide a performance advantage.

So far, the methodology relied heavily on Fourier-space, which requires periodic boundaries and a uniform discretization for an efficient fast Fourier transform (FFT) algorithm to be used. Opposed to this are real-space approaches that use a very fine discretiza-

tion in the vicinity of contact edges and a much coarser grid everywhere else to save memory and computation time. One example of such an approach is the one pursued by Putignano *et. al.* [89], which works in a displacement-controlled manner and was later generalized to viscoelastic contacts [90]. App. C discusses a similar design for a non-uniform real-space solver for axisymmetric contacts that follows the principles of conventional GFMD as closely as possible. In the reported state, it is technically working but nowhere near the necessary accuracy to compete with its Fourier-based counterpart. The description was included anyway, since it may provide some important insights or guidelines for future developments to benefit from.

2.4.2   Viscoelastic GFMD

The MD-inspired nature of GFMD makes it particularly capable of simulating realistic contact dynamics rather than just quasi-static systems. This is especially important for applications involving soft polymers, whose mechanical properties are noticeably affected by the rate (i.e. frequency ω) at which they are deformed. In that regard, the most general feature that all rubbers and elastomers have in common is that their Young's modulus (monotonically) increases from an asymptotic quasi-static value $E_0 := E(\omega \to 0)$ to an asymptotic high-frequency value $E_\infty := E(\omega \to \infty)$. While the exact shape of the underlying function varies, theoretical descriptions usually rely on linear models because of their mathematical simplicity. The well-known standard linear solid (SLS) is described in detail in App. E, while the present chapter focuses on the two employed numerical implementations and the differences between them. For simplicity, it is assumed that the Poisson's ratio ν of the material is approximately independent of ω and only the rate dependence of the Young's modulus needs to be considered.

The majority of the simulations reported in Publ. **IV** were performed using the viscoelastic material model described in Ref. [25], which is based on the Kelvin-Voigt (KV) representation of the SLS (see App. E.1). It uses a single EOM obtained by completely eliminating the internal displacement variable in the KV element using the external stress and its time derivative. To ensure stability, this derivative has to be smoothed by a low-pass filter (LPF), which makes the accuracy of the short-term material response time-step sensitive. However, it also makes the method computationally efficient compared to explicitly simulating the KV elements, especially when mostly the long-term response is of interest. This made the method particularly suited for the comparisons to experiments, where the simulations take multiple days to finish. Compared to the original KV implementation of Ref. [25], the Green's function of the semi-infinite body had to be replaced with that of the finite elastic film, i.e. Eq. (2.21). The resulting EOM can be written as

$$\tilde{G}^{-1}(q, \omega = 0)\big(\tau \dot{\tilde{u}}(\mathbf{q}, t) + \tilde{u}(\mathbf{q}, t)\big) = \tilde{\sigma}_{\text{ext}}(\mathbf{q}, t) + \frac{\tau}{s}\dot{\tilde{\sigma}}_{\text{ext}}(\mathbf{q}, t), \qquad (2.27)$$

where τ is the characteristic relaxation time and $s = E_\infty/E_0$.

The new model implemented for Publ. **III** and **IV** follows a different approach based on

the generalized Maxwell model (see App. E.2). In this case, the internal degrees of freedom in the Maxwell elements are explicitly simulated over time, making the short-term response arbitrarily accurate and stable. Furthermore, due to the adjustable number of Maxwell elements being joined in parallel, the model can reproduce a much broader range of relaxation functions. It does, however, come at the cost of a noticeably higher computational demand and memory consumption. The EOM in Eq. (2.26) still applies, except that the function $\tilde{G}$ corresponds to the high-frequency limit, i.e. assuming a contact modulus of $E_\infty/(1 - \nu^2)$ instead of $E_0/(1 - \nu^2)$. The stress resulting from the individual Maxwell elements is simply added to the external stress $\tilde{\sigma}_{\text{ext}}$ and the damping parameters $m(q)$ and η_0 are chosen so that all $\mathbf{q}$ are critically damped for the stiffness $k_\infty(q) := \tilde{G}^{-1}(q, \omega \to \infty)$. For each $\mathbf{q}$, there are N additional internal variables $\tilde{u}_n(\mathbf{q}, t)$, $n \in 1 \dots N$ corresponding to N Maxwell elements. The Maxwell parameters $\eta_n(q)$ and $k_n(q)$ are chosen according to the particular shape of the $E(\omega)$ curve that is reproduced, as explained in Publ. **IV**. The EOM is now a system of equations that reads

$$\tilde{\sigma}_{\text{ext}}(\mathbf{q}, t) + \sum_{n=1}^{N} k_n(q)\tilde{u}_n(\mathbf{q}, t) = k_\infty(q)\tilde{u}(\mathbf{q}, t) + \eta_0(\mathbf{q})\dot{\tilde{u}}(\mathbf{q}, t) + m(\mathbf{q})\ddot{\tilde{u}}(\mathbf{q}, t). \quad (2.28a)$$

$$\eta_n(q)\dot{u}_n(\mathbf{q}, t) = k_n(q)(\tilde{u}(\mathbf{q}, t) - \tilde{u}_n(\mathbf{q}, t)), \qquad n \in 1 \dots N. \quad (2.28b)$$

2.4.3 Cohesive-zone model (CZM)

The normal interaction between two surfaces is usually modeled within the small-slope approximation: If the slopes of both topographies are small, the local normal vector is approximately the same everywhere at any time, which we define parallel to the z-direction. This allows us to use a one-dimensional interaction model that is merely a function of the local gap g between the surfaces evaluated in z-direction. While the contemporary GFMD implementation technically supports the option to simulate two elastic surfaces in contact with each other, this section will exclusively assume the case in which one surface is elastic and movable while the other is rigid and immovable. Note that within the small-slope framework, two (frictionless) elastic bodies 1 and 2 with contact moduli E_1^* and E_2^* and topographies $h_1(\mathbf{r})$ and $h_2(\mathbf{r})$ are equivalent to one rigid surface with $h(\mathbf{r}) = h_1(\mathbf{r}) + h_2(\mathbf{r})$ and one flat elastic surface with contact modulus $E^* = E_1^* E_2^*/(E_1^* + E_2^*)$ [3]. Therefore, without loss of generality, most descriptions of contact mechanics use one rigid and one deformable solid. This convention was also assumed for all numerical results reported in Chap. 4.

Probably the most commonly used interaction potential is the adhesion-less "hard wall", which simply defines an infinitely large energy barrier at $g = 0$ preventing the two bodies from interpenetrating. In numerical realizations, this is not achievable by a literal implementation of such a potential. The GFMD code implements hard-wall interaction as part of the elastic response rather than a force-separation law in real space. At the start of one time step, all displacement modes of the elastic body are propagated according to the current stress acting on them. After that, all points that now penetrate

the rigid body are shifted back in z direction to where they sit exactly on the surface. Only then is the elastic stress response evaluated for the next time step, so it automatically includes the hard-wall component. This is quite efficient given that stresses never need to be evaluated in real space, saving two Fourier transforms (one forward and one backward) per time step. However, since forcing individual surface points to different positions heavily disturbs the natural harmonic oscillation of the displacement modes, it is prone to becoming unstable. It is also difficult to combine this method with a displacement control, since the overlap elimination affects the mean displacement in an unpredictable way. For these reasons, there is also a "soft-wall" potential. It features a simple repulsive harmonic potential for $g < 0$, which is evaluated in real space. This is formally the same as using a surface energy of $\Delta\gamma = 0$ in the cosine-CZM, which will be introduced in the following. For example, Publ. **I** made use of a hard-wall interaction while Publ. **V** relied on a soft wall instead.

The CZM employed in all adhesive simulations reported in Publ. **I, III** and **IV** was the cosine-shaped potential proposed by Ref. [91]. It maximizes numerical stability by defining a continuously differentiable potential, whose second derivative is bounded everywhere. This inherent threshold to the interaction stiffness also limits the maximum characteristic eigenfrequency of all degrees of freedom in the system, at least as long as they are independent of each other. This makes it relatively easy to find an appropriate time step in the molecular dynamics solver, relaxing towards equilibrium position as fast as possible without creating instabilities. In addition to $\Delta\gamma$, we need one other parameter to uniquely define the interaction law, for which we usually use the range of adhesion ρ. This way, the cosine interaction potential Γ_{cosine} as a function of the local gap $g = g(\mathbf{r})$ at a point with lateral coordinates $\mathbf{r} = (x, y)$ reads

$$\Gamma_{\text{cosine}}(g) = -\Delta\gamma \cdot \begin{cases} \{1 - (\pi g/\rho)^2/4\} & \text{for } g \leq 0 \\ \{1 + \cos(\pi g/\rho)\}/2 & \text{for } 0 < g < \rho \,, \\ 0 & \text{for } g \geq 0 \end{cases} \tag{2.29}$$

which approaches the Johnson, Kendall and Roberts (JKR) limit as $\rho \to 0$. The resulting interfacial stress σ_{cosine} and stiffness k_{cosine} are given as

$$\sigma_{\text{cosine}}(g) = -\frac{\partial\Gamma(g)}{\partial g} = -\frac{\pi\Delta\gamma}{2\rho} \cdot \begin{cases} \pi g/\rho & \text{for } g \leq 0 \\ \sin(\pi g/\rho) & \text{for } 0 < g < \rho \\ 0 & \text{for } g \geq 0 \end{cases} \tag{2.30a}$$

$$\text{and} \quad k_{\text{cosine}}(g) = \frac{\partial^2\Gamma(g)}{\partial g^2} = \frac{\pi^2\Delta\gamma}{2\rho^2} \cdot \begin{cases} 1 & \text{for } g \leq 0 \\ \cos(\pi g/\rho) & \text{for } 0 < g < \rho \,. \\ 0 & \text{for } g > 0 \end{cases} \tag{2.30b}$$

The stiffness is formally undefined in the singular isolated point $g = \rho$ but both the left- and right-sided limits exist and are finite. Moreover, the maximum negative stiffness in the adhesive regime is well-defined and equal to the repulsive stiffness $\max(k_{\text{cosine}}) = \pi^2\Delta\gamma/(2\rho^2)$.

To ensure the stability of the numerical procedure, the elastic stiffness k_{el} resulting from the constitutive equation, according to Eq. (2.21), also needs to be taken into account. The maximum elastic stiffness is that belonging to the maximum wave vector $q_{max} = \sqrt{\max(q_x^2) + \max(q_y)^2}$ (assuming that $q_{max} \gg 1/h$). In most cases, the periodically repeated simulation cell will either be one-dimensional $(D = 1)$ with length L and N discretization points, or two-dimensional $(D = 2)$ with dimensions $L \times L$ and discretization $N \times N$. This leads to $q_{max} = \sqrt{D}N\pi/L$ and consequently $\max(k_{el}) = q_{max}E^*/2 = E^*\sqrt{D}N\pi/(2L)$ (again assuming $q_{max} \gg 1/h$). On a slightly oversimplified level, k_{el} and k_{cosine} can be interpreted as two springs working against each other. To avoid instabilities equivalent to rupture in the elastic solid, k_{el} must always be larger than $-k_{cosine}$, i.e. $\kappa_{pot} := -\min(k_{cosine})/\max(k_{el}) < 1$. κ_{pot} is the relative curvature of the interaction potential acting as a safety factor. The interaction potential in GFMD simulations is usually set up taking $\Delta\gamma$ and κ_{pot} as input parameters and calculating ρ automatically from Eq. (2.30b), i.e.

$$\rho = \sqrt{\frac{\pi^2 \Delta\gamma}{2\kappa_{pot}\max(k_{el})}} = \sqrt{\frac{\pi\Delta\gamma L}{\kappa_{pot}E^*N\sqrt{D}}}. \tag{2.31}$$

Since the interfacial interaction is local in real space, it would be more precise to compare k_{cosine} to the elastic stiffness of a deformation exciting all $\mathbf{q}$-modes equally. That would correspond to a concentrated displacement in a single point $\mathbf{r}$ rather than the amplitude of a sinusoidal displacement undulation with wavelength $2\pi/q_{max}$. This could potentially reduce or even eliminate the need to repeatedly check if κ_{pot} has to be adjusted from one simulation to the next.

To demonstrate the useful properties of the cosine-shaped interaction potential, we will compare it to some commonly-used alternatives. Probably the best-known adhesive CZM is the one proposed by Dugdale and Barenblatt [92, 93]. The adhesive part of its potential energy has a linear shape and is combined with a repulsive hard wall. This comes with the disadvantage of a diverging second derivative, making the interaction sensitive to small perturbations wherever the local gap is close to $g = \rho$. In practice, this means that either very small time steps and long relaxations are necessary to reach complete equilibrium, or that the simulation keeps very gently fluctuating around the equilibrium. These fluctuation usually constitute an error of significantly less than 1%, seeing that only a very small fraction of the points in the simulation cell are near that critical $g = \rho$ state. In the context of Publ. **III**, some simulations were run with a Dugdale model attraction law combined with harmonic repulsion. As briefly discussed but not explicitly shown, the scaling relation between time and Tabor parameter is valid regardless of the exact shape of the interaction potential, at least for indenters with polynomial height profiles. The displacement and the stress profiles, on the other hand, look distinctly different in the vicinity of the contact edge, as Fig. 2.7 shows.

The previously discussed potentials are explicitly cut off at a distance of $\rho \geq 0$ from the opposite surface. This leads to small computation times and quickly approaches the short-ranged limit. Since the most relevant type of adhesive interaction for the real-world version of the studied systems is the van-der-Waals (vdW) force, the most accurate
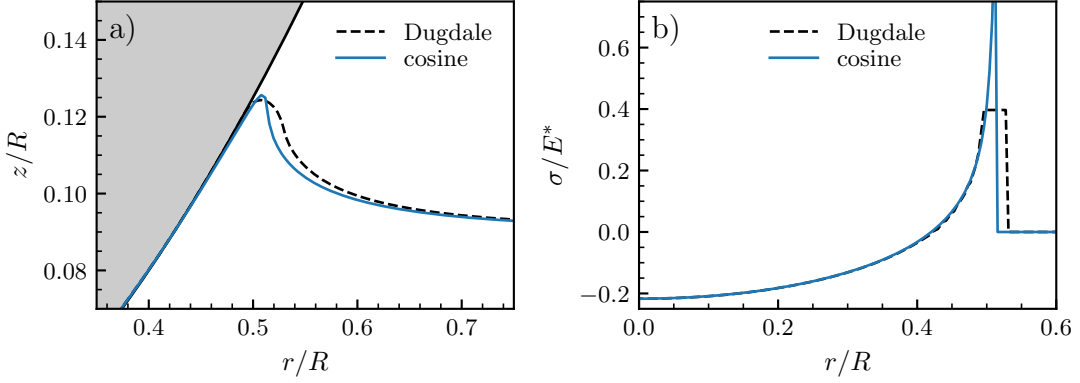
Figure 2.7: a) displacement profile and b) stress distribution obtained for an adhesive Hertzian contact using two different CZMs. The range of adhesion ρ in the Dugdale model was set to $\rho_{\text{Dugdale}} = 3.8\rho_{\text{cosine}}$ to achieve approximately the same far-field displacement.

model to use would probably be a Buckingham or Lennard-Jones (LJ) interaction law. Both of these potentials describe the interaction between the molecules making up a macroscopic body, where the attractive component is proportional to the inverse sixth power of the distance between particles. This relationship is an exact result for vdW, obtained by averaging the interaction between the random spontaneous and induced dipole moments occurring in the electron distributions of particles [32, 94]. To derive an expression for the interaction between points on surfaces, the potential has to be integrated over the respective area elements [95]. In the case of LJ, this ultimately leads to the stress-distance relation [83, 96, 97]

$$\sigma_{\text{LJ}}(g) = \frac{8\Delta\gamma}{3\rho}\left(\left(\frac{g}{\rho}+1\right)^{-9} - \left(\frac{g}{\rho}+1\right)^{-3}\right). \tag{2.32}$$

Note that compared to Ref. [83], the equilibrium position was shifted to $g = 0$ instead of $g = \rho$. Some contact mechanics studies also use a Morse type of interaction potential [91], which comprises a sum of two exponential functions:

$$\sigma_{\text{Morse}}(g) = \frac{2\Delta\gamma}{\rho}(\exp(-2g/\rho) - \exp(-g/\rho)). \tag{2.33}$$

This shape of potential also originates from atomic interactions, whereas the attractive term is more representative of the embedding energy in metallic or covalent bonding than vdW adhesion. One advantage is that, contrary to LJ, Morse does not diverge in the repulsive regime.

Fig. 2.8 directly compares the introduced CZMs in terms of their stress-gap curve. The individual values of ρ were chosen so that they all take on the same slope in $g = 0$, because this stiffness is what typically limits the efficiency and stability of GFMD simulations. It is evident that at a given computational workload, the cosine-shaped potential is by far the most short-ranged option, producing the largest negative stress. As shown in Fig. 2.7b, this makes it much easier to approach the theoretical JKR limit, which features stress singularities at the contact edge. The repulsive part of Γ_{cosine}, on the other hand, is relatively soft, which is arguably its most severe disadvantage. The

interpenetration of the contacting bodies often constitutes a non-negligible deviation from the usual reference case that is the hard wall limit. In principle, this problem can be alleviated by adjusting the CZM, albeit only at the cost of computational stability or efficiency.
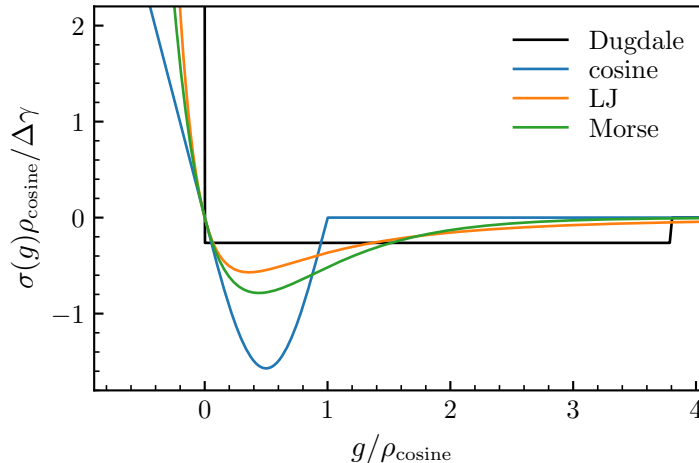
Figure 2.8: Normal stress σ as a function of local gap g according to the Dugdale (black), cosine (blue), Lennard-Jones (orange) and Morse potential (green). All values of ρ have been adjusted so that all curves (except Dugdale) have the same stiffness at $g = 0$, i.e. $\rho_{\text{LJ}} = \rho_{\text{cosine}}\sqrt{32}/\pi$ and $\rho_{\text{Morse}} = \rho_{\text{cosine}}2/\pi$. Since the Dugdale model does not have a well-defined stiffness, $\rho_{\text{Dugdale}} = 3.8\rho_{\text{cosine}}$ was chosen, just as in Fig. 2.7.

2.4.4 Tangential interaction

In the contemporary GFMD implementation, in-plane traction forces are modeled in terms of Amontons's law with a velocity-independent Coulomb friction coefficient in gross slip condition. At each in-plane point $\mathbf{r}$ of the elastic body's surface, the lateral stress $\boldsymbol{\sigma} = (\sigma_{\text{xz}}, \sigma_{\text{yz}})$ is simply given by

$$\boldsymbol{\sigma}(\mathbf{r}) = -\mu_{\text{c}}\hat{\mathbf{v}}_{\text{rel}}(\mathbf{r})|\sigma_{\text{zz}}(\mathbf{r})|, \tag{2.34}$$

where μ_{c} is the Coulomb friction coefficient and $\hat{\mathbf{v}}_{\text{rel}}$ the unit vector in the direction of the local relative in-plane velocity between the two surfaces. The absolute value of σ_{zz} is considered here to also create traction in adhesive contact elements while avoiding anti-friction. Publ. **V** did not consider any adhesive contacts, so $|\sigma_{\text{zz}}(\mathbf{r})|$ could be replaced with the normal pressure $p_{\text{z}}(\mathbf{r}) \geq 0 \, \forall \, \mathbf{r}$.

Since only steady-state sliding in gross-slip condition is considered in this work, it pertains to relatively large velocities, where the assumption of Coulomb friction is justified. Most real systems show a velocity-dependent friction coefficient at low values of v_{rel}, for which there is no universal function. A common case is a Stokes-type drag friction regime at low velocities, where $\mu \propto v_{\text{rel}}$, which transitions into either a logarithmic or power-law behavior $\mu \propto v_{\text{rel}}^{\beta}$ with $0 < \beta < 1$ and then eventually levels to a constant value μ_{c} at higher velocities [98, 99]. Consequently, the velocity-independent Coulomb regime is arguably the most universal feature in solid friction.

Eq. (2.34) combines the Coulomb model with the empirical law that the friction force is not proportional to the nominal contact area, but rather to the normal load. This realization is usually attributed to Amontons, although it had already been discovered by Leonardo da Vinci two centuries earlier [100, 101]. It needs to be kept in mind that this principle was observed on the macroscopic scale, and it is still unclear to what extent it holds when microscopic roughness is taken into account. This is because, for small average contact pressures, the mean pressure $\bar{p}$ and the true area of contact A_c are approximately proportional to each other (see Sect. 3.2). Hence, from a macroscopic measurement, it is not possible to discern between a microscopic mechanism that is proportional to A_c and one that is proportional to the local pressure $p_z(\mathbf{r})$ (i.e. a locally valid Amontons's law as in Eq. (2.34)) [102]. Some studies suggest that the microscopic friction stress is actually constant within the contact area for low values of $\bar{p}$, while a contribution proportional to the local $p_z(\mathbf{r})$ only starts to become relevant at large compressions [103]. The relative influence of these two components seems to depend on how well the two surfaces adhere to each other [104].

Chapter 3

State of the art

3.1 Quasi-static single asperity contacts

The elastic constitutive equations outlined in Sect. 2.3 are easiest to solve for axisymmetric systems, where the method of dimensionality reduction can be applied [105]. The general solution method for non-adhesive contacts in terms of the Hankel transform has been described by Sneddon [106] and the adhesive case by Yao and Gao [107]. The first explicit solutions for adhesive contacts were extensions of the Hertz contact theory for paraboloid bodies [3]. Johnson, Kendall and Roberts (JKR) derived their theory by adding an inverted flat-punch stress profile to the elliptic Hertzian stress distribution [108,109]. This produces the characteristic integrable stress singularities at the edge of the contact that asymptotically scale with the inverse square root of the distance from the edge, which can also be seen in the numerical data presented in Fig. 3.1b. An alternative approach to JKR is to keep the displacement profile unchanged from the purely repulsive case and only add the adhesive stress distribution outside of the contact area instead. This method effectively just adds an offset load pressing down the indenter, which balances the adhesive force acting outside the contact. [1] The corresponding solution is often credited to Derjaguin, Müller and Toporov (DMT) [110], but was already published as early as 1932 by Bradley [111]. The respective pull-off force predictions of JKR and DMT for a rigid sphere of radius R detaching from an elastic half-space are

$$F_{\text{JKR}} = \frac{3}{2}\Delta\gamma\pi R \quad \text{and} \tag{3.1}$$

$$F_{\text{DMT}} = 2\Delta\gamma\pi R. \tag{3.2}$$

Contrary to the pull-off force prediction of the circular flat punch (see Eq. (2.3)), the result does not depend on the elastic properties of the half-space. The discrepancy in the prefactor between the two approaches is due to the fact that JKR corresponds to the limiting case of infinitely short-ranged adhesion and the DMT model to an infinitely

---

[1]This equivalence only happens to work out for a parabolic indenter shape. For other shapes, the integration of the interaction over the infinitely large non-contact area would either vanish or diverge.

large range of interaction ρ. The intermediate case was solved by Maugis and later Popov *et. al.* assuming a Dugdale model for the finite-ranged interactions [112, 113].

The so-called Tabor coefficient [114]

$$\mu_T := R^{1/3} \left(\frac{\Delta\gamma}{E^*} \right)^{2/3} \rho^{-1} \tag{3.3}$$

provides a dimensionless measure for the inverse range of adhesion ρ^{-1}, where JKR corresponds to the limit $\mu_T \gg 1$ and DMT to $\mu_T \ll 1$. In the literature (e.g. Refs. [115, 116]), μ_T is sometimes formulated in terms of the maximum adhesive stress σ_{th} rather than ρ. This stress can generally be substituted with $\alpha\Delta\gamma/\rho$, where the dimensionless prefactor α depends on the specific model used for the normal interaction between the surfaces (see Sect. 2.4.3). Consequently, the only difference between the σ_{th}-based definition and Eq. (3.3) is effectively a dimensionless prefactor of order unity. Nevertheless, this discrepancy needs to be taken into account when comparing systems with specific values of μ_T between different publications. In the case of a Dugdale CZM, both ways to define μ_T are exactly equivalent, i.e., $\alpha = 1$. However, in the present study, most results pertain to the cosine-shaped attraction model with harmonic repulsion, for which $\alpha = \pi/2$, as indicated by Eq. (2.30a).

The concept of the Tabor parameter can easily be generalized to the flat punch [117], polynomial indenters [118] and also to randomly rough surfaces by using the rms radius of curvature in place of R [58, 59]. Furthermore, in the appendix of Publ. **III**, we explicitly show that the same definition of Tabor parameter applies to both 1D and 2D contacts. In the JKR limit, the adhesive one-dimensional parabolic indenter can also be solved analytically [119].
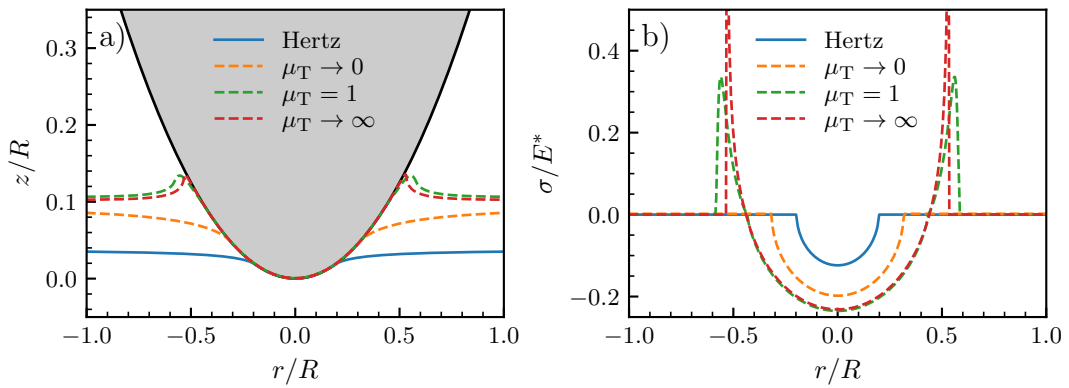
Figure 3.1: Comparison between the adhesion-less Hertz indenter (solid blue line) and simulations near the DMT limit ($\mu_T \approx 0.01$, dashed orange line) and JKR limit ($\mu_T \approx 3$, dashed red line) and an intermediate case ($\mu_T = 1$, dashed green line) in terms of a) displacement profile and b) stress distribution. In all cases, the indenter is pressed down with the force $F = 0.01 E^*/R^2$ and the surface energy was set to $\Delta\gamma = 0.01 R E^*$.

Using the numerical method outlined by Greenwood [120], Ciavarella *et. al.* [121] have found that the JKR limit is not yet fulfilled at $\mu_T \approx 5$, where they still saw a deviation of almost 50% in terms of the load-displacement hysteresis. This has recently been

confirmed by GFMD simulations [91], showing that especially the premature jump into contact makes it difficult to approach the short-ranged limit. A Tabor parameter of 10 was still very far from the JKR load-displacement relationship, while the detachment curves are already indiscernible for $\mu_{\mathrm{T}} \approx 2$. Convergence of the hysteresis was rather slow, with the relative error disappearing with the cubic root of the mesh size when ρ is calculated as in Eq. (2.31).

3.2   Quasi-static rough contacts

Intuitively, it is tempting to think of rough contacts as a collection of many individual asperity contacts. The most famous model following this idea is the one developed by Greenwood and Williamson (GW) [65]. In its original version, it approximates rough surfaces as infinitely many Hertzian asperities with identical radius R. The normal (z-)coordinates of the paraboloids are distributed according to a Gaussian distribution with a standard deviation equal to the known rms height of the surface. Taking adhesion into account is as straight-forward as replacing the Hertz equations with those from JKR [122], DMT [123] or even a more general single-asperity description with a finite range of adhesion, like the Maugis-Dugdale model [124]. GW theory was the first successful analytical rationalization of the commonly observed linear relationship between external normal pressure p_z and relative contact area a_r for small p_z/E^*. However, probing GW's implications more closely reveals multiple flaws, mostly originating from the neglected elastic interaction between asperities [47,125] and poor representation of the real roughness [126]. Most notably, the predicted range of linearity between p_z and a_r is orders of magnitude too small and the corresponding proportionality factor vanishes in the limit of infinitely large surfaces [127]. The practical applicability of the model further suffers from the definition of a representative radius of curvature of the topography. The second derivative of the height profile strongly depends on the smallest scales, which are particularly challenging to measure. Nevertheless, probably because of its simplicity and instructional character, research trying to correct some of GW's shortcomings is still ongoing [128–133]. Very similar to GW in spirit but slightly more elaborate is the model developed by Bush *et. al.* [134], in which the prediction of linearity between p_z and a_r does not vanish in the thermodynamic limit [96].

A completely different approach to the problem was taken by Persson [23]. He started from the inherent multi-scale nature of roughness and realized that as the magnification ζ (corresponding to the maximum wave number) is increased and finer length scales of roughness are added, the stress histogram is smeared out in a diffusive process [135]. This is because the underlying partial differential equation is isomorphic to Fick's second law, where ζ replaces time and the stress replaces the lateral coordinate. Solving this equation allows the most important contact properties to be calculated either as a closed-form solution or in the shape of integral equations depending only on the contact modulus E^* and the PSD of the rough surface $C(\mathbf{q})$. The linearity between external pressure p_z and relative contact area a_r is predicted to depend on the rms gradient $\bar{g}$ of the roughness profile according to [136]

$$a_r \approx \frac{\sqrt{8/\pi}}{E^*\bar{g}} p_z \tag{3.4}$$

for small dimensionless pressures $p_z/E^*\bar{g}$. Brute-force numerical studies show the dimensionless numerator to be closer to 2 than $\sqrt{8/\pi} \approx 1.6$, albeit slightly dependent on resolution (i.e. maximum magnification ζ) [136,137]. Eq. (3.4) represents a much more rigorous explanation for this well-known linearity than GW, especially because it approximates a much wider range of pressures. Furthermore, describing the topography

based on its complete PSD is a much more accurate representation than the replacement with parabolic asperities in GW. Unsurprisingly, this reliance on the PSD makes Persson's original model most accurate near full contact, where the displacement of the elastic body exactly follows the rough topography. A more recent version of the theory improves the overall accuracy by explicitly incorporating partial contact [138]. With this enhancement, good agreement is observed between simulations and most of the theoretical predictions [136,139], although a systematic analysis of the underlying assumptions reveals that the close agreement is partially thanks to fortuitous error cancellation [135].

Persson applied the same principles to the adhesive case using an effective surface energy $\gamma_{eff}(\zeta)$ in place of the constant (ideally flat) surface energy $\Delta\gamma$ [41,50]. Its value depends on magnification and is calculated from the sum of surface energy U_{ad} and the corresponding elastic strain energy U_{el}, i.e. $U_{el} + U_{ad} = -\gamma_{eff}A_0$, where A_0 is the nominal contact area. It is important to note that the calculation of U_{ad} in his description uses the real contact area rather than the projected one. For this reason, for small roughness amplitudes and/or small elastic moduli, $\gamma_{eff} > \Delta\gamma$, which implies a macroscopic increase of adhesion with roughness amplitude. This is in agreement with multiple experimental studies [39,40,42] and provides a rationalization of the empirical Dahlquist criterion [49,50].

In Persson's framework for adhesive contacts, the pull-off stress can be calculated by inserting a magnification-dependent adhesive detachment stress σ_a. Its determination can be based on a Griffith approach given the surface energy γ_{eff}, e.g. assuming a penny-shaped crack whose diameter corresponds to the topographical wavelength [41,140]. For simple geometries, this fracture mechanics approach is exact in the limit of infinitely short-ranged surface interaction. In the case of finite-ranged adhesion, the interaction potential $\Phi(g)$ depending on the local separation g between the surfaces needs to be integrated over g for the calculation of γ_{eff} [141]. Using this generalization, the theory's predictions also match numerical calculations for adhesive rough contacts, except that the relative repulsive contact area is slightly underestimated and the attractive area overestimated. A similar result has been observed when Persson's theory is applied to 1D contacts [139], suggesting that the mismatch in contact area is a small systematic error arising in the case of partial contact. Joe and Barber [96,97] presented another solution of the adhesive contact problem, which closely followed the principles of Persson's theory. However, they included some simplifications accounting for their choice of a Lennard-Jones interaction law without hard-wall repulsion. Once again, they found good agreement with numerical (GFMD) data in terms of γ_{eff} and force-displacement relations.

Except for a few available closed-form expressions, the equations in Persson's theory usually require numerical solution techniques. However, even without knowing exact solutions, some tendencies and limiting cases can easily be justified using simple mathematical arguments. For example, in the limit of infinite magnification, adhesion vanishes for Hurst exponents $H \leq 0.5$. This can be understood in terms of the areal elastic energy density V_{el}/A_0 that would be necessary to form full contact even at the smallest scales.

With a strictly self-affine, isotropic PSD $C(q) \propto q^{-2-2H}$ according to Eq. (2.5) for wave vectors larger than q_0, that energy would equate to

$$V_{\mathrm{el}}/A_0 = \int \mathrm{d}^2 q \frac{qE^*}{2} C(q) \propto E^* \int\limits_{q_0}^{\infty} \mathrm{d}q q^{-2H}, \qquad (3.5)$$

which diverges for $H \leq 0.5$. On the other hand, for $H > 0.5$ and a PSD with roll-off regime following Eq. (2.6), the integrand constituting this energy has a maximum at $q = q_{\mathrm{r}}$, suggesting that $\lambda_{\mathrm{r}} = 2\pi/q_{\mathrm{r}}$ is the most important lateral length scale in the system. These arguments are based on full contact but provide a reasonable way to qualitatively rationalize results measured on rough contacts, whether they are adhesive or not.

When it comes to direct comparisons between the predictive capabilities of various theoretical and numerical methods, the most extensive study to date is the *Contact Mechanics Challenge* [47, 142]: any interested research groups were challenged to make predictions for the same well-defined rough contact problem, which could even be realized experimentally, highlighting the real-world implications of the study [143]. The combined effort of the challenge's participants reveals a couple of clear differences between approaches: computationally expensive brute-force numerical solutions, like those based on molecular dynamics (MD) or on Green's functions, are generally the most accurate. Heavily simplified models like the Winkler foundation or GW-based approaches lead to qualitatively wrong tendencies in terms of the interfacial gap, stress probabilities and contact patch distributions, with the relative contact area being at least quantitatively off. Persson's theory, on the other hand, provides qualitatively correct predictions in almost all cases, especially for high external pressures pertaining to large relative contact areas.

3.3 Stickiness criteria

Due to the complexity of explicitly solving Persson's theory, there have been multiple attempts to narrow down rough surface adhesion into so-called "stickiness criteria", which estimate the roughness threshold below which a surface feels macroscopically sticky. The first such approach was outlined by Persson and Tosatti (PT) [50], based on the simple idea that the work of adhesion is reduced by the elastic energy required to form contact. The corresponding closed-form criterion for stickiness can be derived by neglecting the surface slope in the determination of the adhesive energy and assuming that the effective surface energy $\Delta\gamma_{\text{eff}} = \Delta\gamma - V_{\text{el}}/A_0 > 0$ [144]. For a surface with a self-affine spectrum with Hurst exponent $H > 0.5$ between wave vectors $q_0 = 2\pi/\lambda_0$ and ∞ (see Eq. (2.5)), the criterion reads

$$\bar{h}_{\text{PT}} < \sqrt{\frac{2H-1}{\pi H}}\sqrt{\lambda_0 \frac{\Delta\gamma}{E^*}}. \tag{3.6}$$

Wang and Müser recently confirmed the validity of this criterion, only adjusting it by a factor of 2 [59]. The central property of Eq. (3.6) is the proportionality to $\sqrt{\lambda_0}$, which represents the largest lateral length scale in the topography. Microscopic properties have little effect, except when $H \le 0.5$, in which case Eq. (3.6) is invalid and stickiness is instead predicted to vanish completely, regardless of $\bar{h}$.

Ciavarella [66] used the stress-displacement relationship obtainable from a BAM assumption to arrive at a similar criterion. Once again, it depends only on the macroscopic roughness parameter $\sqrt{\lambda_0}$ and differs from PT solely in the prefactor. The same procedure was later applied to a roughness spectrum that is truncated at a certain maximum wavevector q_1 [144], revealing that the criterion is substantially less sensitive to changes in $\zeta = q_1/q_0$ and H than PT, even converging for $H \le 0.5$ and $\zeta \to \infty$. Although this result is questionable from a purely mathematical point of view, it seems reasonable in real-world applications: Given that the assumptions of continuum mechanics are fundamentally wrong at the molecular level, it certainly makes sense to terminate the spectrum at a maximum wavenumber q_1 representative of typical atomic distances or vdW interaction ranges.

Opposed to this group of very similar macroscopic criteria is the criterion by Pastewka and Robbins (PR) [57]. They assumed that each repulsive area element A_{rep} is enclosed by a "ring" of attractive contact with width d_{att}, which depends on the typical absolute value of the surface slope h' at the contact perimeter as well as the range of adhesion ρ. The displacement profile in the vicinity of the (repulsive) contact area is described by the adhesion-less case, where the displacement varies with the 3/2 power of the distance from the contact perimeter. This assumption puts this theory in the Bradley/DMT limit of long-ranged adhesion, even though it explicitly takes ρ into account. A_{rep} is determined assuming a paraboloid with radius of curvature calculated from the rms curvature h'' of the surface. Hence, the model depends on both the rms gradient and rms curvature, making it highly sensitive to small-scale features (large wave numbers, see Eq. (A.8c)). Finally, a surface is assumed to feel sticky whenever a non-zero relative

contact area is obtained even at an external pressure of 0, i.e the slope of the contact area-pressure curve is initially negative. This leads to the criterion

$$\frac{h'\rho}{2}\frac{E^*}{\Delta\gamma}\left(\frac{h'^2}{h''\rho}\right)^{2/3} < 1, \tag{3.7}$$

which does not converge for $\zeta \to \infty$. Using an explicit value for ζ for the same self-affine roughness profile as above (Eq. (2.5)), Eq. (3.7) adopts the form

$$\bar{h}_{\mathrm{PR}} < \lambda_0^{3/5}\rho^{2/5}\left(\frac{\Delta\gamma}{E^*\rho}\right)^{3/5} f(H, \zeta), \tag{3.8}$$

where $f(H, \zeta)$ is a dimensionless geometric factor containing the spectral properties of the surface. Compared to the previous models, PR explicitly take the range of adhesion ρ into account and scales with the 3/5 rather than 1/2 power of λ_0. Another criterion with the same exponents was derived by Violano *et. al.* [145], also using the DMT assumption but estimating the adhesive contact area based on Persson's theory rather than a single asperity description. Consequently, their criterion converges for $\zeta \to \infty$, which makes it more easily comparable to the ones proposed by Persson-Tosatti, Wang-Müser and Ciavarella. Neglecting the weak dependence on H for $H > 0.5$, their result can be written as [145]

$$\bar{h}_{\mathrm{Vio}} < \lambda_0^{3/5}\rho^{2/5}\left(\frac{\Delta\gamma}{E^*\rho}\right)^{3/5}\left(\frac{9}{8\pi}\right)^{3/5}, \tag{3.9}$$

which can be seen as a special case of Eq. (3.8) for intermediate magnifications ($\zeta \approx 10^3$) and large Hurst exponents ($H \approx 0.8$).

Rigorous comparisons between criteria and precise numerical data are provided in Ref. [59], making a strong case for the PT and related criteria. However, it should be noted that in the case of large $\Delta\gamma > V_{\mathrm{el}}/A_0$, the starting configuration is often already in full contact and detaches uniformly. This scenario is rarely observed in reality and usually overestimates the pull-off stress by multiple orders of magnitude, as described in the context of the adhesion paradox in Sect. 2.1. Furthermore, the authors always start the detachment from a zero load configuration and neglect the effect of the preload, which plays a critical role in many real systems, especially with viscoelastic dynamics [146, **IV**].

In summary, simple closed-form expressions for the stickiness of surfaces exist but are not suited for quantitative adhesion predictions. Estimating the pull-off force or adhesive hysteresis would require the numerical evaluation of Persson's theory for the PSD in question. Applying this procedure to real surfaces, however, is complicated by the challenges of the precise experimental roughness characterization necessary to determine the PSD (see Sect. 2.2.2). Furthermore, most practically relevant adhesive materials have viscoelastic mechanical properties, where the quasi-static theories fail and brute-force simulations are currently the only available option.

3.4 Fibrillar adhesives

So far, the elastic body has been assumed to be initially flat, which is a necessary prerequisite for the translational invariance of the problem, lending itself to the Green's function method. The situation changes when the elastic material itself has a topography that cannot be approximated as flat (i.e. it violates the small-slope approximation), as is definitely the case for pillar arrays. Therefore, their theoretical description typically relies on different methods, which shall be roughly outlined here.

For the most part, the improved adhesive performance of fibrillar compared to unstructured surfaces can be explained by a combination of two factors: i) fibrils are more compliant than bulk since they have room to expand and contract laterally and can buckle [5] and ii) a propagating interfacial crack is trapped and has to re-initiate repeatedly at every fibril, requiring a larger energy release rate than the propagation of an ideal straight crack [5, 7, 147]. The latter effect is also referred to as the flaw tolerance of the structure [148].
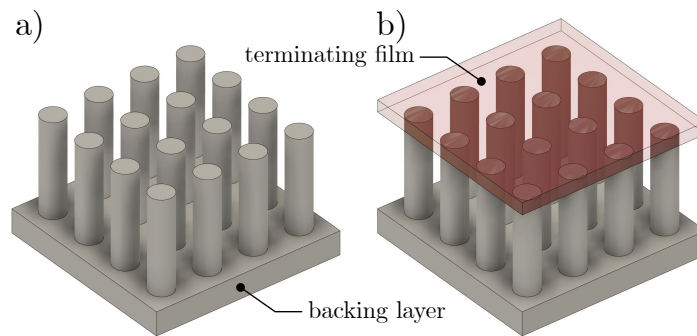
Figure 3.2: Schematic image of a simple cylindrical pillar array a) without and b) with a terminating layer (semi-transparent red).

Hui *et. al.* [5] have studied pillar structures theoretically and found that for very small fibril radii, the pull-off process is no longer sensitive to interfacial crack propagation but rather limited by the theoretical strength σ_{th}. However, fibrils this thin are probably not practical, since the absolute contact area would be very small, and because they would have a tendency to clump together [9, 149]. In practice, the pull-off is most likely limited by fracture mechanics, in which case the authors derive a pull-off stress σ_{po} under the assumption of a perfectly sticky interface.

The interaction between fibrils and a propagating crack has multiple aspects, whose relative contributions depend on the individual system in question. First of all, the fibrils can be thought of as introducing periodic "notches" in the crack front, effectively blunting it and reducing the stress concentration. This model has been studied theoretically by Gao and Rice [150, 151] and later been introduced in a numerical contact mechanics solver [152]. Second, the fibril interface does not feature a pre-existing crack, each time requiring the initiation of a new one releasing the entire elastic energy stored in the fibril. This constitutes a much larger energy barrier than that of conventional

crack propagation. Finally, the resulting discontinuous detachment sequence leads to more viscoelastic dissipation in the material, further increasing the load-displacement hysteresis. As a result of these mechanisms, experimental studies have reported an increase in the energy release rate compared to a flat interface without fibrils by a factor of 4-10 [7] and 10-20 [153] for different geometries.

Bio-inspired fibrillar surfaces also provide a lot of different design choices to tweak their properties into certain directions. For simple homogeneous cylindrical pillars as in Fig. 3.2a, the adjustable parameters are the thickness of the backing layer, the fibril distribution pattern (most commonly square or hexagonal), the distribution density and the aspect ratio, which is the ratio between their height and diameter. These are the parameters that primarily control the stiffness and effective area on the array level. However, most of the mechanistic optimization happens at the level of the individual fibril. One approach is to slow down the detachment by reducing the stress concentrations at the edges associated with the cylindrical shape. This can for example be achieved by composite pillar designs that are softer at the edges, which can increase the pull-off force by (up to) a factor of ~ 7 in rough contacts [10]. The fibrils' disadvantage of reduced absolute contact area compared to a flat block of bulk material is sometimes mitigated by the introduction of different cup shapes at the tips of pillars [13,15]. The optimization of the cup as well as the individual pillar geometry was even tackled with the help of machine learning, indicating that the optimal shape is slightly thicker at the base than near the cup end [12]. However, they only looked at the contact with a rigid flat counter-face without roughness. The logical continuation of the cup-terminated fibril is to cover the entire fibril array with a tightly bonded, very soft, continuous film as sketched in Fig. 3.2b. The mechanical properties of these film-terminated structures and their adhesive performance in contact with rough surfaces is therefore studied in Publ. **II**.

The assumption of translational invariance in the elastic theory becomes less problematic when the terminating film is added to the fibril array. However, neither the film nor the fibril layer can be treated as semi-infinite, as assumed in the previous Sections. There are studies on thin, confined elastic films in contact with a circular flat punch [19, 22, 119,154], albeit mostly focused on asymptotic limits. For incompressible elastomers and intermediate film thicknesses, some experimental studies have proposed fit functions for the effective contact modulus, from which the adhesive pull-off force can be derived [20, 154,155]. Publ. **I** aims to provide a much simpler model based on analytical scaling relations, with an approach that is valid for arbitrary Poisson's ratios. Furthermore, it provides highly accurate numerical reference data for pull-off force and Poisson's ratio measurements. Publ. **II** uses the stiffness expressions of finite-thickness elastomers to rationalize the stickiness observed for film-terminated fibrillar adhesives designed for medical applications.

3.5 Viscoelastic contacts

As already pointed out in Sect. 2.1, almost all adhesive applications include soft polymeric materials, whose mechanical behavior is dominated by molecular relaxation processes [79]. Consequently, experimental observations frequently show that even at low deformation velocities of a few micrometers per second, the measured work of separation is substantially higher than the quasi-static prediction and further increases with higher speed [156–158]. Replacing the quasi-static elastic material model with a viscoelastic one severely complicates the history dependence of adhesive rough contacts. Therefore, many investigations on viscoelastic adhesives still focus on single asperity contacts and attempt to identify tendencies that, at least qualitatively, generalize to rough surfaces.

Gent and Schulz [156] tested an adhesive contact with a multitude of wetting liquids, which let them probe a wide range of surface energies $\Delta\gamma$, in tack as well as peel tests. They found that in almost all cases, the effective work of adhesion $w(v_{\mathrm{c}})$ at a crack velocity v_{c} is of the shape

$$w(v_{\mathrm{c}}) = \Delta\gamma(1 + cv_{\mathrm{c}}^{n}), \tag{3.10}$$

where c and n are material-specific constants and the temperature-dependent $c = ka_{\mathrm{T}}^{n}$ depends on the Williams, Landel and Ferry (WLF) parameter a_{T}. n is often observed to be between 0.1 and 0.8, where formally deriving it from the diffusion of free elastomeric chains would suggest that it is exactly 0.5 [159]. The previously defined surface energy $\Delta\gamma = w(0)$ is nothing but the work of adhesion required to separate two flat surfaces quasi-statically.

The WLF model is an empirical law describing the time-temperature superposition (TTSP) of viscoelastic material properties [160]: Decreasing the temperature from T_1 to $T_2 < T_1$ reduces the thermally activated mobility of the molecular structure and makes the polymer stiffer. This effect is equivalent to increasing the excitation frequency or deformation rate by the factor a_{T_2}/a_{T_1} relative to the characteristic speeds of internal relaxation processes. WLF find a_{T} to be well-described by a reference temperature T_{s} and the two coefficients C_1 and C_2 in the relation

$$\log a_{\mathrm{T}} = -\frac{C_1(T - T_{\mathrm{s}})}{C_2 + T - T_{\mathrm{s}}}, \tag{3.11}$$

where using $C_1 = 8.86$, $C_2 = 101.6\,\mathrm{K}$ and $T_{\mathrm{s}} = T_{\mathrm{g}} + 50\,\mathrm{K}$ for a polymer with glass transition temperature T_{g} has been found to be a surprisingly universal description applying to many different viscoelastic materials [115, 157, 161, 162].

Maugis [157] applied the Gent-Schulz law and WLF model to adhesive fracture mechanics to derive an expression for the velocity-dependent work of adhesion for two contacting spheres and for peeling experiments. In classical Griffith fracture, the variation of the free energy $\mathcal{F}$ with respect to the contact area A is given by

$$\frac{\mathrm{d}\mathcal{F}}{\mathrm{d}A} = G - w, \tag{3.12}$$

which defines the strain energy release rate G containing information on how all other energy contributions (all except the surface energy) change with the contact area. For

a quasi-static, displacement-controlled system, G is simply the derivative of the elastic strain energy with respect to contact area, where the equilibrium condition is given by $G = w$ and $\partial G / \partial A > 0$. In a dynamic system, however, assuming that viscoelastic losses occur predominantly in the vicinity of the contact line, $G > w$ is necessary to accelerate the crack, where this excess acceleration can be written via Gent-Schulz as

$$G - w = w f(a_{\mathrm{T}} v_{\mathrm{c}}) \tag{3.13a}$$

$$\Leftrightarrow \quad G = w(1 + f(a_{\mathrm{T}} v_{\mathrm{c}})), \tag{3.13b}$$

with $f(a_{\mathrm{T}} v_{\mathrm{c}}) = k(a_{\mathrm{T}} v_{\mathrm{c}})^n$. This framework was then used by Muller [115] to derive a differential equation allowing to calculate the contact area over time, assuming a displacement-controlled detachment at constant velocity. Violano $et.$ $al.$ [26, 27] have recently compared Muller's model to experiments conducted on a patterned surface comprised of many single asperities and found it to apply reasonably well.

An aspect that has proven difficult in the description by crack propagation is the stress singularity at the crack front. This singularity can be eliminated either by defining a cohesive zone at the tip [163, 164] or by an energy-based approach [165]. Hui $et.$ $al.$ [166] have compared the predictions from these two approaches, finding that the only significant difference between them is the estimation of the cohesive zone, which, however, can be used as a fit parameter. Persson and Brener [80] use the maximum stress given by the employed cohesive-zone model (CZM) to define a quasi-static cut-off wave vector q_0, which is decreased for non-zero velocity v to $q_{\mathrm{c}}(v) = q_0(1 - f(E^*(\omega), v))$, effectively blunting the crack tip [82]. Their model closely reproduces GFMD results, showing that the dissipated power has a maximum at intermediate velocities. This is to be expected, given that the imaginary part of $E(\omega)$ vanishes in both the low- and high-frequency limit. The pull-off force $F_{\mathrm{po}}(v)$, on the other hand, increases monotonically, until it reaches $F_{\mathrm{po}}(v \to 0) E_\infty / E_0$, where $F_{\mathrm{po}}(v \to 0)$ usually corresponds to the JKR prediction in Eq. (3.1).

Strictly speaking, since both adhesion and viscoelasticity are hysteretic processes, there is no generally valid relationship for contact radius and crack front speed, which makes it impossible to provide an exact estimate of the energy release rate. Consequently, all models have to make assumptions on the branch of the general hysteresis that they describe. For example, the previously introduced model by Persson and Brener assumes that detachment starts from a relaxed configuration at an infinitely large initial contact radius a_{max}. Later on, he adjusted the theory by introducing a low-frequency cutoff $\omega_{\mathrm{L}} \sim v_{\mathrm{c}} / a_{\mathrm{max}}$ for a crack starting at a_{max} with a speed v_{c} [167]. With this adjustment, the pull-off force does not grow monotonically with velocity anymore but drops off after an intermediate maximum, similar to the dissipated energy. Together with Lorenz $et.$ $al.$ [168], he also postulated that for closing cracks, viscoelasticity reduces the crack closing energy by the same factor by which it increases the crack opening energy in the Gent-Schulz equation:

$$w^{(\mathrm{closing})}(v) = \frac{\Delta \gamma}{(1 + c v^n)}, \tag{3.14}$$

which is supported by recent numerical studies by Violano and Afferrante [83, 169].

However, the authors also point out that the Persson-Brener approach still falls short of capturing the influence of the initial configuration of the system. For example, they observed that when detachment starts from an unrelaxed state, the viscoelastic dissipation is not concentrated in the vicinity of the crack front and the bulk cannot be neglected anymore. Therefore, they proposed to use the cut-off $\omega_L \sim v/a_{max}$ in Persson's theory with the macroscopic velocity v rather than the crack speed. In the case of a relaxed starting configuration, they enhanced Persson's previous approach to account for the finite initial contact area by also adjusting the stress cut-off σ_{th} according to a semi-empirical description of the stress intensity factor for a finite crack geometry [170]. They found that, due to the finite initial contact size, the pull-off force falls short of reaching $F_{po}(v \to 0)E_\infty/E_0$, even for very high velocities. With these modifications, the Persson-Brener model is in good agreement with their reference data gathered using a contemporary finite element method (FEM) implementation.

Once again, a few words on the influence of the range of adhesion are in order, which is particularly interesting in viscoelastic contacts. At high velocity, the material responds with a higher elastic modulus, which means an effective reduction of the Tabor parameter (see Eq. (3.3)), potentially approaching the behavior of the long-range limit. This blurs out the stress concentrations at the crack tips, which eventually leads to a uniform contact rupture instead of a detachment by crack propagation. This has been observed in GFMD [82] as well as FEM [171] simulations, where the latter also showed that the influence of the initial configuration becomes almost negligible for small μ_T. Furthermore, decreasing the range of adhesion ρ increases the maximum stress σ_{th} in the cohesive zone model, which makes the crack tip sharper and enhances the dissipated energy, which, in turn, slows down the crack speed. Since it is very challenging to simulate macroscopic bodies with realistic atomic interaction ranges, it would be very valuable to know how a result obtained at medium to large ρ can be applied to real systems with a much smaller ρ. This question was tackled by Publ. **III** to better rationalize the good agreement between numerical and experimental data in Publ. **IV** in spite of a mismatch in their values of ρ.

The results outlined above mostly pertain to the Hertzian tip geometry, but similar studies have also been conducted for general polynomial indenters [172] and the circular flat punch [173,174]. In the latter case, since the contact area at the start of detachment is always the entire circle, there is (almost) no influence of the initial configuration, so that the detachment mechanism effectively depends only on the velocity at which the indenter is pulled off. Publ. **III** will also feature non-Hertzian indenter shapes but with focus on the contact formation (crack closure) process rather than detachment (crack opening).

Applying any of these concepts to real rough surfaces is difficult because of the issues already outlined in Sect. 3.2: Modeling a collection of single asperities neglects any elastic interaction between them and is generally not a good representation of roughness. A more accurate approach would require the inclusion of viscoelasticity in a true multi-scale model like Persson's theory. For the adhesion-less case, this is relatively simple, seeing

that Persson's original publication was already formulated with an arbitrary viscoelastic modulus [23]. For normal detachment or attachment problems, however, the solution requires the governing equations to be integrated numerically over time (or an inverse FT with respect to temporal frequency ω). Only in the case of steady-state sliding at constant normal pressure and lateral velocity $\mathbf{v}$ can the problem be simplified, where for each wave vector $\mathbf{q}$, the only relevant temporal frequency is $qv\cos\Phi$, where Φ is the angle between $\mathbf{v}$ and $\mathbf{q}$ [23]. For an adhesive system, however, it seems virtually impossible to capture the time dependence of the contact, considering that even the quasi-static case does not allow the determination of a unique relationship between contact area and external parameters like displacement or pressure. Consequently, research in this direction has to rely on brute-force simulations for now. Recently, a numerical study on 1D rough contacts found that the adhesive and viscoelastic hystereses are approximately additive [28], whereas the 2D contact study in Publ. **IV** shows that the general case is more complicated than that. It does, however, show a very strong influence of the initial configuration in good agreement with the included experiments performed under almost identical conditions.

3.6   Elastic coupling and friction

In Sect. 2.4, the Green's function method was applied to solve the equation system of linear elasticity under the given boundary conditions in Fourier space. As can be seen from the matrix nature of the equation

$$\tilde{\boldsymbol{\sigma}}(\mathbf{q}) = \boldsymbol{\Phi}(\mathbf{q})\tilde{\mathbf{u}}(\mathbf{q}),$$

lateral stresses can affect the normal displacement and vice versa, a phenomenon which we refer to as elastic coupling between lateral and normal direction. Consequently, a contact mechanics problem is uncoupled if one of the following two conditions is met: i) all lateral stresses are 0 or ii) all off-diagonal terms of $\boldsymbol{\Phi}$ vanish. The latter condition is fulfilled if $h \gg 1/|\mathbf{q}|$ $\forall$ $\mathbf{q}$ and at the same time $\nu = 0.5$, i.e. for semi-infinite, incompressible elastic solids. This allows many contact problems involving polymer materials to be closely approximated as uncoupled. In the general case and especially in frictional contacts, on the other hand, it should be obvious that the effect of coupling cannot be neglected. The description of these phenomena in terms of $\boldsymbol{\Phi}$, the coefficients of which are given in App. B, is in the spirit of Publ. **V**.

Historically, elastic coupling was originally introduced by Flamant [175], who modified Boussinesq's solution [18] to describe the stresses and deformations inside an infinitely large elastic wedge loaded along its edge. In the limiting case where the wedge has an opening angle of 180°, this represents the first analytical solution for the elastic deformation of a flat surface, to which normal and tangential stresses are applied simultaneously. However, the solution was limited to semi-infinite solids and line contacts.

The effects of coupling in axisymmetric contacts were investigated by Hamilton [176,177]. He derived analytical expressions for the entire stress state in the elastic body in frictional sliding contact with a rigid Hertzian indenter, where x is the sliding direction. The equation reveals how the lateral stress component σ_{11} becomes asymmetric along x once the indenter experiences sliding friction in x-direction. Furthermore, the location of the maximum von Mises stress depends on the imposed microscopic Coulomb friction coefficient μ_c. For small values of μ_c, it is located underneath the surface of the elastic body close to the symmetry axis of the indenter, where the trailing edge only shows a smaller local maximum. As μ_c is increased past 0.3, the maximum on the trailing edge becomes global and the local maximum underneath the surface is smeared out until it vanishes completely for $\mu_c > 0.5$. To derive these relations, Hamilton made the simplifying assumption that the elastic body is semi-infinite and constrained the normal stress $\sigma_{zz}(x,y,0)$ to exactly follow the Hertzian solution.

Scheibert *et. al.* [178] derived the stress distribution in an elastically coupled contact under less stringent boundary conditions. First of all, they did not constrain the normal pressure but rather just the contact area, revealing that the normal stress also becomes asymmetric along sliding direction. Furthermore, they limited their analysis to incompressible elastomers, but took the finite thickness of the material into account. This let them compute the stress on the bottom of the elastic slab opposite to the indenter

contact, which they could compare to real-world measurements. The good agreement between their model and experiments was the first direct proof for the practical significance of elastic coupling.

The final simplification that can be dropped is the circularity of the contact area, at which point the system becomes impossible to describe analytically, and numerical solutions need to be developed, instead. To some extent, this was already done in the original GFMD implementation of Campaña *et. al.* [30], where the stiffness tensor components were fitted to Molecular Dynamics calculations. In the continuum framework, a numerical solver of this kind was first implemented for 1D contacts by Menga *et. al.* [29, 73]. They also introduced a differentiation between two types of coupling: Material coupling (compressibility-induced coupling) is due to the deviation of the Poisson ratio ν from 0.5, while geometric coupling (confinement-induced coupling) originates from the finite thickness of the elastic body. They showed that in the former case, the contact area is shifted toward the trailing edge, reducing the effective macroscopic friction compared to the imposed microscopic friction coefficient μ_c. Geometric coupling has the opposite effect, where the contact is skewed toward the leading edge and the overall friction increases. The gap is decreased and the total contact area increased for both couplings when compared to the $\mu_c = 0$ case. Publ. **V** represents the next step of generalization, where realistic two-dimensional contacts are considered and analyzed with respect to many more contact properties, aiming to provide a comprehensive and detailed study of coupling with applications to a wide variety of phenomena in engineering and materials science. The investigated aspects include i) the elastic-plastic transition as indicated by the von Mises stress fields in realistic rough sliding contacts, ii) localization of defect initiation sites revealed by local maxima in the most tensile eigenstress and iii) fluid flow through the interface. Complementing this publication is the perturbation approach presented in App. D providing a rigorous mathematical approach to identifying the origin of the observed tendencies.

Chapter 4

Results and discussion

4.1 Effect of Poisson's ratio and confinement

In Publ. **I**, we studied a circular flat punch with radius a in contact with an infinitely large elastic film of thickness h supported by a rigid foundation. In the adhesion-less case, the contact area does not depend on the external compressive force F, so the total displacement u_0 is simply proportional to F. This allows us to investigate the system in terms of the effective modulus $\bar{E}$ of the contact, which is defined as the proportionality factor between the mean stress $\bar{\sigma}$ and strain $\bar{\varepsilon}$:

$$\bar{E} = \frac{\bar{\sigma}}{\bar{\varepsilon}} = \frac{Fh}{u_0 \pi a^2}. \tag{4.1}$$

Dimensional analysis suggests that this stiffness must be proportional to the contact modulus E^* of the elastic material and can otherwise only depend on the dimensionless measure for confinement, h/a. Unfortunately, there is no known closed-form expression for this dependence. To provide an analytic approximation of $\bar{E}(h/a)$, we apply a simple scaling argument to the Green's function $G^{(\mathrm{n})}$ in Eq. (2.21), which represents a wavelength-dependent compliance. Since the indenter radius a is the only lateral length scale in the system, we evaluate $G^{(\mathrm{n})}$ for a single representative wave number which must be proportional to $q_{\mathrm{a}} = (2\pi/a)$, where the proportionality factor can be derived from well-known asymptotic limits. This provides us with the analytic prediction shown in Fig. 4.1, which is compared to numeric data and exact asymptotic limits, showing that all qualitative tendencies are correctly reproduced. The quantitative error, on the other hand, is around 50% for $h/a \approx 2$ and can become as large as $\pi^2/2$ for strongly confined, (almost) incompressible elastic films. In principle, these tendencies allow the Poisson's ratio to be determined from measurements of $\bar{E}$, for which Publ. **I** provides useful reference data.

Since the elastic energy stored in the system can be expressed in terms of $\bar{E}$, it can be
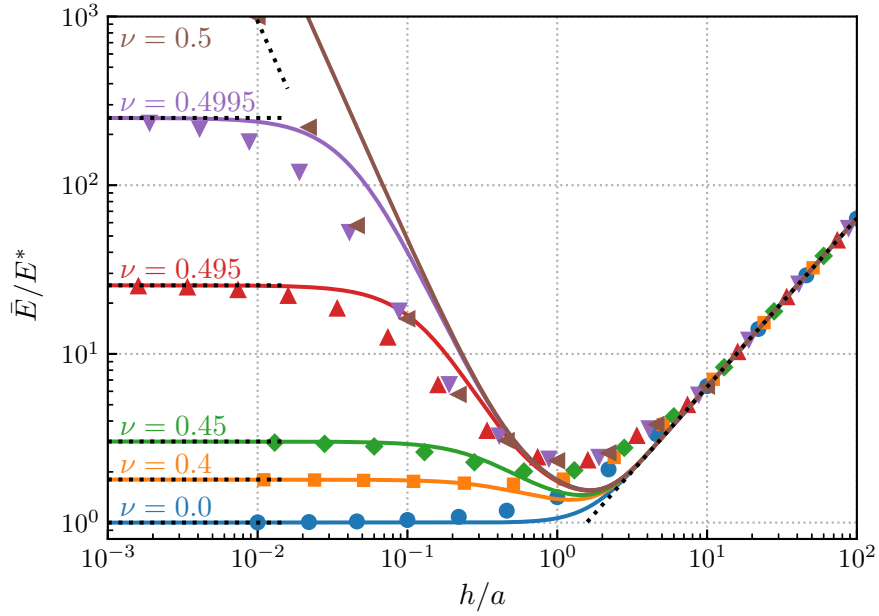
Figure 4.1: Effective modulus of flat-punch contacts for a variety of Poisson's ratios as a function of confinement parameter h/a. Solid lines represent the analytical model, symbols are GFMD data points and dotted lines are exact asymptotic limits. The figure is adapted from Publ. **I**.

substituted into the energy balance to derive the adhesive pull-off stress σ_{po} as

$$\sigma_{po} = \sqrt{\frac{4\bar{E}(h/a)\Delta\gamma/h}{2 + \partial \ln \bar{E}(h/a)/\partial \ln a}}. \tag{4.2}$$

Inserting numerical data for $\bar{E}(h/a)$ into Eq. (4.2), we calculate the curves shown in Fig. 4.2 for the pull-off stress as a function of Poisson's ratio and confinement. However, determining the pull-off stress in this way assumes that the contact area remains circular, which is not necessarily true for $\nu > 0.4$. This is because the stiffness function $1/G^{(n)}$ has a pronounced minimum at intermediate wave numbers $q \approx 1.5 \ldots 2/h$, favoring the evolution of wrinkles at the interface. Examples for the complicated detachment mechanisms are provided at the end of Publ. **I** based on adhesive GFMD simulations with thermal noise. Similar configurations have been observed experimentally [22, 179–182].
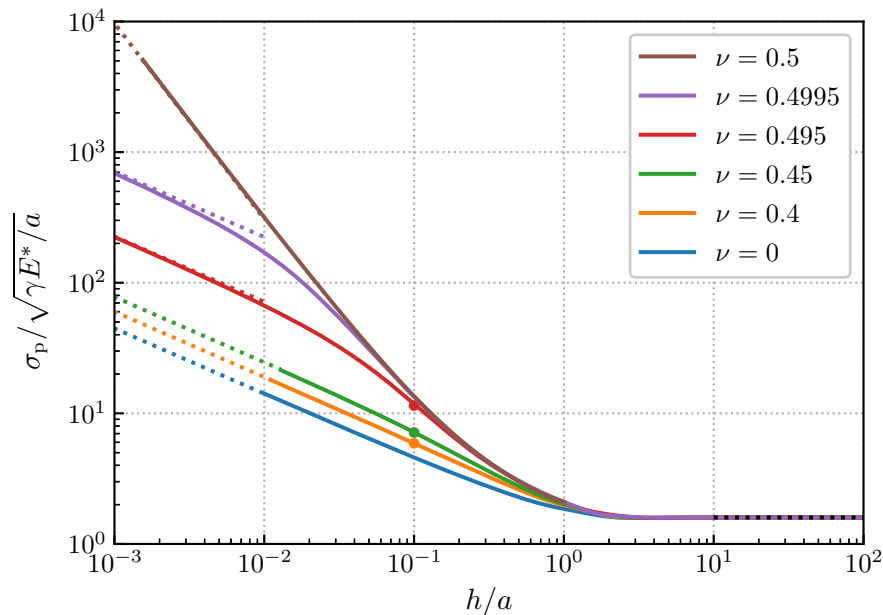
Figure 4.2: Pull-off stress of flat-punch contacts for a variety of Poisson's ratios as a function of the confinement parameter h/a. Solid lines represent interpolated curves calculated inserting the numerical data in Fig. 4.1 into Eq. (4.2). Dotted lines are exact asymptotic limits and circles are results obtained from adhesive GFMD pull-off simulations. The figure is adapted from Publ. **I**.

4.2 Film-terminated fibrillar microstructures

Publ. **II** studies the adhesion of film-terminated fibrillar adhesives compared to film-terminated solid blocks and plain fibril structures without the terminal layer. The blocks and fibril arrays are both manufactured from the same MDX4-4210 silicone material with a Young's modulus of $E_{\mathrm{MDX}} \approx 1\,\mathrm{MPa}$, while the films consist of a soft skin adhesive (SSA) with a much smaller modulus of $E_{\mathrm{SSA}} \approx 0.1\,\mathrm{MPa}$. Experiments on flat and rough surfaces are complemented by measurements on sinusoidal structures, whose wavelengths approximately correspond to the roll-off wavelength λ_{r} of the roughness spectra of interest. As explained in Sect. 3.2, the range of wavelengths near λ_{r} generally dominates the elastic energy necessary to form an intimate contact.

In the spirit of Sect. 4.1, we use the Green's function in Eq. (2.21) to estimate the wavelength-dependence of the elastic deformation energy. This is a rather qualitative argument, given that the fibril structure needs to be approximated as a flat continuum with isotropic properties (see Sect. 2.3.2). Since the fibrils have enough free volume available to expand and contract laterally, we replace them with a solid with Poisson's ratio $\nu = 0$. This description is asymptotically exact for wavelengths that considerably exceed the distance between adjacent pillars, where both the model and the fibril structure approach a so-called Winkler foundation. In the case of very short wavelengths, on the other hand, the St. Venant principle suggests that mostly the soft surface film will be deformed, for which we can model the fibrils underneath as a rigid foundation. These two modes of deformation at different wavelengths are depicted in Fig. 4.3a and 4.3b.

At intermediate wavelengths, the preferred mode should be the one with the lower corresponding elastic energy, which we then use to roughly approximate the total deformation energy in Fig. 4.3c.
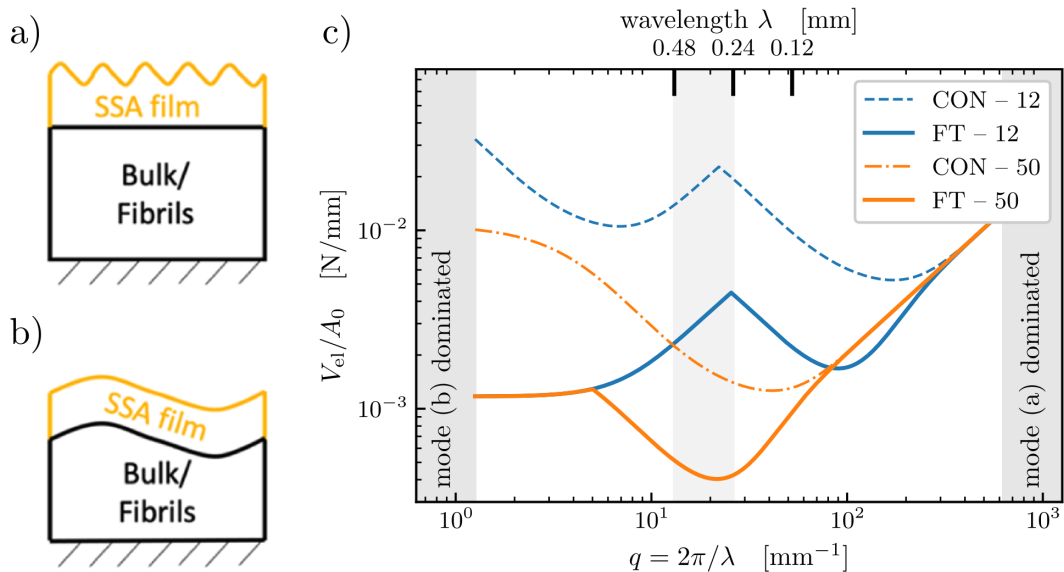
Figure 4.3: a) and b) schematic representation of two different idealized deformation modes. c) Minimum of the two elastic energies corresponding to these deformations, evaluated for different adhesive structures as indicated by the legend. Therein, the abbreviation "CON" stands for a solid silicone block, while "FT" stands for a fibrillar structure. The numbers behind the hyphen indicate the thickness of the terminating layer in micrometers. The figure is adapted from Publ. **II**.

Despite the simplified nature of the model outlined by Fig. 4.3, it can be used to rationalize many of the tendencies observed in the adhesion measurements. We consider, once again, that in order to form intimate contact with a rough counter-surface, the adhesive structure has to be compliant, i.e. the necessary deformation energy in Fig. 4.3c must be small. For long wavelength undulations that reach through the surface layer, a sparse distribution of fibrils is always more compliant than a solid block of the same material. This is an important part of why the fibril structures generally show a stronger adhesion in Fig. 4.4. The influence of the terminating film also turns out to be in line with this stiffness argument: Since the SSA material of the film is much softer than the silicone underneath, it is usually beneficial to increase the film thickness from 12 to 50 µm. Of course, this improvement is more noticeable for the films on top of the solid silicone block than those on top of the fibril structure, because the latter is already much more deformable on its own.

Given that the beneficial effect of low stiffness results from the necessity to conform to the counter-face, this advantage disappears when the surfaces are sufficiently flat and smooth. We can observe this on the far left of Fig. 4.4b, where the stiff, solid silicone blocks reach much higher pull-off forces than the more compliant fibril structures. For such flat-on-flat contacts, we can assume that the load-displacement curve resembles that of the well-known adhesive flat-punch solution, which is linear all the way until the point of instantaneous detachment. More importantly, the area under the curve is

exactly the surface energy $\Delta\gamma$, which can be considered to be constant between all data points in Fig. 4.4b. Therefore, a higher stiffness implies a larger slope and ultimately a higher force value at the moment of detachment. This trend is clearly highlighted by the two exemplary load-displacement curves in Fig. 4.5a. Only the "roundness" of both curves represents a significant deviation from the ideal model, which can most likely be attributed to viscoelastic effects.

Based on the previous argument, it would also seem reasonable to expect the overall stiffer system with the 12 μm layer to show a stronger flat-surface adhesion than the 50 μm layer. However, Fig. 4.4a shows the opposite to be the case. To shed some light on why this might be, we take another result from Sect. 4.1 into account: If a confined film with thickness h is brought into contact with a circular flat punch of radius $a < h/2$, its mechanical response is almost indiscernible from that of an unconfined (semi-infinite) body. It is reasonable to assume that in this case, the internal stress field caused by the punch barely interacts with the opposite interface. In the present system of fibrillar adhesives, both the silicone and the counter-surface can be approximated as rigid compared to the much softer SSA. Hence, the film can be considered to be confined between the counter-surface and a circular flat punch (representing the fibril). Since the radius of the fibrils was 25 μm, the 50 μm film can just be approximated as semi-infinite. For the structure with the 12 μm film, on the other hand, the stress field caused by the fibril reaches the counter-face and may provide an additional driving force for premature detachment. To validate this hypothesis, the internal stresses were characterized by FEM simulations. Their results are depicted in Fig. 4.5c.
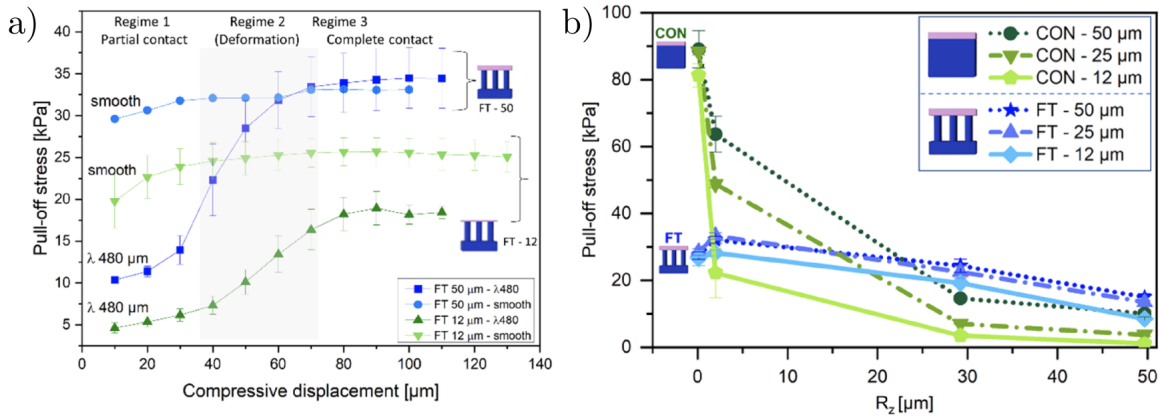
Figure 4.4: Pull-off stress σ_{po} measured for different film-terminated adhesive structures with two different film thicknesses (12 and 50 μm). a) σ_{po} for fibrillar structures in contact with a flat or sinusoidal surface with wavelength $\lambda = 480$ μm as a function of the compressive displacement from which detachment is initiated. b) σ_{po} for film-terminated fibrillar and solid block structures as a function of the average maximum height R_z of the rough counterface. The figures are adapted from Publ. **II**.

Fig. 4.4a shows another distinct difference between the two film thicknesses: At very large compressive displacements, the pull-off stress measured on the sinusoidal surface reaches the smooth-surface value in the case of the 50 μm film but not the 12 μm layer. This may be explainable by the lateral stretching of the thin film, which was very obvious

in the in-situ contact images reported in Fig. 4.5b. However, this remains a somewhat empirical explanation, since it is not an easy task to incorporate this large-displacement effect in the first-order deformation models that we have assumed thus far.
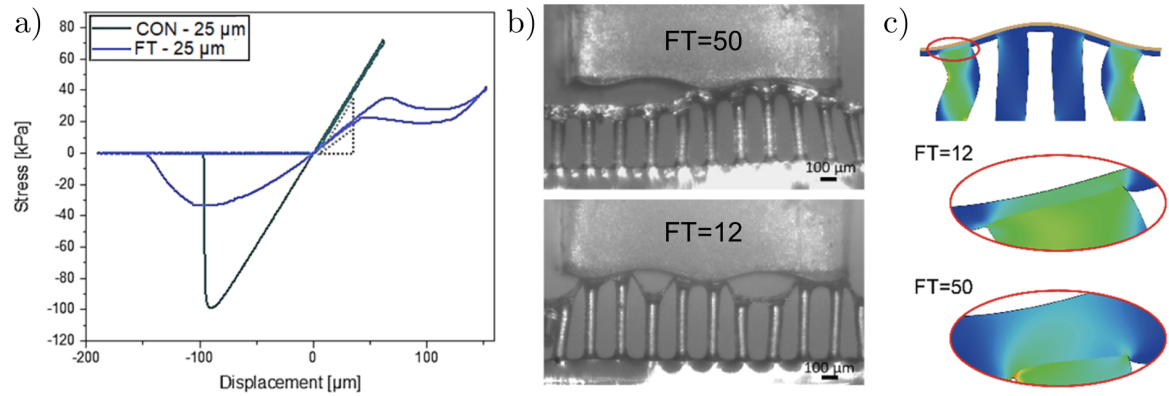
Figure 4.5: a) Stress-displacement curve measured for the flat surface detachment of a film-terminated bulk ("CON") and fibril ("FT") structure with 25 µm film thickness. b) In-situ observation of the detachment of a fibril array with 12 and 50 µm terminal layer. c) FEM result for the von Mises stress profile in the material when in full contact with a stiff sinusoidal surface with a wavelength of 480 µm and amplitude of 25 µm. The figures are adapted from Publ. **II**.

4.3   Viscoelastic contact formation

Publ. **II** only briefly touched on the viscoelastic properties of the materials involved, even though the roundness of the load-displacement curves in Fig. 4.5a indicates a clear deviation from the ideal quasi-static flat surface detachment. To study the temporal contact evolution, we consider again the simple model system of a single rigid indenter in contact with a semi-infinite viscoelastic body. More specifically, we limit ourselves to axisymmetric indenters for which the local height h is described by the n-th power of the distance r from the origin:

$$h(r) = \frac{R}{n}\left(\frac{r}{R}\right)^n,\tag{4.3}$$

where R is a characteristic length, corresponding to the radius of curvature for $n = 2$.

The mechanical properties of the material are modeled according to the SLS, so that there is a well-defined configuration at time $t = 0$ corresponding to the high-frequency modulus $E_\infty = 100E_0$ (see App. E). We employ the viscoelastic GFMD implementation described in Publ. **IV** to simulate the evolution of the contact radius $r_c(t)$ over time and report it in terms of a correlation function $C(t)$ defined as

$$C(t) = \frac{r_c(t) - r_c(0)}{r_c(\infty) - r_c(0)},\tag{4.4}$$

where the quasi-static and instantaneous radii $r_c(\infty)$ and $r_c(0)$ are obtained from conventional quasi-static GFMD. All simulations are run with an adhesive surface energy of $\Delta\gamma = 0.01E^*R$ under zero external load. The quasi-static contact modulus E^* as well as R are set to 1 and the range of adhesion ρ in the cosine-shaped interaction potential is adjusted between individual calculations to probe a wide range of different Tabor parameters μ_T, see Sect. 2.4.3 and 3.1.

By fitting the final stages of $C(t)$ with an exponential function, we identify a characteristic long-term relaxation time τ. Normalizing the time axis by τ lets the different measurements superimpose surprisingly well for all values of μ_T and n, as depicted in Fig. 4.6a. This agreement can be explained by the increase in local dissipation at the contact line as the range of adhesion is decreased. A smaller value of ρ increases the slope of the displacement profile and thereby the local velocity during relaxation, which is equivalent to changing the viscoelastic time scale. To elaborate on this trend, the measured relaxation time τ is plotted against μ_T in Fig. 4.6b, revealing that τ scales with $\mu_T^{1.8}$ for all investigated indenter geometries. The simulations were repeated for one-dimensional polynomial indenters, with the cosine-potential as well as a Dugdale interaction, which all showed the same scaling relation.

Due to the uniform lateral discretization in GFMD, it is not feasible to simulate macroscopic systems with atomic/molecular interactions. With the identified scaling law, however, we can systematically extrapolate from relatively cheap simulations to such realistic multi-scale systems: By simply increasing the relaxation time of the viscoelastic model, a simulation with medium-ranged adhesion can closely reproduce the relaxation
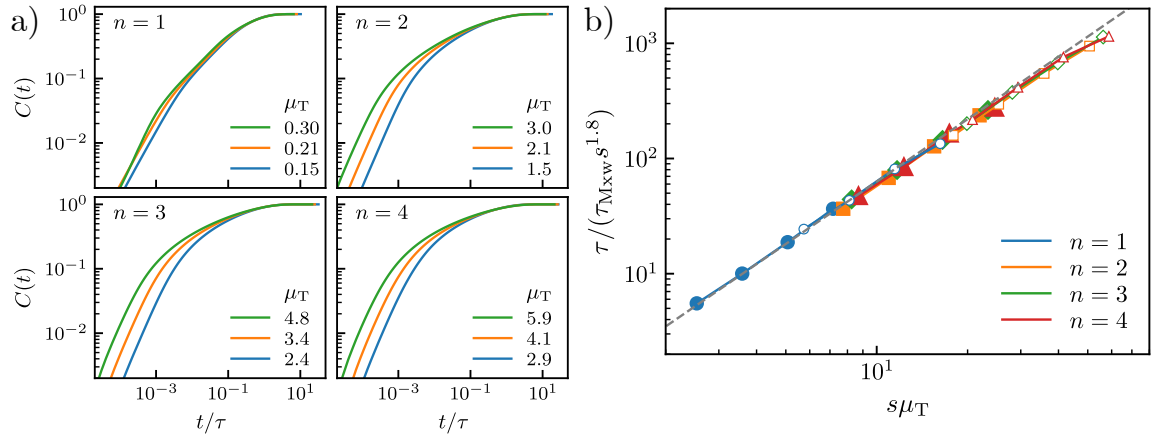
Figure 4.6: a) Contact radius evolution over time, determined in terms of $C(t)$ for different Tabor parameters μ_T and polynomial indenters of various exponents n. b) Long-time relaxation times τ obtained from the exponential model fit, plotted against the Tabor parameter μ_T. Solid symbols represent rotationally symmetric indenters, while open open symbols are 1D contacts with the same polynomial height functions as their 2D counterparts. The figures are adapted from Publ. **III**.

dynamics the same material with short-ranged interactions. This principle will be applied in Sect. 4.4, where GFMD simulations are directly compared to experiments.

4.4 Coaction of viscous and multi-stability hysteresis

As already discussed in Chap. 1, it has historically challenging to model real contacts that combine viscoelastic dissipation with adhesive multi-stability. Therefore, Publ. **IV** investigates whether the new viscoelastic GFMD version is capable of reproducing the dynamics of such systems. For this purpose, we define a model system that can be realized in GFMD as well as the laboratory to run direct comparisons of the contact signature evolution and load-displacement relationship. We choose a circular flat punch indenter, to which single-wavelength topography is added, forming a triangular pattern of small asperities, as shown in Fig. 4.7a. The radius of the punch is $a = 375\,\mu m$, the wavelength $\lambda = 150\,\mu m$ and the "amplitude" $z_0 = 4\,\mu m$. This indenter is then 3D-printed, where some of the resulting imperfections have to be incorporated back into the computer model of the surface to be used in simulations. The fabricated indenter is then installed opposite of a soft polydimethylsiloxane (PDMS) substrate in a dedicated tack test apparatus with an optical system for in-situ observation. A schematic of this setup is shown in Fig. 4.7b.
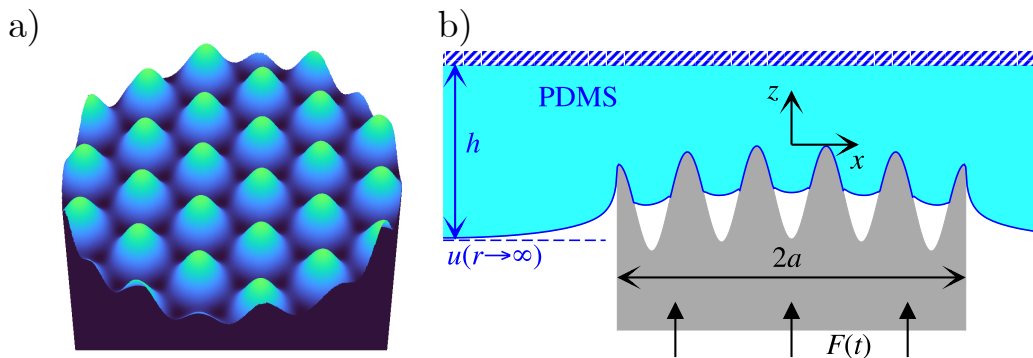
Figure 4.7: a) Illustration of the computer-generated topography. b) Sketch of the tack test setup with the indenter in contact with the PDMS substrate. The figures are adapted from Publ. **IV**.

The mechanical properties of PDMS are modeled with a quasi-static Young's modulus of $2\,MPa$ and a standard linear solid (SLS). Our best guess for the surface energy between the two materials is the generic value of $50\,mJ\,m^{-2}$. The center of mass (COM) displacement in the simulation is corrected for the effect of periodic boundary conditions (PBC), while for experimental data, the finite stiffness of the apparatus has to be eliminated. Furthermore, the mismatch in range of adhesion originating from the numerical resolution limit is accounted for as described in 4.3. Since the SLS is not suited to capture the real viscoelastic properties of PDMS exactly [81], the relaxation time constant τ was adjusted empirically and then kept constant for all simulations with the same adhesive interaction model.

The tack tests are conducted in displacement-controlled fashion, approaching at a constant speed v_{ext} until a predefined compressive force F_{pl} is reached, at which point the velocity is multiplied by -1. Values for v_{ext} ranged from 1 to $25\,\mu m\,s^{-1}$ and preload

forces from 1 to 80 mN. Fig. 4.8 shows the resulting load-displacement curves from experimental as well as numerical tack tests. They show very good agreement in all cases, except maybe for the highest velocity at $F_{pl} = 60$ mN. Moreover, a certain systematic mismatch between the overall stiffness in experiments and simulations remains, in spite of the extensive compliance correction applied to both methods. Both the numerical and experimental data have in common that the load-displacement hysteresis generally appears to have two individual contributions: At the smallest velocity, all curves show a distinct bulge around a compressive displacement of 5 μm followed by the second bulge near 0 on the x-axis, which corresponds to a rather small pull-off force. As the velocity and preload increase, the first bulge moves closer to the second one until they coincide, at which point the observed pull-off force is drastically increased. Owing to the continuous observation of the contact evolution, we identified that the first bulge corresponds to the detachment of saddle points and the second one to the peaks of asperities. This will be elaborated on in the following.
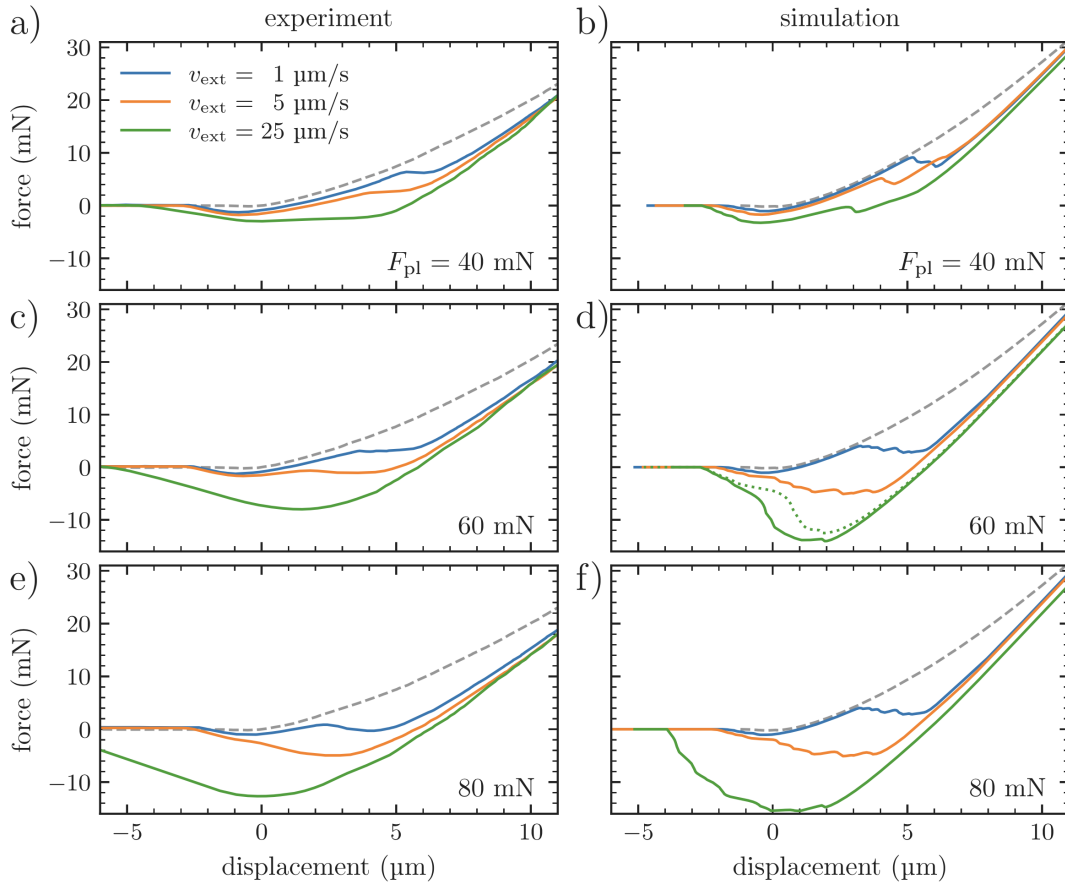
Figure 4.8: Load-displacement curves obtained during detachment at different velocities. Experimental results are on the left and numerical data in the right column. The preload force F_{pl} is increased from 40 to 80 mN from top to bottom. The figure is adapted from Publ. **IV**.

Fig. 4.9 compares the real and simulated contact images at different times to show that even the local evolution of the contact matches reasonably well between them. The first column of pictures was taken at the time t_{pl} of the preload force and the second column 12.5% later into the tack test. In the last two columns were synchronized based

on detachment events rather than time, so that the t values differ slightly between experiment and GFMD: The third column corresponds to the first bulge in the load-displacement curves at a displacement of approximately $5\,\mu\mathrm{m}$ and the last column to the pull-off force. Between these two moments, all the saddle points detach while the asperities stay in contact.
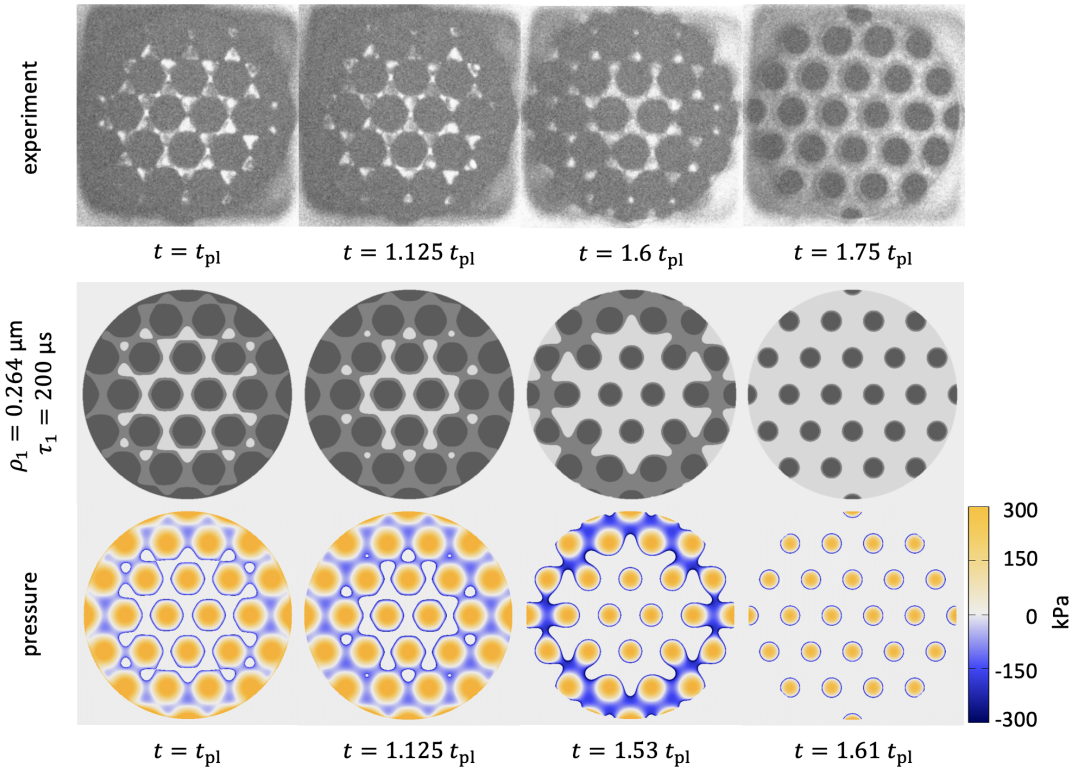
Figure 4.9: Contact signatures observed during experimental (top row) and numerical tack tests (bottom two rows) for $F_{\mathrm{pl}} = F(t_{\mathrm{pl}}) = 40\,\mathrm{mN}$ and $v_{\mathrm{ext}} = 1\,\mu\mathrm{m\,s^{-1}}$. In the first two rows, the darkest gray color represents "contact" and the light color "non-contact", while the medium gray level was added for simulated data to represent points with a positive interfacial gap smaller than the wavelength of light ($\sim 500\,\mathrm{nm}$). Hence, it is not exactly clear what the dark areas in the experimental images must be compared to in the numerical pictures: either dark gray, medium gray or something in between. The figure is adapted from Publ. **IV**.

Due to the specific properties of the viscoelastic simulation, the COM motion shows a retardation from the fist to the second column in Fig. 4.9: the contact is still growing although the surfaces already move apart. To some extend, this phenomenon depends on the time resolution of the simulation, which affects the inaccuracy introduced by the LPF in the Kelvin-Voigt solution algorithm (see Sect. 2.4.2). Perhaps more importantly, the significantly increased relaxation time necessary to match the local dissipation at the crack front inevitably slows down the macroscopic dynamics, too.

In Publ. **IV**, we report the same tests for another indenter geometry, where the saddle points are close enough to the asperities that they always detach concurrently, which significantly reduces the effect of the preload force. Furthermore, we employ a 3-element generalized Maxwell model for viscoelasticity, which only marginally affects the detachment process.

4.5   Significance of elastic coupling and friction

In Publ. **V**, we investigated the influence of friction at the interface. For this purpose, the 3D version of GFMD was implemented together with a simple Coulomb friction model, as described in App. B and Sect. 2.4.4, respectively. Once again, it makes sense to isolate the phenomenon of interest as much as possible, so that we study it in the context of non-adhesive contacts and start with a single Hertzian asperity before we introduce roughness. The investigated system and the corresponding coordinate system are defined in Fig. 4.10a.
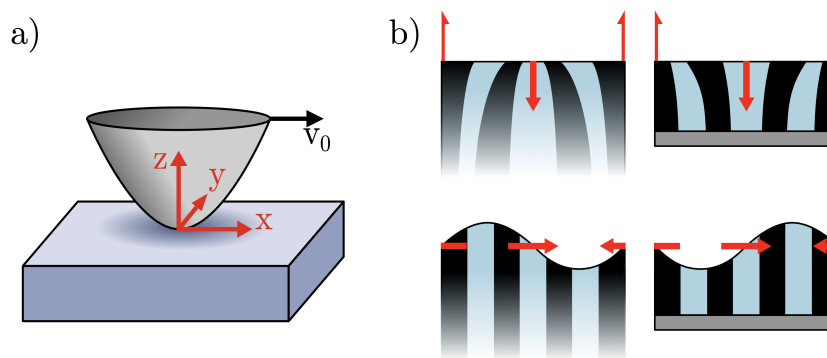
Figure 4.10: a) Schematic of the investigated system of an indenter sliding across the surface of the elastic body. b) Illustration of the Displacement field (black stripes) caused by a sinusoidal surface stress, the minima and maxima of which are indicated by the red arrows.

The impact of in-plane friction is mediated on the normal component of the contact by what is referred to as the "elastic coupling" originating from the off-diagonal components of the Green's function tensor. Since these terms vanish when $\nu = 0.5$ and simultaneously $h \to \infty$, coupling can be induced either by the material's compressibility or the geometric confinement (finite thickness) of the elastic body. The two types of coupling in their isolated forms are illustrated in Fig. 4.10b: For confined elastic bodies, the lateral friction causes the surface to bulge up in front of the indenter and down at the trailing edge, while semi-infinite materials with a Poisson's ratio below 0.5 show the opposite effect. At the same time, the normal stress at the surface induces a displacement component towards or away from the symmetry axis of the indenter. The mathematical formulation of this figure is given as a table in the appendix of Publ. **V**. From there, all trends observed for the single asperity contact can be explained using the perturbation-based analysis presented in App. D, the most important part of which shall be summarized here.

Taking the time derivative of the lateral displacement component in Fig. 4.10b reveals that inside the contact area, the relative velocity v_{rel} between elastic body and indenter increases as a result of confinement-induced coupling and decreases in case of compressibility-induced coupling. This relative velocity enters into the calculation of the dissipated power P_{diss} according to

$$P_{\text{diss}} = \int \mathrm{d}^2 r \, w_{\text{diss}} = \mu_{\text{c}} \int \mathrm{d}^2 r \, p_{\text{z}}(\mathbf{r}) v_{\text{rel}}(\mathbf{r}), \tag{4.5}$$

where w_{diss} is the areal density of the dissipated power, p_{z} is the normal pressure and

μ_c the Coulomb friction coefficient. Consequently, compared to the uncoupled case, confinement increases the total dissipation by friction while compressibility decreases it.

The calculation in App. D also shows that the normal stress field changes as a result of coupling: Confinement shifts the pressure maximum towards the leading edge and compressibility towards the trailing edge of the contact. This, in turn, affects the distribution of the eigenvalues of the stress tensor and the von Mises stress, both of which are characterized in Fig. 4.11. While the von Mises stress tends to be largest in the center of contact patches, the maximum tensile stress is always concentrated at the trailing edges (see panels b and d). Compared to the coupling-free reference case of an incompressible, infinitely thick elastic body, these stress maxima are typically increased by up to 30% due to coupling. The inclusion of Fig. 4.11a and Fig. 4.11c is meant to highlight that explicitly taking friction and 3D elasticity into account yields completely different results compared to taking the conventional static contact and artificially adding a lateral component in post-processing.
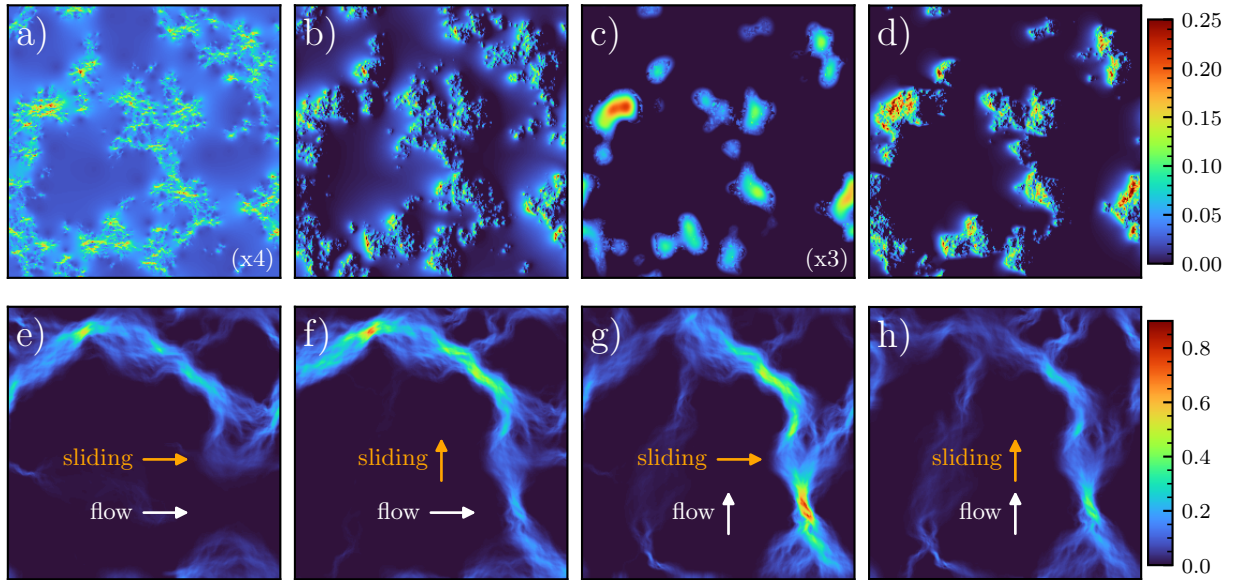
Figure 4.11: Results obtained for a self-affine surface with Hurst exponent $H = 0.8$ with maximum wavelength λ_l and rms height $0.01\lambda_l$, where all calculations pertain to a relative contact area of $a_r \approx 0.2$. The compressible material corresponds to $\nu = 0.25$ and the confined one to $\nu = 0.49$ and thickness $h = 0.1\lambda_l$. All stresses are given in units of the contact modulus E^*, while the current density is normalized by the maximum value observed under frictionless conditions. Panels a)-d) show the maximum tensile stress eigenvalue at the surface of a frictional contact, where a) and b) show the compressible body and c) and d) the incompressible, confined one. a) and c) are calculated from static simulations, where the friction component was added in post-processing, while b) and d) represent genuine brute-force 3D GFMD simulations. The images in e)-h) show the current density calculated through Reynolds flow calculations for different sliding and fluid flow directions, as indicated by the arrows in each picture.

Another consequence of elastic coupling is that the overall contact area increases and the interfacial gap decreases for both types of coupling. This naturally brings up the question how coupling may affect fluid flow through the interface. For a simple model system with a single type of asperity, Publ. **V** finds that fluid flow is generally unaffected

or enhanced in the direction parallel to sliding and impeded in the transverse direction. In rough contacts, the picture becomes a bit more complicated, since channels parallel to sliding also contribute to transerse flow and vice versa. Hence, the percolation threshold is asymptotically isotropic for infinitely large surfaces. Fig. 4.11e-h shows how individual channels become significantly more or less active depending on the alignment of sliding and flow direction. Overall, the flow was reduced in all cases, where the average relative reduction was between 11 and 30% and generally larger in the perpendicular direction.

4.6 How close are simulations to reality?

One of the central goals of this thesis was to make our contact mechanics models more realistic. So far, this chapter has summarized published articles, each of which brought up and answered its own respective questions. This section, on the other hand, will take some unpublished results and experiences into account and specifically discuss the individual assumptions and properties of our model, how realistic they are, and how they could be further improved in the future.

4.6.1 General assumptions

Despite the generalizations introduced throughout this thesis, our analytical and numerical contact models still heavily rely on approximations, most notably the linearity between stress and strain. This means that certain effects are formally assumed to be small, namely all displacements u (linear elasticity) and their time derivatives $\dot{u}$ (linear viscoelasticity). The model's accuracy naturally decreases as one of these parameters becomes very large, although the range of validity of rigorous first-order approximations is often surprisingly large. More subtle, but just as important, is the assumption of a flat elastic surface, which we exploit in the form of translational invariance in the derivation of the Green's function. Unfortunately, this prevents us from applying GFMD to the elastic pillar structures investigated in Publ. **II**, which can at most be considered piece-wise flat. Furthermore, we always describe the elastic material as a continuum, which is fundamentally wrong at wavelengths corresponding to molecular distances.

While we certainly stayed clear of atomic length scales in our theoretical investigations, we did not always stay in the limit of small displacements: in Publ. **II**, the amplitudes of the sinusoidal counter-surfaces were often large enough for the pillars to visibly bend. The experimental side-view images of the contacts suggest that the resulting stretch of the terminating layer might be the dominant large-deformation contribution. To account for this effect, the corresponding strain could be estimated by the arc length of the sinusoidal profile divided by its wavelength.

Another question that comes to mind regarding the model in Publ. **II** is whether it produces similar stress fields to the real system. The stress field on the surface of an elastic pillar (without film termination) in contact with a rigid flat surface depends on the boundary conditions: if the interface is friction-less, the stress field is uniform, while for the ideally sticky case, it shows stress singularities proportional to $d^{-0.4}$, where d is the distance from the contact edge [5, 183]. The elastic model, on the other hand, describes a laterally infinite, flat body as an isotropic approximation of the entire fibril array. Hence, a circular contact with a rigid counter-face simply corresponds to a cylindrical flat punch solution, which produces stress singularities proportional to $d^{-0.5}$. Interestingly, this resembles the stress at the interface of a perfectly sticky elastic fibril, even if it is derived under a slip boundary condition. The 3D GFMD implementation could be used to analyze the influence of the interfacial boundary condition in more detail. This could

be compared to experiments controlling the interfacial slip by addition of lubricants or glue to find out what boundary conditions are closest to reality. Without such a study, we can only speculate to what extent the model matches the experiment.

4.6.2   Material model

In Sect. 2.3.1, we exploited the elastic-viscoelastic correspondence principle to generalize the constitutive equation from the quasi-static to the viscoelastic case. In our case, this is carried out in Fourier space, as it was already done by Persson and many following studies [23,56,72]. In the case of a semi-infinite block of material, this is not problematic, since $E^*(\omega)$ is the only time-dependent property and depends neither on real-space coordinate $\mathbf{r}$ nor on the wavevector $\mathbf{q}$. For the finite elastic body, on the other hand, the Green's function has a non-trivial dependence on the elastic parameter ν, which must also be substituted with $\nu(\omega)$. The resulting $\nu(\omega)$-dependence of the constitutive equations is not invariant with respect to a Fourier transform in the spatial coordinate, at which point it becomes a non-trivial question whether the correspondence principle applies. This problem could only be avoided if the ω-dependence of the Poisson's ratio was negligible, which is generally not true [184]. Unfortunately, there is next to no experimental data on the q-dependence of $E^*(\omega)$ and $\nu(\omega)$ because most viscometric testing methodologies correspond to measuring the $q \to 0$ limit. The most promising approach to analyze the wave-number dependence would probably be to derive the viscoelastic properties from the propagation of surface waves, as described in Ref. [185].

4.6.3   Numerical resolution limits

There are many effective ways to improve the spatial resolution of simulations beyond simple extrapolation. To account for the finite spatial resolution, it has been suggested to reduce the surface energy $\Delta\gamma$ by the areal elastic energy necessary to form full contact at all wavevectors $q > q_{max}$ corresponding to the resolution limit [59, 96, 186]. This was exemplarily done in Fig. 4.12, where a partial contact configuration was chosen to put this approach to the test. The simulations were run at constant range of adhesion, where for the highest resolution $\Delta\gamma/E^*\lambda_r = 0.0002$, which was then reduced to 0.000176 and 0.000156 for the earlier spectral cut-offs. The agreement between all three simulations is rather impressive, considering the significant loss of topographical detail from one simulation to the next.

Publ. **III** and **IV** have shown that temporal resolution can be much improved using a scaling relation. An aspect that has only been mentioned briefly is the influence of the parameter $s = E_\infty/E_0$ of the viscoelastic model on the contact dynamics. Since polymers in the glassy region usually have a stiffness of a few GPa, realistic values for s are of the order of 10^3 to 10^5 for soft adhesives. The models used in Chap. 4 all use a smaller value for s, because increasing it would require much shorter time scales to be resolved (assuming that the slope of the $E(\omega)$ curve remains unchanged). However,
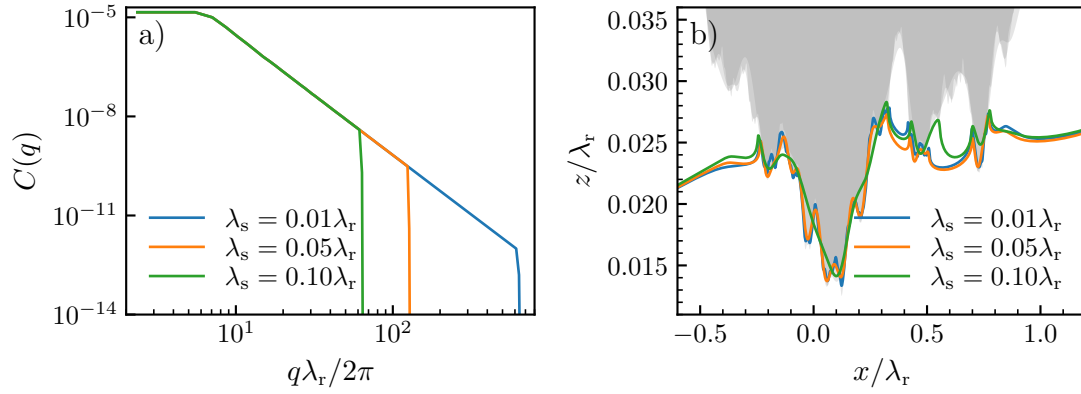
Figure 4.12: Adhesive contact configuration of a semi-infinite elastic body in contact with a rough surface. The cut-off of the PSD was adjusted from $\lambda_s = 0.01\lambda_r$ to $0.1\lambda_r$, as indicated by the respective PSDs in a). If the surface energy is adjusted for the elastic energy in the missing part of the spectrum, the different cut-offs lead to very similar contact topologies, as depicted in b).

these short time scales do not need to be mimicked when the long-term relaxation is of interest. To illustrate this, Fig. 4.13 compares three viscoelastic models with different values of s but similar behavior at low frequencies ω. They lead to similar contact relaxations even for a rough surface contact.
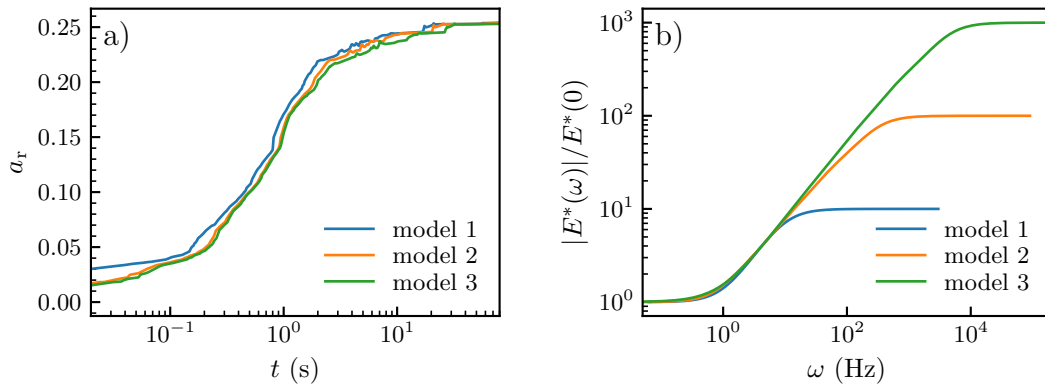
Figure 4.13: Relaxation of a 1D randomly rough contact at zero external stress with different viscoelastic models. a) highlights the evolution of the relative contact area a_r over time, while b) shows the corresponding $E(\omega)$.

The effect of the slope of the $E(\omega)$ relation was briefly discussed in the context of Publ. **III** because realistic viscoelastic measurements tend to show a smaller slope than the one produced by the SLS model. The long-term evolution once again did not show any significant sensitivity to the exact shape of the rest of the $E(\omega)$ curve, as long as the low-ω regimes are similar. It may even be possible to identify another scaling relation describing how the slope of the contact radius-time curve depends on the slope of the $E(\omega)$ curve. It is certainly not effective to directly simulate an experimentally measured viscoelastic relaxation spectrum, which can spread across up to 30 orders of magnitude in time [81]. Even on the most powerful modern hardware, a GFMD simulation at a resolution of 4096×4096 with 10^{30} time steps would not finish within the expected lifetime of our solar system.

Chapter 5

Conclusions

I have systematically generalized the GFMD simulation technique and applied it to contact mechanics problems involving thin films, viscoelastic materials and frictional interfaces. Thanks to direct comparisons to well-designed experiments, my colleagues and I have verified that the implemented changes have significantly improved the agreement between model and reality. Therefore, the results presented in Chap. 4 provide valuable insight into a wide range of practically relevant contact phenomena, which are out of reach of conventional models.

Publ. **I** introduced a simple estimate for the effective stiffness of a thin elastic slab in contact with a circular flat punch based on dimensional analysis. The rigid foundation, on which the deformable film is resting, increases the effective stiffness of the system, which is particularly noticeable for (nearly) incompressible materials and indentations whose lateral length scale exceeds the thickness of the film. The derived equation allows us to predict the adhesive pull-off force as a function of Poisson's ratio and geometric confinement. Furthermore, we find and explain a transition in the detachment mechanism from ideal radial crack propagation to the formation of small-scale wrinkles. The study provides analytical estimates as well as a broad range of reference data for confined polymer contacts, such as rubber seals and adhesive tapes.

In Publ. **II**, the above model for thin films was successfully applied to rationalize the real-world performance of fibril structures which are covered with a soft skin adhesive (SSA) film. These film-terminated patterns are designed for optimal adhesion to skin in applications such as wearable electronics or wound dressing. Increasing the thickness of the terminal film usually provides better adhesion to skin-like rough surfaces, because the SSA is softer than the fibrillar base structure and can easily conform to the counterface. On a flat polished surface, on the other hand, a thinner film and an overall stiffer structure tends to provide larger pull-off forces.

Publ. **IV** shows that it is imperative to take the viscoelastic nature of soft adhesion into account in order to achieve quantitative agreement between model and reality. A great overlap between numerical and experimental curves is observed, where the contact images assert that the same trends and features are obtained for the right reasons. The

viscoelastic velocity-dependence of the hysteresis associated with topographical saddle points is perfectly captured by the GFMD simulations, leaving an error of at most 20% in the final pull-off force. Achieving this level of agreement between model and reality requires the viscoelastic and adhesive model parameters to be re-scaled compared to the realistic ones. This is because of the relationship between the microscopic range of interaction and the macroscopic viscoelastic time scale, which Publ. **III** identifies as a surprisingly universal scaling law: the macroscopic contact evolution time is proportional to the 1.8 power of the inverse range of adhesion.

Finally, the description of the elastic properties was generalized to take the coupling between normal and transverse stresses and displacements into account in Publ. **V**. Our numerical results reveal that with coupling taken into account, the presence of interfacial friction breaks the symmetry of the deformation fields, increases local stress concentrations and reduces the fluid flow through the interface. The variation of these properties has crucial implications for many practical applications, such as lubrication and wear in contacts involving coatings, seals and bearings. Especially the observed trends for local stress maxima imply that calculations that neglect coupling may significantly underestimate the probability of material failure. Unfortunately, the determination of the interfacial boundary conditions and local friction law is a tall order for experiments, so that no direct comparisons were performed in the context of this study. Since the observed coupling effects were often in the range of 10%, the observable changes would most likely be smaller than the experimental uncertainties connected to the phenomena that cause them.

Chapter 6

Outlook

In spite of the many improvements and insights reported in this work, the GFMD simulation method still appears to have a lot of unused potential. First of all, the 3D implementation has only been used in a purely theoretical study that ignored adhesion. Applying it to adhesion could finally answer the question whether it is most realistic to assume friction-less or sticky interfaces or something in between. To what extend the interface relies on friction is a very common source of uncertainty in experimental contacts, into which further direct comparisons to GFMD could grant valuable insight. To this end, the implemented friction law should be generalized to a realistic velocity-dependent model using a Stokes relationship for small sliding speeds (similarly to Refs. [187, 188]). In fact, this has already been implemented, but has not yet been used. Moreover, the 3D elasticity implementation currently does not make use of the viscoelastic material model, although it is well known that the viscoelastic contribution to friction is significant for soft materials [24, 189]. To further highlight this effect, Fig. 6.1 shows the results of a few exemplary simulations: The contact between elastic body and rough counter-face was first relaxed at constant pressure for different periods of time t_{relax}. After this initial relaxation, the rough interface started sliding, at which point the lateral stress (evaluated from the normal stress acting on a slope) becomes anisotropic, amounting to a net friction in the interface. Depending on the duration of the initial relaxation, the friction peak at the onset of the sliding motion can take on completely different values. In all cases, the friction eventually levels off towards the same constant value representative of steady-state sliding at the given normal pressure. The simulated system represents a realistic topography of a mechanically processed metallic surface and the elastomer models a rubber seal inside a machine that is first standing still and then starts moving. This kind of scenario is comparable to a wide range of applications with great industrial significance.

For further research into film-terminated adhesives and skin mechanics, it would be desirable to implement the (friction-less) Green's function for the coated half-space, as given in Appendix A2 of Ref. [72]. When modeling the mechanics of skin, the "coating" would represent the stratum corneum and the half-space underneath the epidermis. This would be the most accurate model for skin that GFMD is compatible with. Since the
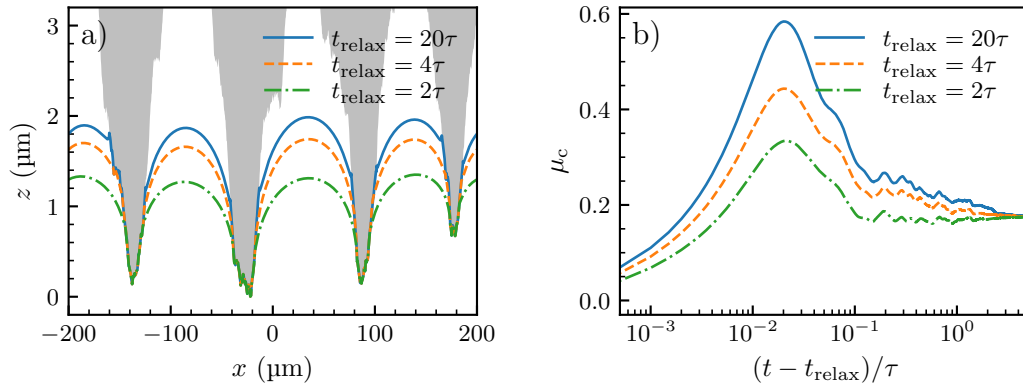
Figure 6.1: Simulation of a rubber surface forming a contact with a rough interface for a time t_{relax} before the two surfaces start moving laterally with respect to each other. a) shows the displacement profiles at the end of the relaxation and b) the time evolution of the lateral stress obtained after the respective systems start sliding. The simulations used the Kelvin-Voigt SLS model of viscoelasticity with relaxation time τ. The longer the initial relaxation, the higher the initial friction peak associated with the viscoelastic dissipation.

Green's function method inherently assumes translational invariance in the plane, it cannot directly incorporate the anisotropic features of skin, which would certainly be required to improve the model further.

From a practical perspective, the GFMD simulation code could be made much easier to use, potentially even for non-scientists. This would most likely require the addition of a graphical user interface (GUI), for which the code base would need to be overhauled. As of the writing of this thesis, the potential for a redesign of the entire program is discussed but not actively pursued. The subsequent implementation of any of the just-mentioned improvements would greatly benefit from a more modular layout, allowing individual units to be tested independently. In the current state, implementing new features can be quite challenging and new users often need months to familiarize themselves with the method. In principle, if GFMD could become as easy to use as typical FEM software, it might be a serious contender for becoming one of the standards for numerical contact mechanics calculations. At this point, the best widely available option is certainly the quasi-static solver included in the *contact.engineering* website [69].

Bibliography

[1] K. Kendall, "An Adhesion Paradox," *J. Adhes.*, vol. 5, no. 1, pp. 77–79, 1973.

[2] K. Kendall, *Molecular Adhesion and Its Applications.* New York: Springer, 2001.

[3] H. Hertz, "Über die Berührung fester elastischer Körper," *J. für Reine Angew. Math.*, vol. 92, pp. 156–171, 1881.

[4] K. Autumn, M. Sitti, Y. A. Liang, A. M. Peattie, W. R. Hansen, S. Sponberg, T. W. Kenny, R. Fearing, J. N. Israelachvili, and R. J. Full, "Evidence for van der Waals adhesion in gecko setae," *Proc. Natl. Acad. Sci.*, vol. 99, no. 19, pp. 12252–12256, 2002.

[5] C. Y. Hui, N. J. Glassmaker, T. Tang, and A. Jagota, "Design of biomimetic fibrillar interfaces: 2. Mechanics of enhanced adhesion," *J. R. Soc. Interface*, vol. 1, no. 1, pp. 35–48, 2004.

[6] H. Gao and H. Yao, "Shape insensitive optimal adhesion of nanoscale fibrillar structures," *Proc. Natl. Acad. Sci. U. S. A.*, vol. 101, no. 21, pp. 7851–7856, 2004.

[7] N. J. Glassmaker, A. Jagota, and C. Y. Hui, "Adhesion enhancement in a biomimetic fibrillar interface," *Acta Biomater.*, vol. 1, no. 4, pp. 367–375, 2005.

[8] K. Autumn, C. Majidi, R. E. Groff, A. Dittmore, and R. Fearing, "Effective elastic modulus of isolated gecko setal arrays," *J. Exp. Biol.*, vol. 209, no. 18, pp. 3558–3568, 2006.

[9] H. E. Jeong and K. Y. Suh, "Nanohairs and nanotubes: Efficient structural elements for gecko-inspired artificial dry adhesives," *Nano Today*, vol. 4, no. 4, pp. 335–346, 2009.

[10] S. C. L. Fischer, E. Arzt, and R. Hensel, "Composite Pillars with a Tunable Interface for Adhesion to Rough Substrates," *ACS Appl. Mater. Interfaces*, vol. 9, no. 1, pp. 1036–1044, 2017.

[11] V. Tinnemann, E. Arzt, and R. Hensel, "Switchable double-sided micropatterned adhesives for selective fixation and detachment," *J. Mech. Phys. Solids*, vol. 123, pp. 20–27, 2019.

[12] D. Son, V. Liimatainen, and M. Sitti, "Machine Learning-Based and Experimentally Validated Optimal Adhesive Fibril Designs," *Small*, p. 2102867, 2021.

[13] Y. Wang and R. Hensel, "Bioinspired Underwater Adhesion to Rough Substrates by Cavity Collapse of Cupped Microstructures," *Adv. Funct. Mater.*, vol. 31, no. 31, p. 2101787, 2021.

[14] L. Barnefske, F. Rundel, K. Moh, R. Hensel, X. Zhang, and E. Arzt, "Tuning the Release Force of Microfibrillar Adhesives by Geometric Design," *Adv. Mater. Interfaces*, vol. 9, no. 33, p. 2201232, 2022.

[15] V. Tinnemann, L. Hernández, S. C. L. Fischer, E. Arzt, R. Bennewitz, and R. Hensel, "In Situ Observation Reveals Local Detachment Mechanisms and Suction Effects in Micropatterned Adhesives," *Adv. Funct. Mater.*, vol. 29, no. 14, p. 1807713, 2019.

[16] R. Hensel, J. Thiemecke, and J. A. Booth, "Preventing Catastrophic Failure of Microfibrillar Adhesives in Compliant Systems Based on Statistical Analysis of Adhesive Strength," *ACS Appl. Mater. Interfaces*, vol. 13, no. 16, pp. 19422–19429, 2021.

[17] M. Samri, J. Thiemecke, E. Prinz, T. Dahmen, R. Hensel, and E. Arzt, "Predicting the adhesion strength of micropatterned surfaces using supervised machine learning," *Mater. Today*, vol. 53, pp. 41–50, 2022.

[18] J. Boussinesq, *Application des potentiels*. Mémoires de la société des sciences, de l'agriculture et des arts de Lille, Paris: Gauthier-Villars, 2 ed., 1885.

[19] A. N. Gent, "Compression of rubber blocks," *Rubber Chem. Technol.*, vol. 67, no. 3, pp. 549–558, 1994.

[20] J. F. Ganghoffer and A. N. Gent, "Adhesion of a Rigid Punch to a Thin Elastic Layer," *J. Adhes.*, vol. 48, no. 1-4, pp. 75–84, 1995.

[21] W. Mönch and S. Herminghaus, "Elastic instability of rubber films between solid bodies," *Europhys. Lett.*, vol. 53, no. 4, pp. 525–531, 2001.

[22] R. E. Webber, K. R. Shull, A. Roos, and C. Creton, "Effects of geometric confinement on the adhesive debonding of soft elastic solids," *Phys. Rev. E - Stat. Physics, Plasmas, Fluids, Relat. Interdiscip. Top.*, vol. 68, no. 2, p. 021805, 2003.

[23] B. N. J. Persson and E. Tosatti, "The effect of surface roughness on the adhesion of elastic solids," *J. Chem. Phys.*, vol. 115, no. 12, pp. 5597–5610, 2001.

[24] N. Menga, C. Putignano, G. Carbone, and G. P. Demelio, "The sliding contact of a rigid wavy surface with a viscoelastic half-space," *Proc. R. Soc. A Math. Phys. Eng. Sci.*, vol. 470, no. 2169, p. 20140392, 2014.

[25] S. Sukhomlinov and M. H. Müser, "On the viscous dissipation caused by randomly rough indenters in smooth sliding motion," *Appl. Surf. Sci. Adv.*, vol. 6, p. 100182, 2021.

[26] G. Violano, A. Chateauminois, and L. Afferrante, "Rate-dependent adhesion of viscoelastic contacts. Part II: Numerical model and hysteresis dissipation," *Mech. Mater.*, vol. 158, p. 103884, 2021.

[27] G. Violano, A. Chateauminois, and L. Afferrante, "Rate-dependent adhesion of viscoelastic contacts, Part I: Contact area and contact line velocity within model randomly rough surfaces," *Mech. Mater.*, vol. 160, p. 103926, 2021.

[28] F. Pérez-Ràfols, J. S. Van Dokkum, and L. Nicola, "On the interplay between roughness and viscoelasticity in adhesive hysteresis," *J. Mech. Phys. Solids*, vol. 170, p. 105079, 2023.

[29] N. Menga, L. Afferrante, and G. Carbone, "Effect of thickness and boundary conditions on the behavior of viscoelastic layers in sliding contact with wavy profiles," *J. Mech. Phys. Solids*, vol. 95, pp. 517–529, 2016.

[30] C. Campañá and M. H. Müser, "Practical Green's function approach to the simulation of elastic semi-infinite solids," *Phys. Rev. B - Condens. Matter Mater. Phys.*, vol. 74, no. 7, pp. 19–21, 2006.

[31] D. H. Kaelble and J. Moacanin, "A surface energy analysis of bioadhesion," *Polymer (Guildf).*, vol. 18, no. 5, pp. 475–482, 1977.

[32] J. Israelachvili, *Intermolecular and Surface Forces.* Burlington: Academic Press, 3 ed., 2011.

[33] B. N. J. Persson and J. Biele, "On the Stability of Spinning Asteroids," *Tribol Lett*, vol. 70, no. 2, p. 34, 2022.

[34] A. Y. Stark, M. R. Klittich, M. Sitti, P. H. Niewiarowski, and A. Dhinojwala, "The effect of temperature and humidity on adhesion of a gecko-inspired adhesive: Implications for the natural system," *Sci. Rep.*, vol. 6, p. 30936, 2016.

[35] C. T. Mitchell, C. B. Dayan, D.-M. Drotlef, M. Sitti, and A. Y. Stark, "The effect of substrate wettability and modulus on gecko and gecko-inspired synthetic adhesion in variable temperature and humidity," *Sci. Rep.*, vol. 10, no. 1, p. 19748, 2020.

[36] G. He, M. H. Müser, and M. O. Robbins, "Adsorbed Layers and the Origin of Static Friction," *Science*, vol. 284, no. 5420, pp. 1650–1652, 1999.

[37] A. Oláh, H. Hillborg, and G. J. Vancso, "Hydrophobic recovery of UV/ozone treated poly(dimethylsiloxane): adhesion studies by contact mechanics and mechanism of surface modification," *Appl. Surf. Sci.*, vol. 239, no. 3-4, pp. 410–423, 2005.

[38] A. Tiwari, J. Wang, and B. N. J. Persson, "Adhesion paradox: Why adhesion is usually not observed for macroscopic solids," *Phys. Rev. E*, vol. 102, no. 4, p. 42803, 2020.

[39] G. A. D. Briggs and B. J. Briscoe, "The effect of surface topography on the adhesion of elastic solids," *J. Phys. D Appl. Phys.*, vol. 10, no. 18, pp. 2453–2466, 1977.

[40] K. N. G. Fuller and A. D. Roberts, "Rubber rolling on rough surfaces," *J. Phys. D Appl. Phys.*, vol. 14, no. 2, pp. 221–239, 1981.

[41] B. N. J. Persson, "Adhesion between an elastic body and a randomly rough hard surface," *Eur. Phys. J. E*, vol. 8, no. 4, pp. 385–401, 2002.

[42] C. S. Davis, D. Martina, C. Creton, A. Lindner, and A. J. Crosby, "Enhanced adhesion of elastic materials to small-scale wrinkles," *Langmuir*, vol. 28, no. 42, pp. 14899–14908, 2012.

[43] A. Gujrati, S. R. Khanal, L. Pastewka, and T. D. B. Jacobs, "Combining TEM, AFM, and Profilometry for Quantitative Topography Characterization Across All Scales," *ACS Appl. Mater. Interfaces*, vol. 10, no. 34, pp. 29169–29178, 2018.

[44] T. D. B. Jacobs, T. Junge, and L. Pastewka, "Quantitative characterization of surface topography using spectral analysis," *Surf. Topogr. Metrol. Prop.*, vol. 5, no. 1, p. 013001, 2017.

[45] A. Sanner, W. G. Nöhring, L. A. Thimons, T. D. B. Jacobs, and L. Pastewka, "Scale-dependent roughness parameters for topography analysis," *Appl. Surf. Sci. Adv.*, vol. 7, p. 100190, 2022.

[46] T. D. B. Jacobs, N. Miller, M. H. Müser, and L. Pastewka, "The surface-topography challenge: Problem definition," *arXiv*, p. 2206.13384, 2022.

[47] M. H. Müser, W. B. Dapp, R. Bugnicourt, P. Sainsot, N. Lesaffre, T. A. Lubrecht, B. N. J. Persson, K. Harris, A. Bennett, K. Schulze, S. Rohde, P. Ifju, W. G. Sawyer, T. Angelini, H. Ashtari Esfahani, M. Kadkhodaei, S. Akbarzadeh, J. J. Wu, G. Vorlaufer, A. Vernes, S. Solhjoo, A. I. Vakis, R. L. Jackson, Y. Xu, J. Streator, A. Rostami, D. Dini, S. Medina, G. Carbone, F. Bottiglione, L. Afferrante, J. Monti, L. Pastewka, M. O. Robbins, and J. A. Greenwood, "Meeting the Contact-Mechanics Challenge," *Tribol. Lett.*, vol. 65, no. 4, p. 118, 2017.

[48] K. Kendall, "The adhesion and surface energy of elastic solids," *J. Phys. D. Appl. Phys.*, vol. 4, no. 8, pp. 1186–1195, 1971.

[49] C. A. Dahlquist, "Pressure-sensitive adhesives," in *Treatise Adhes. Adhes.* (R. L. Patrick, ed.), (New York), pp. 219–260, Marcel Dekker, 1969.

[50] B. N. J. Persson, "Theory of rubber friction and contact mechanics," *J. Chem. Phys.*, vol. 115, no. 8, pp. 3840–3861, 2001.

[51] B. Dubuc, S. W. Zucker, C. Tricot, J. F. Quiniou, and D. Wehbi, "Evaluating the fractal dimension of surfaces," *Proc. R. Soc. Lond. A*, vol. 425, no. 1868, pp. 113–127, 1989.

[52] S. Chowdhury, A. Roy, I. Bodemann, and S. K. Banerjee, "Two-Dimensional to Three-Dimensional Growth of Transition Metal Diselenides by Chemical Vapor Deposition: Interplay between Fractal, Dendritic, and Compact Morphologies," *ACS Appl. Mater. Interfaces*, vol. 12, no. 13, pp. 15885–15892, 2020.

[53] A. R. Hinkle, W. G. Nöhring, R. Leute, T. Junge, and L. Pastewka, "The emergence of small-scale self-affine surface roughness from deformation," *Sci. Adv.*, vol. 6, no. 7, p. eaax0847, 2020.

[54] M. A. Issa, M. A. Issa, M. S. Islam, and A. Chudnovsky, "Fractal dimension - a measure of fracture roughness and toughness of concrete," *Eng. Fract. Mech.*, vol. 70, no. 1, pp. 125–137, 2003.

[55] S. Ouchi and M. Matsushita, "Measurement of self-affinity on surfaces as a trial application of fractal geometry to landform analysis," *Geomorphology*, vol. 5, no. 1-2, pp. 115–130, 1992.

[56] G. Carbone, M. Scaraggi, and U. Tartaglino, "Adhesive contact of rough surfaces: Comparison between numerical calculations and analytical theories," *Eur. Phys. J. E*, vol. 30, no. 1, pp. 65–74, 2009.

[57] L. Pastewka and M. O. Robbins, "Contact between rough surfaces and a criterion for macroscopic adhesion," *Proc. Natl. Acad. Sci. U. S. A.*, vol. 111, no. 9, pp. 3298–3303, 2014.

[58] M. H. Müser, "A dimensionless measure for adhesion and effects of the range of adhesion in contacts of nominally flat surfaces," *Tribol. Int.*, vol. 100, no. 10, pp. 41–47, 2016.

[59] A. Wang and M. H. Müser, "Is there more than one stickiness criterion?," *Friction*, vol. 11, no. 6, pp. 1027–1039, 2023.

[60] A. Majumdar and B. Bhushan, "Role of Fractal Geometry in Roughness Characterization and Contact Mechanics of Surfaces," *J. Tribol.*, vol. 112, no. 2, pp. 205–216, 1990.

[61] M. H. Müser, "On the Linearity of Contact Area and Reduced Pressure," *Tribol. Lett.*, vol. 65, no. 4, pp. 1–2, 2017.

[62] Y. Zhou and M. H. Müser, "Effect of Structural Parameters on the Relative Contact Area for Ideal, Anisotropic, and Correlated Random Roughness," *Front. Mech. Eng.*, vol. 6, p. 59, 2020.

[63] B. N. J. Persson, O. Albohr, U. Tartaglino, A. I. Volokitin, and E. Tosatti, "On the nature of surface roughness with application to contact mechanics, sealing, rubber friction and adhesion," *J. Phys. Condens. Matter*, vol. 17, no. 1, p. R1, 2005.

[64] T. R. Thomas, "Characterization of surface roughness," *Precis. Eng.*, vol. 3, no. 2, pp. 97–104, 1981.

[65] J. A. Greenwood, "Contact of nominally flat surfaces," *Proc. R. Soc. London. Ser. A. Math. Phys. Sci.*, vol. 295, no. 1442, pp. 300–319, 1966.

[66] M. Ciavarella, "A very simple estimate of adhesion of hard solids with rough surfaces based on a bearing area model," *Meccanica*, vol. 53, no. 1-2, pp. 241–250, 2018.

[67] P. Massart, *Concentration inequalities and model selection*, vol. 1896. Berlin: Springer Berlin Heidelberg, 2007.

[68] A. Wang and M. H. Müser, "On the usefulness of the height-difference-autocorrelation function for contact mechanics," *Tribol. Int.*, vol. 123, pp. 224–233, 2018.

[69] M. C. Röttger, A. Sanner, L. A. Thimons, T. Junge, A. Gujrati, J. M. Monti, W. G. Nöhring, T. D. B. Jacobs, and L. Pastewka, "Contact.engineering – Create, analyze and publish digital surface twins from topography measurements across many scales," *Surf. Topogr.: Metrol. Prop.*, vol. 10, no. 3, p. 35032, 2022.

[70] E. M. Lifschitz and L. D. Landau, *Theory of Elasticity*. Oxford: Pergamon Press, 2 ed., 1970.

[71] G. Carbone and L. Mangialardi, "Analysis of the adhesive contact of confined layers by using a Green's function approach," *J. Mech. Phys. Solids*, vol. 56, no. 2, pp. 684–706, 2008.

[72] M. Scaraggi and D. Comingio, "Rough contact mechanics for viscoelastic graded materials: The role of small-scale wavelengths on rubber friction," *Int. J. Solids Struct.*, vol. 125, pp. 276–296, 2017.

[73] N. Menga, "Rough frictional contact of elastic thin layers: The effect of geometrical coupling," *Int. J. Solids Struct.*, vol. 164, pp. 212–220, 2019.

[74] S. P. Venugopalan, L. Nicola, and M. H. Müser, "Green's function molecular dynamics: Including finite heights, shear, and body fields," *Model. Simul. Mater. Sci. Eng.*, vol. 25, no. 3, pp. 0–13, 2017.

[75] R. von Mises, "Mechanik der festen Körper im plastisch-deformablen Zustand," *Nachrichten von der Gesellschaft der Wissenschaften zu Göttingen, Math. Klasse*, pp. 582–592, 1913.

[76] R. M. Christensen, *Theory of Viscoelasticity*. New York: Academic Press, 2 ed., 1982.

[77] F. J. Rizzo and D. J. Shippy, "An Application of the Correspondence Principle of Linear Viscoelasticity Theory," *SIAM J. Appl. Math.*, vol. 21, no. 2, pp. 321–330, 1971.

[78] T. Ohkami and J.-I. Murai, "Identification procedure for viscoelastic materials using correspondence principle," *Commun. Numer. Methods Eng.*, vol. 14, no. 6, pp. 497–504, 1998.

[79] B. Schnurr, F. Gittes, F. C. MacKintosh, and C. F. Schmidt, "Determining Microscopic Viscoelasticity in Flexible and Semiflexible Polymer Networks from Thermal Fluctuations," *Macromolecules*, vol. 30, no. 25, pp. 7781–7792, 1997.

[80] B. N. J. Persson and E. A. Brener, "Crack propagation in viscoelastic solids," *Phys. Rev. E*, vol. 71, no. 3, pp. 1–8, 2005.

[81] A. Tiwari, L. Dorogin, M. Tahir, K. W. Stöckelhuber, G. Heinrich, N. Espallargas, and B. N. J. Persson, "Rubber contact mechanics: Adhesion, friction and leakage of seals," *Soft Matter*, vol. 13, no. 48, pp. 9103–9121, 2017.

[82] M. H. Müser and B. N. J. Persson, "Crack and pull-off dynamics of adhesive, viscoelastic solids," *Europhys. Lett.*, vol. 137, no. 3, p. 36004, 2022.

[83] L. Afferrante and G. Violano, "On the effective surface energy in viscoelastic Hertzian contacts," *J. Mech. Phys. Solids*, vol. 158, p. 104669, 2022.

[84] L. Afferrante and G. Violano, "The adhesion of viscoelastic bodies with slightly wavy surfaces," *Tribol. Int.*, vol. 174, p. 107726, 2022.

[85] C. Müller, "sintharic/Data-Coupling-2023-07: Submitted version (MIT License)." https://doi.org/10.5281/zenodo.8360035, 2023. Accessed: 2024-03-13.

[86] R. Bugnicourt, P. Sainsot, N. Lesaffre, and A. A. Lubrecht, "Transient frictionless contact of a rough rigid surface on a viscoelastic half-space," *Tribol. Int.*, vol. 113, pp. 279–285, 2017.

[87] E. Bitzek, P. Koskinen, F. Gähler, M. Moseler, and P. Gumbsch, "Structural Relaxation Made Simple," *Phys. Rev. Lett.*, vol. 97, no. 17, p. 170201, 2006.

[88] Y. Zhou, M. Moseler, and M. H. Müser, "Solution of boundary-element problems using the fast-inertial-relaxation-engine method," *Phys. Rev. B*, vol. 99, no. 14, pp. 1–8, 2019.

[89] C. Putignano, L. Afferrante, G. Carbone, and G. Demelio, "A new efficient numerical method for contact mechanics of rough surfaces," *Int. J. Solids Struct.*, vol. 49, no. 2, pp. 338–343, 2012.

[90] G. Carbone and C. Putignano, "A novel methodology to predict sliding and rolling friction of viscoelastic materials: Theory and experiments," *J. Mech. Phys. Solids*, vol. 61, no. 8, pp. 1822–1834, 2013.

[91] A. Wang, Y. Zhou, and M. H. Müser, "Modeling adhesive hysteresis," *Lubricants*, vol. 9, no. 2, pp. 1–30, 2021.

[92] D. S. Dugdale, "Yielding of steel sheets containing slits," *J. Mech. Phys. Solids*, vol. 8, no. 2, pp. 100–104, 1960.

[93] G. I. Barenblatt, "The Mathematical Theory of Equilibrium Cracks in Brittle Fracture," in *Adv. Appl. Mech.*, pp. 55–129, Elsevier, 1962.

[94] M. H. Müser, S. V. Sukhomlinov, and L. Pastewka, "Interatomic potentials: achievements and challenges," *Adv. Phys. X*, vol. 8, no. 1, p. 2093129, 2022.

[95] B. Derjaguin, "Untersuchungen über die Reibung und Adhäsion, IV," *Kolloid-Zeitschrift*, vol. 69, no. 2, pp. 155–164, 1934.

[96] J. Joe, M. Scaraggi, and J. R. Barber, "Effect of fine-scale roughness on the tractions between contacting bodies," *Tribol. Int.*, vol. 111, pp. 52–56, 2017.

[97] J. Joe, M. D. Thouless, and J. R. Barber, "Effect of roughness on the adhesive tractions between contacting bodies," *J. Mech. Phys. Solids*, vol. 118, pp. 365–373, 2018.

[98] M. H. Müser, "Nature of Mechanical Instabilities and Their Effect on Kinetic Friction," *Phys. Rev. Lett.*, vol. 89, no. 22, p. 224301, 2002.

[99] O. M. Braun and M. Peyrard, "Dependence of kinetic friction on velocity: Master equation approach," *Phys. Rev. E*, vol. 83, no. 4, 2011.

[100] G. Amontons, "De la résistance causée dans les machines," *Mém. Académie R. Sci.*, pp. 206–227, 1699.

[101] P. J. Blau, "Amontons' Laws of Friction," in *Encycl. Tribol.* (Q. J. Wang and Y.-W. Chung, eds.), p. 71, Boston: Springer US, 2013.

[102] I. M. Sivebaek, V. N. Samoilov, and B. N. J. Persson, "Frictional properties of confined polymers," *Eur. Phys. J. E*, vol. 27, no. 1, pp. 37–46, 2008.

[103] A. M. Homola, J. N. Israelachvili, P. M. McGuiggan, and M. L. Gee, "Fundamental experimental studies in tribology: The transition from interfacial friction of undamaged molecularly smooth surfaces to normal friction with wear," *Wear*, vol. 136, no. 1, pp. 65–83, 1990.

[104] A. Berman, C. Drummond, and J. Israelachvili, "Amontons' law at the molecular level," *Tribol. Lett.*, vol. 4, no. 2, pp. 95–101, 1998.

[105] V. L. Popov and M. Heß, *Method of dimensionality reduction in contact mechanics and friction.* Springer Berlin Heidelberg, 2015.

[106] I. N. Sneddon, "The relation between load and penetration in the axisymmetric Boussinesq problem for a punch of arbitrary profile," *Int. J. Eng. Sci.*, vol. 3, no. 1, pp. 47–57, 1965.

[107] H. Yao and H. Gao, "Optimal shapes for adhesive binding between two elastic bodies," *J. Colloid Interface Sci.*, vol. 298, no. 2, pp. 564–572, 2006.

[108] K. L. Johnson, "A note on the adhesion of elastic solids," *Br. J. Appl. Phys.*, vol. 9, no. 5, pp. 199–200, 1958.

[109] K. L. Johnson, K. Kendall, and A. D. Roberts, "Surface energy and the contact of elastic solids," *Proc. R. Soc. London. A. Math. Phys. Sci.*, vol. 324, no. 1558, pp. 301–313, 1971.

[110] B. V. Derjaguin, V. M. Muller, and Y. P. Toporov, "Effect of contact deformations on the adhesion of particles," *J. Colloid Interface Sci.*, vol. 53, no. 2, pp. 314–326, 1975.

[111] R. S. Bradley, "The cohesive force between solid surfaces and the surface energy of solids," *London, Edinburgh, Dublin Philos. Mag. J. Sci.*, vol. 13, no. 86, pp. 853–862, 1932.

[112] D. Maugis, "Adhesion of spheres: The JKR-DMT transition using a Dugdale model," *J. Colloid Interface Sci.*, vol. 150, no. 1, pp. 243–269, 1992.

[113] E. Willert, I. A. Lyashenko, and V. L. Popov, "Influence of the Tabor parameter on the adhesive normal impact of spheres in Maugis-Dugdale approximation," *Comput. Part. Mech.*, vol. 5, no. 3, pp. 313–318, 2017.

[114] D. Tabor, "Surface forces and surface interactions," *J. Colloid Interface Sci.*, vol. 58, no. 1, pp. 2–13, 1977.

[115] V. M. Muller, "On the theory of pull-off of a viscoelastic sphere from a flat surface," *J. Adhes. Sci. Technol.*, vol. 13, no. 9, pp. 999–1016, 1999.

[116] M. Ciavarella and A. Papangelo, "A generalized Johnson parameter for pull-off decay in the adhesion of rough surfaces," *Phys. Mesomech.*, vol. 21, no. 1, pp. 67–75, 2018.

[117] Y. Jiang, D. S. Grierson, and K. T. Turner, "Flat punch adhesion: Transition from fracture-based to strength-limited pull-off," *J. Phys. D. Appl. Phys.*, vol. 47, no. 32, p. 325301, 2014.

[118] Z. Zheng and J. Yu, "Using the Dugdale approximation to match a specific interaction in the adhesive contact of elastic objects," *J. Colloid Interface Sci.*, vol. 310, no. 1, pp. 27–34, 2007.

[119] J. Y. Chung and M. K. Chaudhury, "Soft and hard adhesion," *J. Adhes.*, vol. 81, no. 10-11, pp. 1119–1145, 2005.

[120] J. A. Greenwood, "Adhesion of small spheres," *Philos. Mag.*, vol. 89, no. 11, pp. 945–965, 2009.

[121] M. Ciavarella, J. A. Greenwood, and J. R. Barber, "Effect of Tabor parameter on hysteresis losses during adhesive contact," *J. Mech. Phys. Solids*, vol. 98, pp. 236–244, 2017.

[122] D. T. K. N. G. Fuller, "The effect of surface roughness on the adhesion of elastic solids," *Proc. R. Soc. London. A. Math. Phys. Sci.*, vol. 345, no. 1642, pp. 327–342, 1975.

[123] D. Maugis, "On the contact and adhesion of rough surfaces," *J. Adhes. Sci. Technol.*, vol. 10, no. 2, pp. 161–175, 1996.

[124] C. Morrow, M. Lovell, and X. Ning, "A JKR-DMT transition solution for adhesive rough surface contact," *J. Phys. D Appl. Phys.*, vol. 36, no. 5, pp. 534–540, 2003.

[125] J. A. Greenwood and J. J. Wu, "Surface Roughness and Contact: An Apology," *Meccanica*, vol. 36, no. 6, pp. 617–630, 2001.

[126] C. Campañá, M. H. Müser, and M. O. Robbins, "Elastic contact between self-affine surfaces: Comparison of numerical stress and contact correlation functions with analytic predictions," *J. Phys. Condens. Matter*, vol. 20, no. 35, p. 354013, 2008.

[127] M. H. Müser, "Response to "A Comment on Meeting the Contact-(Mechanics) Challenge"," *Tribol. Lett.*, vol. 66, no. 1, pp. 1–6, 2018.

[128] J. I. McCool, "Extending the Capability of the Greenwood Williamson Microcontact Model," *J. Tribol.*, vol. 122, no. 3, pp. 496–502, 2000.

[129] M. Ciavarella, V. Delfine, and G. Demelio, "A "re-vitalized" Greenwood and Williamson model of elastic contact between fractal surfaces," *J. Mech. Phys. Solids*, vol. 54, no. 12, pp. 2569–2591, 2006.

[130] M. Ciavarella, J. A. Greenwood, and M. Paggi, "Inclusion of "interaction" in the Greenwood and Williamson contact theory," *Wear*, vol. 265, no. 5-6, pp. 729–734, 2008.

[131] G. Carbone, "A slightly corrected Greenwood and Williamson model predicts asymptotic linearity between contact area and load," *J. Mech. Phys. Solids*, vol. 57, no. 7, pp. 1093–1102, 2009.

[132] A. I. Vakis, "Asperity Interaction and Substrate Deformation in Statistical Summation Models of Contact Between Rough Surfaces," *J. Appl. Mech.*, vol. 81, no. 4, p. 041012, 2013.

[133] H. Song, A. I. Vakis, X. Liu, and E. V. der Giessen, "Statistical model of rough surface contact accounting for size-dependent plasticity and asperity interaction," *J. Mech. Phys. Solids*, vol. 106, pp. 1–14, 2017.

[134] A. W. Bush, R. D. Gibson, and T. R. Thomas, "The elastic contact of a rough surface," *Wear*, vol. 35, no. 1, pp. 87–111, 1975.

[135] W. B. Dapp, N. Prodanov, and M. H. Müser, "Systematic analysis of Persson's contact mechanics theory of randomly rough elasticsurfaces," *J. Phys. Condens. Matter*, vol. 26, no. 35, p. 355002, 2014.

[136] N. Prodanov, W. B. Dapp, and M. H. Müser, "On the contact area and mean gap of rough, elastic contacts: Dimensional analysis, numerical corrections, and reference data," *Tribol. Lett.*, vol. 53, no. 2, pp. 433–448, 2014.

[137] B. N. J. Persson, F. Bucher, and B. Chiaia, "Elastic contact between randomly rough surfaces: Comparison of theory with numerical results," *Phys. Rev. B*, vol. 65, no. 18, p. 184106, 2002.

[138] C. Yang and B. N. J. Persson, "Contact mechanics: contact area and interfacial separation from small contact to full contact," *J. Phys. Condens. Matter*, vol. 20, no. 21, p. 215214, 2008.

[139] G. Carbone, B. Lorenz, B. N. J. Persson, and A. Wohlers, "Contact mechanics and rubber friction for randomly rough surfaces with anisotropic statistical properties," *Eur. Phys. J. E*, vol. 29, no. 3, pp. 275–284, 2009.

[140] B. N. J. Persson, "Adhesion between Elastic Bodies with Randomly Rough Surfaces," *Phys. Rev. Lett.*, vol. 89, no. 24, pp. 1–4, 2002.

[141] B. N. J. Persson and M. Scaraggi, "Theory of adhesion: Role of surface roughness," *J. Chem. Phys.*, vol. 141, no. 12, pp. 1–18, 2014.

[142] M. H. Müser and W. B. Dapp, "The contact mechanics challenge: Problem definition," *arXiv*, p. 1512.02403, 2015.

[143] A. I. Bennett, K. L. Harris, K. D. Schulze, J. M. Urueña, A. J. McGhee, A. A. Pitenis, M. H. Müser, T. E. Angelini, and W. G. Sawyer, "Contact Measurements of Randomly Rough Surfaces," *Tribol. Lett.*, vol. 65, no. 4, 2017.

[144] G. Violano, A. Papangelo, and M. Ciavarella, "Stickiness of randomly rough surfaces with high fractal dimension: is there a fractal limit?," *Tribol. Int.*, vol. 159, p. 106971, 2021.

[145] G. Violano, L. Afferrante, A. Papangelo, and M. Ciavarella, "On stickiness of multiscale randomly rough surfaces," *J. Adhes.*, vol. 97, no. 6, pp. 509–527, 2021.

[146] L. Dorogin, A. Tiwari, C. Rotella, P. Mangiagalli, and B. N. J. Persson, "Role of Preload in Adhesion of Rough Surfaces," *Phys. Rev. Lett.*, vol. 118, no. 23, p. 238001, 2017.

[147] A. Ghatak, L. Mahadevan, J. Y. Chung, M. K. Chaudhury, and V. Shenoy, "Peeling from a biomimetically patterned thin elastic film," *Proc. R. Soc. A Math. Phys. Eng. Sci.*, vol. 460, no. 2049, pp. 2725–2735, 2004.

[148] H. Gao, B. Ji, M. J. Buehler, and H. Yao, "Flaw tolerant bulk and surface nanostructures of biological systems," *Mech. Chem. Biosyst*, vol. 1, no. 1, pp. 37–52, 2004.

[149] C. Majidi, R. E. Groff, Y. Maeno, B. Schubert, S. Baek, B. Bush, R. Maboudian, N. Gravish, M. Wilkinson, K. Autumn, and R. S. Fearing, "High Friction from a Stiff Polymer Using Microfiber Arrays," *Phys. Rev. Lett.*, vol. 97, no. 7, p. 076103, 2006.

[150] H. Gao and J. R. Rice, "Nearly Circular Connections of Elastic Half Spaces," *J. Appl. Mech.*, vol. 54, no. 3, pp. 627–634, 1987.

[151] H. Gao and J. R. Rice, "A first-order perturbation analysis of crack trapping by arrays of obstacles," *J. Appl. Mech. Trans. ASME*, vol. 56, no. 4, pp. 828–836, 1989.

[152] A. Sanner and L. Pastewka, "Crack-front model for adhesion of soft elastic spheres with chemical heterogeneity," *J. Mech. Phys. Solids*, vol. 160, p. 104781, 2022.

[153] J. Y. Chung and M. K. Chaudhury, "Roles of discontinuities in bio-inspired adhesive pads," *J. R. Soc. Interface.*, vol. 2, no. 2, pp. 55–61, 2005.

[154] Y. Y. Lin, C. Y. Hui, and H. D. Conway, "Detailed elastic analysis of the flat punch (tack) test for pressure-sensitive adhesives," *J. Polym. Sci. Part B Polym. Phys.*, vol. 38, no. 21, pp. 2769–2784, 2000.

[155] R. Hensel, R. M. McMeeking, and A. Kossa, "Adhesion of a rigid punch to a confined elastic layer revisited," *J. Adhes.*, vol. 95, no. 1, pp. 44–63, 2019.

[156] A. N. Gent and J. Schultz, "Effect of Wetting Liquids on the Strength of Adhesion of Viscoelastic Material," *J. Adhes.*, vol. 3, no. 4, pp. 281–294, 1972.

[157] D. Maugis and M. Barquins, "Fracture mechanics and the adherence of viscoelastic bodies," *J. Phys. D. Appl. Phys.*, vol. 11, no. 14, pp. 1989–2023, 1978.

[158] M. Barquins and D. Maugis, "Tackiness of Elastomers," *J. Adhes.*, vol. 13, no. 1, pp. 53–65, 1981.

[159] M. Barquins, "Influence of Dwell Time on the Adherence of Elastomers," *J. Adhes.*, vol. 14, no. 1, pp. 63–82, 1982.

[160] M. L. Williams, R. F. Landel, and J. D. Ferry, "The temperature dependence of relaxation mechanisms in amorphous polymers and other glass-forming liquids," *J. Am. Chem. Soc.*, vol. 77, no. 14, pp. 3701–3707, 1955.

[161] J. D. Ferry, *Viscoelastic properties of polymers.* John Wiley & Sons, 1980.

[162] D. Maugis, "Subcritical crack growth, surface energy, fracture toughness, stick-slip and embrittlement," *J. Mater. Sci.*, vol. 20, no. 9, pp. 3041–3073, 1985.

[163] R. A. Schapery, "A theory of crack initiation and growth in viscoelastic media - I. Theoretical development," *Int. J. Fract.*, vol. 11, no. 1, pp. 141–159, 1975.

[164] J. A. Greenwood, "The theory of viscoelastic crack propagation and healing," *J. Phys. D Appl. Phys.*, vol. 37, no. 18, pp. 2557–2569, 2004.

[165] P. G. de Gennes, "Soft Adhesives," *Langmuir*, vol. 12, no. 19, pp. 4497–4500, 1996.

[166] C.-Y. Hui, B. Zhu, and R. Long, "Steady state crack growth in viscoelastic solids: A comparative study," *J. Mech. Phys. Solids*, vol. 159, p. 104748, 2022.

[167] B. N. J. Persson, "Crack propagation in finite-sized viscoelastic solids with application to adhesion," *Europhys. Lett.*, vol. 119, no. 1, p. 18002, 2017.

[168] B. Lorenz, B. A. Krick, N. Mulakaluri, M. Smolyakova, S. Dieluweit, W. G. Sawyer, and B. N. J. Persson, "Adhesion: role of bulk viscoelasticity and surface roughness," *J. Phys. Condens. Matter*, vol. 25, no. 22, p. 225004, 2013.

[169] G. Violano and L. Afferrante, "Size effects in adhesive contacts of viscoelastic media," *Eur. J. Mech. - A/Solids*, vol. 96, p. 104665, 2022.

[170] N. E. Dowling, *Mechanical behavior of materials.* Philadelphia, PA: Pearson Education, 1993.

[171] G. Violano and L. Afferrante, "On the Long and Short-Range Adhesive Interactions in Viscoelastic Contacts," *Tribol Lett*, vol. 70, no. 3, p. 68, 2022.

[172] A. Papangelo, "Adhesion between a power-law indenter and a thin layer coated on a rigid substrate," *Facta Univ. Ser. Mech. Eng.*, vol. 16, no. 1, pp. 19–28, 2018.

[173] E. Willert and V. L. Popov, "Detachment of adhesive normal contact between a rigid circular flat punch and a viscoelastic half-space," *arXiv*, p. 1805.07288, 2018.

[174] A. Papangelo and M. Ciavarella, "Detachment of a Rigid Flat Punch from a Viscoelastic Material," *Tribol Lett*, vol. 71, no. 2, p. 48, 2023.

[175] A. Flamant and Others, "Sur la répartition des pressions dans un solide rectangulaire chargé transversalement," *CR Acad. Sci. Paris*, vol. 114, no. 1892, pp. 1465–1468, 1892.

[176] G. M. Hamilton and L. E. Goodman, "The Stress Field Created by a Circular Sliding Contact," *J. Appl. Mech.*, vol. 33, no. 2, pp. 371–376, 1966.

[177] G. M. Hamilton, "Explicit equations for the stresses beneath a sliding spherical contact," *Proc. Inst. Mech. Eng. Part C J. Mech. Eng. Sci.*, vol. 197, no. 1, pp. 53–59, 1983.

[178] J. Scheibert, A. Prevost, G. Debrégeas, E. Katzav, and M. Adda-Bedia, "Stress field at a sliding frictional contact: Experiments and calculations," *J. Mech. Phys. Solids*, vol. 57, no. 12, pp. 1921–1933, 2009.

[179] A. J. Crosby, K. R. Shull, H. Lakrout, and C. Creton, "Deformation and failure modes of adhesively bonded elastic layers," *J. Appl. Phys.*, vol. 88, no. 5, pp. 2956–2966, 2000.

[180] K. R. Shull, C. M. Flanigan, and A. J. Crosby, "Fingering instabilities of confined elastic layers in tension," *Phys. Rev. Lett.*, vol. 84, no. 14, pp. 3057–3060, 2000.

[181] K. R. Shull and C. Creton, "Deformation behavior of thin, compliant layers under tensile loading conditions," *J. Polym. Sci. Part B Polym. Phys.*, vol. 42, no. 22, pp. 4023–4043, 2004.

[182] A. Ghatak and M. K. Chaudhury, "Adhesion-induced instability patterns in thin confined elastic film," *Langmuir*, vol. 19, no. 7, pp. 2621–2631, 2003.

[183] D. B. Bogy, "Two Edge-Bonded Elastic Wedges of Different Materials and Wedge Angles Under Surface Tractions," *J. Appl. Mech.*, vol. 38, no. 2, pp. 377–386, 1971.

[184] R. Caracciolo and M. Giovagnoni, "Frequency dependence of Poisson's ratio using the method of reduced variables," *Mech. Mater.*, vol. 24, no. 1, pp. 75–85, 1996.

[185] T. J. Royston, Z. Dai, R. Chaunsali, Y. Liu, Y. Peng, and R. L. Magin, "Estimating material viscoelastic properties based on surface wave measurements: A comparison of techniques and modeling assumptions," *J. Acoust. Soc. Am.*, vol. 130, no. 6, pp. 4126–4138, 2011.

[186] A. Wang and M. H. Müser, "On the adhesion between thin sheets and randomly rough surfaces," *Front. Mech. Eng.*, vol. 8, p. 965584, 2022.

[187] R. W. Stark, G. Schitter, and A. Stemmer, "Velocity dependent friction laws in contact mode atomic force microscopy," *Ultramicroscopy*, vol. 100, no. 3-4, pp. 309–317, 2004.

[188] N. Menga, F. Bottiglione, and G. Carbone, "Exploiting surface textures dynamics for dry friction control," *Nonlinear Dyn*, vol. 111, no. 4, pp. 3099–3112, 2022.

[189] N. Menga, L. Afferrante, G. P. Demelio, and G. Carbone, "Rough contact of sliding viscoelastic layers: numerical calculations and theoretical predictions," *Tribol. Int.*, vol. 122, pp. 67–75, 2018.

[190] A. D. Poularikas, *Handbook of formulas and tables for signal processing*. Berlin: Springer Berlin Heidelberg, 1998.

[191] A. Meurer, C. P. Smith, M. Paprocki, O. Čertík, S. B. Kirpichev, M. Rocklin, A. Kumar, S. Ivanov, J. K. Moore, S. Singh, T. Rathnayake, S. Vig, B. E. Granger, R. P. Muller, F. Bonazzi, H. Gupta, S. Vats, F. Johansson, F. Pedregosa, M. J.

Curry, A. R. Terrel, Š. Roučka, A. Saboo, I. Fernando, S. Kulal, R. Cimrman, and A. Scopatz, "SymPy: symbolic computing in Python," *PeerJ Comput. Sci.*, vol. 3, p. e103, 2017.

[192] M. Abramowitz, I. A. Stegun, and R. H. Romer, *Handbook of Mathematical Functions with Formulas, Graphs, and Mathematical Tables*. National Bureau of Standards, 10th ed., 1964.

[193] K. L. Johnson, *Contact Mechanics*, vol. 9. Cambridge: Cambridge University Press, 1985.

[194] C. Müller and M. H. Müser, "Analytical and numerical results for the elasticity and adhesion of elastic films with arbitrary Poisson's ratio and confinement," *J. Adhes.*, vol. 99, no. 4, pp. 648–671, 2023.

[195] G. M. Lana, X. Zhang, C. Müller, R. Hensel, and E. Arzt, "Film-Terminated Fibrillar Microstructures with Improved Adhesion on Skin-like Surfaces," *ACS Appl. Mater. Interfaces*, vol. 14, no. 41, pp. 46239–46251, 2022.

[196] G. Moreira Lana, K. Sorg, G. I. Wenzel, D. Hecker, R. Hensel, B. Schick, K. Kruttwig, and E. Arzt, "Self-Adhesive Silicone Microstructures for the Treatment of Tympanic Membrane Perforations," *Adv. NanoBiomed Res.*, vol. 1, no. 10, p. 2170101, 2021.

[197] C. Müller and M. H. Müser, "How short-range adhesion slows down crack closure and contact formation," *J. Chem. Phys.*, vol. 159, no. 23, p. 234705, 2023.

[198] C. Müller, M. Samri, R. Hensel, E. Arzt, and M. H. Müser, "Revealing the coaction of viscous and multistability hysteresis in an adhesive, nominally flat punch: A combined numerical and experimental study," *J. Mech. Phys. Solids*, vol. 174, p. 105260, 2023.

[199] C. Müller, M. H. Müser, G. Carbone, and N. Menga, "Significance of Elastic Coupling for Stresses and Leakage in Frictional Contacts," *Phys. Rev. Lett.*, vol. 131, no. 15, p. 156201, 2023.

Appendix

A   Properties of the 2D real Fourier transform

The following information can be found in almost any graduate mathematics text book containing a chapter on the Fourier transform (FT) x^*. However, these books usually focus on the one-dimensional version rather than its 2D counterpart, which is the one that is relevant to contact mechanics. Fortunately, the 2D FT simply follows from two 1D FTs with respect to two independent variables applied one after the other, requiring no additional mathematics. Therefore, most of the properties that follow can be directly derived from the 1D definitions with nothing but basic knowledge of calculus and complex algebra. Nevertheless, for the reader's convenience, the most important points necessary to follow some of the arguments of this thesis are summarized here.

Since we often perform the Fourier Transform on height profiles, we define a function $h(\mathbf{r})$ defined for in-plane coordinates $\mathbf{r} = (x, y) \in \mathbb{R}^2$. Its continuous Fourier transform (CFT) $\tilde{h}(\mathbf{q})$ is then a function of the wavevector $\mathbf{q} = (q_\mathrm{x}, q_\mathrm{y}) \in \mathbb{R}^2$ and given by[1]

$$\tilde{h}(\mathbf{q}) := \frac{1}{2\pi} \int\limits_{-\infty}^{\infty} \mathrm{d}x \int\limits_{-\infty}^{\infty} \mathrm{d}y \, h(\mathbf{r}) \exp(-i\mathbf{qr}) \qquad \text{(A.1a)}$$

$$\Leftrightarrow h(\mathbf{r}) := \frac{1}{2\pi} \int\limits_{-\infty}^{\infty} \mathrm{d}q_\mathrm{x} \int\limits_{-\infty}^{\infty} \mathrm{d}q_\mathrm{y} \, \tilde{h}(\mathbf{q}) \exp(i\mathbf{qr}). \qquad \text{(A.1b)}$$

For brevity, we can write this as $\tilde{h}(\mathbf{q}) = \mathrm{FT}(h(\mathbf{r}))$ and $h(\mathbf{r}) = \mathrm{IFT}(\tilde{h}(\mathbf{q}))$.

For the commonly studied case of axisymmetric height profiles $h(\mathbf{r}) = h(r)$ without random roughness, the 2D Fourier transform simplifies into a Hankel transform. Thanks to $\mathbf{qr} = qr \cos(\varphi)$ and h as well as $\tilde{h}$ purely depending on $r = |\mathbf{r}|$ and $q = |\mathbf{q}|$, we can show that [190]

$$\tilde{h}(q) = \int\limits_{0}^{\infty} \mathrm{d}r \, r J_0(qr) h(r) \quad \text{and} \qquad \text{(A.2a)}$$

$$h(r) = \int\limits_{0}^{\infty} \mathrm{d}q \, q J_0(qr) \tilde{h}(q), \qquad \text{(A.2b)}$$

---

[1]This is the conventional symmetric definition, meaning that both the forward and inverse FT are normalized by 2π. Other conventions are equivalent except for dimensionless prefactors.

with the Bessel function of the first kind and zeroth order

$$J_0(x) := \frac{1}{\pi} \int_0^\pi \mathrm{d}\varphi \exp(\mathrm{i}x\cos(\varphi)).$$

Since measurements and simulations require the surface profile to be discretized, it may be beneficial to also define the discrete Fourier transform (DFT) explicitly. In order to be able to use the FFT algorithm for its computation, the discretization needs to be uniform, i.e. $x_n = n\Delta x$ and $y_m = m\Delta y$, with $n, m \in \mathbb{N}$. Furthermore, the discretization in Fourier space means that instead of working with an infinitely large surface, we have to take a representative rectangular surface element with dimensions $(L_\mathrm{x}, L_\mathrm{y})$ and periodically repeat it in both lateral directions. This way, the allowed wave numbers in x- and y-direction are integer multiples of the respective discrete wave numbers $\Delta q_\mathrm{x} = 2\pi/L_\mathrm{x}$ and $\Delta q_\mathrm{y} = 2\pi/L_\mathrm{y}$ corresponding to the size of the chosen representative unit cell. Moreover, we define the numbers of discretization points N_x and N_y, which define the lower bounds in real space $\Delta x = L_\mathrm{x}/N_\mathrm{x}$ and $\Delta y = L_\mathrm{y}/N_\mathrm{y}$ and the outer bounds in Fourier space $-\pi/\Delta x \leq q_\mathrm{x} < \pi/\Delta x$ and $-\pi/\Delta y \leq q_\mathrm{y} < \pi/\Delta y$. Since h is now discrete in both real and Fourier space, we can write it as a function of two integer indices rather than continuous variables, i.e. $h(n\Delta x, m\Delta y) \equiv h(n, m)$ and $\tilde{h}(k\Delta q_\mathrm{x}, l\Delta q_\mathrm{y}) \equiv \tilde{h}(k, l)$. Consequently, the forward and backward discrete Fourier transform (DFT) are defined by[2]

$$\tilde{h}(k, l) = \sum_n \sum_m h(n, m) \exp\left(-2\pi\mathrm{i}(kn/N_\mathrm{x} + lm/N_\mathrm{y})\right) \quad \text{and} \tag{A.3a}$$

$$h(i, j) = \frac{1}{N_\mathrm{x}N_\mathrm{y}} \sum_k \sum_l \tilde{h}(k, l) \exp\left(+2\pi\mathrm{i}(kn/N_\mathrm{x} + lm/N_\mathrm{y})\right), \tag{A.3b}$$

with $n \in [0, N_\mathrm{x} - 1]$, $m \in [0, N_\mathrm{y} - 1]$, $k \in [-N_\mathrm{x}/2, N_\mathrm{x}/2 - 1]$ and $l \in [-N_\mathrm{y}/2, N_\mathrm{y}/2 - 1]$. The argument of the exponential function is the same as the $\pm\mathrm{i}\mathbf{q}\mathbf{r}$ in Eq. (A.1), except that this time, we have used $\mathbf{q} = (k\Delta q_\mathrm{x}, l\Delta q_\mathrm{y})$ and $\mathbf{r} = (n\Delta x, m\Delta y)$ and simplified the exponent accordingly. Note that the limits given above for the indices n, m, k and l assume that N_x and N_y are even, which is neither a mathematical nor a numerical necessity, but rather a common convention. Furthermore, because of 2π-periodicity, the sum in the inverse transform can just as well be defined from 0 to $N_\mathrm{x} - 1$ and $N_\mathrm{y} - 1$. The advantage of the above definition is that it automatically guarantees the correct absolute value of the wave-vector.

Eqs. (A.1) and (A.3) represent the general definitions valid for any scalar function $h \in \mathbb{C}$. Since contact mechanics exclusively deals with real surfaces $h \in \mathbb{R}$, both the continuous and the discrete version of the FT become *hermitean*, i.e.

$$\tilde{h}(-\mathbf{q}) = \tilde{h}^*(\mathbf{q}). \tag{A.4}$$

This means that (almost) half of the terms in Eq. (A.3) are redundant for real-valued functions h. Using this and the Euler identity, $\exp(\mathrm{i}x) = \cos(x) + \mathrm{i}\sin(x)$, would allow us to derive a completely equivalent real-valued representation of the DFT containing

---

[2]Contrary to the CFT, the most common convention for the DFT is asymmetric, i.e. only the inverse transform is normalized.

a sum of sine and cosine functions with real prefactors instead of complex exponentials. However, the present notation is preferred because complex algebra tends to be much easier to use than trigonometric formulae.

One of the most important and well-known features of the FT is its interaction with differentiation and integration, where especially the derivatives are relevant for the present work. The corresponding relations also follow from the definitions by assuming that the order of integration (or summation) and differentiation is interchangeable[3]:

$$\frac{\partial h(\mathbf{r})}{\partial x} = \text{IFT}\big(iq_x\tilde{h}(\mathbf{q})\big) \tag{A.5a}$$

$$\frac{\partial h(\mathbf{r})}{\partial y} = \text{IFT}\big(iq_y\tilde{h}(\mathbf{q})\big). \tag{A.5b}$$

Strictly speaking, these two equations are only exact in the case of the CFT since all methods of discrete differentiation are approximations. The resulting error is most noticeable if $\tilde{h}(k,l)$ does not vanish for large absolute values of k and l (i.e. large $|\mathbf{q}|$).

In the following, we need to take advantage of the orthogonality of the FT's base functions. Intuitively, orthogonality means that basis functions indexed by different wavevectors are (linearly) independent, which makes the Fourier representation of a function exact and unique. Mathematically, this follows from

$$\int_{-\infty}^{\infty} dx \exp(iq_x x)\exp(-iq'_x x) = 2\pi\delta(q_x - q'_x) \quad \text{and} \tag{A.6a}$$

$$\sum_{n=0}^{N_x-1} \exp(ix_n q_k)\exp(-ix_n q_{k'}) = N_x\delta_{kk'}, \tag{A.6b}$$

where $q_k = k\Delta q_x$, δ_{ij} is the Kronecker delta and $\delta(x)$ the Dirac delta distribution. Of course, the same equations hold true if x, q_x, Δq_x and N_x are replaced by y, q_y, Δq_y and N_y, respectively. These two equations are the origin of the prefactors in Eqs. (A.1) and (A.3) and can further be used to derive what is known as Parseval's theorem, which, in its continuous and discrete versions, reads

$$\int_{-\infty}^{\infty} dx \int_{-\infty}^{\infty} dy\, h^2(x,y) = \int_{-\infty}^{\infty} dq_x \int_{-\infty}^{\infty} dq_y\, \tilde{h}(\mathbf{q})\tilde{h}^*(\mathbf{q}) \quad \text{and} \tag{A.7a}$$

$$\sum_n \sum_m h^2(n,m) = \frac{1}{N_x N_y} \sum_k \sum_l \tilde{h}(k,l)\tilde{h}^*(k,l). \tag{A.7b}$$

In the context of contact mechanics, the discrete version is especially useful, because it can be used to calculate averages across the periodically repeated surface element. In combination with Eq. (A.5), we obtain three equations which are used extensively to

---

[3]This can be considered true for all physically relevant intents and purposes.

determine statistical properties:

$$\langle h \rangle_{\mathbf{r}} = \frac{1}{N_{\mathrm{x}} N_{\mathrm{y}}} \tilde{h}(\mathbf{q} = \mathbf{0}) \tag{A.8a}$$

$$\langle h^2(x, y) \rangle_{\mathbf{r}} = \frac{1}{(N_{\mathrm{x}} N_{\mathrm{y}})^2} \sum_k \sum_l \tilde{h}(k, l) \tilde{h}^*(k, l) \tag{A.8b}$$

$$\langle |\boldsymbol{\nabla} h(x, y)|^2 \rangle_{\mathbf{r}} = \frac{1}{(N_{\mathrm{x}} N_{\mathrm{y}})^2} \sum_k \sum_l |\mathbf{q}|^2 \tilde{h}(k, l) \tilde{h}^*(k, l). \tag{A.8c}$$

This is how we can calculate the mean and rms height and gradient directly in Fourier space without having to apply the inverse transform first. Moreover, Parseval's theorem is what makes the calculation of the elastic energy (see Sect. 2.3) according to

$$V_{\mathrm{el}} = \int \mathrm{d}^3 r\, C_{\alpha\beta\gamma\delta} \varepsilon_{\gamma\delta}(\mathbf{r}) \varepsilon_{\alpha\beta}(\mathbf{r}) \tag{A.9}$$

equivalent to

$$V_{\mathrm{el}} = \int \mathrm{d}^2 q\, \Phi_{\alpha\beta}(\mathbf{q}) \tilde{u}_{\alpha}(\mathbf{q}) \tilde{u}_{\beta}(\mathbf{q}), \tag{A.10}$$

the formal proof of which would also take the definition of strain (Eq. (2.12)) into account, as well as Eq. (A.5). However, it is also intuitively understandable that both real and Fourier space must contain the same information about the system. Note that the version in Fourier space is only a two-dimensional integral because the influence of the third dimension is completely contained in $\boldsymbol{\Phi}$, which we call the Green's stiffness tensor describing the elastic properties. Its inverse, $\tilde{\mathbf{G}} = \boldsymbol{\Phi}^{-1}$ is therefore referred to as a Green's compliance tensor.

The property that makes the FT applicable to the Green's function formalism is known as the convolution theorem. If $f(\mathbf{r})$ and $g(\mathbf{r})$ are functions just like $h(\mathbf{r})$ with their respective Fourier transforms $\tilde{f}(\mathbf{q})$ and $\tilde{g}(\mathbf{q})$, then

$$\mathrm{FT}\left(\int \mathrm{d}^2 r'\, f(\mathbf{r}') g(\mathbf{r} - \mathbf{r}') \right) = \tilde{f}(\mathbf{q}) \tilde{g}(\mathbf{q}). \tag{A.11}$$

B The 3D Green's function tensor

The content of this section has been automatically generated from a *Jupyter* notebook. All mathematical operations have been performed by the *SymPy* [191] computer algebra package.

B.1 Green's stiffnesses in Fourier space

Formulation for wavevector parallel to x direction

The stiffness tensor is formulated for $\mathbf{q} = (q_x, 0)$ with $q_x > 0$. To account for negative q_x, any imaginary components can be multiplied by $q_x/|\mathbf{q}|$ to ensure that all expressions remain hermitean. This is automatically achieved later on when the matrix is rotated into an arbitrary coordinate system.

$$\Phi_{11}^{(x)}(q, h) = \frac{E^* q (1 - \nu)^2 (-2hq + (3 - 4\nu) \sinh(2hq))}{-h^2 q^2 + (3 - 4\nu)^2 \sinh^2(hq)}$$

$$\Phi_{12}^{(x)}(q, h) = 0$$

$$\Phi_{13}^{(x)}(q, h) = \frac{iE^* q (1 - \nu) \left(-h^2 q^2 + (1 - 2\nu)(3 - 4\nu) \sinh^2(hq)\right)}{-h^2 q^2 + (3 - 4\nu)^2 \sinh^2(hq)}$$

$$\Phi_{22}^{(x)}(q, h) = \frac{E^* q (1 - \nu)}{2 \tanh(hq)}$$

$$\Phi_{23}^{(x)}(q, h) = 0$$

$$\Phi_{33}^{(x)}(q, h) = \frac{E^* q (1 - \nu)^2 \cdot (2hq + (3 - 4\nu) \sinh(2hq))}{-h^2 q^2 + (3 - 4\nu)^2 \sinh^2(hq)}$$

$$\mathbf{\Phi}^{(x)} = \begin{bmatrix} \Phi_{11}^{(x)}(q, h) & 0 & \Phi_{13}^{(x)}(q, h) \\ 0 & \Phi_{22}^{(x)}(q, h) & 0 \\ -\Phi_{13}^{(x)}(q, h) & 0 & \Phi_{33}^{(x)}(q, h) \end{bmatrix}$$

We find the limiting cases for $h \to \infty$:

$$\Phi_{11}^{(x)}(q, \infty) = -\frac{2E^* q (\nu - 1)^2}{4\nu - 3}$$

$$\Phi_{13}^{(x)}(q, \infty) = -\frac{iE^* q (\nu - 1)(2\nu - 1)}{4\nu - 3}$$

$$\Phi_{22}^{(x)}(q, \infty) = -\frac{E^* q (\nu - 1)}{2}$$

$$\Phi_{33}^{(x)}(q, \infty) = -\frac{2E^* q (\nu - 1)^2}{4\nu - 3}$$

and the limiting cases for $q \to 0$:

$$\Phi_{11}^{(\mathrm{x})}(0,h) = \frac{E^*\left(1-\nu\right)}{2h} + \frac{E^* h q^2 \left(-4\nu^2 + 7\nu - 3\right)}{6 \cdot (2\nu - 1)} + O\left(q^3\right)$$

$$\Phi_{13}^{(\mathrm{x})}(0,h) = \frac{i E^* q \left(-4\nu^2 + 5\nu - 1\right)}{4 \cdot (2\nu - 1)} + O\left(q^3\right)$$

$$\Phi_{22}^{(\mathrm{x})}(0,h) = \frac{E^*\left(1-\nu\right)}{2h} + \frac{E^* h q^2 \cdot (1-\nu)}{6} + O\left(q^3\right)$$

$$\Phi_{33}^{(\mathrm{x})}(0,h) = \frac{E^*\left(-\nu^2 + 2\nu - 1\right)}{h\left(2\nu - 1\right)} + \frac{E^* h q^2 \left(-4\nu^2 + 7\nu - 3\right)}{6 \cdot (2\nu - 1)} + O\left(q^3\right)$$

The elastic energy stored in the deformation at a certain wave vector is generally given by:

$$V_{\mathrm{el}}(q, h, \tilde{u}_1, \tilde{u}_2, \tilde{u}_3) = \sum_{\substack{1 \leq \beta \leq 3 \\ 1 \leq \alpha \leq 3}} \tilde{u}_\alpha \Phi_{\alpha\beta}(q, h) \tilde{u}_\beta^*$$

or in the above case:

$$V_{\mathrm{el}}^{(\mathrm{x})}(q, h, \tilde{u}_1, \tilde{u}_2, \tilde{u}_3) = \frac{\tilde{u}_1 \Phi_{11}^{(\mathrm{x})}(q, h) \tilde{u}_1^*}{2} + \frac{\tilde{u}_1 \Phi_{13}^{(\mathrm{x})}(q, h) \tilde{u}_3^*}{2} + \frac{\tilde{u}_2 \Phi_{22}^{(\mathrm{x})}(q, h) \tilde{u}_2^*}{2} - \frac{\tilde{u}_3 \Phi_{13}^{(\mathrm{x})}(q, h) \tilde{u}_1^*}{2} + \frac{\tilde{u}_3 \Phi_{33}^{(\mathrm{x})}(q, h) \tilde{u}_3^*}{2}$$

Derivation of the normal Green's function $G^{(\mathrm{n})}$

The traditional Green's function $G^{(\mathrm{n})}$ is derived for normal (z-) direction under the assumption that the stresses in the lateral directions vanish. Mathematically, this means that the first derivates of the above energy with respect to the lateral displacement components are 0:

$$\frac{\partial}{\partial \mathrm{Re}(\tilde{u}_1)} V_{\mathrm{el}}^{(\mathrm{x})}(q, h, \mathrm{Re}(\tilde{u}_1), \mathrm{Im}(\tilde{u}_1), \mathrm{Re}(\tilde{u}_2), \mathrm{Im}(\tilde{u}_2), \mathrm{Re}(\tilde{u}_3), \mathrm{Im}(\tilde{u}_3)) = 0$$

$$\frac{\partial}{\partial \mathrm{Im}(\tilde{u}_1)} V_{\mathrm{el}}^{(\mathrm{x})}(q, h, \mathrm{Re}(\tilde{u}_1), \mathrm{Im}(\tilde{u}_1), \mathrm{Re}(\tilde{u}_2), \mathrm{Im}(\tilde{u}_2), \mathrm{Re}(\tilde{u}_3), \mathrm{Im}(\tilde{u}_3)) = 0$$

$$\frac{\partial}{\partial \mathrm{Re}(\tilde{u}_2)} V_{\mathrm{el}}^{(\mathrm{x})}(q, h, \mathrm{Re}(\tilde{u}_1), \mathrm{Im}(\tilde{u}_1), \mathrm{Re}(\tilde{u}_2), \mathrm{Im}(\tilde{u}_2), \mathrm{Re}(\tilde{u}_3), \mathrm{Im}(\tilde{u}_3)) = 0$$

$$\frac{\partial}{\partial \mathrm{Im}(\tilde{u}_2)} V_{\mathrm{el}}^{(\mathrm{x})}(q, h, \mathrm{Re}(\tilde{u}_1), \mathrm{Im}(\tilde{u}_1), \mathrm{Re}(\tilde{u}_2), \mathrm{Im}(\tilde{u}_2), \mathrm{Re}(\tilde{u}_3), \mathrm{Im}(\tilde{u}_3)) = 0$$

Solving the resulting equation system gives:

$$\text{Re}(\tilde{u}_1) = \frac{i\,\text{Im}(\tilde{u}_3)\Phi_{13}^{(x)}(q,h)}{\Phi_{11}^{(x)}(q,h)}$$

$$\text{Im}(\tilde{u}_1) = -\frac{i\,\text{Re}(\tilde{u}_3)\Phi_{13}^{(x)}(q,h)}{\Phi_{11}^{(x)}(q,h)}$$

$$\text{Re}(\tilde{u}_2) = 0$$

$$\text{Im}(\tilde{u}_2) = 0$$

and, for the elastic energy,

$$V_{el}^{(n)} = \frac{(\text{Im}(\tilde{u}_3)^2 + \text{Re}(\tilde{u}_3)^2)\left(\Phi_{11}^{(x)}(q,h)\Phi_{33}^{(x)}(q,h) + \left(\Phi_{13}^{(x)}\right)^2(q,h)\right)}{2\Phi_{11}^{(x)}(q,h)}$$

Sanity check

If the above equations were implemented correctly, the resulting compliance should be exactly identical to Eq. A.9 in Ref. [56]:

$$\tilde{G}^{(n)}(q,h) = \frac{\text{Im}(\tilde{u}_3)^2 + \text{Re}(\tilde{u}_3)^2}{2V_{el}^{(n)}}$$

$$\tilde{G}^{(n)}(q,h) = -\frac{2\cdot(4\nu\sinh(2hq) + 2hq - 3\sinh(2hq))}{E^*q\left(8\nu^2 - 4\nu\cosh(2hq) - 12\nu + 2h^2q^2 + 3\cosh(2hq) + 5\right)}$$

Formulation for arbitrary wavevector

In isotropic systems, the stiffness matrix calculated above must hold true irrespective of what we define as the x direction. Therefore, the stiffness matrix for an arbitrary orientation of $\mathbf{q}$ with the same absolute value $q = |\mathbf{q}|$ simply follows from rotation:

$$\mathbf{\Phi}^{(x)} = \begin{bmatrix} \Phi_{11}^{(x)}(q,h) & 0 & \Phi_{13}^{(x)}(q,h) \\ 0 & \Phi_{22}^{(x)}(q,h) & 0 \\ -\Phi_{13}^{(x)}(q,h) & 0 & \Phi_{33}^{(x)}(q,h) \end{bmatrix}$$

$$\mathbf{q} = \begin{bmatrix} q\cos(\alpha) \\ q\sin(\alpha) \end{bmatrix}$$

$$\mathbf{R} = \begin{bmatrix} \cos(\alpha) & -\sin(\alpha) & 0 \\ \sin(\alpha) & \cos(\alpha) & 0 \\ 0 & 0 & 1 \end{bmatrix}$$

$$\tilde{\boldsymbol{\sigma}} = \boldsymbol{\Phi}\tilde{\mathbf{u}}$$

$$\mathbf{R}\tilde{\boldsymbol{\sigma}}^{(x)} = \boldsymbol{\Phi}\mathbf{R}\tilde{\mathbf{u}}^{(x)}$$

$$\tilde{\boldsymbol{\sigma}}^{(x)} = \mathbf{R}^{-1}\boldsymbol{\Phi}\mathbf{R}\tilde{\mathbf{u}}^{(x)}$$

$$\boldsymbol{\Phi} = \mathbf{R}\boldsymbol{\Phi}^{(x)}\mathbf{R}^{-1}$$

we substitute

$$\cos(\alpha) = \frac{q_x}{q}$$

$$\sin(\alpha) = \frac{q_y}{q}$$

to get

$$\boldsymbol{\Phi} = \begin{bmatrix} \frac{q_x^2 \Phi_{11}^{(x)}(q,h)}{q^2} + \frac{q_y^2 \Phi_{22}^{(x)}(q,h)}{q^2} & \frac{q_x q_y \left(\Phi_{11}^{(x)}(q,h) - \Phi_{22}^{(x)}(q,h) \right)}{q^2} & \frac{q_x \Phi_{13}^{(x)}(q,h)}{q} \\ \frac{q_x q_y \left(\Phi_{11}^{(x)}(q,h) - \Phi_{22}^{(x)}(q,h) \right)}{q^2} & \frac{q_x^2 \Phi_{22}^{(x)}(q,h)}{q^2} + \frac{q_y^2 \Phi_{11}^{(x)}(q,h)}{q^2} & \frac{q_y \Phi_{13}^{(x)}(q,h)}{q} \\ -\frac{q_x \Phi_{13}^{(x)}(q,h)}{q} & -\frac{q_y \Phi_{13}^{(x)}(q,h)}{q} & \Phi_{33}^{(x)}(q,h) \end{bmatrix}$$

B.2 Green's compliance tensor in Fourier space

Once again, only the matrix aligned with x direction is considered. Invert stiffness matrix to get the compliance (which is usually considered to be the actual Green's tensor):

$$\mathbf{G}^{(x)} = \left(\boldsymbol{\Phi}^{(x)} \right)^{-1}$$

$$\mathbf{G}^{(x)} = \begin{bmatrix} \frac{\Phi_{33}^{(x)}(q,h)}{\Phi_{11}^{(x)}(q,h)\Phi_{33}^{(x)}(q,h) + \left(\Phi_{13}^{(x)} \right)^2 (q,h)} & 0 & -\frac{\Phi_{13}^{(x)}(q,h)}{\Phi_{11}^{(x)}(q,h)\Phi_{33}^{(x)}(q,h) + \left(\Phi_{13}^{(x)} \right)^2 (q,h)} \\ 0 & \frac{1}{\Phi_{22}^{(x)}(q,h)} & 0 \\ \frac{\Phi_{13}^{(x)}(q,h)}{\Phi_{11}^{(x)}(q,h)\Phi_{33}^{(x)}(q,h) + \left(\Phi_{13}^{(x)} \right)^2 (q,h)} & 0 & \frac{\Phi_{11}^{(x)}(q,h)}{\Phi_{11}^{(x)}(q,h)\Phi_{33}^{(x)}(q,h) + \left(\Phi_{13}^{(x)} \right)^2 (q,h)} \end{bmatrix}$$

$$\tilde{G}_{11}^{(x)}(q,h) = \frac{2 \left(-4\nu \sinh(2hq) + 2hq + 3\sinh(2hq) \right)}{E^* q \left(8\nu^2 - 4\nu \cosh(2hq) - 12\nu + 2h^2 q^2 + 3\cosh(2hq) + 5 \right)}$$

$$\tilde{G}_{13}^{(\mathsf{x})}(q,h) = \frac{i\left(8\nu^2 \sinh^2(hq) - 10\nu\sinh^2(hq) - h^2q^2 + 3\sinh^2(hq)\right)}{E^*q\,(\nu-1)\left(4\nu^2 - 4\nu\sinh^2(hq) - 8\nu + h^2q^2 + 3\sinh^2(hq) + 4\right)}$$

$$\tilde{G}_{22}^{(\mathsf{x})}(q,h) = -\frac{2\tanh(hq)}{E^*q\,(\nu-1)}$$

$$\tilde{G}_{33}^{(\mathsf{x})}(q,h) = -\frac{8\nu\sinh(2hq) + 4hq - 6\sinh(2hq)}{E^*q\,(8\nu^2 - 4\nu\cosh(2hq) - 12\nu + 2h^2q^2 + 3\cosh(2hq) + 5)}$$

Calculate limiting cases for $h \to \infty$:

$$\tilde{G}_{11}^{(\mathsf{x})}(q,\infty) = \frac{2}{E^*q}$$

$$\tilde{G}_{13}^{(\mathsf{x})}(q,\infty) = -\frac{i\,(2\nu-1)}{E^*q\,(\nu-1)}$$

$$\tilde{G}_{22}^{(\mathsf{x})}(q,\infty) = -\frac{2}{E^*q\,(\nu-1)}$$

$$\tilde{G}_{33}^{(\mathsf{x})}(q,\infty) = \frac{2}{E^*q}$$

Calculate limiting cases for $q \to 0$:

$$\tilde{G}_{11}^{(\mathsf{x})}(0,h) = -\frac{2h}{E^*(\nu-1)} + \frac{h^3q^2(-4\nu-3)}{3E^*(\nu^2-2\nu+1)} + O\left(q^3\right)$$

$$\tilde{G}_{13}^{(\mathsf{x})}(0,h) = \frac{ih^2q(4\nu-1)}{2E^*(\nu^2-2\nu+1)} + O\left(q^3\right)$$

$$\tilde{G}_{22}^{(\mathsf{x})}(0,h) = -\frac{2h}{E^*(\nu-1)} + \frac{2h^3q^2}{3E^*(\nu-1)} + O\left(q^3\right)$$

$$\tilde{G}_{33}^{(\mathsf{x})}(0,h) = \frac{h(1-2\nu)}{E^*(\nu^2-2\nu+1)} + \frac{\nu h^3q^2\cdot(1-4\nu)}{3E^*(\nu^3-3\nu^2+3\nu-1)} + O\left(q^3\right)$$

The formulation of **G** for arbitrary **q** is completely analogous to **Φ** since the principles of isotropy and rotation invariance still apply.

C   Real-space GFMD (rGFMD)

While working on Publ. **III**, the idea came up to simulate the axisymmetric contacts with a more efficient method that takes advantage of dimensional reduction. The idea was to apply the Green's function in real space rather than Fourier space and use a non-uniform discretization that is automatically adjusted on the fly as the contact changes. This section will explain the underlying theory of the approach and compare the performance of its numerical implementation against conventional Fourier-based GFMD (called fGFMD in the context of this Section). The latter option clearly comes out on top in the following analysis, which is why the development of the real-space method was not pursued much further. Nevertheless, it is possible that minor modifications could significantly boost its efficiency in the future.

C.1   The real-space convolution kernel

This section derives the convolution kernel used in rGFMD for axisymmetric contacts including one rigid and one initially flat, semi-infinite, isotropic, linearly elastic body. The function in question represents the cause-effect relationship between the normal displacement field $u(\mathbf{r})$ and the normal stress field $\sigma(\mathbf{r})$ for all in-plane coordinates $\mathbf{r}$. As discussed in Sect. 2.3.2, the solution in terms of their Fourier transforms $\tilde{u}$ and $\tilde{\sigma}$ is given by

$$\tilde{\sigma}(\mathbf{q}) = \frac{qE^*}{2}\tilde{u}(\mathbf{q}), \tag{C.1}$$

which we can interpret as the Fourier transform of the following convolution equation with kernel K:

$$\sigma(\mathbf{r}) = \int \mathrm{d}^2 r'\, u(\mathbf{r}')K(\mathbf{r} - \mathbf{r}') \tag{C.2a}$$

$$= \mathrm{IFT}(\tilde{\sigma}(\mathbf{q})) = \mathrm{IFT}\Big(\frac{qE^*}{2}\tilde{u}(\mathbf{q})\Big) \tag{C.2b}$$

$$= \frac{1}{2\pi}\int \mathrm{d}^2 q \exp(\mathrm{i}\mathbf{q}\mathbf{r})\frac{qE^*}{2}\frac{1}{2\pi}\int \mathrm{d}^2 r' \exp(-\mathrm{i}\mathbf{q}\mathbf{r}')u(\mathbf{r}') \tag{C.2c}$$

$$\Rightarrow \quad K(\mathbf{r} - \mathbf{r}') = \frac{E^*}{8\pi^2}\int \mathrm{d}^2 q\, q \exp(\mathrm{i}\mathbf{q}(\mathbf{r} - \mathbf{r}')). \tag{C.2d}$$

Note that this defines the convolution with K as the inverse operation to the convolution with the Green's function G in Sect. 2.3.2. We now want to derive the algebraic expression for K in rotationally symmetric systems, which we denote as K'. The coefficient K' relates the stress at distance r from the origin and the normal displacement concentrated within an infinitesimally thin ring with radius r'. Defining $\Delta r := |\mathbf{r} - \mathbf{r}'|$

and $\mathbf{q}(\mathbf{r} - \mathbf{r}') = q\Delta r \cos(\alpha)$, α being the angle between $\mathbf{q}$ and $\mathbf{\Delta r}$, we get

$$K'(\mathbf{r}, \mathbf{r}') = \frac{E^*}{8\pi^2} \int_0^\infty \mathrm{d}q\, q^2 \int_0^{2\pi} \mathrm{d}\alpha \exp(iq\Delta r \cos(\alpha)) \tag{C.3a}$$

$$= \frac{E^*}{4\pi\Delta r^3} \int_0^\infty \mathrm{d}x\, x^2 J_0(x) \tag{C.3b}$$

$$= -\frac{E^*}{4\pi\Delta r^3}, \tag{C.3c}$$

where we have introduced $x \equiv q\Delta r$ and $J_0(x)$, which is the Bessel function of the first kind and zeroth order, as defined in Eq. (A.2). The integral in Eq. (C.3b) might formally diverge by oscillation, although rigorously testing this hypothesis is beyond the scope of this thesis. *WolframAlpha* can determine its indefinite version in terms of the generalized hypergeometric function, which, however, it cannot compute in the limit of $x \to \infty$. Instead, we opt to take the pragmatic approach and introduce convergence by multiplying the integrand with an exponential factor that rapidly approaches 0 for very large values of x and realize that, regardless of the the factor in the exponent, the integral evaluates to -1. We can now insert this expression into Eq. (C.2) and reformulate it using the law of cosines ($\Delta r^2 = r^2 + r'^2 - 2rr' \cos(\varphi)$, where φ is the angle between $\mathbf{r}$ and $\mathbf{r}'$):

$$\sigma(\mathbf{r}) = \int \mathrm{d}^2 r'\, u(\mathbf{r}') K'(\mathbf{r}, \mathbf{r}') \tag{C.4a}$$

$$= \int_0^\infty \mathrm{d}r'\, u(r') \frac{-E^*}{4\pi} r' \int_0^{2\pi} \mathrm{d}\varphi \left(r^2 + r'^2 - 2rr' \cos(\varphi)\right)^{-3/2} \tag{C.4b}$$

$$= \int_0^\infty \mathrm{d}r'\, u(r') \frac{-E^*}{4\pi} r'^{-2} (\rho^2 + 1)^{-3/2} \underbrace{\int_0^{2\pi} \mathrm{d}\varphi \left(1 - \underbrace{\frac{2\rho}{\rho^2 + 1}}_{=:k} \cos(\varphi)\right)^{-3/2}}_{=:I(\rho)}, \tag{C.4c}$$

where $\rho = r/r'$. The integral $I(\varphi)$ converges only for $k < 1$, i.e. for all $\rho \neq 1$, to:

$$I(\rho) = \frac{4(\rho^2 + 1)^{3/2}}{(\rho + 1)^2 |\rho - 1|} E\left(\frac{-4\rho}{(\rho - 1)^2}\right), \tag{C.5}$$

where E is the complete elliptic integral of the second kind, not to be confused with the Young's modulus of the material. The combination of Eqs. (C.4) and (C.5) provides us with the final expressions for K' and the "axisymmetric convolution",

$$K'(r, r') = \frac{-E^*}{\pi r'^2} \frac{E\left(\frac{-4\rho}{(\rho - 1)^2}\right)}{(\rho + 1)^2 |\rho - 1|} \quad \text{and} \tag{C.6a}$$

$$\sigma(r) = \int_0^\infty \mathrm{d}r'\, u(r') K'(r, r'). \tag{C.6b}$$

As should be expected, K' diverges in the continuum limit at $r = r'$ (i.e. $\rho = 1$). This problem can be avoided by discretizing the problem, dividing the radial axis into N "bins", where the i'th bin represents a ring of width Δr_i at a distance r_i from the origin. This way, Eq. (C.6) becomes

$$\sigma(r_i) \approx \sum_{j=1}^{N} \Delta r_j u(r_j) \frac{-E^*}{\pi r_j^2} \frac{E\left(\frac{-4\rho_{ij}}{(\rho_{ij}-1)^2}\right)}{(\rho_{ij}+1)^2 |\rho_{ij}-1|} \tag{C.7a}$$

$$=: \sum_{j=1}^{N} u(r_j) K'_{ij}, \tag{C.7b}$$

with $\rho_{ij} = r_i/r_j$. Since N is finite in the numerical implementation, this sum ends at a finite maximum radial coordinate r_N. In principle, this inaccuracy can be made arbitrarily small thanks to non-uniform discretization. At large r, far away from the axisymmetric indenter at the origin, Δr can be chosen much larger than inside the contact. Furthermore, to some extent, it should be possible to continue the sum analytically by adding the continuous integral from Eq. (C.6) with boundaries $r_N + \Delta r_N/2$ and ∞. In this regime of large r_j, it can be assumed that $u(r_j)$ converges as $1/r_j$ and for $\rho \ll 1$, the Kernel can be replaced by its Taylor series expansion (see Eq. (C.10)). Issues can potentially arrive at intermediate values of ρ, where the integrand cannot be replaced by an analytic expression that can easily be integrated analytically. Note that while the simulation has not yet reached the static solution, the stress does not vanish outside the contact area and therefore needs to be calculated everywhere with maximum possible precision.
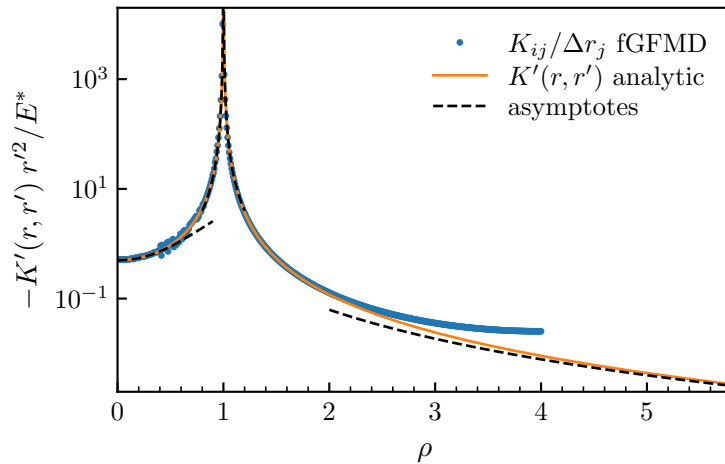
Figure C.1: The analytical kernel $K'(r/r')$ and its asymptotes compared to numerical results obtained from conventional Fourier-based GFMD (fGFMD).

The previously neglected case of $r = r'$ or $i = j$ can be treated in the discrete case by recalling that we have assumed the elastic body to be semi-infinite. Therefore, a uniform COM displacement $u(r_j) = u_0 \, \forall \, j$ must not give rise to any stress, i.e. $\sigma_i = 0 \, \forall \, i$. This

is equivalent to the sum rule

$$\sum_{j=1}^{N} K'_{ij} u_0 = 0 \tag{C.8a}$$

$$K'_{ii} = -\sum_{j \neq i} K'_{ij}. \tag{C.8b}$$

It is possible to rationalize another sum rule: At any given state of displacement and stress field, for the surface to not experience a net acceleration, the total force F_{tot} resulting from the elastic response must be 0. With the area element $A_i = 2\pi r_i \Delta r_i$, this condition becomes

$$F_{\text{tot}} = \sum_{i} A_i K'_{ij} = 0. \tag{C.9}$$

This equation turns out to be equivalent to Eq. (C.8) because K'_{ij} has the useful property that $A_j K'_{ji} = A_i K'_{ij}$, which can be seen by simply substituting in the definition.

The above derivation was tested by comparing the analytically predicted K'_{ij} with the result of a conventional Fourier-GFMD (fGFMD) simulation, which simply reads in a ring-shaped initial displacement field and calculates the corresponding elastic stress in a single time step. For the result to be representative, the simulation cell must be significantly larger that the radius r' of the displacement ring. At sufficient distance from the periodic boundaries, the corresponding simulation result is in very good agreement with the theory, as shown in Fig. C.1. The plotted asymptotic relations are given by

$$K'(r/r') \approx -\frac{E^*}{r'^2} \begin{cases} \left(\frac{1}{2} + \frac{9}{8}\rho^2 + \frac{225}{128}\rho^4 \right) & \text{for } \rho \ll 1 \\ \frac{1}{2\pi}(\rho - 1)^{-2} & \text{for } |\rho - 1| \ll 1 \\ \frac{1}{2}\rho^{-3} & \text{for } \rho \gg 1 \end{cases} \tag{C.10}$$

Finally, it may be useful to point out a technical detail concerning the determination of the transcendental function E. Although there are many scientific libraries providing a numerical implementation for this function, most of them do not take negative arguments into account. Care needs to be taken to determine whether a given package defines E for the argument k or $m = k^2$ (following the nomenclature of *WolframAlpha*). Implementations using k usually do not take complex arguments, i.e. negative values of m, which is the only case relevant to Eqs. (C.6) and (C.7a). For example, the scientific Python module `scipy.special` uses the exact convention used above, even defined for negative arguments m, while the `gsl` and `boost` libraries for C/C++ both provide only the version for positive real values of k. The latter definition can be extended to complex k using the relationships between E and other elliptic functions, as described in the Handbook of mathematical functions [192, p. 593].

C.2   Numerical performance

The accuracy of the real-space solution is compared to the Fourier-based method in terms of the quasi-static Hertzian contact with radius $R = 1$ and force $F = 0.1 E^* R^2$,

where the analytical solution is known [193, p. 59ff]. Note that in this case, the final result of both approaches is independent of the algorithm used for the numerical solution. Fig. C.2 shows how the real-space solution converges toward the target displacement and
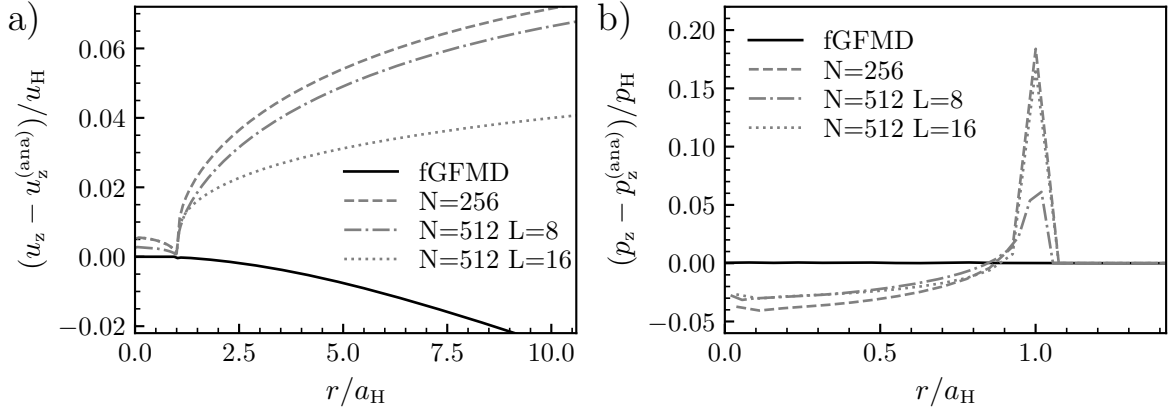
Figure C.2: Convergence of the a) displacement and b) pressure field with N for the real-space solution (calculated using GFMD) compared to the analytical solution. From the dashed to the dash-dotted line, the system size L stays constant and the resolution is doubled, mostly improving the accuracy of the stress field. On the contrary, the dotted line doubles L at constant resolution, which considerably improves the displacement field. p_H, u_H and a_H are the analytical solutions for the maximum contact pressure, macroscopic displacement and contact radius, respectively. The black solid line corresponds to the solution calculated in Fourier space at 256×256 resolution with period $L = 6R \gg a_H$.

stress profiles, where increasing the circular system size mostly improves the accuracy in displacement and the refining the discretization affects the pressure field. However, the resolution as well as the system size would need to be drastically increased to approach the exceptional accuracy that is obtained when the problem is solved in Fourier space. This is especially true for the stress field, but surprisingly also applies to the displacement as long as the periodic boundaries of the Fourier method are sufficiently far away.

We also want to compare the computational efficiency of the corresponding GFMD implementations. At the given resolution of $N = 256$, the rGFMD method was approximately four times faster than fGFMD, although it should be noted that fGFMD was sped up by the FIRE algorithm, which had not been implemented in rGFMD. Reducing the period length (at constant N) would make fGFMD almost equally efficient, while sacrificing accuracy only in terms of the displacement field. Computational complexity scales approximately with N^2 for both the Fourier and real-space method. This is because a 1D convolution in real-space is an N^2 operation and fGFMD needs to simulate two dimensions, both with asymptotic complexity of the FFT proportional to $N \log(N)$. In summary, with uniform spacing, rGFMD cannot compete with fGFMD. The slight advantage in computation time does not make up for the significant loss in accuracy, especially with respect to the stress field.

To assess the improvement expected from non-uniform spacing, Fig. C.3 shows four different variants in terms of their deviation from the analytical solution. Making r_i a quadratic function of the grid index i at constant N improves the local resolution inside the contact area and wastes less computation time for points outside the contact. This
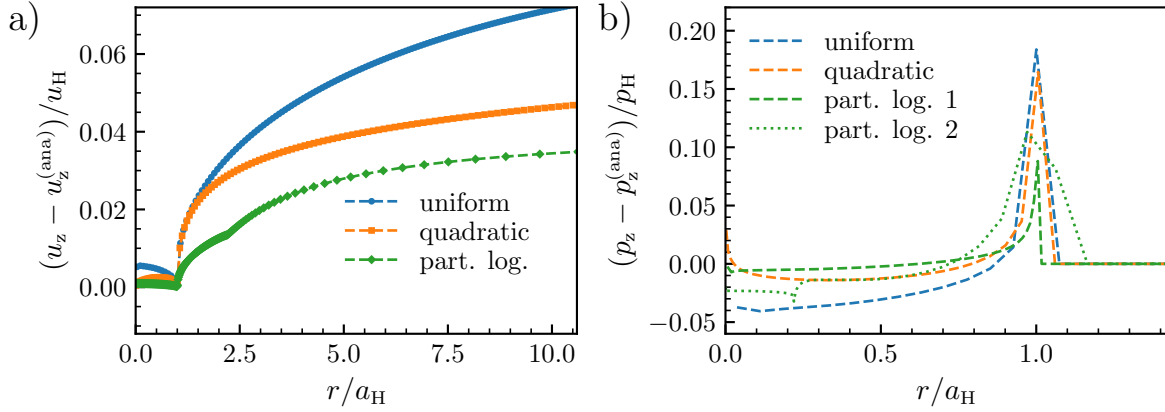
Figure C.3: Comparison of uniform and non-uniform real-space discretizations for a) displacement and b) pressure field. All cases use 256 discretization points, where the dashed blue line represents uniform spacing, the orange line increases spacing quadratically and the green lines start with a very fine uniform discretization and then switch to a logaritmic spacing outside (green dashed) or inside (green dotted) the contact. Non-uniform grids tend to improve accuracy, but introduce artifacts at the points where the discretization changes.

leads to an overall improvement in stress and displacement fields, except for the center ($r = 0$), where it introduces an artifact in the form of a stress peak. The partially logarithmic grid takes this idea one step further and introduces a transition index j_c, at which the shape of Δr_j as a function of j suddenly changes. This introduces artifacts at the exact location $r_c = r_{j_c}$ of the discretization transition. If r_c lies inside the contact region, a kink is introduced in the stress field (dotted green line). Otherwise, a discontinuity shows up in the displacement field (dashed green line). Given these observations, it is not really clear how well a self-adjusting non-uniform grid would perform in practice. Once again, these results pertain to the described real-space method, irrespective of the algorithm used for computation.

Although the issues arising from non-uniform discretization already make the real-space method impractical, the concept of changing the discretization on the fly was still tested. To this end, Fig. C.4 shows the displacement evolution over time step, where two constant uniform discretizations are compared to a simulation that switches between the same two grids halfway through the calculation. The grid update requires an extrapolation of the previous field to the new coordinates, which was realized by the accelerated cubic spline interpolation of the *gsl* library. With this method, the re-equilibration after the grid update takes less than 10% of the total simulation time, as indicated by the duration of green line's jump in Fig. C.4. When replacing the cubic spline with a simple piecewise-linear interpolation, this process took significantly more time (not shown explicitly). The perturbation resulting from grid update would certainly lead to a significant error in the case of viscoelastic systems, where a realistic time evolution is much more important than in the quasi-static case. As of the writing of this thesis, the first attempt at a viscoelastic implementation has not proven to yield quantitatively correct dynamics even for a constant uniform grid, which is why it is not explicitly discussed here.
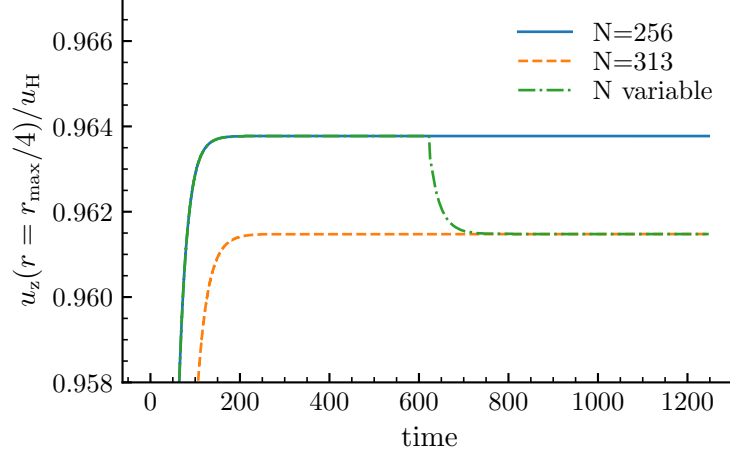
Figure C.4: Displacement trajectories for two rGFMD simulations with constant uniform $N = 256$ and $N = 313$ grids and one simulation that switches from $N = 256$ to $N = 313$ discretizations at time $t = 600$. It takes only a few time steps to re-equilibrate after the interpolation.

D   Perturbation approach to elastic coupling

In Publ. **V**, the discussion of the coupling effect in single asperity systems was rather qualitative in nature, focusing on intuitive access in favor of mathematical precision. This section treats the single wavelength undulation and its implications on friction more rigorously in what can be considered a perturbation theory approach.

We consider the friction-less case ($\mu_c = 0$) as the known reference and interpret μ_c as a small perturbation. We assume that the indenter predominantly causes a deformation of a single representative wavevector $\mathbf{Q} = (Q, 0)$. Since this choice aligns the coordinate system with the sliding direction, we assume the representation in App. B, except the superscript "(x)" on the tensor components is omitted for brevity. Furthermore, $\tilde{G}_{\alpha\beta}$ and $\Phi_{\alpha\beta}$ imply $\tilde{G}_{\alpha\beta}(Q)$ and $\Phi_{\alpha\beta}(Q)$, respectively, where $\tilde{\mathbf{G}}(Q) = \mathbf{\Phi}^{-1}(Q)$ is the Green's compliance tensor corresponding to $\mathbf{Q}$.

In 0th and 1st order (indicated by the superscript in round brackets), we get

$$\tilde{\boldsymbol{\sigma}}^{(0)}(\mathbf{Q}) = \begin{pmatrix} 0 \\ \tilde{\sigma}_z^{(0)}(\mathbf{Q}) \end{pmatrix} \tag{D.1a}$$

$$\tilde{\mathbf{u}}^{(0)}(\mathbf{Q}) = \mathbf{G}(Q)\tilde{\boldsymbol{\sigma}}^{(0)}(\mathbf{Q}) \tag{D.1b}$$

$$\Delta\tilde{\boldsymbol{\sigma}}^{(1)}(\mathbf{Q}) = \begin{pmatrix} -\mu_c\tilde{\sigma}_z^{(0)}(\mathbf{Q}) \\ 0 \end{pmatrix} \tag{D.1c}$$

$$\Delta\tilde{\mathbf{u}}^{(1)}(\mathbf{Q}) = \mathbf{G}(Q)\Delta\tilde{\boldsymbol{\sigma}}^{(1)}(\mathbf{Q}) \tag{D.1d}$$

Carrying out the matrix multiplication with the coefficients given by App. B, we obtain:

$$\tilde{\mathbf{u}}^{(1)}(\mathbf{Q}) \approx \tilde{\mathbf{u}}^{(0)}(\mathbf{Q}) + \Delta\tilde{\mathbf{u}}^{(1)}(\mathbf{Q})$$
$$= \begin{pmatrix} \tilde{G}_{13} - \mu_c\tilde{G}_{11} \\ \tilde{G}_{33} - \mu_c\tilde{G}_{31} \end{pmatrix} \tilde{\sigma}_z^{(0)}(\mathbf{Q}). \tag{D.2}$$

Note that $\tilde{\sigma}_z^{(0)} = -p_3$ is negative by engineering convention for a compressive normal load ($\sigma_z = -p_3 \cos(Qx)$) and the indenter, which is moving in positive x-direction, causes a positive frictional shear stress $\Delta\sigma_x^{(1)}$. This is why the x-component in Eq. (D.1c) needs a minus sign. Consequently, in steady-state sliding, the local velocity variation is given as

$$\frac{du_x}{dt} \approx -v_0 \frac{\partial u_x^{(1)}}{\partial x} = v_0 p_3 Q \big(\mu_c \tilde{G}_{11} \sin(Qx) - \text{Im}\big\{ \tilde{G}_{13} \big\} \cos(Qx) \big). \tag{D.3}$$

The (0-th order) cosine term amounts to a negative velocity inside the contact for the confined, incompressible body, where $\text{Im}\big\{ \tilde{G}_{13} \big\} > 0$. Since the indenter is moving in positive x-direction, this negative velocity of the elastic surface increases the relative velocity v_{rel} between the two bodies and enhances the dissipated energy P_{diss} and thereby the effective friction coefficient. $\text{Im}\big\{ \tilde{G}_{13} \big\}$ becomes negative for semi-infinite, compressible materials, which means that v_{rel} and P_{diss} are reduced instead. Furthermore, the (first-order) sine term in Eq. (D.3) reduces the local velocity on the leading half of the contact and increases it on the trailing side. All of these tendencies can be observed throughout Publ. **V**.

In the next step, we need to take the constraint into account that the indenter imposes on the displacement. In our model and simulation, a local overlap between the bodies gives rise to a stress in normal direction, which is trying to reduce the overlap to 0. The lateral stress changes simultaneously to ensure that Amontons's law remains locally fulfilled in the entire surface. In our single-wavelength displacement system, we can write this as:

$$\Delta\tilde{\boldsymbol{\sigma}}^{(2)}(\mathbf{Q}) = \boldsymbol{\Phi}(Q) \begin{pmatrix} \mu_c \\ -1 \end{pmatrix} \Delta\tilde{u}_z^{(1)} \tag{D.4}$$

$$= \boldsymbol{\Phi}(Q) \begin{pmatrix} -\mu_c^2 \tilde{G}_{31} \\ \mu_c \tilde{G}_{31} \end{pmatrix} \tilde{\sigma}_z^{(0)}(\mathbf{Q}) \tag{D.5}$$

$$= \begin{pmatrix} -\mu_c^2 \Phi_{11} \tilde{G}_{31} + \mu_c \Phi_{13} \tilde{G}_{31} \\ -\mu_c^2 \Phi_{31} \tilde{G}_{31} + \mu_c \Phi_{33} \tilde{G}_{31} \end{pmatrix} \tilde{\sigma}_z^{(0)}(\mathbf{Q}) \tag{D.6}$$

In first-order approximation (i.e. $\mu_c \ll 1$), the normal stress is primarily modified by

$$\Delta\sigma_z^{(2)}(x) \approx \text{Re}\left(\mu_c \Phi_{33} \tilde{G}_{31} \tilde{\sigma}_z^{(0)}(\mathbf{Q}) \exp(iQx) \right)$$
$$= \mu_c p_3 \Phi_{33} \text{Im}(\tilde{G}_{31}) \sin(Qx). \tag{D.7}$$

Due to the symmetry (or "hermitean-ness", to be precise) of the tensors, $\text{Im}(\tilde{G}_{31})$ has the same sign as $\text{Im}(\tilde{\Phi}_{13})$, as shown in Figure SI-1 of Publ. **V**: $\text{Im}(\tilde{G}_{31})$ is negative for confined elastic bodies and positive for semi-infinite ones. Therefore, for the confined case, the pressure (negative stress) is larger on the right-hand side (leading edge) of the contact, while for the semi-infinite case, it is larger on the left-hand side (trailing edge). Once again, this matches the results in Figure SI-2, this time the second row.

E   The standard linear solid (SLS)

The content of this section has been automatically generated from a *Jupyter* notebook. All mathematical operations have been performed by the *SymPy* [191] computer algebra package.
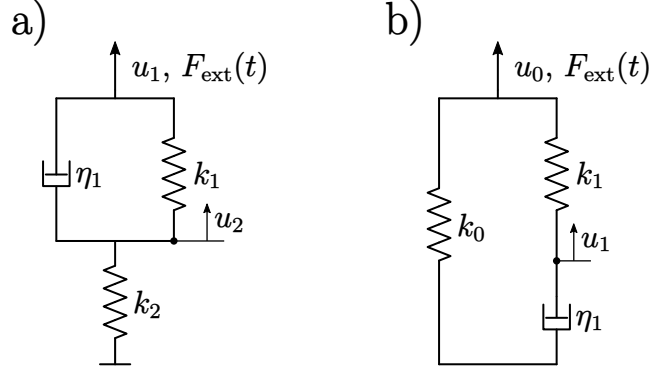
Figure E.1:   Schematic of the Standard Linear Solid (SLS) in a) Kelvin-Voigt and b) Maxwell representation.

E.1   Kelvin-Voigt representation

System of differential equations:

$$\eta \left(\frac{d}{dt} u_1(t) - \frac{d}{dt} u_2(t) \right) + k_1 \left(u_1(t) - u_2(t) \right) = F_{\text{ext}} \left(\hat{F}, \omega, t \right)$$

$$\eta \left(-\frac{d}{dt} u_1(t) + \frac{d}{dt} u_2(t) \right) + k_1 \left(-u_1(t) + u_2(t) \right) + k_2 u_2(t) = 0$$

Ansatz:

$$F_{\text{ext}} \left(\hat{F}, \omega, t \right) = \hat{F} e^{i\omega t}$$

$$\begin{bmatrix} u_1(t) \\ u_2(t) \end{bmatrix} = \begin{bmatrix} \hat{u}_1 e^{i\omega t} \\ \hat{u}_2 e^{i\omega t} \end{bmatrix}$$

Substitute ansatz into ODE system:

$$\hat{F} e^{i\omega t} = \left(\hat{u}_1 - \hat{u}_2 \right) \left(i\eta\omega + k_1 \right) e^{i\omega t}$$

$$\left(-i\eta\omega \left(\hat{u}_1 - \hat{u}_2 \right) + \hat{u}_2 k_2 - k_1 \left(\hat{u}_1 - \hat{u}_2 \right) \right) e^{i\omega t} = 0$$

Divide by the Ansatz and rewrite into a matrix equation:

$$\begin{bmatrix} \hat{u}_1 \left(-i\eta\omega - k_1 \right) + \hat{u}_2 \left(i\eta\omega + k_1 \right) \\ \hat{u}_1 \left(-i\eta\omega - k_1 \right) + \hat{u}_2 \left(i\eta\omega + k_1 + k_2 \right) \end{bmatrix} = \begin{bmatrix} -\hat{F} \\ 0 \end{bmatrix}$$

Invert the equation, find $\hat{u}$:

$$\hat{u}_1 = -\frac{\hat{F}\left(-\eta\omega + ik_1 + ik_2\right)}{\eta\omega k_2 - ik_1 k_2}$$

Determine the complex stiffness:

$$\hat{F} = \hat{u}_1 k_{\mathrm{KV}}(\omega)$$

$$k_{\mathrm{KV}}(\omega) = \frac{k_2\left(\eta\omega - ik_1\right)}{\eta\omega - ik_1 - ik_2}$$

$$k_{\mathrm{KV}}(\omega) = \frac{i\eta\omega k_2^2}{\eta^2\omega^2 + (k_1 + k_2)^2} + \frac{k_2\left(\eta^2\omega^2 + k_1\left(k_1 + k_2\right)\right)}{\eta^2\omega^2 + (k_1 + k_2)^2}$$

$$|k_{\mathrm{KV}}(\omega)| = \frac{k_2\sqrt{\eta^2\omega^2 + k_1^2}}{\sqrt{\eta^2\omega^2 + k_1^2 + 2k_1 k_2 + k_2^2}}$$

Reformulate using $\tau = \eta/k_1$:

$$k_{\mathrm{KV}}(\omega) = \frac{k_1 k_2\left(\omega\tau - i\right)}{\omega\tau k_1 - ik_1 - ik_2}$$

$$k_{\mathrm{KV}}(\omega) = \frac{i\omega\tau k_1 k_2^2}{\omega^2\tau^2 k_1^2 + (k_1 + k_2)^2} + \frac{k_1 k_2\left(\omega^2\tau^2 k_1 + k_1 + k_2\right)}{\omega^2\tau^2 k_1^2 + (k_1 + k_2)^2}$$

$$|k_{\mathrm{KV}}(\omega)| = \frac{k_1 k_2\sqrt{\omega^2\tau^2 + 1}}{\sqrt{\omega^2\tau^2 k_1^2 + k_1^2 + 2k_1 k_2 + k_2^2}}$$

Reformulate using $a = k_2/k_1$:

$$k_{\mathrm{KV}}(\omega) = -\frac{ak_1\left(\omega\tau - i\right)}{-\omega\tau + ia + i}$$

$$k_{\mathrm{KV}}(\omega) = \frac{i\omega\tau a^2 k_1}{\omega^2\tau^2 + (a + 1)^2} + \frac{ak_1\left(\omega^2\tau^2 + a + 1\right)}{\omega^2\tau^2 + (a + 1)^2}$$

$$|k_{\mathrm{KV}}(\omega)| = \frac{ak_1\sqrt{\omega^2\tau^2 + 1}}{\sqrt{\omega^2\tau^2 + a^2 + 2a + 1}}$$

Limiting cases (in different representations):

$$k_{\mathrm{KV}}(\infty) = k_2$$

$$k_{\mathrm{KV}}(0) = \frac{k_2}{a+1}$$

$$k_{\mathrm{KV}}(0) = \frac{k_1 k_2}{k_1 + k_2}$$

Reformulate using $k_0 = k(0)$ and $s = k(\infty)/k(0)$:

$$s = a + 1$$

$$k_{\mathrm{KV}}(\omega) = \frac{k_0 s\,(i\omega\tau + 1)}{i\omega\tau + s}$$

$$k_{\mathrm{KV}}(\omega) = \frac{i\omega\tau k_0 s\,(s-1)}{\omega^2\tau^2 + s^2} + \frac{k_0 s\,(\omega^2\tau^2 + s)}{\omega^2\tau^2 + s^2}$$

$$|k_{\mathrm{KV}}(\omega)| = \frac{k_0 s\sqrt{\omega^2\tau^2 + 1}}{\sqrt{\omega^2\tau^2 + s^2}}$$

$$\tan(\varphi) = \frac{\omega\tau\,(s-1)}{\omega^2\tau^2 + s}$$
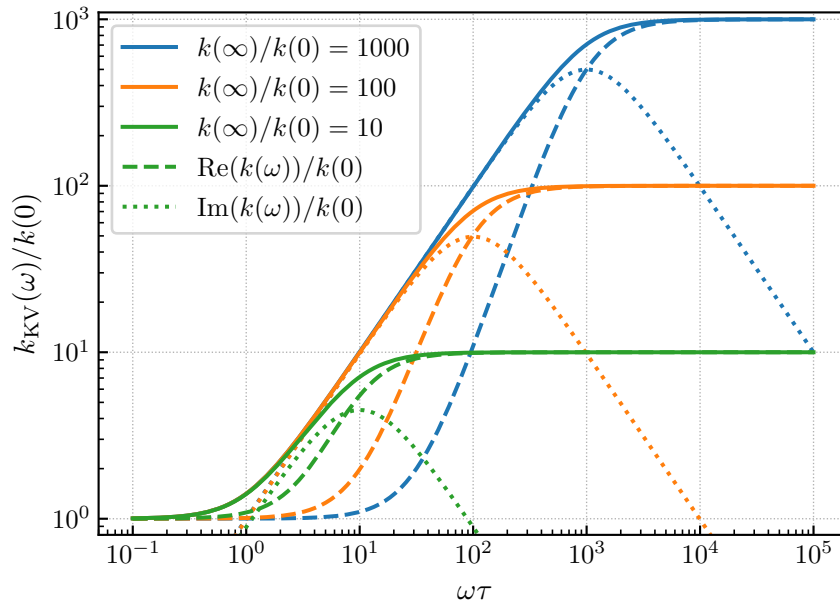
Figure E.2: Absolute value (solid), real part (dashed) and imaginary part (dotted line) of the stiffness of the SLS in KV representation with relaxation time τ and different ratios k_∞/k_0.

E.2   Maxwell representation

System of differential equations:

$$k_0 u_0(t) + k_1 \left(u_0(t) - u_1(t) \right) = F_{\text{ext}} \left(\hat{F}, \omega, t \right)$$

$$\eta \frac{d}{dt} u_1(t) + k_1 \left(-u_0(t) + u_1(t) \right) = 0$$

Ansatz:

$$\begin{bmatrix} u_0(t) \\ u_1(t) \end{bmatrix} = \begin{bmatrix} \hat{u}_0 e^{i\omega t} \\ \hat{u}_1 e^{i\omega t} \end{bmatrix}$$

Substitute ansatz into ODE system:

$$\hat{F} e^{i\omega t} = \left(\hat{u}_0 k_0 + k_1 \left(\hat{u}_0 - \hat{u}_1 \right) \right) e^{i\omega t}$$

$$\left(i\eta \hat{u}_1 \omega - k_1 \left(\hat{u}_0 - \hat{u}_1 \right) \right) e^{i\omega t} = 0$$

Divide by the Ansatz and rewrite into a matrix equation:

$$\hat{F} = \hat{u}_0 k_0 + k_1 \left(\hat{u}_0 - \hat{u}_1 \right)$$

$$i\eta \hat{u}_1 \omega - k_1 \left(\hat{u}_0 - \hat{u}_1 \right) = 0$$

$$\begin{bmatrix} \hat{u}_0 \left(-k_0 - k_1 \right) + \hat{u}_1 k_1 \\ -\hat{u}_0 k_1 + \hat{u}_1 \left(i\eta\omega + k_1 \right) \end{bmatrix} = \begin{bmatrix} -\hat{F} \\ 0 \end{bmatrix}$$

Invert the equation, find $\hat{u}$:

$$\hat{u}_0 = -\frac{\hat{F} \left(-\eta\omega + ik_1 \right)}{\eta\omega k_0 + \eta\omega k_1 - ik_0 k_1}$$

Determine the complex stiffness:

$$\hat{F} = \hat{u}_0 k_{\text{MW}}(\omega)$$

$$k_{\text{MW}}(\omega) = \frac{\eta\omega k_0 + \eta\omega k_1 - ik_0 k_1}{\eta\omega - ik_1}$$

$$k_{\text{MW}}(\omega) = \frac{i\eta\omega k_1^2}{\eta^2\omega^2 + k_1^2} + \frac{\eta^2\omega^2 \left(k_0 + k_1 \right) + k_0 k_1^2}{\eta^2\omega^2 + k_1^2}$$

$$|k_{\text{MW}}(\omega)| = \frac{\sqrt{\eta^2\omega^2 k_0^2 + 2\eta^2\omega^2 k_0 k_1 + \eta^2\omega^2 k_1^2 + k_0^2 k_1^2}}{\sqrt{\eta^2\omega^2 + k_1^2}}$$

Reformulate using $\tau = \eta/k_1$:

$$\eta = \tau k_1$$

$$k_{\text{MW}}(\omega) = \frac{\omega\tau k_0 + \omega\tau k_1 - ik_0}{\omega\tau - i}$$

$$k_{\mathrm{MW}}(\omega) = \frac{i\omega\tau k_1}{\omega^2\tau^2 + 1} + \frac{\omega^2\tau^2\left(k_0 + k_1\right) + k_0}{\omega^2\tau^2 + 1}$$

$$|k_{\mathrm{MW}}(\omega)| = \frac{\sqrt{\omega^2\tau^2 k_0^2 + 2\omega^2\tau^2 k_0 k_1 + \omega^2\tau^2 k_1^2 + k_0^2}}{\sqrt{\omega^2\tau^2 + 1}}$$

Limiting cases:

$$k_{\mathrm{MW}}(\infty) = k_0 + k_1$$

$$k_{\mathrm{MW}}(0) = k_0$$

Reformulate using $s = k_\infty/k_0$:

$$s = \frac{k_0 + k_1}{k_0}$$

$$k_{\mathrm{MW}}(\omega) = \frac{k_0\left(\omega\tau s - i\right)}{\omega\tau - i}$$

$$k_{\mathrm{MW}}(\omega) = \frac{i\omega\tau k_0\left(s - 1\right)}{\omega^2\tau^2 + 1} + \frac{k_0\left(\omega^2\tau^2 s + 1\right)}{\omega^2\tau^2 + 1}$$

$$|k_{\mathrm{MW}}(\omega)| = \frac{k_0\sqrt{\omega^2\tau^2 s^2 + 1}}{\sqrt{\omega^2\tau^2 + 1}}$$

$$\tan\left(\varphi\right) = \frac{\omega\tau\left(s - 1\right)}{\omega^2\tau^2 s + 1}$$

Compare Maxwell to Kelvin-Voigt:

$$k_{\mathrm{MW}}\left(\frac{\omega}{s}\right) = k_{\mathrm{KV}}(\omega)$$
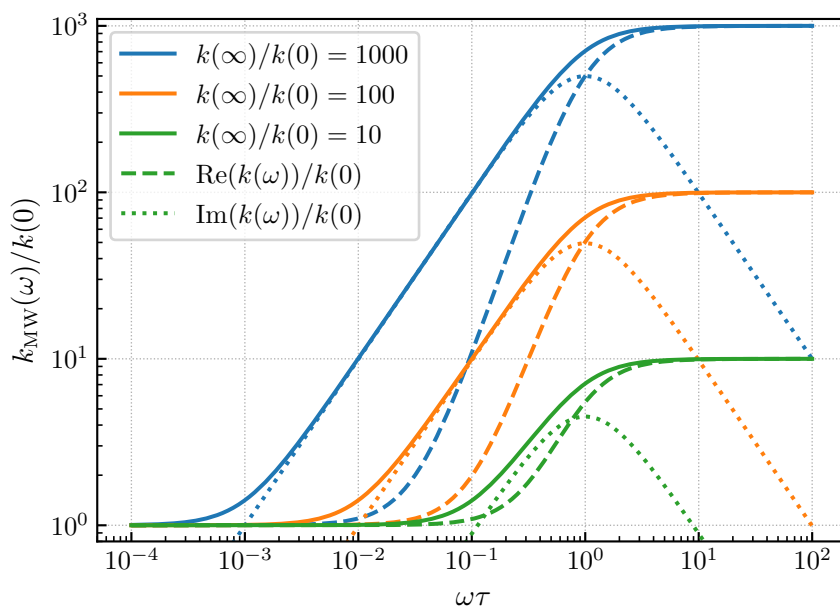
Figure E.3: Absolute value (solid), real part (dashed) and imaginary part (dotted line) of the stiffness of the SLS in Maxwell representation with relaxation time τ and different ratios k_∞/k_0.

Publications

I Influence of Poisson's ratio and confinement

Permission

Contributions of co-authors

Christian Müller: methodology: GFMD implementation, software, investigation: GFMD simulations, formal analysis, writing–original draft.
Martin H. Müser: conceptualization, formal analysis, supervision, writing–original draft.

The study was conceptualized by M.H.M., inspired by his discussions with René Hensel.

All simulations were set up, run and post-processed by C.M. under the supervision of M.H.M., including small adjustments to the GFMD source code. Ideas on how to evaluate and visualize results came from both authors and were then realized by C.M. The analytical treatment was outlined by M.H.M., where most of the final calculations were then carried out by C.M.

The original manuscript was prepared and revised by both authors. Everyone agreed on the publication of the article in the Journal of Adhesion and its inclusion in this thesis.

Taylor & Francis
Taylor & Francis Group

Analytical and numerical results for the elasticity and adhesion of elastic films with arbitrary Poisson's ratio and confinement

Christian Müller[a] and Martin H. Müser[a,b]

[a]INM - Leibniz Institute for New Materials, Saarbrücken, Germany; [b]Department. Of Materials Science and Engineering, Saarland University, Saarbrücken, Germany

ABSTRACT

We present an approximate, analytical treatment for the linearly elastic response of a film with arbitrary Poisson's ratio v, which is indented by a flat cylindrical punch while resting on a rigid foundation. Our approach is based on a simple scaling argument allowing the vast changes of the elastomer's effective modulus $\bar{E}$ with the ratio of film height h and indenter radius a to be described with a compact, analytical expression. This yields exact asymptotics for large and small reduced film heights h/a, whereby it also reproduces the observation that $\bar{E}(h/a)$ has a pronounced minimum for $v > 0.49$ at $h/a \approx 1.6$. Using Green's function molecular dynamics (GFMD), we demonstrate that the predictions for $\bar{E}(h/a)$ are reasonably correct and generate accurate reference data for effective modulus and pull-off force. GFMD also reveals that the nature of surface instabilities occurring during stable crack growth as well as the crack initiation itself depend sensitively on the way how continuum mechanics is terminated at small scales, that is, on parameters beyond the two dimensionless numbers h/a and v defining the continuum problem.

1. Introduction

This paper revisits the contact mechanics of confined, linearly elastic layers of height h sandwiched between a rigid surface and a circular rigid punch of radius a. A central quantity of such films is the effective modulus $\bar{E}$ [1] as a function of the reduced height h/a and the Poisson's ratio v. $\bar{E}$ is defined as the ratio of mean contact stress and relative height change. The arguably most important reason for wanting to know $\bar{E}(h/a)$ is that it allows the pull-off stress $\sigma_p \leq$ [2,3] and the fracture mechanisms of confined elastomers to be determined.[4–8] For large h/a or small v, adhesive contact failure is sudden, *i.e.*, the tensile force drops discontinuously from its maximum value to zero under quasi-static loading, even when the system is displacement driven. However, stable crack growth occurs for (nearly) incompressible elastomers

CONTACT Martin H. Müser ✉ martin.mueser@mx.uni-saarland.de 🖅 INM - Leibniz Institute for New Materials, 66123 Saarbrücken, Germany

once h/a falls below approximately two. As h/a drops below unity, the contact shape is no longer circular during stable crack growth but clearly symmetry broken[4,6–9] so that contact features have a characteristic linear dimension λ minimizing the total energy.[4,8,10–13]

The limits of unconfined $(h/a \to \infty)$[14] and incompressible $(v = 0.5)$, highly confined $(h/a \to 0)$[15] elastomers were solved more than half a century ago. Over time, amendments to the latter case were made with respect to boundary conditions, the geometry of the elastomer, and other details.[1,4,12,16] However, intermediate confinements $h/a \approx 1$ have not yet been solved analytically for extended two-dimensional films, although solutions for poker-chip specimens[17,18] as well as elastomeric strips[19] can be found. Extended films have only been treated numerically with finite-element (FE) simulations,[2,3,5,7,20,21] which lead to the suggestion of semi-empirical relationships between $\bar{E}/E^*$ and h/a,[3,5,20] where $E^* = E/(1 - v^2)$ is the contact modulus and E the Young's modulus. They turn out to benefit the interpretation of real-laboratory experiments, in particular, to explain different crack propagation mechanisms during detachment.[4,6–8] A deeper understanding of the $\bar{E}(h/a)$ dependence might also prove useful in interpreting observations made on confined elastomers in contact with rough indenters.[22–24]

Unfortunately, most existing semi-empirical $\bar{E}(h/a)$ relations were only designed for Poisson's ratios equal to or just below 0.5 so that confinement effects of various soft materials with small Poisson's ratios, such as foams, corks or soft isotropic metamaterials with negative Poisson's ratio are not quantitatively understood. Moreover, as demonstrated in this work, the extreme confinement limit, in which deviations from ideal incompressible matter have not yet been described satisfactorily for the given elastic film geometry. While instabilities of the elastomer surface were studied analytically for arbitrary Poisson's ratios,[10,25] the focus was quickly laid on ideally incompressible elastomers.[10,12,21] In addition, no physically motivated, closed-form expressions for the dependence of the effective modulus on the reduced film height have been proposed.

The original main motivation for this article was to identify a non-empirical relationship for $\bar{E}(h/a, v)$, which allows us to easily rationalize the minimum in $\bar{E}(h/a, v)$ and estimate the range of Poisson's ratios, in which an elastomer film behaves as if it were incompressible. To this end, we propose that the energy needed to deform the elastic film should be most sensitive to the stiffness of a surface undulation with a wavevector in the order of the inverse punch radius. Even if such a simple scale argument may not outperform existing, more empirical models for all possible combinations of h/a and v, it should improve our

ability to estimate $\bar{E}(h/a, v)$, in particular in the limit of extreme confinement and/or small Poisson's ratio. It certainly behoves us to examine numerically the accuracy of any scaling relation, which we do by running Green's function molecular dynamics (GFMD) simulations.[26] This also allows us to produce reference data for the pull-off stress as a function of h/a and v. While simulating the detachment process, we realized that the analysis of surface instabilities that occur during stable crack growth at $h/a \lesssim 1$ is interesting in its own right. We therefore include an in-depth analysis of how substrate symmetry, lattice trapping, and stochastic irregularities in the form of thermal noise, as well as their interplay affect the patterns that occur when the surface morphology becomes unstable during detachment.

The remainder of this article is organized as follows: Model and numerical methods are introduced in Section 2. Our scaling approach is presented in Section 3. Section 4 contains a comparison between theory and simulations as well as additional simulation results. Conclusions are drawn in Section 5.

2. Model and methods

2.1. Model

The investigated model system consists of isotropic, linearly elastic films of varying film height h resting on a perfectly flat and perfectly rigid foundation with a surface normal in the z direction. The in-plane extent of film and foundation are taken to be infinitely large and a no-slip condition is assumed between them. The opposite surface of the elastomer interacts with a rigid circular punch of radius a through a hard-wall constraint with a slip condition. Such systems can be effectively simulated by assuming periodic boundary conditions in the xy plane, as long as the linear dimension L of the periodically repeated simulation cell exceeds the punch radius a by a sufficiently large padding, which is most effectively chosen to be larger than but of order $\min(h, a)$.

In the just-defined setup, the elastic energy of the elastomer is given by[27–29]

$$V_{\text{ela}} = \sum_{\mathbf{q}} \frac{qE^*}{4} c(v, qh) |\tilde{u}(\mathbf{q})|^2 \tag{1}$$

where $\mathbf{q}$ is an in-plane wave vector with absolute value q, $\tilde{u}(\mathbf{q})$ is the Fourier coefficient of the displacement field of the elastomer's surface facing the indenter and

$$c(v, qh) = \frac{(3 - 4v)\cosh(2qh) + 2(qh)^2 - 4v(3 - 2v) + 5}{(3 - 4v)\sinh(2qh) - 2qh}. \tag{2}$$

For an infinitely large system without periodic boundaries, the sum on the r.h. s. of Eq. (1) will be replaced with an appropriate integral. For some of the calculations presented in this study, knowledge of the asymptotes of $c(v, qh)$ is useful. A Taylor expansion reveals them to be

$$c(v, qh) = \begin{cases} 1 & \text{for } qh \gg 1 \\ c_1(v)/(qh) & \text{for } qh \ll 0.5 - v \quad \text{and } v < 0.5 \\ 1.5/(qh)^3 & \text{for } qh \ll 1 \quad \text{and } v = 0.5. \end{cases} \tag{3}$$

with

$$c_1(v) = \frac{2(1 - v)^2}{1 - 2v}. \tag{4}$$

In our analytical treatment, the interaction between indenter and elastomer is a non-overlap constraint. In addition, a surface energy γ is gained per unit area where surfaces touch. The model is then replaced with a cohesive zone model for the numerical solution of the contact problem, which is described next.

2.2. Methods

The contact problems were solved numerically using Green's function molecular dynamics (GFMD) simulations.[26] GFMD is a boundary-value method, in which Newton's equations of motion for the displacement fields are solved in their Fourier representation. In compression simulations, we use an exact non-overlap constraint in conjunction with the fast-inertial relaxation (FIRE)[30] algorithm as described in Ref.[31] Typical simulations assume the linear dimension of the periodically repeated simulation cell to be three times the punch diameter and a discretization of the displacement field into $2,048 \times 2,048$ elements. While exploiting the circular symmetry of the problem would have allowed us to reduce the computational cost of the simulations substantially, we found it more time effective to use the implemented methods.

Although knowledge of V_{ela} as a function of normal displacement and h/a determined from purely repulsive experiments is sufficient to deduce the adhesive pull-off force, see Section 3.3, simulations mimicking tensile loading were also conducted. This was not only done to double-check our pull-off force calculations but also to investigate the dynamics and failure mechanisms that occur during the detachment of confined elastomers. For this purpose, adhesion is modeled with a cohesive zone model (CZM), in which the gap-dependent surface energy has the form[32]

$$\gamma(g) = -\gamma \times \begin{cases} \{\cos(kg) + 1\}/2 & \text{for } 0 \leq kg \leq \pi/\Delta a \\ \{1 - (kg)^2/4\} & \text{for } g < 0 \end{cases} \tag{5}$$

and zero else, where g is the gap between elastomer and punch. The parameter k was generally set such that the maximum stiffness of surface undulations was slightly more than twice the maximum (negative) curvature of the potential defining the CZM, $i.e.$, $k^2 = \frac{0.4}{r} q_{max} E^* c(v, q_{max}h)$, where $q_{max} = \sqrt{2}\pi/\Delta a$ and Δa the linear mesh discretization. In this way, the interaction is effectively as short ranged as possible while avoiding lattice trapping. The latter refers to a situation, where an individual degree of freedom, $e.g.$, a GFMD discretization point, can have two or more mechanically stable positions, while all other points remain fixed. When addressing lattice trapping, the parameter k was set to 3.75 times its default value. To improve the convergence rate, the mass-weighting GFMD variant was used for adhesive simulations.[31] Computing time is furthermore reduced by progressively increasing spatial resolution and decreasing the rate of retraction upon approaching the point of maximum tensile force.

To also model the response of elastomers to small perturbations, some simulations were conducted at finite temperature with the help of a recently introduced GFMD thermostat.[33] To this end, the thermal energy was kept at about 0.1% of the adhesive energy gained in a single mesh element in which the elastomer makes perfect contact with the indenter.

2.2.1. Finite-size corrections
If the origin of the coordinate system coincides with the center of the flat punch, the macroscopic displacement u_0 is defined as $u(0) - u(r \to \infty)$. Thus, the best simple estimate for u_0 when using a finite square-shaped simulation cell with length L is to replace $u_\infty \equiv u(r \to \infty)$ with $u(L/2, L/2)$.

To reduce the finite-size error, we use a correction appropriate for semi-infinite elastomers[34] but damp it with the weight function $w(h/a) = \tanh(h/a)$ for small h/a:

$$u_\infty \approx u(L/2, L/2) + 5 w(h/a) \{u(L/2, L/2) - u(L/2, 0)\}. \tag{6}$$

The damping of the usual correction is needed because for finite h/a, the displacement field approaches u_∞ exponentially quickly with increasing distance r from the origin rather than with $1/r$.

3. Theory

As has been done before,[2,3,35] we define the effective modulus $\bar{E}$ as the ratio of the mean (compressive) contact stress $\bar{\sigma} = F/(\pi a^2)$ and the relative height change of the elastomer to the contact area, $\bar{\varepsilon} = u_0/h$, even if the uncompressed elastomer is a film rather than a free-standing cylinder of radius a, for

which $\bar{E}$ was originally introduced.[35] Here, u_0 is the normal displacement of the elastomer's surface right below the punch from its equilibrium height in the absence of an indenter. Thus, $\bar{E}$ is given by

$$\bar{E} = \frac{\bar{\sigma}}{\bar{\varepsilon}} = \frac{Fh}{u_0 \pi a^2}. \tag{7}$$

Since a does not change with u_0 for a flat punch under compression, it follows that F is proportional to u_0 within linear elasticity. Thus, the elastic energy is simply given by $V_{\text{ela}} = Fu_0/2$ so that

$$V_{\text{ela}} = \left(\pi a^2\right) \frac{\bar{E}}{2h} u_0^2. \tag{8}$$

As already argued in the introduction, the only in-plane length defining the contact problem is the punch radius a. Thus, under compression, dimensional analysis suggests that the elastic energy should predominantly reside in undulations with wave numbers of the order of $q_a = 2\pi/a$ given that $q \to 0$ or $q \to \infty$ modes are not dominant. In this case, a good estimate for the elastic energy would be

$$V_{\text{ela}} = \left(\pi a^2\right) \mathcal{O}(q_a) E^* c\{\nu, \mathcal{O}(q_a)h\} u_0^2. \tag{9}$$

In order to eliminate the big-O notation in Eq. (9), we introduce two proportionality factors α and β. Comparing the resulting elastic energy to Eq. (8) yields

$$\frac{\bar{E}}{E^*} \approx \frac{1}{2} \alpha \beta q_a h c\{\nu, \beta q_a h\}, \tag{10}$$

which is the central analytical result of this work. Sections 3.1 and 3.2 are concerned with a parametrization of α and β, while Section 3.3 summarizes how to deduce depinning forces from the h/a dependence of $\bar{E}$.

To further motivate our approach, Figure 1 shows displacement and stress fields in real space for the various confinements, which range from small ($h/a \gg 1$) and intermediate ($h/a = 1$) via large ($1 - 2\nu \ll (h/a)^2 \ll 1$) to extreme ($(h/a)^2 \ll 1$). These data are complemented by the elastic energy associated with individual $\tilde{u}(\mathbf{q})$ modes in the right column of Figure 1, which clearly supports the scaling hypothesis that energy predominantly resides in modes with wavelengths of order a.

The top row of Figure 1 shows the well-established properties of the flat-punch solution for semi-infinite elastomers. On the other end, in the two bottom rows, Figure 1 reveals a qualitative difference between large and extreme confinement, which may often be underappreciated, although the principle is known from works addressing poker-chip and
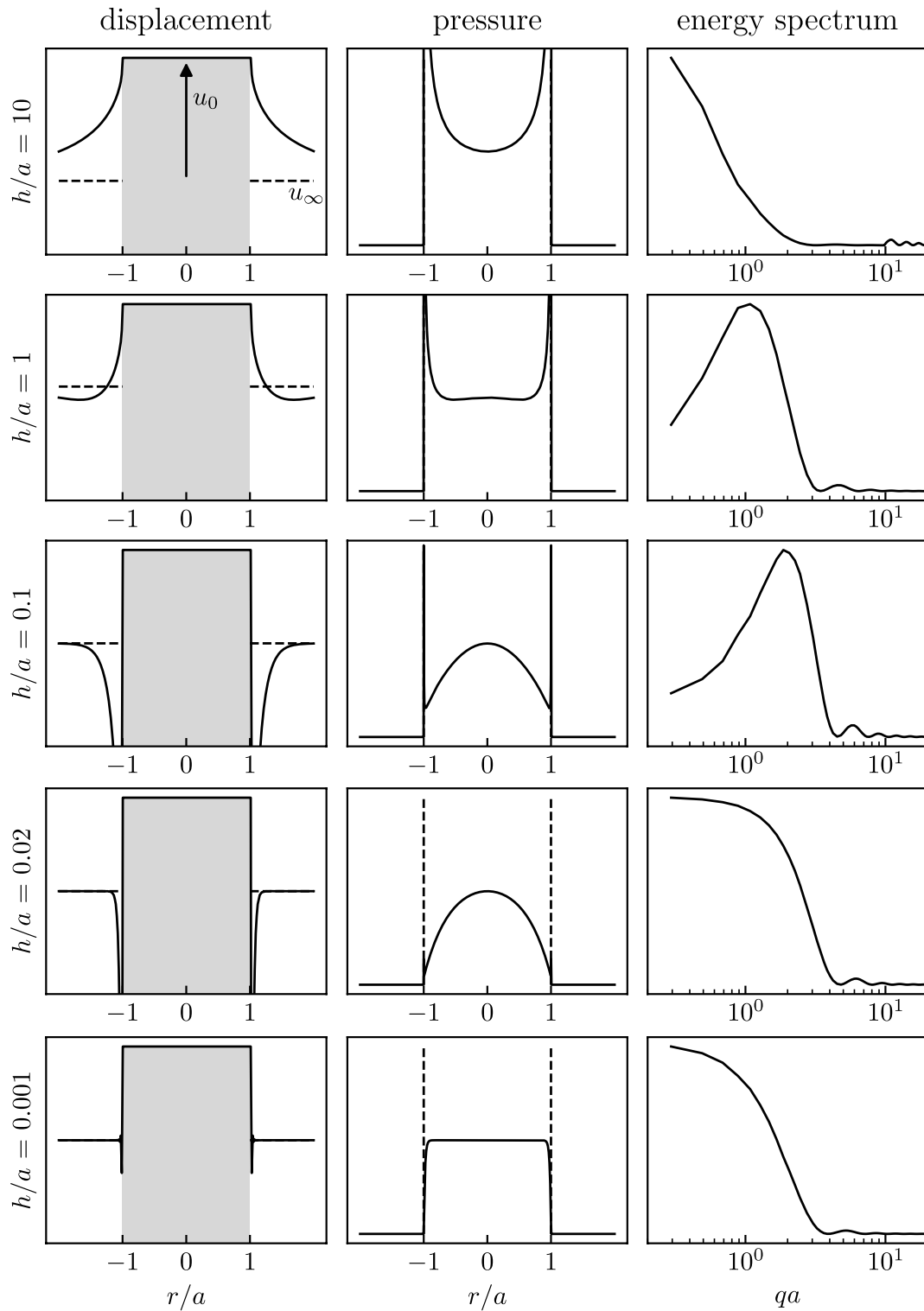
Figure 1. Displacement field (left column), stress field (center column), and energy spectrum (right column), *i.e.*, individual summands of the r.h.s. of Eq. (1), for $v = 0.4995$ at different values of the reduced height h/a. The ordinate axis is linear in all cases.

elastic-strip geometries.[17–19] Specifically, for $1 - 2v < (h/a)^2 \ll 1$, the stress profile at the origin is close to an inverted parabola while for $(h/a)^2 \ll 1 - 2v$, the stress is constant within (most of) the contact. It should also be noted that in all cases, a stress singularity occurs at the contact edge, which in our numerical treatment – and in reality – is cut off by the finite range of the interaction potential, whose precise effective value can be a function of the microscopic roughness.[33] In addition, the corresponding intensity decreases with decreasing h/a and thus disappears in the limit of $h/a \to 0$.

3.1. Asymptotic scaling

In many cases, nearly incompressible elastomers are treated as perfectly incompressible and their Poisson's ratio is approximated with $v = 0.5$.[4–6,35] However, analyzing the asymptotic behavior of $\bar{E}$ for $h/a \to 0$ reveals a more concise picture, which is presented in the following.

   The ratio $\bar{E}/E^*$ can only be a function of the two dimensionless numbers defining the problem, namely v and h/a. The asymptotic limits for $\bar{E}/E^*$ at extreme and small confinement can be deduced from existing solutions for the considered confined elastomer. As will be shown in the remaining part of this Section 3.1, they turn out to be

$$\frac{\bar{E}}{E^*} = \begin{cases} 2h/(\pi a) & \text{for } h/a \gg 1 \\ c_1(v)/2 & \text{for } h/a \ll \sqrt{1 - 2v} \quad \text{and } v < 0.5 \\ 3a^2/(32h^2) & \text{for } h/a \ll 1 \quad \text{and } v = 0.5, \end{cases} \tag{11}$$

where $c_1(v)$ was introduced in Eq. (4).

   The condition $(h/a)^2 \ll 1 - 2v$ for $v < 0.5$ in Eq. (11) is motivated by the observation that for v close to 0.5, the scaling of the function $c(v, h/a)$ has two different small-h/a scaling regimes. The threshold between these regimes is characterized by the transition from a parabolic to a constant stress distribution as illustrated by Figure 1. Based on this we introduce the terminology that a film is extremely confined if h/a is small compared to $\sqrt{1 - 2v}$ and largely confined if this condition does not hold but h is still small compared to a.

3.1.1. Unconfined limit

The unconfined limit is nothing but a regular flat punch in contact with a semi-infinite half space.[14] Inserting its well-known stress–displacement relation $F = 2aE^* u_0$ into Eq. (7) yields the first case given in Eq. (11).

3.1.2. Extreme confinement limit

For $h/a \to 0$ and $v < 0.5$, the proportionality between the elastic energy of a single height undulation and $|\tilde{u}(\mathbf{q})|^2$ does not depend noticeably on the wave number q. Due to Parseval's theorem, a linear relation between local displacement and local stress occurs within most of the contact. This is why the stress is approximately constant within the contact in the bottom row of Figure 1 and zero outside so that its Fourier transform is

$$\tilde{\sigma}(\mathbf{q}) = \frac{\bar{\sigma}}{2\pi} \int d^2 r \, e^{i\mathbf{q}\cdot\mathbf{r}} \, \Theta(a - r) \tag{12}$$

$$= \bar{\sigma} a J_1(aq)/q, \tag{13}$$

$\Theta(\ldots)$ being the Heaviside step function, $\mathbf{r} = (x, y)$ the in-plane position with $r = |\mathbf{r}|$ and $J_n(\ldots)$ the Bessel function of the first kind of order n. Using the stress–strain relation that follows from Eq. (1) yields a displacement at the origin $u_0 \equiv u(r = 0)$ of

$$u_0 = \frac{1}{2\pi} \int d^2 q \, \frac{a}{q} J_1(aq) \frac{2}{q c(v, qh)} \frac{\bar{\sigma}}{E^*} \tag{14}$$

$$\Rightarrow \frac{u_0/h}{\bar{\sigma}} = \frac{2}{\tilde{h} E^*} \int_0^\infty d\tilde{q} \, \frac{J_1(\tilde{q})}{\tilde{q} c\left(v, \tilde{q}\tilde{h}\right)}, \tag{15}$$

where $\tilde{h} = h/a$ is the reduced height and $\tilde{q} = qa$. By definition, the l.h.s. of Eq. (15) and thus its r.h.s. is nothing but the inverse of the effective elastic modulus $\bar{E}$.

The integral on the r.h.s. of Eq. (15) probably has no closed-form analytical solution and is even difficult to solve numerically because of the oscillations of the Bessel function. To reduce the effect of the oscillations, we rewrite the integral as

$$I = \int_0^\infty d\tilde{q} \, \frac{f(\tilde{q}) + f(\tilde{q} + \pi)}{2} + \frac{1}{2} \int_0^\pi d\tilde{q} f(\tilde{q}), \tag{16}$$

$f(\tilde{q})$ being the integrand on the r.h.s. of Eq. (15). In its rewritten form, the integral can be easily seen to have its dominant contribution from small $\tilde{q}$ when $\tilde{h}$ is small. This property does not change after using the appropriate small-$\tilde{q}$ approximation for $c(v, \tilde{q})$ in the integrand. As a consequence, I can be solved analytically to be $\tilde{h}/c_1(v)$ in the large-confinement limit for $v < 0.5$, which ultimately translates into the corresponding expression stated in Eq. (11).

3.1.3. Large-confinement limit

For $v = 0.5$ and h sufficiently small compared to a, or, alternatively, $v < 0.5$ and h/a in the intermediate scaling regime, the stiffness of a mode is no longer independent of q but instead proportional to q^{-2}. As a consequence, the stress is no longer constant in the contact area but assumes the functional form[35]

$$\sigma(r) = \sigma_0 \left(1 - r^2/a^2\right) \Theta(a - r) \tag{17}$$

with $\sigma_0 = 2\bar{\sigma}$, see also the second to last row in Figure 1. It should be noted that this stress distribution was originally derived for a finite elastomer of originally cylindrical shape sandwiched between two rigid planes and assuming a stick condition. However, Gent[35] already expected the functional dependence of $\bar{E}$ on h/a for his set-up to be similar to that of films.

Proceeding as in Section 3.1.2, we first determine $\tilde{\sigma}(\mathbf{q})$ to be

$$\tilde{\sigma}(\mathbf{q}) = \int_0^a \mathrm{d}r\, rJ_0(qr)\sigma(r) = \sigma_0 a^2 \left(\frac{J_1(\tilde{q})}{\tilde{q}} - 2\frac{J_2(\tilde{q})}{\tilde{q}^2} + \frac{J_3(\tilde{q})}{\tilde{q}}\right). \tag{18}$$

The displacement in the origin then becomes

$$u_0 = \frac{2a\sigma_0}{E^*} \int_0^\infty \mathrm{d}\tilde{q}\, \frac{1}{c(v, \tilde{q}\tilde{h})} \left(\frac{J_1(\tilde{q})}{\tilde{q}} - 2\frac{J_2(\tilde{q})}{\tilde{q}^2} + \frac{J_3(\tilde{q})}{\tilde{q}}\right) \tag{19}$$

$$\overset{\text{Eq.(3)}}{\Longrightarrow} \frac{u_0/h}{\bar{\sigma}} = \frac{8\tilde{h}^2}{3E^*} \int_0^\infty \mathrm{d}\tilde{q}\left(\tilde{q}^2 J_1(\tilde{q}) - 2\tilde{q}J_2(\tilde{q}) + \tilde{q}^2 J_3(\tilde{q})\right). \tag{20}$$

As in the previous section, the integral cannot be solved analytically and the integrand oscillates too much to allow for a numerically robust integration. We therefore proceed again as described in the text around Eq. (16). This time, we did not identify a closed-form expression for the small-q expansion, but found a numerical value of 4 with six significant digits, so that we believe 4 to be the exact value for the integral on the r.h.s. of Eq. (20). Thus, comparing the r.h.s. of Eq. (20) with the definition of $\bar{E}$ yields the large-confinement limit for $\bar{E}$ and $v = 0.5$.

3.2. Intermediate reduced film heights

In the previous section, we derived the asymptotic dependence of $\bar{E}$ on h/a at large and small h/a. We now want to ascertain how to chose α and β. To this end, we define $\tilde{E}_s = \bar{E}_s/E^*$ as the r.h.s. of Eq. (10). Inserting the asymptotes of $c(v, qh)$ from Eq. (3) into Eq. (10) yields

$$\frac{\bar{E}_s}{E^*} = \begin{cases} \alpha\beta q_a h/2 & \text{for } h/a \gg 1 \\ c_1(v)\alpha/2 & \text{for } h/a \ll \sqrt{1 - 2v} \quad \text{and } v < 0.5 \\ 3\alpha/\left\{4\beta^2 (q_a h)^2\right\} & \text{for } h/a \ll 1 \quad\quad\ \text{and } v = 0.5. \end{cases} \tag{21}$$

Comparing this result to Eq. (11) reveals that $\bar{E}_\text{s}$ scales properly with h/a in the asymptotic limits. However, when expressing the elastic energy of the system and the subsequent effective modulus, there are three equations and just two parameters

$$\alpha\beta = 2/\pi^2 \qquad \text{for any } v \tag{22a}$$

$$\alpha = 1 \qquad \text{for } v < 0.5 \tag{22b}$$

$$\alpha\beta^{-2} = \pi^2/2 \qquad \text{for } v = 0.5. \tag{22c}$$

Thus, Eqs. (22b) and (22c) give conflicting optimum parameter choices for $v < 0.5$ and $v = 0.5$. They are $\alpha = 1$, $\beta = 2/\pi^2$ for $v < 0.5$ and $\alpha = 2/\pi$, $\beta = \sqrt[3]{4/\pi^4}$ for $v = 0.5$.

An exact representation of $\bar{E}(h/a)/E^*$ may be achievable by adding (infinitely) many summands as they occur on the r.h.s. of Eq. (10). To make these sums satisfy the asymptotic limits, Eq. (22) must be generalized to sum rules. However, we did not find that proceedings along those lines appeared to be promising. Therefore, we will only use the single wave-number, asymptotically correct approximations for $\bar{E}(h/a)$.

3.3. Deducing depinning force and range of stable crack growth from the effective modulus

Refs.[3–6,8] relate $\bar{E}(h/a)$ (or its inverse) to the energy release rate G, from which the pull-off force and crack propagation dynamics can be deduced. Similar to Yang and Li,[36] we start from the total energy formulation rather than the energy release rate, as we find this more direct and more intuitive.

The total potential energy of our system in an externally potential producing a constant force F reads

$$U = \frac{\bar{E}(h/a_\text{c})}{2} \left(\frac{u_0}{h}\right)^2 (\pi h a_\text{c}^2) - \pi a_\text{c}^2 \gamma - F u_0, \tag{23}$$

where a negative value of F implies a (positive) tensile force causing a negative displacement u_0. In this nomenclature, a_c is the actual contact radius, which may now be different from the punch radius a.

In equilibrium, u_0 and contact radius a_c both minimize the potential energy, i. e., $\partial U/\partial a = \partial U/\partial u_0 = 0$. In stable equilibrium, the Hessian produced by the second-order derivatives of U w.r.t. u_0 and a_c must be positive definite. When the system is displacement-driven, this condition reduces to $\partial^2 U/\partial a_\text{c}^2 > 0$.

The generalized force acting on the radius a_c, $F_a \equiv -\partial U/\partial a_\text{c}$, is easily deduced as

$$F_a = 2\pi\gamma a_c - \pi\bar{E}(h/a_c)\frac{u_0^2}{h}a_c + \frac{\pi}{2}\frac{\partial\bar{E}(h/a_c)}{\partial a_c}\frac{u_0^2 a_c^2}{h}. \tag{24}$$

This equation allows a_c to be determined self-consistently for a given u_0. However, it has to be kept in mind that a_c cannot grow for positive F_a when a_c is equal to the punch radius a. This is why the case of $a_c = a$ and $a_c < a$ must be treated separately.

The contact radius starts shrinking when $F_a(u_0, a_c = a) = 0^-$ on retraction. Inserting this condition into Eq. (24) and solving for u_0 yields

$$u_0 = -\sqrt{\frac{4\gamma h}{2\bar{E}(h/a_c) + a_c\partial\bar{E}(h/a_c)/\partial a_c}}, \tag{25}$$

which has to be evaluated at $a_c = a$ to deduce the normal displacement at the point, where the contact is just about to start shrinking for the first time. The normal force acting on the punch can then be deduced from $\partial U/\partial u_0 = 0$ to be

$$F(a_c) = -\sqrt{\frac{4\bar{E}(h/a_c)\gamma/h}{2 + \partial\ln\bar{E}(h/a_c)/\partial\ln a_c}}\pi a_c^2. \tag{26}$$

Evaluating this force at $a_c = a$ gives the depinning or pull-off force $F_p \equiv -F(a)$, which is the maximum tensile force occurring right before the contact radius starts shrinking. Different representations of the same equation can also be found using the energy release rate and/or assuming the load-driven case.[2,16]

As mentioned above, the previously determined contact radius a_c is only stable if $\partial^2 U/\partial a_c^2 > 0$, which can be written in a convenient form that reproduces $\partial U/\partial a_c$, which is 0 in equilibrium:

$$\frac{\partial^2 U}{\partial a_c^2} = \frac{1}{a_c}\frac{\partial U}{\partial a_c} + \frac{\pi u_0\bar{E}}{2h}\left(\frac{\partial^2\ln\bar{E}}{(\partial\ln a_c)^2} + \left(\frac{\partial\ln\bar{E}}{\partial\ln a_c}\right)^2 + 2\frac{\partial\ln\bar{E}}{\partial\ln a_c}\right) > 0. \tag{27}$$

The dividing line between stable and unstable crack propagation is defined by the condition $\partial F_a/\partial a_c = 0$. It can be cast

$$\frac{\partial^2\ln\bar{E}(h/a_c)}{(\partial\ln a_c)^2} + \left(\frac{\partial\ln\bar{E}(h/a_c)}{\partial\ln a_c}\right)^2 + 2\frac{\partial\ln\bar{E}(h/a_c)}{\partial\ln a_c} = 0. \tag{28}$$

This criterion together with Eq. (21) can be used to explain why there is no stable crack growth in an adhesive contact between a flat punch and a semi-infinite elastomer. For confined bodies, especially when v is close to 0.5, this procedure is no longer applicable, since the contact area is usually not circular.

4. Results and discussion

4.1. Effective modulus

Figure 2 compares numerical results for $\bar{E}/E^*$ to the analytical results from the previous section using adjustable parameters α and β following from Eq. (22). It is shown that the simple scaling approach reproduces the overall trends fairly well. By design, the asymptotic limits are matched for $v < 0.5$. Moreover, the location of the minimum in $\bar{E}(h/a)/E^*$, so it exists for a given Poisson's ratio, almost coincides between theory and simulation. However, the value of $\bar{E}/E^*$ in the minimum has an error of a few 10%. Errors are largest in the regime where a $v \lesssim 0.5$ elastomer shows similar behavior to an ideally incompressible solid. This can be rationalized by the $h/a \to 0$ asymptotics of a $v = 0.5$ body, which would require the parameters α and β to be redefined. For reasons of completeness, we note that the minimum of $\bar{E}(h/a)/E^*$ for $v = 0.5$ is located at $h/a = 1.665$ in our analytical treatment and at $h/a \approx 1.23 \pm 0.02$ in the GFMD data. The relatively large numerical uncertainty of the minimum location results from the minimum being shallow.

To better resolve the discrepancies between the scaling approach and the numerical data, Figure 3 shows the ratio $\bar{E}_{\mathrm{GFMD}}/\bar{E}_{\mathrm{s}}$ as a function of reduced height. For $v < 0.45$, relative errors turn out to be quite insensitive to v for any h/a. They can be approximated reasonably well with a single Gaussian constructed according to
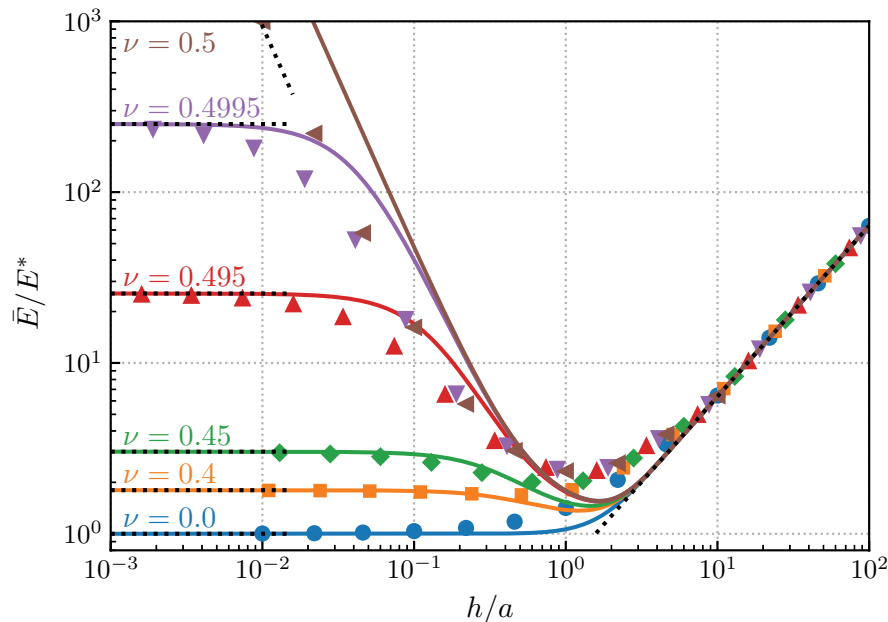
Figure 2. Reduced effective modulus $\bar{E}/E^*$ as a function of the reduced film height h/a for different Poisson's ratios v. Solid lines are theoretical predictions based on our scaling approach, symbols represent numerical results. Dotted lines indicate the asymptotic limits described in Eq. (21).
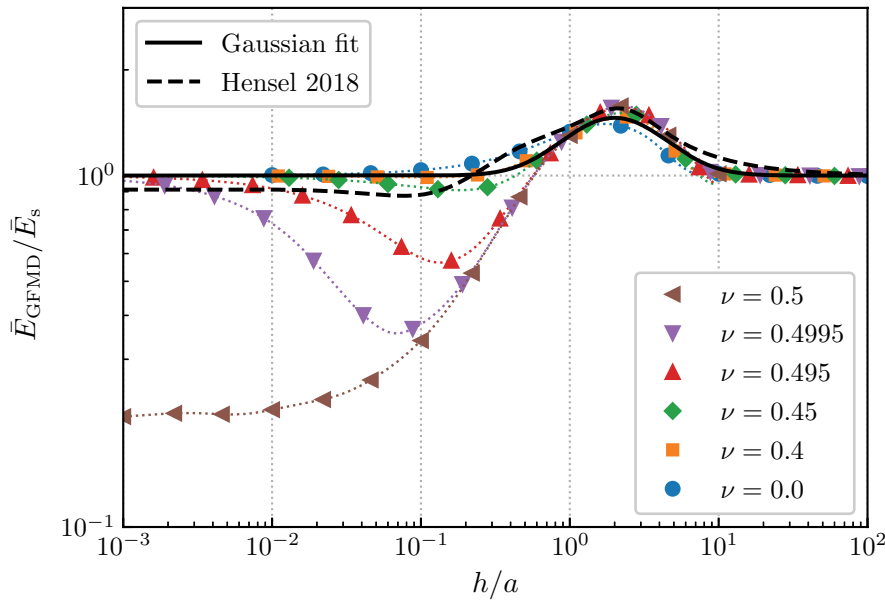
Figure 3. Ratio of numerical and theoretical effective modulus, $\bar{E}_{\text{GFMD}}/\bar{E}_s$. The solid line reflects Eq. (29) and the dashed line represents the empirical fit function from Ref.[3] evaluated for $v = 0.495$. Dotted lines are drawn to guide the eye.

$$\frac{\bar{E}_{\text{GFMD}}}{\bar{E}_s} - 1 = A \exp\left\{ -\ln^2\left(\tilde{h}/\tilde{h}_0 \right) / \left(2B^2 \right) \right\} \qquad (29)$$

with $A = 0.46$, $B = 0.75$, and $\tilde{h}_0 = 2$. A similar insensitivity of $\bar{E}_{\text{GFMD}}/\bar{E}_s$ on v holds for large v only as long as $h/a \geq 1$. Interestingly, all $\bar{E}_{\text{GFMD}}/\bar{E}_s$ curves almost coincide at $\bar{h}/a = 1$, where they assume the value of $4/3$ within a 3% margin. Unfortunately, the relative errors can exceed a factor of 1.5 for $(h/a)^2 > 1 - 2v$ while $h/a \ll 1$. Nonetheless, they always remain below a factor of $\pi^2/2$.

Since previous works[2,3,5,7,21] considered mostly stick conditions for the elastomer-punch interface, comparing our numerical data to existing data or (semi-) empirical approximations for $\bar{E}(h/a)$ may not appear meaningful at first sight. However, we note that the overall trends are similar and that comparisons between different boundary conditions and comparisons between FEM and GFMD data may yet be insightful. We find Hensel et al.'s[3] (well, ugly) fit function to match our data most beautifully, which is shown exemplarily for $v = 0.495$ in Figure 3, in particular for $0.5 < h/a < 10$. Interestingly, for $h/a < 0.5$, their fit function is close to our analytical result. Thus, it does not capture the minimum associated with the large Poisson's ratios, which may well be because Hensel et al. assumed stick conditions between punch and elastomer.

4.2. Pull-off stress

In order to deduce the adhesive pull-off stress $\sigma_p = F_{\mathrm{p}}/(\pi a^2)$ from $\bar{E}(h/a)$, we replace $\partial \ln \bar{E}/\partial \ln a_{\mathrm{c}}$ in Eq. (26) with $-\partial \ln \bar{E}/\partial \ln \tilde{h}$ so that

$$\sigma_{\mathrm{p}} = \sqrt{\frac{4\bar{E}(\tilde{h})\gamma}{a\tilde{h}\left(2 - \partial \ln \bar{E}(\tilde{h})/\partial \ln \tilde{h}\right)}}. \tag{30}$$

The derivatives are evaluated numerically from the GFMD data shown in Figure 2 using cubic spline interpolation. Results for the pull-off stress are shown in Figure 4. To ensure their correctness, the pull-off stresses were also computed for selected values of v at $h/a = 0.1$ with simulations mimicking tack tests. Agreement was always within 2%. Since direct adhesive simulations are much more demanding and more prone to discretization errors than computations of $\bar{E}$ using non-overlap constraints, we believe the presented results to have errors well below 2%.

Using our analytical expression for $\bar{E}(h/a)$ directly to estimate the pull-off stress turned out to be disappointing. However, using the asymptotic scaling for σ_{p} yields relatively satisfactory results, because it allows one to transition from $v < 0.5$ to $v = 0.5$ scaling when crossing over from extreme to large confinement. Likewise, it is beneficial to transition from $v = 0.5$ to $h/a \rightarrow \infty$ scaling when crossing over from confined to unconfined.
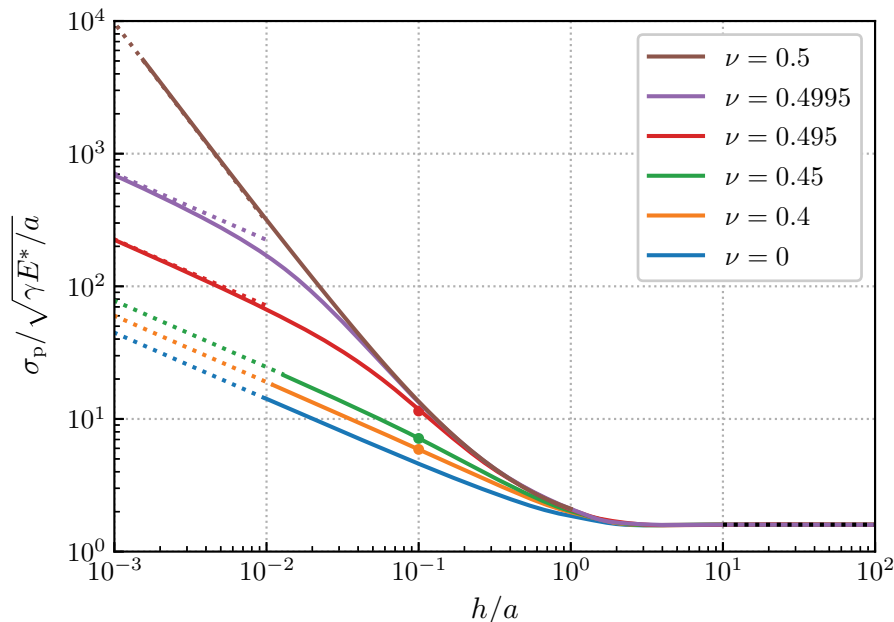
Figure 4. Computed pull-off stress as a function of confinement h/a for a wide range of Poisson's ratios v. Dotted lines, full lines, and circles represent asymptotic limits, analysis of the numerical $\bar{E}(h/a)$ curves, and results from adhesive GFMD simulations, respectively.

The asymptotic solutions for σ_{p} can be obtained from Eq. (30) by exploiting once more Eq. (11):

$$\sigma_{\mathrm{p}} = \begin{cases} \sqrt{8\gamma E^*/(\pi a)} & \text{for } h/a \gg 1 & (31a) \\ \sqrt{c_1(v)\gamma E^*/\left(a\tilde{h}\right)} & \text{for } h/a \ll \sqrt{1-2v} \quad \text{and } v < 0.5 & (31b) \\ \sqrt{3\gamma E^*/\left(32ta\,\tilde{h}^3\right)} & \text{for } h/a \ll 1 \qquad\qquad \text{and } v = 0.5. & (31c) \end{cases}$$

Related scaling relations have been proposed before[1,4,7,12,13,15,16,36] for varying boundary conditions (BCs), however, generally assuming $v = 0.5$. Historically first, Kendall[15] identified Eq. (31a) for the unconfined system using, as we do, a frictionless elastomer-punch interface. In the opposite limit, $h/a \to 0$, he found $\sigma_{\mathrm{p}} \propto 1/\sqrt{h}$, which differs from our Eq. (31c) because Kendall used a slip condition for the elastomer–substrate interface, while we assumed a stick condition. Yang and Li[36] confirmed Kendall's scaling relation, albeit they corrected the numerical prefactor by multiplying Kendall's result with $\sqrt{E^*/K}$, where K is the bulk modulus. In the case where Yang and Li employ our BCs, they also find Eq. (31c). In fact, Yang and Li considered all four possible combinations of elastomer-punch and elastomer-substrate BCs. However, they only considered $v = 0.5$.

4.2.1. Deducing v from mechanical measurements

In order for our calculations to benefit the determination of the Poisson's ratio from mechanical measurements or, rather that of $\Delta v = 0.5 - v$, our results for $\bar{E}$ and σ_{p} are best represented as functions of v for fixed values of h/a, as is done in Figure 5. This way E^* and/or σ_{p} only need to be determined once for
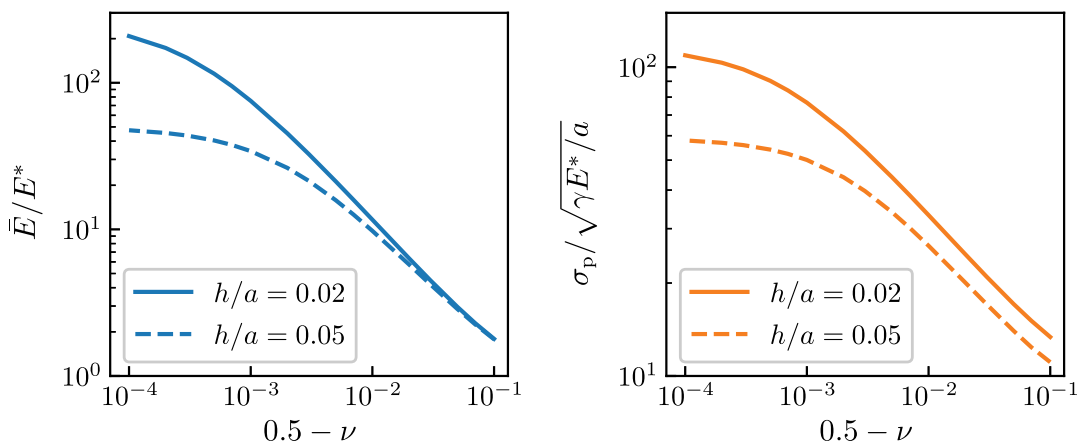
Figure 5. GFMD results for the dimensionless, effective modulus $\bar{E}/E^*$ and the predicted reduced pull-off stress $\sigma_{\mathrm{p}}/\sqrt{\gamma E^*/a}$ for Poisson's ratios $v = 0.4999$ to 0.4 for the confinements $h/a = 0.02$ and $h/a = 0.05$.

a semi-infinite elastomer and once more for a confined elastomer. Similar approaches to determine Δv experimentally from $\bar{E}(h/a)$ have already been pursued successfully.[37,38]

Information as that presented in Figure 5 is certainly only beneficial as long as we are not yet too deep in the extreme confinement limit since $\bar{E}$ and σ_p are no longer sensitive to $\log(\Delta v)$ in that regime.

Using very small h/a from the beginning is not necessarily effective either, since it might be equally important and infeasible to accurately align the flat punch as well as to account for the effects arising from the combined compliance of substrate, punch, and driving apparatus. Thus, for Δv suspected to exceed 10^{-3} and 10^{-4}, we would recommend to use $h/a = 0.05$ and $h/a = 0.02$, respectively.

Determining Poisson's ratios of confined layers to less than 10^{-4} might be possible through optical measurements of the bulge arising right next to the indenter.[39] However, we could not identify bulge characteristics, *i.e.*, appropriately undimensionalized bulge widths or heights, which appear to be promising candidates. The thin slit between the indenter and elastomer seems to have the largest sensitivity to $\log(\Delta v)$. Unfortunately, its determination would require extremely smooth surfaces and a high-accuracy measurement of the buried gap.

4.3. *Crack formation and propagation*

Crack growth during punch retraction becomes stable for sufficiently confined elastomers and large Poisson's ratios, *i.e.*, below a critical film height $h_c(v)$. Evaluating the stability condition, Eq. (28), for $v = 0.5$, we locate the transition near $h_c(0.5)/a = 3.44$ from the GFMD data and at $h_c(0.5)/a = 3.692$ from our scaling ansatz. As v decreases, the estimates for $h_c(v)/a$ move to smaller values. However, $h_c(v)/a$ becomes tedious to evaluate numerically from GFMD data once the elastomer is no longer very close to being incompressible.

Once h/a is well below unity, elastic instabilities, so-called fingering instabilities, occur for (nearly) incompressible elastomers,[4,6–9] which result in wavy displacement fields below the indenter. Their characteristic wave number q was related to a minimum in the stiffness of surface undulations, $\kappa = qE^*c(qh,v)/4$.[4,8,10–13] It is located at $q = 2.12/h$ for $v = 0.5$ and at $q = 1.553/h$ for $v = 0.4$. These values translate to wavelengths of $\lambda = 2.964h$ and $\lambda = 4.046h$, respectively. The minimum moves to larger wavelengths, with further decreasing v and disappears completely at $v = 0.25$.

Simulations[12,13] reveal elastic instabilities similar to those observed experimentally, thereby supporting the theoretical analysis. It yet seems unclear why and how the simulated patterns in two-dimensional contacts[13] break the
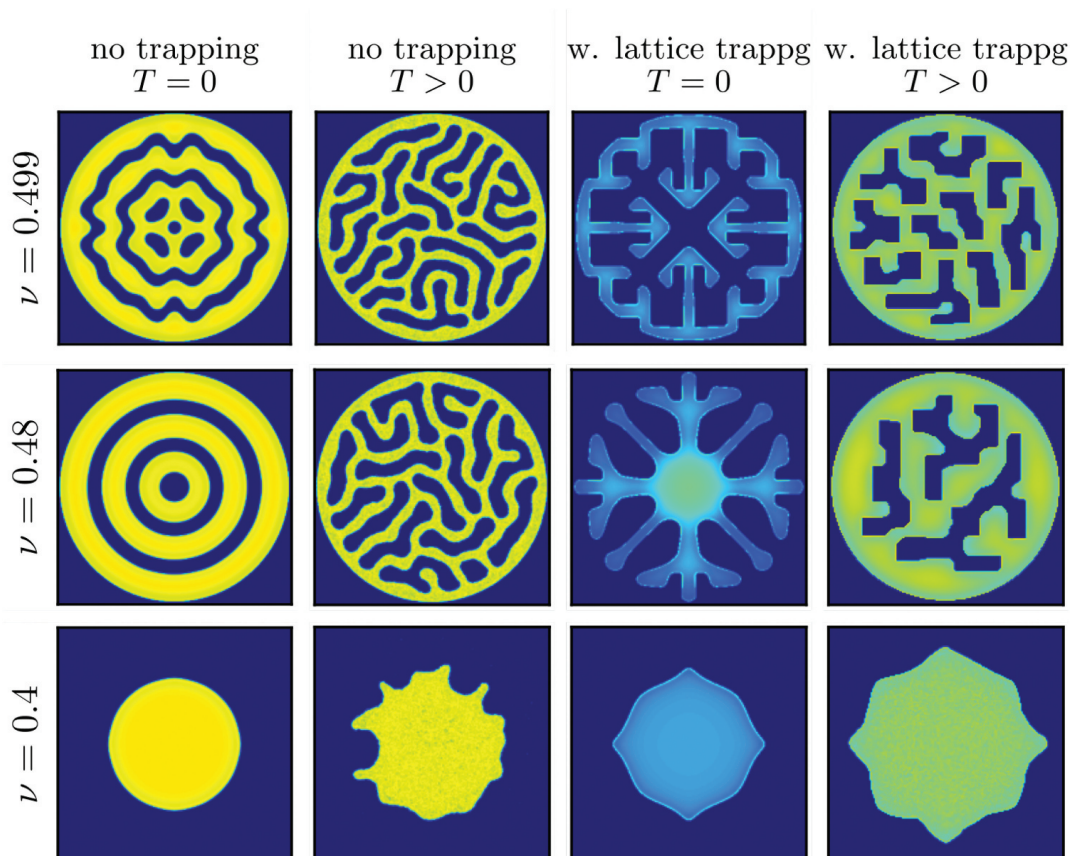
Figure 6. Stress heat maps at selected moments during detachment for a confined elastomer with reduced height $h/a = 0.06$. Bright colors indicate high stress, black represents non contact. Poisson's ratios are kept constant in each row and take the values $v = 0.499, 0.48, 0.4$ from top to bottom. Columns differ in the way how continuum mechanics is terminated at the small scale, *i. e.*, with and without thermal noise, and with and without lattice trapping.

symmetry of the mathematical problem, which has circular symmetry in the absence of discretization and periodic boundary conditions. To elucidate this issue further, we simulated the detachment process for three different Poisson's ratios using different ways in which the continuum model was terminated at small scales. Some of the most intriguing snapshots taken during detachment are compiled in Figure 6.

Every graph in a row in Figure 6 reflects the same continuum model in that v and h/a is kept constant. However, they differ in terms of their discretization – leading to or suppressing lattice trapping at small scales – and in terms of the absence or presence of random noise, which is introduced with a Langevin thermostat. Despite representing the same continuum limit, all four graphs within a row look qualitatively different with the exception of the two right panels in the bottom row, which are both singly connected contact domains with the four-fold symmetry of the discretized model.

The most highly symmetric patterns are obtained when thermal noise and lattice trapping are absent. While the $v = 0.4$ and $v = 0.48$ systems have circular symmetry, the $v = 0.499$ configuration reduces to a four-fold symmetry axis. The symmetry reduction is not due to the presence of periodic boundary conditions in our square domain but results from the discretization of the elastomer's surface into grid points forming a square lattice. We come to this conclusion because increasing the buffer between the punch and the boundary of the simulation cell does not change the point at which circular symmetry is broken. However, we observed that the rate of retraction can matter. For example, a complete loss of symmetry can occur even in the absence of thermal noise when decreasing from very small to extremely small retraction rates. Since our four-fold symmetry axis is only broken by the order in which numbers are added up, the complete loss of symmetry can only result from an accumulation of round-off errors. We suspect that a similar round-off error progression to significant digits is responsible for the low-symmetry configurations produced by Gonuguntla et al.,[13] owing to them using a highly efficient conjugate gradient minimization method and/or because computers used smaller data precision in 2006 than they do nowadays. Given our results, we predict that instability patterns assume a quasi-circular symmetry, when elastomers are retracted quickly if the original surfaces are sufficiently planar.

Switching on temperature yield configurations similar to those observed experimentally and more so for a fine discretization avoiding lattice trapping. Specifically, the snapshots shown in the "no-trapping, $T > 0$" column resemble typical experimental images[4,6–9] for $v > 0.45$ and the contact shown for $v = 0.4$ in that column is similar to that depicted in Fig. 9a of Ref.[8] for $v = 0.4$. Due to lattice trapping, the non-contact patches show $90°$ corners oriented w. r.t. the microscopic shape, similar to but substantially stronger than in the pioneering simulations by Gonuguntla et al.,[13] who thus must have also discretized their domain into squares.

In the presence of thermal noise, the width of contact and of non-contact domains is similar in size. Their combined width indeed satisfies $\lambda \approx 3h$, which is the expected wavelength for nearly incompressible elastomers introduced at the beginning of this section. However, contact generally appears broader than non-contact due to (close-to) circular symmetry. This difference might matter for a comparison between single-wavelength pen-on-paper theory and real or realistic patterns. In addition, the surface tension can shift the characteristic wavelength to larger values.[9,13]

We also analyze the effect of lattice trapping. For this phenomenon to occur, it does not matter whether the range of adhesion is decreased at fixed discretization $\Delta x = \Delta y$ or the mesh size is increased at fixed range of adhesion, as long as Δx is clearly less than typical contact and non-contact widths. Lattice
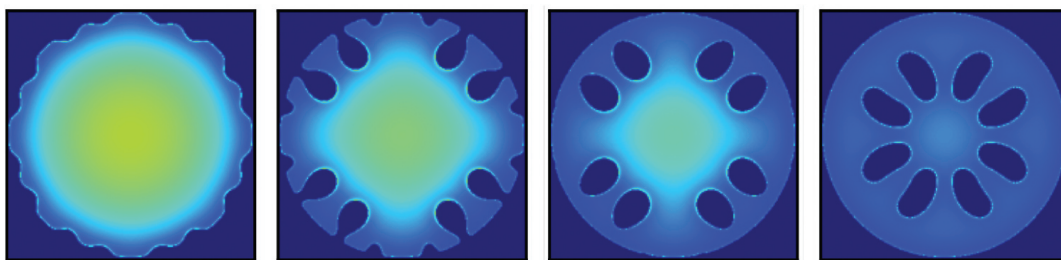
Figure 7. Stress heat maps showing the nucleation of edge cracks and their motion toward the punch center. The number of time steps between subsequent images were 9000, 2000 and 14000 from left to right.

trapping also counteracts symmetry reduction, as revealed most clearly in the bottom row of Figure 7, where thermal fluctuations are no longer strong enough to roughen the contact line during the course of the simulation. In other words, symmetry reduction can become an activated process in the case of lattice trapping whereby contact domains become thicker than non-contact regions upon retraction.

Unfortunately, our simulations do not correlate very well with some experiments regarding one aspect: for $v > 0.45$, we usually observe the nucleation of non-contact below the punch center, while experiments often find finger-shaped non-contact regions to emerge from the rim of the punch and then to move inward.[4,6–8]

Reasons for this discrepancy might be (i) the simulations ignore the effect of air pressure, which certainly favors the primary detachment to occur at the contact edge, (ii) the simulations neglect shear stress, which can be large near the contact periphery, (iii) no attempts were made to model viscoelastic effects, and (iv) the edge singularities in the normal stress are cut off too early due to a coarse discretization. Nonetheless, other experiments observed, as we did, crack nucleation in the center,[9,11,13,38] especially in cases where $h/a \ll 0.1$.

It is beyond the scope of this work to test all four hypotheses for why our non-contact domains nucleate in the centerin particular, as testing the first three does not fall into the realm of our model. However, we did investigate the fourth hypothesis by increasing the resolution from our default value to 4096×4096 for a $h/a = 0.1$ punch and $v = 0.495$ elastomer while decreasing the range of adhesion and the rate of retraction so that the ratio of local elastic stiffness and maximum curvature of the tensile potential remained constant. As a consequence, the detachment nucleates at the periphery of the contact as is revealed in Figure 7 for the fine discretization, while it nucleated in the center for the coarser simulation.

5. Summary

In this work, we combine and streamline existing approaches to the mechanics of confined elastomers interacting with a flat punch. In doing so, we identify a relatively simple, yet physically motivated expression for how the effective modulus of the confined layer, $\bar{E}$, depends on its Poisson's ratio v and the ratio of elastomer height and punch radius h/a. Using our approach, the Poisson's ratios no longer have to be close to 0.5. One consequence of this is that large confinement can be distinguished from extreme confinement, for which deviations from ideal incompressibility cannot be ignored. A central benefit of the pursued scaling ansatz is that the asymptotic dependence of $\bar{E}(h/a \to 0)$ allows the simulated pull-off force to be estimated reasonably well for any combination of v and h/a. Of course, in real-laboratory experiments, the compliance of the substrate, the indenter, or, more generally speaking, the system must be considered when deducing $\bar{E}$ in the extreme-confinement limit. Moreover, eliminating viscoelastic retardation implies (unrealistic?) requirements on the patience of experimentalists.

The central assumption of the analytical part of our study is that the elastic energy of a confined elastomer stems predominantly from surface undulations with wavelengths in the vicinity of the punch radius. This leads to a closed-form expression in Eq. (10) for $\bar{E}(h/a)$ with two parameters of order unity, whose precise value can be fixed by demanding the asymptotic limits of $h/a \to 0$ and $h/a \to \infty$ to be exactly reproduced. The pursued treatment can be repeated for boundary conditions (BCs) other than ours, which is a slip BC between the elastomer-punch interface and a stick BC for the elastomer–substrate interface. In these cases, the relation for the stiffness of the surface undulation of the wave vector q has to be derived or looked up in the literature,[11,27–29,36] *i.e.*, the replacement of Eq. (2). All remaining steps to estimate $\bar{E}(h/a)$ for other BCs can certainly be done by repeating the procedures worked out in this study. However, if both interfaces have slip boundary conditions, qualitatively different behavior ensues and other scaling relations apply than in the remaining three cases.[20,36] Investigating those is beyond the scope of this paper.

The analytical calculations are augmented with Green's function molecular dynamics (GFMD) simulations. They yield accurate reference data for the reduced elastic modulus and pull-off force as functions of reduced height and Poisson's ratios. In particular, the latter can be useful to determine experimentally the deviation of v from $v = 0.5$.

The GFMD simulations also reveal that the initiation and the formation of cracks that occur during stable crack growth depend sensitively on the way in which continuum mechanics is terminated at small scales. For example, the (effective) range of interaction can determine whether cracks initiate from the punch center or from its periphery. Moreover, if

interactions are so short ranged that lattice pinning ensues, small-scale features of the substrate, *e.g.* its crystallinity, can be reflected in the crack at coarse scales.

Acknowledgements

Disclosure statement

No potential conflict of interest was reported by the author(s).

References

[1] Gent, A. N. Fracture Mechanics of Adhesive Bonds. *Rubber Chem. Technol.* 1974, *47*(1), 202–212. DOI: 10.5254/1.3540427.

[2] Ganghoffer, J. F.; Gent, A. N. Adhesion of a Rigid Punch to a Thin Elastic Layer. *J. Adhes.* 1995, *48*(1–4), 75–84. DOI: 10.1080/00218469508028155.

[3] Hensel, R.; McMeeking, R. M.; Kossa, A. Adhesion of a Rigid Punch to a Confined Elastic Layer Revisited. *J. Adhes.* 2018, *95*(1), 44–63. DOI: 10.1080/00218464.2017.1381603.

[4] Webber, R. E.; Shull, K. R.; Roos, A.; Creton, C. Effects of Geometric Confinement on the Adhesive Debonding of Soft Elastic Solids. *Phys. Rev. E - Stat. Phys. Plasma. Fluid. Relat. Interdiscip. Top.* 2003, *68*(2), 11.

[5] Shull, K. R.; Ahn, D.; Chen, W.-L.; Flanigan, C. M.; Crosby, A. J. Axisymmetric Adhesion Tests of Soft Materials. *Macromol. Chem. Phys.* 1998, *199*(4), 489–511. DOI: 10.1002/(SICI)1521-3935(19980401)199:4<489::AID-MACP489>3.0.CO;2-A.

[6] Crosby, A. J.; Shull, K. R.; Lakrout, H.; Creton, C. Deformation and Failure Modes of Adhesively Bonded Elastic Layers. *J. Appl. Phys.* 2000, *88*(5), 2956–2966. DOI: 10.1063/1.1288017.

[7] Shull, K. R.; Flanigan, C. M.; Crosby, A. J. Fingering Instabilities of Confined Elastic Layers in Tension. *Phys. Rev. Lett.* 2000, *84*(14), 3057–3060. DOI: 10.1103/PhysRevLett.84.3057.

[8] Shull, K. R.; Creton, C. Deformation Behavior of Thin, Compliant Layers under Tensile Loading Conditions. *J. Polym. Sci. Part B Polym. Phys.* 2004, *42*(22), 4023–4043. DOI: 10.1002/polb.20258.

[9] Ghatak, A.; Chaudhury, M. K. Adhesion-induced Instability Patterns in Thin Confined Elastic Film. *Langmuir.* 2003, *19*(7), 2621–2631. DOI: 10.1021/la026932t.

[10] Sharma, A.; Ghatak, A.; Chaudhury, M.; Shenoy, V. Meniscus Instability in a Thin Elastic Film. *Phys. Rev. Lett.* 2000, *85*(20), 4329–4332. DOI: 10.1103/PhysRevLett.85.4329.

[11] Mönch, W.; Herminghaus, S. Elastic Instability of Rubber Films between Solid Bodies. *Europhys. Lett.* 2001, *53*(4), 525–531. DOI: 10.1209/epl/i2001-00184-7.

[12] Sarkar, J.; Shenoy, V.; Sharma, A. Patterns, Forces, and Metastable Pathways in Debonding of Elastic Films. *Phys. Rev. Lett.* 2004, *93*(1), 1457–1469. DOI: 10.1103/PhysRevLett.93.018302.

[13] Gonuguntla, M.; Sharma, A.; Sarkar, J.; Subramanian, S. A.; Ghosh, M., and Shenoy, V. Contact Instability in Adhesion and Debonding of Thin Elastic Films. *Phys. Rev. Lett.* 2006, *97*(1 018303).

[14] Sneddon, I. N. The Relation between Load and Penetration in the Axisymmetric Boussinesq Problem for a Punch of Arbitrary Profile. *Int. J. Eng. Sci.* 1965, *3*(1), 47–57. DOI: 10.1016/0020-7225(65)90019-4.

[15] Kendall, K. The Adhesion and Surface Energy of Elastic Solids. *J. Phys. D: Appl. Phys.* 1971, *4*(8), 1186–1195. DOI: 10.1088/0022-3727/4/8/320.

[16] Chung, J. Y.; Chaudhury, M. K. Soft and Hard Adhesion. *J. Adhes.* 2005, *81*(10–11), 1119–1145. DOI: 10.1080/00218460500310887.

[17] Lindsey, G. H.; Schapery, R. A.; Williams, S. M. L.; Zak, A. R. The Triaxial Tension Failure of Viscoelastic Materials. Technical Report 63–152, Aerospace Research Laboratories, 1963.

[18] Lindsey, G. H. Triaxial Fracture Studies. *J. Appl. Phys.* 1967, *38*(12), 4843–4852. DOI: 10.1063/1.1709232.

[19] Lai, Y. H.; Dillard, D. A.; Thornton, J. S. The Effect of Compressibility on the Stress Distributions in Thin Elastomeric Blocks and Annular Bushings. *J. Appl. Mech. Trans. ASME.* 1992, *59*(4), 902–908. DOI: 10.1115/1.2894059.

[20] Lin, Y. Y.; Hui, C. Y.; Conway, H. D. Detailed Elastic Analysis of the Flat Punch (Tack) Test for Pressure-sensitive Adhesives. *J. Polym. Sci. Part B Polym. Phys.* 2000, *38*(21), 2769–2784. DOI: 10.1002/1099-0488(20001101)38:21<2769::AID-POLB60>3.0.CO;2-J.

[21] Sarkar, J.; Sharma, A.; Shenoy, V. Adhesion and Debonding of Soft Elastic Films: Crack Patterns, Metastable Pathways, and Forces. *Langmuir.* 2005, *21*(4), 1457–1469. DOI: 10.1021/la048061o.

[22] Menga, N.; Afferrante, L.; Carbone, G. Effect of Thickness and Boundary Conditions on the Behavior of Viscoelastic Layers in Sliding Contact with Wavy Profiles. *J. Mech. Phys. Sol.* 2016, *95*, 517–529. DOI: 10.1016/j.jmps.2016.06.009.

[23] Menga, N. Rough Frictional Contact of Elastic Thin Layers: The Effect of Geometrical Coupling. *Int. J. Solids Struct.* 2019, *164*, 212–220. DOI: 10.1016/j.ijsolstr.2019.01.005.

[24] Menga, N.; Carbone, G., and Dini, D. Exploring the Effect of Geometric Coupling on Friction and Energy Dissipation in Rough Contacts of Elastic and Viscoelastic Coatings. *J. Mech. Phys. Sol.* 2021, *148* 104273 .

[25] Shenoy, V.; Sharma, A. Stability of a Thin Solid Film with Interactions, 2000. arXiv: cond-mat/0005324.

[26] Campañá, C.; Müser, M. H. Practical Green's Function Approach to the Simulation of Elastic Semi-infinite Solids. *Phys. Rev. B.* aug 2006, *74*(7), 075420. DOI: 10.1103/PhysRevB.74.075420.

[27] Carbone, G.; Mangialardi, L. Analysis of the Adhesive Contact of Confined Layers by Using a Green's Function Approach. *J. Mech. Phys. Solids.* 2008, *56*(2), 684–706. DOI: 10.1016/j.jmps.2007.05.009.

[28] Greenwood, J. A.; Barber, J. R. Indentation of an Elastic Layer by a Rigid Cylinder. *Int. J. Solids Struct.* 2012, *49*(21), 2962–2977. DOI: 10.1016/j.ijsolstr.2012.05.036.

[29] Venugopalan, S. P.; Nicola, L.; Müser, M. H. Green's Function Molecular Dynamics: Including Finite Heights, Shear, and Body Fields. *Model. Simul. Mater. Sci. Eng.* 2017, *25* (3), 0–13. DOI: 10.1088/1361-651X/aa606b.

[30] Bitzek, E.; Koskinen, P.; Gähler, F.; Moseler, M.; Gumbsch, P. Structural Relaxation Made Simple. *Phys. Rev. Lett.* 2006, *97*(17). DOI: 10.1103/PhysRevLett.97.170201.

[31] Zhou, Y.; Moseler, M.; Müser, M. H. Solution of Boundary-element Problems Using the Fast-inertial-relaxation-engine Method. *Phys. Rev. B.* 2019, *99*(14), 144103. DOI: 10.1103/PhysRevB.99.144103.

[32] Wang, A.; Zhou, Y.; Müser, M. Modeling Adhesive Hysteresis. *Lubricants*. 2021, *9:17*, 02.

[33] Zhou, Y.; Wang, A.; Müser, M. How Thermal Fluctuations Affect Hard-wall Repulsion and Thereby Hertzian Contact Mechanics. *Front. Mech. Eng.* 2019, *5:67*, 12.

[34] Müser, M. H. Single-asperity Contact Mechanics with Positive and Negative Work of Adhesion: Influence of Finite-range Interactions and a Continuum Description for the Squeeze-out of Wetting Fluids. *Beilstein J. Nanotechnol.* apr, 2014, *5*, 419–437. DOI: 10.3762/bjnano.5.50.

[35] Gent, A. N. Compression of Rubber Blocks. *Rubber Chem. Technol.* 1994, *67*(3), 549–558. DOI: 10.5254/1.3538691.

[36] Yang, F.; Zhang, X.; Li, J. C. M. Adhesive Contact between a Rigid Sticky Sphere and an Elastic Half Space. *Langmuir*. feb 2001, *17*(3), 716–719. DOI: 10.1021/la0006162.

[37] Tizard, G. A.; Dillard, D. A.; Norris, A. W.; Shephard, N. Development of a High Precision Method to Characterize Poisson's Ratios of Encapsulant Gels Using a Flat Disk Configuration. *Exp. Mech.* 2012, *52*(9), 1397–1405. DOI: 10.1007/s11340-011-9589-6.

[38] Samri, M.; Kossa, A.; Hensel, R. Effect of Subsurface Microstructures on Adhesion of Highly Confined Elastic Films. *J. Appl. Mech. Trans. ASME*. 2021, *88*(3), 1–9. DOI: 10.1115/1.4049182.

[39] Müller, A.; Wapler, M. C.; Wallrabe, U. A Quick and Accurate Method to Determine the Poisson's Ratio and the Coefficient of Thermal Expansion of PDMS. *Soft Matter*. 2019, *15*(4), 779–784. DOI: 10.1039/C8SM02105H.

II Film-terminated fibrillar microstructures

Permission

Contributions of co-authors

Gabriela Moreira Lana: conceptualization, experimental investigation, writing–original draft
Xuan Zhang: conceptualization, investigation: FEM simulations, writing–original draft
Christian Müller: formal analysis, writing–original draft
René Hensel: conceptualization, supervision, writing–review & editing
Eduard Arzt: conceptualization, supervision, writing–review & editing

The study was conceptualized by G.M.L., X.Z., R.H. and E.A. to better understand the influence of topography on the stickiness of soft skin adhesives (SSA) [196].

G.M.L. was responsible for specimen fabrication, adhesion measurements and microscopy. FEM simulations were set up, run and evaluated by X.Z. C.M. analyzed the surface height spectra and developed the approximate linear elastic model in the discussion section of the article. He acknowledges valuable input from Martin H. Müser and Lars Pastewka.

An early version of the manuscript was prepared by G.M.L. and X.Z. and discussed with E.A. and R.H., after which the scope of the study was adjusted and C.M. was added to the project. The draft was then rewritten and extended by G.M.L., X.Z. and C.M. and continuously discussed and revised together with E.A. and R.H. Everyone agreed on the publication of the article in ACS Applied Materials & Interfaces and its inclusion in this thesis.
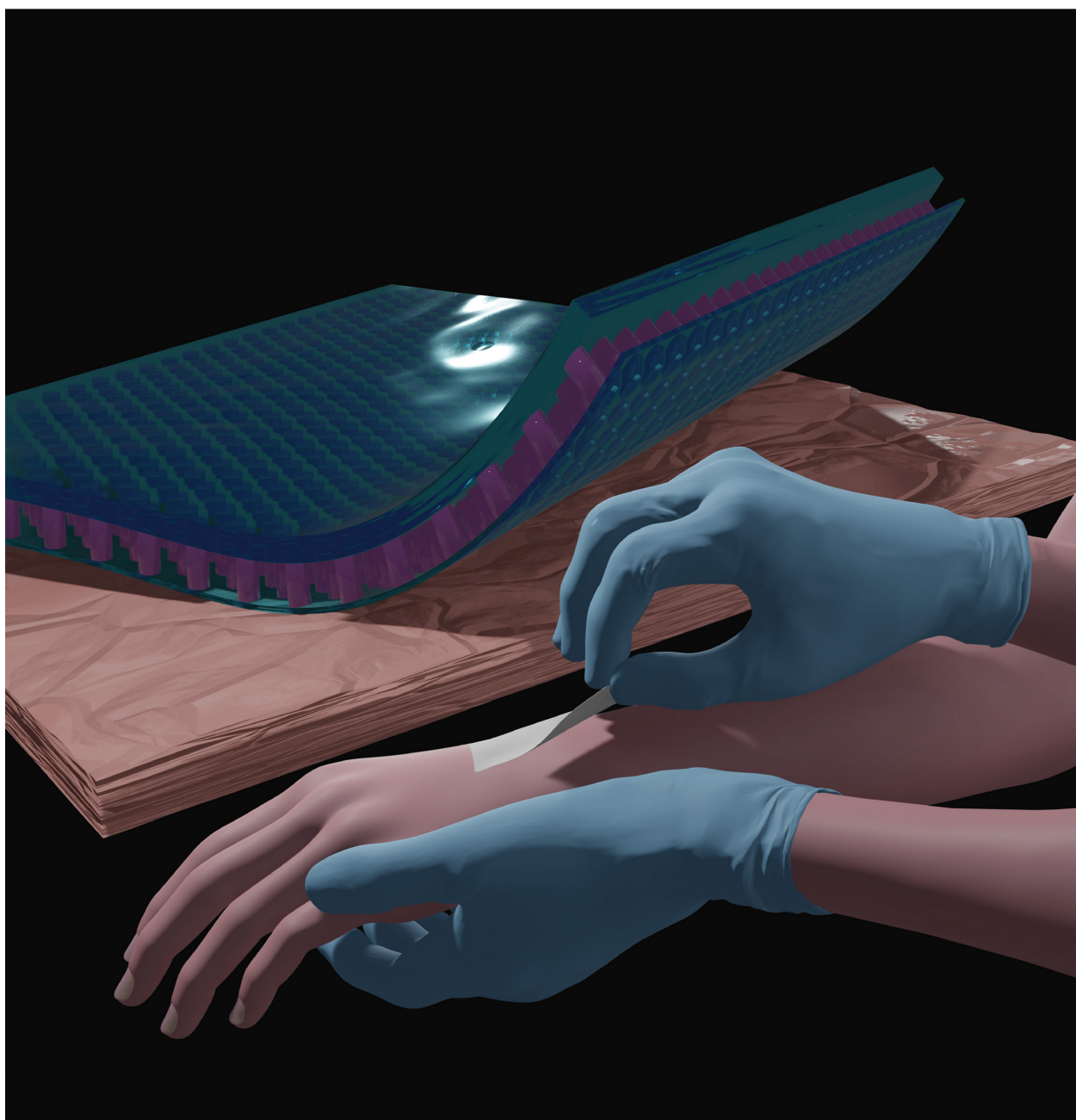
Research Article

Film-Terminated Fibrillar Microstructures with Improved Adhesion on Skin-like Surfaces

Gabriela Moreira Lana, Xuan Zhang, Christian Müller, René Hensel, and Eduard Arzt*

Cite This: *ACS Appl. Mater. Interfaces* 2022, 14, 46239−46251

Read Online

ACCESS | Metrics & More | Article Recommendations

ABSTRACT: Adhesives for interaction with human skin and tissues are needed for multiple applications. Micropatterned dry adhesives are potential candidates, allowing for a conformal contact and glue-free adhesion based on van der Waals interactions. In this study, we investigate the superior adhesion of film-terminated fibrillar microstructures (fibril diameter, 60 μm; aspect ratio, 3) in contact with surfaces of skin-like roughness (R_z 50 μm). Adhesion decays only moderately with increasing roughness, in contrast to unstructured samples. Sinusoidal model surfaces adhere when their wavelengths exceed about four fibril diameters. The film-terminated microstructure exhibits a saturation of the compressive force during application, implying a pressure safety regime protecting delicate counter surfaces. Applications of this novel adhesive concept are foreseen in the fields of wearable electronics and wound dressing.

KEYWORDS: skin adhesives, bioinspired structures, soft layer, dry adhesion, roughness
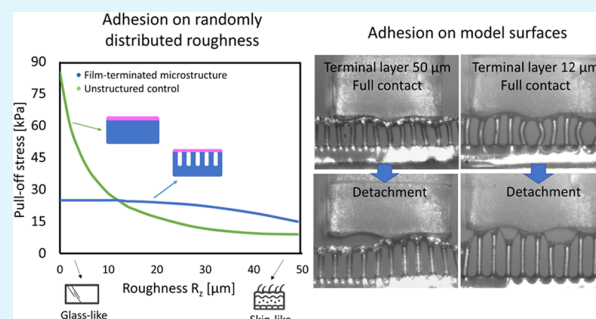
1. INTRODUCTION

Skin-attachable adhesives are experiencing rising demands in healthcare, where potential applications range from flexible and wearable electronics for monitoring and diagnosing biological signals[1−3] to therapeutic devices and wound dressings.[4,5] Biological surfaces and tissues are challenging counter surfaces to stick to, as surface roughness is one key factor for reduced adhesion.[1] This is primarily due to the difficulty of achieving fully conformal contact, which decreases the real contact area and causes heterogeneous stress distributions at the interface.[6] Roughness requires high local deformations and hence counteracts the short-range adhesive molecular forces.[7,8] As a consequence, new adhesives for reliable yet delicate interaction with skin-like surfaces are urgently required.

The efficiency and versatility of several attachment systems in nature, e.g., in geckos, beetles, spiders, or snails, have been a source of inspiration to material scientists and engineers: in many cases, their outstanding locomotion and clinging ability, to various smooth and rough surfaces, are due to patterned micro- and nanostructures on their contact organs. The bioinspired microfibrillar patterns derived from these examples have been widely studied in the past few years.[9−11] More recently, they have proven to be potential candidates as dry and glue-free adhesives to skin. Current solutions for skin adhesives offer too strong adhesion causing damage while being removed,[12,13] in addition to being of single use and leaving residues that can cause skin irritation and allergies.

Therefore, a reliable adhesive with sensitive detachment is needed.[14,15]

Dry adhesion is mediated by conformal contact, enhanced by a low effective elastic modulus, and Van der Waals (vdW) interactions, both of which contribute to useful adhesion even to rough surfaces.[16−19] For skin applications, a film-terminated design was proposed, which modifies the microfibril array by adding a continuous terminal layer made of softer material. This modified microstructure has shown enhanced adhesion by modulating the interfacial stresses and generating a crack trapping mechanism; the result is an interesting synergy between the subsurface microstructure and the soft, thin terminal layer.[19−22] The added layer also performs auxiliary functions: in wound dressings, it can aid in the closure of the wound; and in the treatment of eardrum perforations, it closes the fissure in the membrane, which is important to block pathogens from entering the middle ear during the treatment.[5,23]

As the largest organ in humans, the skin presents an especially complex topography, which can vary over several
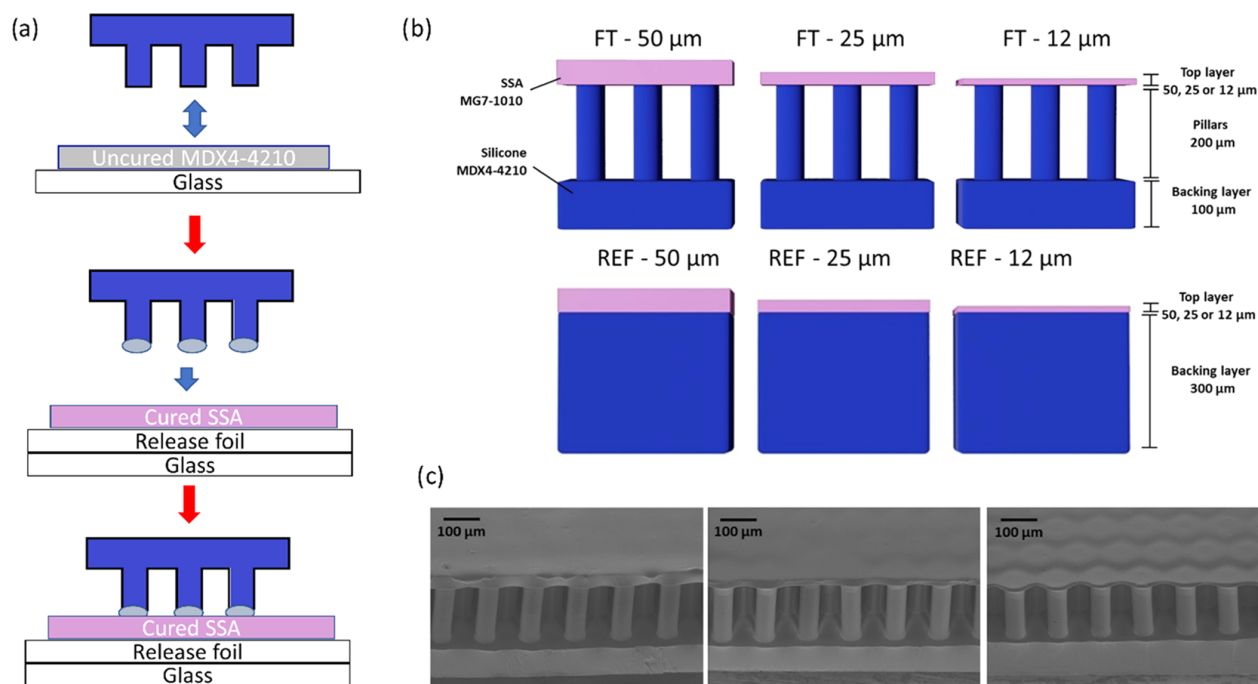
Figure 1. Film-terminated microfibrillar samples. (a) Representation of the film-terminated microstructure fabrication process by integrating an SSA film with a microfibril sample. The tips of the fibrils are dipped in an uncured film and then placed on a cured SSA layer. (b) Schematic cross section of a soft skin adhesive (SSA) film (pink) terminating a silicone microfibrillar array of MDX4-4210 (blue) and of the unstructured control samples. The terminating film has various thicknesses of 12, 25, and 50 μm. (c) Representative scanning electron micrographs of the different samples.

orders of magnitude. The detailed structure depends on many factors, such as body location, age, and humidity.[24−26] Explicit studies that take into account the roughness of skin when optimizing skin adhesives have rarely been published in the literature.

In this paper, we aim to investigate the adhesion mechanism of novel film-terminated microstructures designed to adhere specifically to rough skin without the need for chemical glues, thus not leaving residues on the surface or causing adverse reactions. We conduct a systematic investigation of such microstructures, consisting of two biomedical silicones, on a series of surfaces with random and single-wavelength roughness. Adhesion is analyzed in comparison to unstructured films as control samples. We evaluate experimentally and numerically the effect of the terminal layer thickness and the role of the fibrillar microstructure on the adhesion performance. In this way, we provide a scientific base for this new class of micropatterned skin adhesives.

2. EXPERIMENTAL SECTION

2.1. Fabrication of Film-Terminated and Control Samples. Film-terminated microstructures were fabricated, and the respective unstructured samples with the terminal layer were used as a control to investigate the effect of the subsurface microstructure on adhesion.

Arrays with fibrils of nominal height of 180 μm and diameter of 60 μm (aspect ratio 3) were fabricated by replica molding. The fibrils were arranged hexagonally with center-to-center distances of 120 μm (surface density approximately 23%). A silicon master template (Institute of Semiconductors and Microsystems, TU Dresden, Germany) was used to prepare the negative silicone mold (Elastosil M4601 A/B silicone, Wacker Chemie AG, Munich, Germany). The prepolymer was mixed (ratio 9:1) and poured on the master template. The silicone was then cured in an oven at 75 °C for 3 h. The silicone

mold was treated by air plasma (Atto low pressure plasma system, Electronic Diener, Ebhausen, Germany) for 3 min and then coated with tridecafluoro-1,1,2,2-tetrahydrooctyl-trichlorosilane (AB111444, ABCR, Karlsruhe, Germany) through vapor deposition at 3 mbar for 45 min. The microfibrillar array was made from the biomedical-grade elastomer MDX4-4210 (Dow Silicones, Midland, Michigan). The prepolymer was mixed in a ratio of 10:1, poured on the Elastosil mold, and degassed for 5 min. The mold was then spun at 3000 rpm for 2 min (Spincoater Laurel l WS 650 MZ-23NPPB, North Wales, Pennsylvania) and then placed on a glass substrate, which was previously plasma-treated and coated with MDX4 silicone (3000 rpm for 2 min). The whole set was placed in an oven at 95 °C for 1 h. Finally, the mold and the glass were gently demolded. For the unstructured control samples, a foil of the MDX4-4210 was prepared by spin coating at 500 rpm for 2 min to achieve a thickness comparable to the sum of the backing layer and fibril height for the fibrillar microstructure.

In the second step, the microfibrillar array, or the respective flat film, was film-terminated. Accordingly, a soft skin adhesive film, SSA MG7-1010 (Dow Silicones, Midland, Michigan), was used. Previous reports use a softer material by changing the mixing ratio of the "stiffer" silicone.[27,28] However, this approach makes the product unsuitable for medical applications, as the manufacturer does not predict the reactivity and curing conditions, being, therefore, not medically certified. The SSA was coated on a release foil (Siliconature, SILFLU S 75 M 1R88002 clear) at 800, 2000, and 6000 rpm. The SSA layer was cured at 95 °C for 1 h. To combine the microfibrillar array with the SSA layer, fibril tips were dipped in an uncured MDX4-4210 layer (spun on a glass substrate at 400 rpm) and placed on the cured SSA film. The unstructured control sample was terminated using the same method, dipping the film in an uncured MDX4 layer before placing it on the cured SSA layer. Upon curing in an oven at 95 °C for 1 h, the final specimen was peeled from the release foil. The fibril height increased from 180 to 200 μm (and the aspect ratio from 3 to 3.3) due to the fabrication described above. Considering
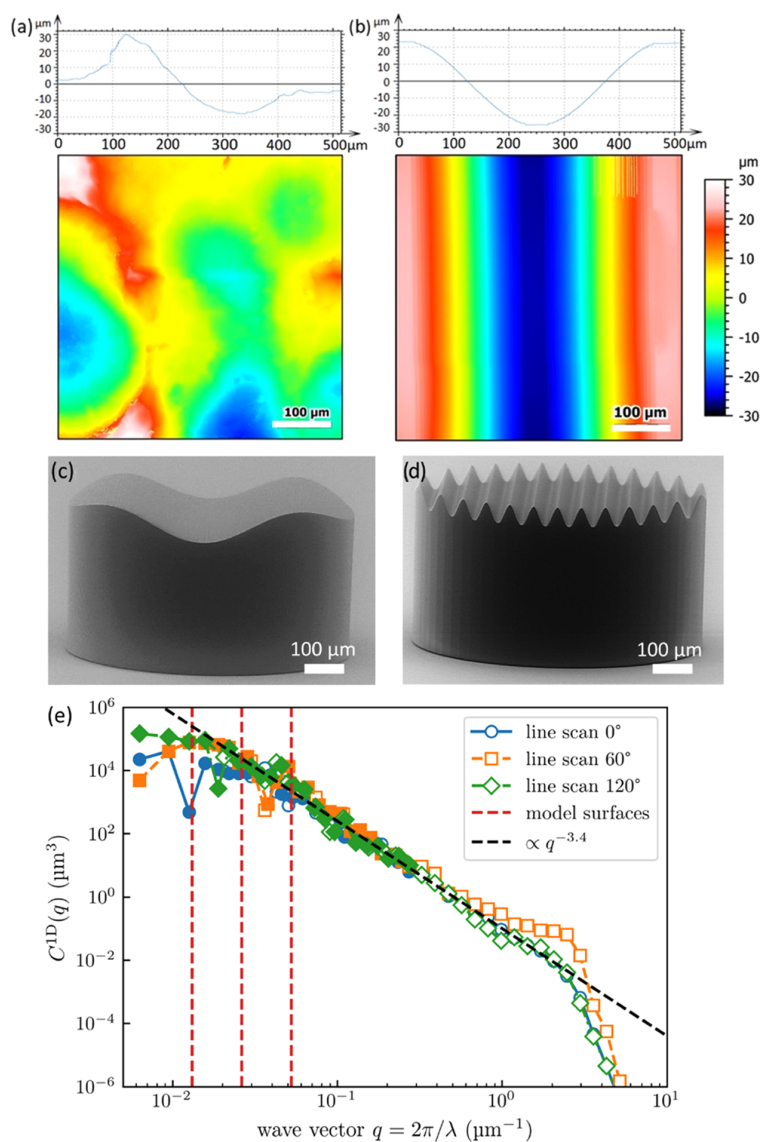
Figure 2. Surface profile and topography of counter surfaces. (a) Scan of skin-like rough surface, in comparison to (b) sinusoidal model surface with 480 μm wavelength. (c) and (d) SEM micrographs of the printed surfaces with the sinusoidal model surface of wavelengths 480 μm and 60 μm, respectively. (e) Power spectral density (PSD) of the Vitro-Skin surface, determined from line scans along different surface directions. Solid markers indicate reliable data, while empty markers indicate unreliable data as limited by the tip radius.[34] The isotropic one-dimensional PSD (C^{1D}) is defined as given in ref 35. The dashed vertical red lines represent the wavelengths of the model surfaces.

biomedical applications, only certified medical products MDX4-4210 and MG7-1010 were used.

Specimens were characterized using an optical microscope (Eclipse LV100ND, Nikon, Tokyo, Japan) and a scanning electron microscope (FEI Quanta 400 ESEM, Thermo Fisher). The specimens were analyzed under low vacuum at 100 Pa and 10 kV voltage for the latter.

Figure 1a presents a summary of the fabrication process of the film-terminated microstructure. The fibrils are fabricated by replica molding and yield precise copies by a relatively inexpensive method. Unlike simple porosity, the fibrils offer an additional advantage of a controlled, periodic structure suitable for subsequent integration of other systems. The cross sections of the film-terminated and respective control samples are illustrated in Figure 1b. The MDX4-4210 fibrillar array (in blue) consisted of a 100 μm backing layer and fibril arrays of 200 μm height and 60 μm diameter, and the SSA MG7-1010 terminating layer (in pink) varied in thickness of 12, 25, and 50 μm. The chosen materials are medically certified for wound dressings

and implantable devices, widening the possibility of application of these microstructured adhesives for different purposes, including wound dressings. For brevity, we denote the samples according to their terminal layer thickness, for instance, FT—12 μm for the film-terminated microstructure with a 12 μm thick terminal layer. The respective unstructured reference samples were fabricated with the MDX4-4210 backing layer of 300 μm and the terminal layer equivalent to the microstructures (12, 25, or 50 μm thickness). In addition, microfibrils without thin film as the terminal layer were also used for control measurements. Scanning electron microscopy (SEM) images of different samples are presented from 45° tilt side view (Figure 1c). We observe that the thinnest film is slightly deformed due to stress relaxation.

2.2. Rheometry. Frequency-dependent storage and loss moduli (G', G'') and the damping factor tan $\delta = G''/G'$ of the polymers were determined using a rheometer (Physica MCR-300, Anton Paar, Graz, Austria) equipped with a cone/plate setup (diameter, 25 mm; gap
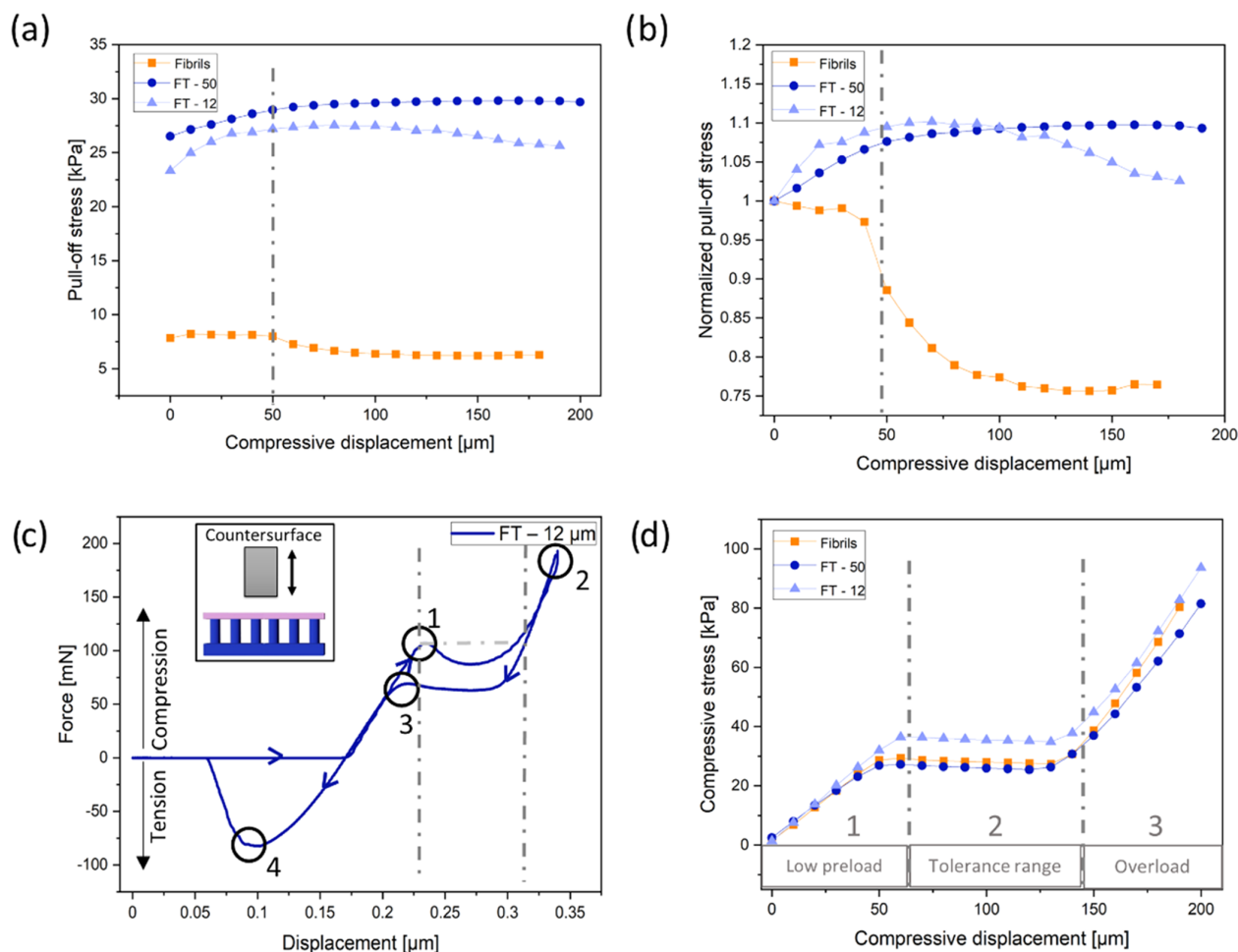
Figure 3. Results of adhesion tests against a smooth epoxy surface. (a) Pull-off stress and (b) normalized pull-off stress (by the pull-off stress at zero compression) as a function of maximum compressive displacement for film-terminated (FT) microfibrils (blue) in comparison to nonterminated fibrillar arrays (orange). The dashed-dotted line indicates the onset of fibril buckling. (c) Force vs displacement display of measurement of the film-terminated sample with 12 μm thick film and a schematic representation of the measurement principle. Points highlight fibril buckling (1), maximum compression (2), unbuckling of fibrils (3), and maximum pull-off force (4). (d) Compressive stress as a function of compressive displacement. Dashed-dotted lines mark three regimes: (1) low preload, (2) compression-tolerant regime, and (3) overload regime, and correspond to the lines in panel (c).

height, 0.054 mm). The prepolymer mixture of components A and B (in a mixing ratio of 10:1 for MDX4-4210 and 1:1 for the SSA) was placed on the device. The polymer was cured between the plates at 90 °C for 30 min. Upon cooling to 25 °C, a frequency sweep measurement from 0.01 to 100 Hz at a constant amplitude of 0.1% was carried out.

The Young's modulus, E, for both materials was calculated from the measured storage modulus in shear, G, considering $E = 2G\,(1 + \nu)$, with $\nu = 0.5$. The elastic modulus values obtained were $E_{MDX4\text{-}4210} = 1.01$ MPa and $E_{SSA} = 0.102$ MPa. Overall, the terminating film was made from softer silicone than the microfibrillar array.

2.3. Adhesion Measurements. Probe tack tests, in which a flat probe is retracted from the adhesive in the perpendicular direction, were performed using a custom-built adhesion testing device.[16,29] Specimens and the counter surface were approached at a rate of 30 μm/s until a predetermined compressive preload or displacement was reached. Contact was held for 1 s, followed by retraction at a rate of 10 μm/s. Measurements were performed at three different positions on each surface. Mean values and standard deviation (error bars) were reported. Counter surfaces were always smaller than specimens; therefore, stresses were calculated by dividing force values by the area of the counter surface. All surfaces were made from epoxy (Résine

Epoxy R123, Soloplast-Vosschemie, Fontail-Cornillon, France), as described in previous reports,[30,31] to keep surface chemistry constant. Epoxy replicas were made from smooth and frosted glass slides (Marienfeld, Lauda Königshofen, Germany) and the front and back sides of Vitro-Skin foil (IMS inc., Portland, ME). Vitro-Skin foil was chosen as it mimics the topography of the human skin.[32,33]

A contour map of the skin-like surface and a cross-sectional profile are depicted in Figure 2a. It presents arithmetic roughness (R_a) of 9.48 μm and a peak-to-valley distance of ~50 μm in accordance with the statistical value $R_z = 50$ μm. Adhesion to such high roughness has not yet been described in the literature; for the film-terminated microstructure, adhesion has only been reported in the literature against the roughness of maximal R_a 2.3 μm.[20] A sinusoidal model surface of wavelength 480 μm is depicted in Figure 2b. The surfaces were imaged using a confocal microscope (MarSurf CM explorer, 50× objective, Mahr, Göttingen, Germany). At a constant peak-to-valley distance of 50 μm, corresponding to the skin-like surface, the following different wavelengths were chosen: $\lambda = 480$, 240, 120, and 60 μm. The model surfaces were fabricated using two-photon lithography (Photonic Professional GT2, Nanoscribe, Eggenstein−Leopoldshafen, Germany). SEM images of the printed sinusoidal model surfaces are presented in Figure 2c,d.
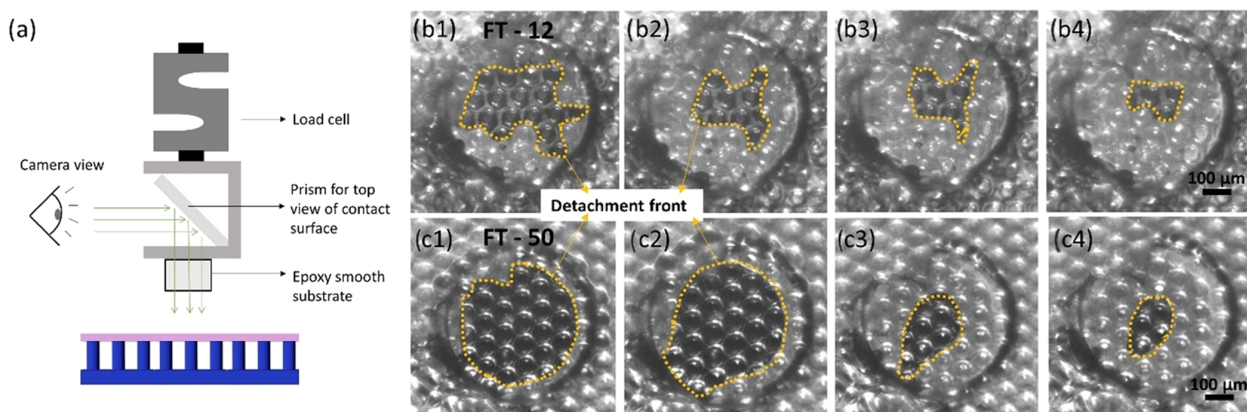
Figure 4. Contact surface imaging during detachment from the smooth surface. (a) Schematic representation of the experimental setup, in which a prism for observation of the contact surface is mounted on the load cell. (b) Screenshots of the contact surface of FT—12 (above) and FT—50 (below) against a smooth surface during detachment (left to right). The detachment front is highlighted by the yellow dotted line.

To rationalize the choice of model surface wavelengths, we analyzed the Vitro-Skin topography using a profilometer (SURFCOM 1500SDS, ACCTee Software, Ostfildern, Deutschland) with a tip of 2 μm diameter and a measuring speed of 0.3 mm/s and characterized by the surface topography analyzer.[35] The corresponding power spectral density (PSD) is shown in Figure 2e, where the reliability of data points was explicitly determined from the curvature of the profilometer's tip radius.[34] Since line scans along different directions look very similar, the surface can be considered isotropic. Assuming a self-affine fractal topography, the slope of the curve would suggest a Hurst exponent of approximately 1.2, outside the range of $[0,1]$, indicating that the surface is not in fact fractal. Recently, Gujrati et al. connected an exponent of −4 in the PSD to macroscopic patterns in surface coatings.[36] The exponent −3.4 could indicate the presence of similar features overlapping with a self-affine power law. Regardless of the exact interpretation, a decrease with a large exponent equivalent to $H > 0.5$ still indicates that long wavelength features within this range have a much more significant influence on contact mechanics than short wavelength features.[37] The sinusoidal model surfaces are chosen close to the roll-off point on the left end of the spectrum, where the graph transitions from the power law behavior to being almost constant. This range is decisive for the elastic energy to contact nominally flat surfaces, as we use in normal tack tests. This condition for the choice of the model surface is explained in more detail in Section 4.3.

2.4. Finite-Element Analysis (FEA). Finite-element analyses (FEA) were carried out using Abaqus (Dassault Systems, Simulia Corporation, RI).[38] The two-dimensional model consisted of an elastic film-terminated sample meshed with a CPS4R element and a rigid sinusoidal surface meshed with R2D2 elements. The dimensions of the model remained the same as in the experiments (all dimensions are normalized by the fibril diameter of 60 μm), i.e., fibril height = 3, center-to-center distance = 2, terminal layer thicknesses = 1/5 or 5/6, sinusoidal amplitude = 5/6, and wavelengths = 4 and 8, separately. Both fibrils and the terminating film were modeled as incompressible neo-Hookean elastic solids with Young's moduli of 1.1 and 0.102 MPa, respectively. Two relative configurations of the fibrils and sinusoidal surface were considered: fibrils were either centered on the maxima or shifted by 60 μm. The interaction property between the film-terminated sample and the wavy surface was defined as "hard contact" for normal contact and "friction with penalty" for tangential contact. To avoid slippage after the contact, the penalty coefficient μ was set to 0.5, corresponding to the friction coefficient in the Coulomb friction law, $\tau_{fric} = \mu P$, where P is the normal contact pressure between the contacting surfaces. The step "dynamic, implicit" was used to calculate the actual deformation by uniaxial loading, during which only the vertical displacement of the top surface of the backing layer was set while other translational degrees of freedom were fixed to mimic the constraint of the backing layer in the experimental sample.

3. RESULTS

3.1. Adhesion to Smooth Counter Surfaces. Figure 3 shows a summary of adhesion results of the FT—12 μm, FT—50 μm, and fibril samples without the terminal layer against a smooth flat epoxy surface. In Figure 3a, the adhesion of the FT samples ranged between 24 and 30 kPa, which was 3−5 times larger than samples without a terminating layer. The FT—50 μm sample consistently led to a higher pull-off stress than that of the FT—12 μm sample, which could be attributed to the vastly reduced influence of the much stiffer fibrils in comparison to the terminal layer.

Compressive load is an important factor for adhesion to achieve optimal contact with the counter surface.[39] We observe that the microfibrils without terminating film exhibited a substantial reduction in adhesion at about 50 μm maximum compressive displacement (dashed-dotted line). This reduction is even clearer in Figure 3b, where the pull-off stress was normalized by its value at zero compression. The initial buckling position (point 1) is shown in an example of force−displacement curve on the FT—12 μm sample in Figure 3c; located at a compression displacement at 50 μm, it corresponds to the position with the large drop in adhesion in Figure 3b. After buckling, the decrease of the compressive force is attributed to the postbuckling instability.[40,41] When the deformed fibrils topple over and contact the backing layer, the compressive load increases again until the maximum compressive load is reached (point 2). Point 3 in the graph marks the elastic recovery of the buckled fibrils. The hysteresis between points 1 and 3 can most likely be attributed to viscoelastic properties of the materials. Finally, detachment occurred, and the pull-off force was obtained from the maximum in the tensile force (point 4).

The evaluation of the compressive load in terms of the maximum compressive displacement is depicted in Figure 3d. Three regimes can be identified: a low preload, a force tolerant, and an overload regime. In the first regime, the pull-off force increases linearly with increasing displacement; the force saturates in regime 2, where the compressive force is insensitive to the displacement; and in regime 3, the
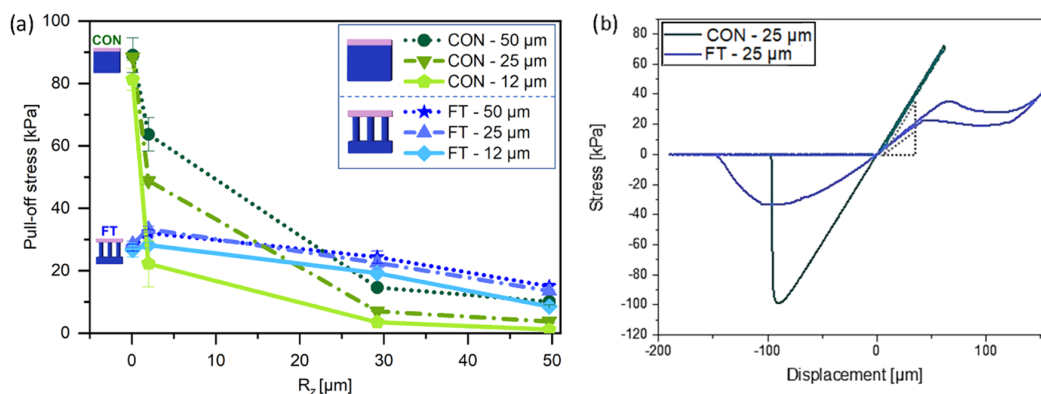
Figure 5. Adhesion against rough surfaces. (a) Pull-off stress of the film-terminated microstructure and control samples, as a function of roughness R_z of the counter surface, from smooth (R_z = 0. 1 μm) to skin-like roughness (R_z = 50 μm) at a preload of 10 kPa and a hold time of 1 s. (b) Example of stress–displacement curve of FT—25 μm and of reference CON—25 μm, subjected to a larger compressive preload.

compressive force increases linearly again with a higher slope, indicating densification of the fully compressed fibrils.

The experimental setup, as well as the detachment process of the film-terminated structure from the smooth epoxy surface, can be seen in Figure 4. The large circular margin in Figure 4b illustrates the surface position and darker regions enclosed by the dashed lines represent the edge of the contact area. The crack initiates from the edge of the counter surface and moves inward for both samples. The crack path (dashed lines) is more tortuous for the thinner backing layer (FT—12 μm) and reflects the underlying fibrillar structure.

3.2. Adhesion Results to Surfaces with Random Roughness. Next, adhesion tests on randomly rough surfaces were conducted to investigate the advantage of the terminal layer design. Figure 5a shows the pull-off stress in terms of the surface roughness R_z (mean peak-to valley distance) ranging from 0.1 to 50 μm. The pull-off stresses for the FT samples with different terminal layer thicknesses are all located between 25 and 30 kPa for the smoothest surface (R_z = 0.1 μm). Under the same measurement conditions, the effect of the terminal layer thickness is not distinguishable. The unstructured control samples, on the other hand, present pull-off stresses between 80 and 90 kPa, up to 3 times higher than the microstructure. In Figure 5b, examples of stress−displacement curves for the microstructured FT—25 sample and the respective unstructured control are presented.

As the roughness R_z was increased to 1.1 μm, we observed a slight increase of pull-off stress for the microstructured samples, more pronounced for the samples FT—50 and FT—25 (27 and 28 kPa to 32 and 33 kPa, respectively) than for FT—12 (26−28 kPa). The control samples, on the other hand, showed a reduction in pull-off stress (88−64 kPa for FT—50 and 81−22 kPa for FT—12).

Further increase in surface roughness led to a decline in pull-off stress for all samples. The decay for the control samples was, however, much more substantial: for roughness R_z = 50 μm (skin-like), CON—50 had the adhesion reduced by 88%, going from 88 kPa to around 10 kPa, and CON—12 had a reduction by 98%, reaching 1.1 kPa at high roughness. Microstructured samples, on the other hand, had a less pronounced decay; FT—50 went to 15 kPa, losing around 43% of the adhesion performance in comparison to a smooth counter surface, and FT—12 went to around 8.5 kPa, a reduction to 32% of its initial value.

3.3. Adhesion Results to Sinusoidal Model Surfaces. Pull-off stresses as a function of compressive displacement for FT—12 μm and FT—50 μm against the different sinusoidal model surfaces are presented in Figure 6a,b. As before, the sample with the thicker terminal layer (FT—50 μm) showed higher adhesion values. The wavelength of the counter surface modulated the adhesive behavior in the following ways.

For wavelengths of 60 and 120 μm, i.e., close to the fibril diameter, the pull-off stress was almost insignificant (around 4 kPa for FT—12 μm and 7.5 kPa for FT—50 μm) and increased only slightly with increasing compressive displacement.

For the longer wavelengths of 240 and 480 μm, adhesion was generally higher and increased in a more pronounced way with a compressive displacement between 30 and 70 μm. The final plateau values were 13 and 25 kPa for FT—12 and 17 and 35 kPa for FT—50.

The transition from low to high adhesion for the long-wavelength surfaces occurred at a compressive displacement of about 50 μm, which corresponds to the amplitude of the sinusoidal surface shape.

In Figure 6c−f, we present in-situ lateral views of the sample FT—50 μm in a compressed state against all of the counter surfaces. A physical impediment to full contact is observed for the counter surfaces with wavelengths 60 and 120 μm, where contact was achievable only near the surface peaks, even at high compression. By contrast, the terminal layer of the microstructure eventually achieved "full" contact with the counter surfaces of wavelengths 240 and 480 μm. The transition between the two different kinds of adhesion behavior seems to occur at the following empirical condition

$$\lambda \approx 4D \tag{1}$$

where D is the fibril diameter and λ is the wavelength. For $\lambda < 4D$, the pull-off stress is low and insensitive to the compressive preload as full contact with the counter surface is always prevented. On the other hand, for $\lambda \geq 4D$, the microstructure could deform almost conformally to the rough surface and the pull-off stress increased with the preload. The performance of the adhesive in the case $\lambda \geq 4D$ was further investigated.

Figure 7a presents a comparison of adhesion results for FT—12 and FT—50 samples against the smooth surface and the model surface of wavelength 480 μm. For the smooth surface, the slight increase of pull-off stress, mostly at the initial
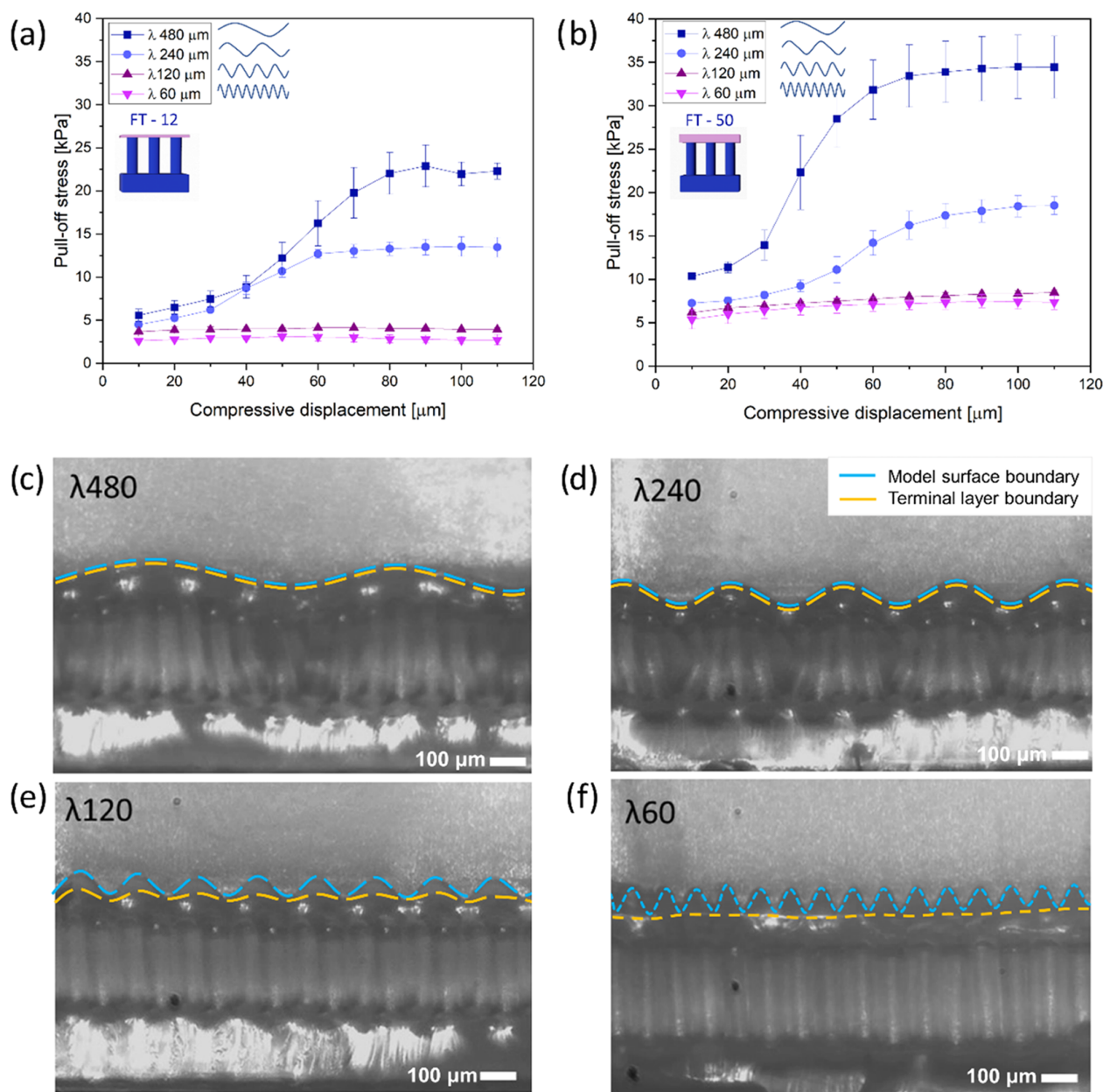
Figure 6. Adhesion of film-terminated microstructures on sinusoidal model surfaces. Pull-off stress vs compressive displacement for the sample with the terminal layer: (a) 12 μm and (b) 50 μm for the surfaces with different wavelengths. Snapshots show side view of FT—50 against surfaces with wavelengths: (c) 480 μm, (d) 240 μm, (e) 120, and (f) 60 μm in the compressed state. Scale bar is 100 μm. Blue dashed lines mark the model surface boundary, and yellow dashed lines indicate the microstructure's terminal layer boundary.

compressive displacement, can be explained by full contact formation and, possibly, by a contribution of the material's viscoelasticity.[42,43] For the sinusoidal model surface, three regimes can be distinguished: In regime 1, the sample and counter surface have low contact; next, in regime 2, the fibrils undergo bending, which allows them to form progressively more contact with inclined areas of the counter surface and creates higher adhesion; finally, in regime 3, the sample reaches close-to-full contact and adhesion enters a plateau. For sample FT—12, the plateau stress values amount to approximately 70% of the values obtained for the smooth surface.

Interestingly, the FT—50 sample reaches, within the error margin, similar adhesion as on the smooth surface.

In Figure 7b, side views of detachment from the model surface with wavelength 480 μm are presented for a single row of fibrils for better visualization. The ability of the fibrillar microstructure to conform to the wavy counter surface is well illustrated and will be discussed below.

3.4. Finite-Element Simulation Results. To obtain better quantitative insights into the contact behavior, information not accessible by the experimental setup, we analyzed the numerical results of our finite-element simulations for samples FT—12 and FT—50 μm in contact with the λ =
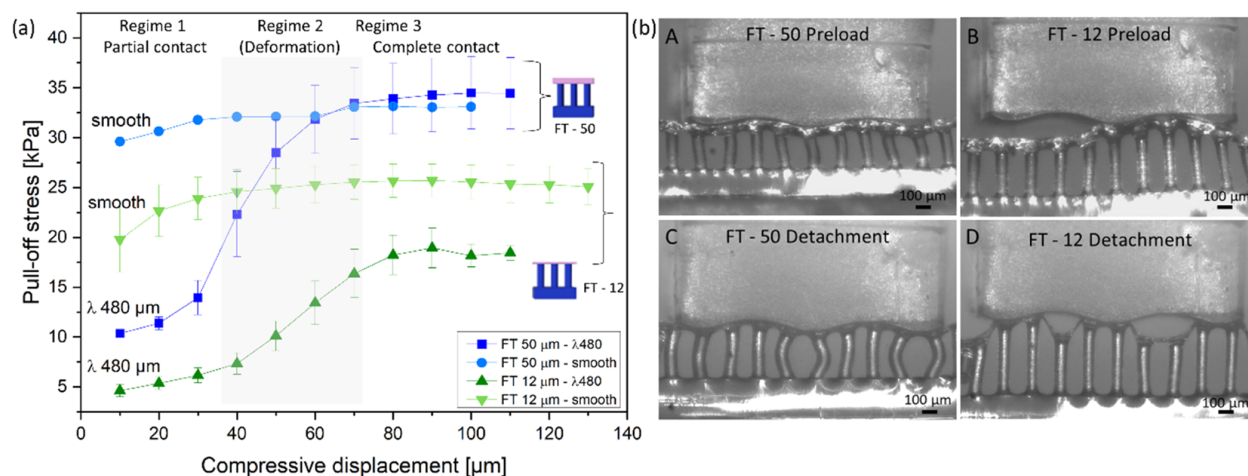
Figure 7. Adhesion of microstructures on model surface 480 μm in comparison to the smooth surface. (a) Pull-off stress as a function of compressive displacement for FT—50 and FT—12 against the smooth surface and model surface of wavelength 480 μm. (b) Side view of single row FT—50 in full contact (A) and detachment (B) and FT—12 in full contact (C) and detachment (D) against the 480 μm wave model. Scale bar is 100 μm.
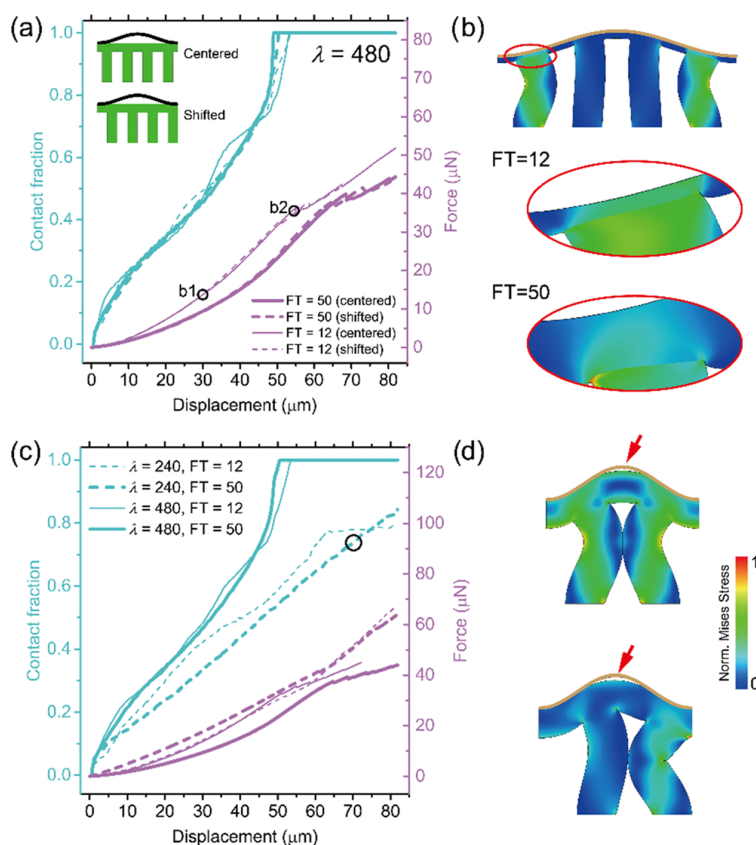
Figure 8. Simulation of compressive force and contact fraction for model surface 480 μm (a and b) and surface 240 μm (c and d). (a) Relations of contact fraction and compressive force vs compressive displacement for FT—12 and FT—50 samples with $\lambda = 480$ μm, in centered and shifted alignment. (b) Snapshots of deformation processes of FT—12, with the highlighted region of the terminal layer of both samples in positions marked "b1" and "b2" in panel (a). (c) Relationship between the contact fraction and compressive force vs compressive displacement for surface $\lambda = 240$ and 480 μm separately. (d) Snapshots at a contact fraction of about 70% and a displacement of about 70 μm of the critical deformation moment when the neighboring fibrils touch each other under centered and shifted arrangements when $\lambda = 240$ μm.

480 μm surface. Contact fraction (i.e., percentage contact area of the total surface) and compressive force were calculated

with increasing compressive displacement for two different alignments: in one case, a fibril was centered on a wave valley
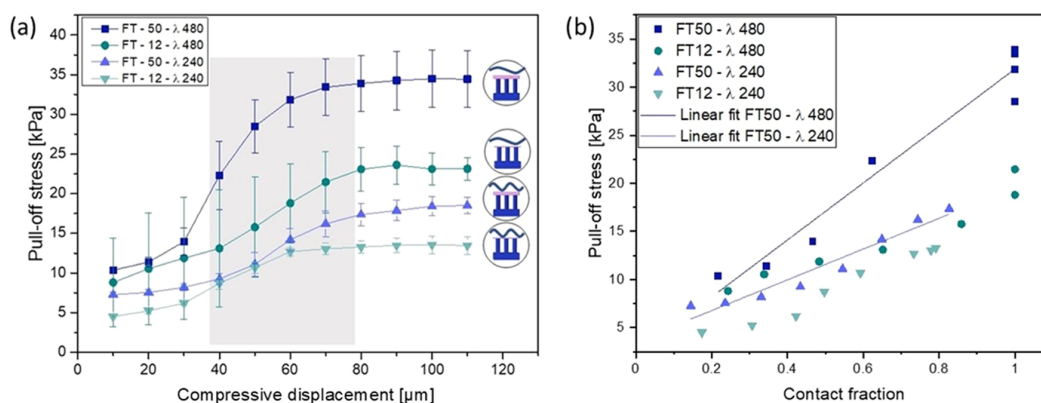
Figure 9. Adhesion on model surfaces 480 and 240 μm. (a) Pull-off stress for FT—50 and FT—12 as a function of maximum displacement for the waves of λ = 480 and 240 μm. A similar trend is observed for the wave 240 μm, in comparison to the larger one, described in detail in the main text. (b) Measured pull-off stress as a function of contact fraction during compression, obtained from the simulations. Linear fit is indicated for FT—50 for both surfaces 480 and 240 μm.

and, in the other, the space between was centered, as indicated in the insets in Figure 8a. The force results overlapped for displacements smaller than 30 μm and subsequently diverged somewhat; the shifted arrangement produced slightly higher force values, but the overall fibril alignment did not strongly affect contact fractions. Full contact was achieved for compressive displacement larger than 55 μm. Figure 8b presents a snapshot of FT—12 samples in full-contact configuration, as well as the terminal layer in both cases in the highlighted region. The FT—12 fibrils underwent severe bending in accordance with the experimental observations in Figure 7.

Subsequently, we compared the simulation results for the cases λ = 240 and 480 μm (Figure 8c). Here, all of the curves represent the average results of the centered and shifted alignments. While, in most cases, the contact area increased monotonically until full contact was reached, significantly higher forces were required for the 240 μm surface. A new event was observed for the λ = 240 μm surface: the contact fraction of the FT—12 sample leveled off at 77% (at a compressive displacement of 65 μm). The snapshots in Figure 8d explain this inability to achieve full contact: at a critical displacement of about 70 μm, severely bent neighboring fibrils start to impinge, which prevents further contact from forming. Although the optical observation in Figure 7b (λ = 240 μm) seems to indicate full contact, the numerical result in Figure 8c reveals that the system may not be able to reach this state in the model topography. This may, to some extent, explain the earlier detachment and lower pull-off stress for λ = 240 μm compared to λ = 480 μm.

Figure 9a shows the pull-off stress for FT—50 and FT—12 on the counter surfaces of λ = 480 and 240 μm. Similarly, for all cases, the pull-off stress increases with increasing displacement and saturates to a plateau value. Although camera images (Figure 6c,d) suggest that the microstructures have contact with both surfaces, 240 and 480 μm, numerical simulations showed that, in fact, the surface 240 μm only reaches 80% of its full contact surface when the maximum displacement is 80 μm. This could possibly cause the lower pull-off stress values when detaching from the 240 μm surface for both FT—12 and FT—50 samples.

The correlations between the contact fraction and pull-off stress are plotted with the help of both experimental and simulation results (Figure 9b), in which the pull-off stress is obtained from experiments, the contact fraction is only acquired by simulations, and the compressive displacement is the bridge. The pull-off stress goes up linearly with the increase of contact fraction in each case. For FT—12 samples, the pull-off stress at the same contact fraction is not significantly influenced by the wavelength λ. On the contrary, FT—50 samples show a wavelength λ dependence: larger λ leads to a higher pull-off stress.

4. DISCUSSION

Envisioning a self-adhesive microstructure for biomedical applications, especially on skin, we propose, in this investigation, a fibrillar array terminated by a soft, thin film, using biomedically certified materials. Roughness of the counter surface is a well-known obstacle for adhesion because it increases the elastic strain energy penalty in the adhesive, attempting to conform to the rough topography. As skin exhibits roughness to various degrees, this paper explores the adhesion of novel skin adhesives to counter surfaces of various roughnesses. The counter surfaces investigated exhibited randomly distributed irregularities, from glass-like to skin-like roughness, complemented by sinusoidal model roughness. The essential observations will now be discussed in turn.

4.1. Comparison of Smooth vs Rough Counter Surfaces: The Benefit of Fibrillar Microstructures. The first result of our work is the observation that the micro-structure did not always lead to improved adhesion: in contact with smooth counter surfaces, unstructured control samples were about three times more adhesive than fibrillar micro-structures (Figure 5a). As the unstructured films can adapt well to a smooth counter surface, the micropatterning of the film-terminated microstructure does not add any advantage to the adhesive behavior; on the contrary, it may be argued that the reduced areal density of the fibrils (about 22.5% of the nominal area) will reduce the effective contact stiffness by a similar factor. Such a difference was observed in Figure 5b, where the slope of the stress−displacement data during compression differed by a factor of approximately 2. Additional contributions may be due to the fibril-induced inhomogeneous stress fields at the interface, which could favor the initiation and propagation of interfacial cracks.
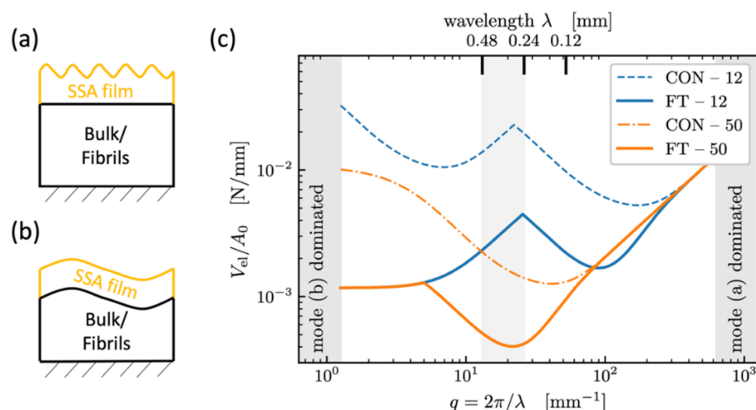
Figure 10. Theoretical model cases for elastic bodies with a sinusoidal counter surface. (a) Mode a: wavelength λ much smaller than layer thickness, (b) mode b: wavelength λ substantially exceeds layer thickness, (c) calculated deformation energies (per area) as functions of wavelength λ or wave vector q. The underlying "bulk/fibril" material is assumed to be stiffer than the terminal layer, providing a rigid constraint. In agreement with the experiment, the best confirmation to a counter surface with a wavelength between 240 and 480 μm (lowest deformation energy) is predicted for FT—50 (shaded).

The situation changes considerably when a counter surface with roughness is considered. Here, the higher compliance of the micropatterned sample with graded modulus will allow much better conformity to the peaks and valleys of the counter surface; this mechanism is clearly illustrated in the side view pictures of Figure 6b for the case of a single-wavelength model surface. It is noteworthy that, for a surface wavelength of 480 μm, the "plateau" value of the thicker terminal layer was about twice that of the thinner layer (Figure 6a). In the full contact state (Figure 7A,C), the sample with the thinner terminal layer, FT—12, exhibits more pronounced fibril bending than sample FT—50. This suggests that the thicker terminal layer contributes more elastic accommodation and requires less fibril bending. As presented in Figure 7 b (B,D), the detachment initiates preferentially in the valley rather than along the surface edges as previously described for the smooth surface. Empirically, it was found that the wavelength must exceed four fibril diameters (eq 1).

4.2. Compressive Behavior of Microstructures: The Benefit of Overload Protection. The behavior of a skin adhesive during attachment is also decisive for its applicability in a biomedical context. The fibrillar microstructures presented here exhibited a beneficial characteristic (Figure 3d): during compression, a plateau regime was encountered (marked "regime 2"), in which the compressive stress acting on the counter surface was insensitive to compressive displacement. Mechanistically, the force plateau is linked to the buckling instability of the microfibrillar array (Figure 3c,d). Considering the Young's modulus, E, of 1.1 MPa, n = 513 microfibrils, a fibril radius, R, of 30 μm, and the fibril height, h, of 200 μm, the critical buckling load can be estimated by Euler buckling theory $P_b = \alpha n E \pi^3 R^4 / 4h^2$, where α = 4 for clamping of both ends.[40,41] Thus, P_b = 0.177 N, and the buckling stress for the surface of 6.2 mm^2 is 28.5 kPa, which is in the same range as obtained experimentally.

This buckling event creates a "cushioning" or "overload protection", which allows for dissipation of any extra applied force through the deformation of the subsurface microstructure.[44] This effect will protect the counter surface against damage when applying a medical device on sensitive or injured tissue.[5] The film-terminated design did not show loss of adhesion even after the fibrils were buckled, which is

advantageous for reliable adhesion compared to microfibrils without film termination. This behavior differs from simple fibril microstructures, in which an overload can lead to elastic instability of the fibrils and hence detachment from the counter surface.[45,46]

4.3. Theoretical Considerations of the Effects of Microstructure and of the Terminal Layer. It is finally attempted to explain some of our observations in the light of theoretical concepts. It was recently found that rough surfaces, both random and sinusoidal, become sticky when their surface energy is more than half the elastic energy needed to bring the surfaces into conformal contact.[47] Since the elastic energy for contacting nominally flat surfaces is dominated by the surface undulations near the "roll-off" wavelengths,[48] it is sufficient to consider a single representative undulation with a wavelength near roll-off. While the exact treatment of a multilayered system would require complicated transfer-matrix techniques,[49,50] simple scaling arguments are presented here. We approximate the mechanics of the fibril structure (with an areal density of 22.5%) as a homogeneous elastic medium with a Young's modulus E that is 22.5% of that of the bulk and Poisson's ratio of zero. It is further considered that surface undulation of wavelength λ penetrates roughly a distance $\lambda/2\pi$ into a semi-infinite solid, which is sometimes referred to as Saint-Venant's principle and is backed up by analytical solutions.[51]

Figure 10 illustrates two modes to be considered: When λ is small compared to the terminal layer thickness $h = h_{layer}$, the layer deforms elastically as if the body below, with much greater Young's modulus, provided a rigid constraint (Figure 10a, mode a). Thus, the energy of deformation is given by[52,53]

$$\frac{V_{el,1}}{A_0}(q, h, v) = \frac{qE^*}{4} c(v, qh)|\tilde{u}|^2 \tag{2}$$

where $\tilde{u}$ is the displacement amplitude, $E^* = E/(1 - v^2)$ is the contact modulus, $q = 2\pi/\lambda$ is the magnitude of the wave vector, and $c(v, qh)$ is a dimensionless geometric prefactor. At large wavelengths (relative to the film thickness, Figure 10b, mode b), the entire sample including the layer is fully deformed and follows the undulation of the counter surface. Since the bottom medium is much stiffer than the layer, we estimate this

deformation energy by evaluating eq 2 only for the bulk/fibril body below the layer. In summary, we obtain $V_{el,mode(a)}(q) = V_{el,1}(q, h_{layer}, \nu_{layer})$ and $V_{el,mode(b)}(q) \approx V_{el,1}(q, h_{bottom}, \nu_{bottom})$.

Figure 10c displays the calculated areal deformation energies as a function of wavelength for the two different terminal layer thicknesses with and without fibril structures. It is generally seen that, with increasing wavelength (decreasing wave vector), the deformation energy decreases at first and then increases again; there is hence a defined wavelength for which adhesion is expected to be optimal. This is a result of the trade-off between higher displacement gradients at low λ and near-incompressibility at large λ. In the experimental wavelength range near the roll-off of the PSD (Figure 2e), fibril structures are predicted to require less deformation energy; consequently, they will more easily form intimate adhesive contact and exhibit a higher pull-off stress. It is also seen that the difference between 12 and 50 μm layer thickness is more noticeable for control specimens (dashed and dash-dotted line, CON—12 and CON—50) than for the fibrillar structures (solid lines FT—12 and FT—50), matching the behavior visible in Figure 5a.

Considering the difference between the 12 and 50 μm film-terminated samples, we have also observed in the finite-element simulations (Figure 8b) that the thinner terminal layer creates higher stress concentrations reaching the interface to the counter surface. If the counter surface is considered rigid and the fibrils are treated as flat punches in contact with the film, a thickness of about twice the fibril radius can already be approximated as infinitely thick in linear elastic theory.[52] This is roughly fulfilled by the 50 μm layer (FT—50), whereas in the FT—12 sample, the stress concentrations due to the fibrils will favor interfacial crack initiation and hence lead to earlier detachment. The fibrillar structure still improves adhesion in comparison to the control samples because it provides a more compliant background medium.[6,54]

Additionally, we estimated the conditions, in which mode a dominates at all wavelengths,[52] i.e., the effect of the patterned background would become negligible. The terminal layer thickness for this condition is approximately 450 μm, which is larger than the fibril length.

5. CONCLUSIONS

The adhesion of fibrillar microstructures terminated by a soft film was investigated against surfaces of different roughness (from smooth to skin-like), as well as against sinusoidal model surfaces of varying wavelengths, with roughness $R_z = 50\ \mu$m mimicking the skin. The effects of varying terminal layer thicknesses and subsurface microfibrils were investigated. The following conclusions can be drawn:

- Improved tolerance to roughness: The film-terminated fibrillar microstructures exhibit improved adhesion to counter surfaces of finite roughness, typical of skin, in comparison to flat samples. Microstructured samples show decay of up to 43% with increasing roughness, while unstructured control samples have a decay of up to 98%. The reason is the better conformity of the microstructures to the surface topography due to their higher effective compliance. We presented a theoretical model of the interaction with a rough surface.

- Threshold wavelength of the counter surface: Our experimental results suggest that, to ensure sufficient

contact, the wavelength of the roughness must obey $\lambda > 4D$, where D is the fibril diameter. The empirical threshold is attributed to a geometrical impediment of the fibrils to achieve the furthest point in the counter surface. Above this limit, adhesion can be tuned by increasing the contact area through compressive preload. These results are in agreement with finite-element simulations, in which contact fraction during compression was evaluated.

- Terminal layer thickness effect: A thinner terminal layer creates local stress concentrations and leads to earlier detachment. The thicker terminal layer reduces the influence of the stiffer background material, making the structure more compliant. A simple preliminary model consideration is presented to explain these effects.

- Overload protection: When sufficiently compressed, the film-terminated microstructure exhibits elastic instability of the fibrils without loss in adhesion. This mechanism leads to a stress plateau, which protects the counter surface against overload and damage during application, a feature relevant for medical applications.

■ AUTHOR INFORMATION

Corresponding Author

Eduard Arzt − *INM—Leibniz Institute for New Materials, 66123 Saarbrücken, Germany; Department of Materials Science and Engineering, Saarland University, 66123 Saarbrücken, Germany;* orcid.org/0000-0002-0834-4540; Email: eduard.arzt@leibniz-inm.de

Authors

Gabriela Moreira Lana − *INM—Leibniz Institute for New Materials, 66123 Saarbrücken, Germany; Department of Materials Science and Engineering, Saarland University, 66123 Saarbrücken, Germany;* orcid.org/0000-0002-8346-6951

Xuan Zhang − *INM—Leibniz Institute for New Materials, 66123 Saarbrücken, Germany;* orcid.org/0000-0002-6155-6825

Christian Müller − *INM—Leibniz Institute for New Materials, 66123 Saarbrücken, Germany;* orcid.org/0000-0002-9480-9753

René Hensel − *INM—Leibniz Institute for New Materials, 66123 Saarbrücken, Germany;* orcid.org/0000-0002-9623-2118

Complete contact information is available at:
https://pubs.acs.org/10.1021/acsami.2c12663

Author Contributions

G.M.L., X.Z., R.H., E.A.: conceptualization; G.M.L.: sample fabrication, adhesion measurements, microscopy; X.Z.: establishment of the simulation model; G.M.L., X.Z., and C.M.: writing—original draft; G.M.L., X.Z., C.M., R.H., and E.A.: review and editing. This manuscript was written through contributions of all authors. All authors have given approval to the final version of the manuscript.

Notes

The authors declare no competing financial interest.

■ REFERENCES

(1) Kwak, M. K.; Jeong, H. E.; Suh, K. Y. Rational Design and Enhanced Biocompatibility of a Dry Adhesive Medical Skin Patch. *Adv. Mater.* **2011**, *23*, 3949−3953.

(2) Tian, L.; Zimmerman, B.; Akhtar, A.; Yu, K. J.; Moore, M.; Wu, J.; Larsen, R. J.; Lee, J. W.; Li, J.; Liu, Y.; Metzger, B.; Qu, S.; Guo, X.; Mathewson, K. E.; Fan, J. A.; Cornman, J.; Fatina, M.; Xie, Z.; Ma, Y.; Zhang, J.; Zhang, Y.; Dolcos, F.; Fabiani, M.; Gratton, G.; Bretl, T.; Hargrove, L. J.; Braun, P. V.; Huang, Y.; Rogers, J. A. Large-Area MRI-Compatible Epidermal Electronic Interfaces for Prosthetic Control and Cognitive Monitoring. *Nat. Biomed. Eng.* **2019**, *3*, 194−205.

(3) Chung, H. U.; Kim, B. H.; Lee, J. Y.; Lee, J.; Xie, Z.; Ibler, E. M.; Lee, K. H.; Banks, A.; Jeong, J. Y.; Kim, J.; Ogle, C.; Grande, D.; Yu, Y.; Jang, H.; Assem, P.; Ryu, D.; Kwak, J. W.; Namkoong, M.; Park, J. B.; Lee, Y.; Kim, D. H.; Ryu, A.; Jeong, J.; You, K.; Ji, B.; Liu, Z.; Huo, Q.; Feng, X.; Deng, Y.; Xu, Y.; Jang, K. I.; Kim, J.; Zhang, Y.; Ghaffari, R.; Rand, C. M.; Schau, M.; Hamvas, A.; Weese-Mayer, D. E.; Huang, Y.; Lee, S. M.; Lee, C. H.; Shanbhag, N. R.; Paller, A. S.; Xu, S.; Rogers, J. A. Binodal, Wireless Epidermal Electronic Systems with in-Sensor Analytics for Neonatal Intensive Care. *Science* **2019**, *363*, No. eaau0780.

(4) Boyadzhieva, S.; Sorg, K.; Danner, M.; Fischer, S. C. L.; Hensel, R.; Schick, B.; Wenzel, G.; Arzt, E.; Kruttwig, K. A Self-Adhesive Elastomeric Wound Scaffold for Sensitive Adhesion to Tissue. *Polymers* **2019**, *11*, No. 942.

(5) Moreira Lana, G.; Sorg, K.; Wenzel, G. I.; Hecker, D.; Hensel, R.; Schick, B.; Kruttwig, K.; Arzt, E. Self-Adhesive Silicone Microstructures for the Treatment of Tympanic Membrane Perforations. *Adv. NanoBiomed Res.* **2021**, *1*, No. 2100057.

(6) Davis, C. S.; Martina, D.; Creton, C.; Lindner, A.; Crosby, A. J. Enhanced Adhesion of Elastic Materials to Small-Scale Wrinkles. *Langmuir* **2012**, *28*, 14899−14908.

(7) Fischer, S. C. L.; Arzt, E.; Hensel, R. Composite Pillars with a Tunable Interface for Adhesion to Rough Substrates. *ACS Appl. Mater. Interfaces* **2017**, *9*, 1036−1044.

(8) Persson, B. N. J.; Albohr, O.; Creton, C.; Peveri, V. Contact Area between a Viscoelastic Solid and a Hard, Randomly Rough, Substrate. *J. Chem. Phys.* **2004**, *120*, 8779−8793.

(9) Arzt, E.; Quan, H.; McMeeking, R. M.; Hensel, R. Functional Surface Microstructures Inspired by Nature—From Adhesion and Wetting Principles to Sustainable New Devices. *Prog. Mater. Sci.* **2021**, *119*, 1−105.

(10) Hensel, R.; Moh, K.; Arzt, E. Engineering Micropatterned Dry Adhesives: From Contact Theory to Handling Applications. *Adv. Funct. Mater.* **2018**, *28*, No. 1800865.

(11) Eisenhaure, J.; Kim, S. A Review of the State of Dry Adhesives: Biomimetic Structures and the Alternative Designs They Inspire. *Micromachines* **2017**, *8*, 1−38.

(12) Cutting, K. F. Impact of Adhesive Surgical Tape and Wound Dressings on the Skin, with Reference to Skin Stripping. *J. Wound Care* **2013**, *17*, 157−162.

(13) Zulkowski, K. Understanding Moisture-Associated Skin Damage, Medical Adhesive Related Skin Injuries and Skin Tears. *Adv. Skin Wound Care* **2017**, *30*, 372−381.

(14) Hwang, I.; Kim, H. N.; Seong, M.; Lee, S. H.; Kang, M.; Yi, H.; Bae, W. G.; Kwak, M. K.; Jeong, H. E. Multifunctional Smart Skin Adhesive Patches for Advanced Health Care. *Adv. Healthcare Mater.* **2018**, *7*, No. 1800275.

(15) Karp, J. M.; Langer, R. Dry Solution to a Sticky Problem. *Nature* **2011**, *477*, 42−43.

(16) Fischer, S. C. L.; Kruttwig, K.; Bandmann, V.; Hensel, R.; Arzt, E. Adhesion and Cellular Compatibility of Silicone-Based Skin Adhesives. *Macromol. Mater. Eng.* **2017**, *302*, No. 1600526.

(17) Drotlef, D. M.; Amjadi, M.; Yunusa, M.; Sitti, M. Bioinspired Composite Microfibers for Skin Adhesion and Signal Amplification of Wearable Sensors. *Adv. Mater.* **2017**, *29*, No. 1701353.

(18) Bae, W. G.; Kim, D.; Kwak, M. K.; Ha, L.; Kang, S. M.; Suh, K. Y. Enhanced Skin Adhesive Patch with Modulus-Tunable Composite Micropillars. *Adv. Healthcare Mater.* **2013**, *2*, 109−113.

(19) Noderer, W. L.; Shen, L.; Vajpayee, S.; Glassmaker, N. J.; Jagota, A.; Hui, C. Y. Enhanced Adhesion and Compliance of Film-Terminated Fibrillar Surfaces. *Proc. R. Soc. A* **2007**, *463*, 2631−2654.

(20) He, Z.; Moyle, N. M.; Hui, C. Y.; Levrard, B.; Jagota, A. Adhesion and Friction Enhancement of Film-Terminated Structures against Rough Surfaces. *Tribol. Lett.* **2017**, *65*, 1−8.

(21) Jagota, A.; Hui, C. Y. Adhesion, Friction, and Compliance of Bio-Mimetic and Bio-Inspired Structured Interfaces. *Mater. Sci. Eng., R* **2011**, *72*, 253−292.

(22) Glassmaker, N. J.; Jagota, A.; Hui, C.-Y.; Noderer, W. L.; Chaudhury, M. K. Biologically Inspired Crack Trapping for Enhanced Adhesion. *Proc. Natl. Acad. Sci. U.S.A.* **2007**, *104*, 10786−10791.

(23) Boyadzhieva, S.; Sorg, K.; Danner, M.; Fischer, S. C. L.; Hensel, R.; Schick, B.; Wenzel, G.; Arzt, E.; Kruttwig, K. A Self-Adhesive Elastomericwound Scaffold for Sensitive Adhesion to Tissue. *Polymers* **2019**, *11*, 1−15.

(24) Korn, V.; Surber, C.; Imanidis, G. Skin Surface Topography and Texture Analysis of Sun-Exposed Body Sites in View of Sunscreen Application. *Skin Pharmacol. Physiol.* **2017**, *29*, 291−299.

(25) Adabi, S.; Hosseinzadeh, M.; Noei, S.; Conforto, S.; Daveluy, S.; Clayton, A.; Mehregan, D.; Nasiriavanaki, M. Universal in Vivo Textural Model for Human Skin Based on Optical Coherence Tomograms. *Sci. Rep.* **2017**, *7*, No. 17912.

(26) Jones, I.; Currie, L.; Martin, R. A Guide to Biological Skin Substitutes The Function of Normal Skin. *Br. J. Plast. Surg. Br. Assoc. Plast. Surg.* **2002**, *55*, 185−193.

(27) Shahsavan, H.; Zhao, B. Biologically Inspired Enhancement of Pressure-Sensitive Adhesives Using a Thin Film-Terminated Fibrillar Interface. *Soft Matter* **2012**, *8*, 8281−8284.

(28) Bai, Y.; Jagota, A.; Hui, C. Y. Frictional Auto-Roughening of a Surface with Spatially Varying Stiffness. *Soft Matter* **2014**, *10*, 2169−2177.

(29) Kroner, E.; Blau, J.; Arzt, E. Note: An Adhesion Measurement Setup for Bioinspired Fibrillar Surfaces Using Flat Probes. *Rev. Sci. Instrum.* **2012**, *83*, 2−5.

(30) Fischer, S. C. L.; Boyadzhieva, S.; Hensel, R.; Kruttwig, K.; Arzt, E. Adhesion and Relaxation of a Soft Elastomer on Surfaces with Skin like Roughness. *J. Mech. Behav. Biomed. Mater.* **2018**, *80*, 303−310.

(31) Eubel, J. M.*Design Und Herstellung Eines Haftsystem Zur Anwendung Auf Dem Trommelfell*; Universität des Saarlandes, 2019.

(32) Koenig, D. W.; Dvoracek, B.; Vongsa, R. In Vitro Prediction of in Vivo Skin Damage Associated with the Wiping of Dry Tissue against Skin. *Skin Res. Technol.* **2013**, *19*, 453−458.

(33) Chen, S.; Bhushan, B. Nanomechanical and Nanotribological Characterization of Two Synthetic Skins with and without Skin Cream Treatment Using Atomic Force Microscopy. *J. Colloid Interface Sci.* **2013**, *398*, 247−254.

(34) Sanner, A.; Nöhring, W. G.; Thimons, L. A.; Jacobs, T. D. B.; Pastewka, L. Scale-Dependent Roughness Parameters for Topography Analysis. *Appl. Surf. Sci. Adv.* **2022**, *7*, No. 100190.

(35) Jacobs, T. D. B.; Junge, T.; Pastewka, L. Quantitative Characterization of Surface Topography Using Spectral Analysis. *Surf. Topogr.: Metrol. Prop.* **2017**, *5*, No. 013001.

(36) Gujrati, A.; Sanner, A.; Khanal, S. R.; Moldovan, N.; Zeng, H.; Pastewka, L.; Jacobs, T. D. B. Comprehensive Topography Characterization of Polycrystalline Diamond Coatings. *Surf. Topogr.: Metrol. Prop.* **2021**, *9*, No. 014003.

(37) Wang, A.; Müser, M. H. On the Usefulness of the Height-Difference-Autocorrelation Function for Contact Mechanics. *Tribol. Int.* **2018**, *123*, 224−233.

(38) Dassault Systems, S. C.*ABAQUS 6.14 Documentation*; Simulia Corp: Providence, RI, USA, 2014.

(39) Shahsavan, H.; Zhao, B. Bioinspired Functionally Graded Adhesive Materials: Synergetic Interplay of Top Viscous-Elastic Layers with Base Micropillars. *Macromolecules* **2014**, *47*, 353−364.

(40) Stark, S.; Begley, M. R.; McMeeking, R. M. The Buckling and Postbuckling of Fibrils Adhering to a Rigid Surface. *J. Appl. Mech.* **2013**, *80*, No. 041022.

(41) Tinnemann, V.; Arzt, E.; Hensel, R. Switchable Double-Sided Micropatterned Adhesives for Selective Fixation and Detachment. *J. Mech. Phys. Solids* **2019**, *123*, 20−27.

(42) Barreau, V.; Hensel, R.; Guimard, N. K.; Ghatak, A.; McMeeking, R. M.; Arzt, E. Fibrillar Elastomeric Micropatterns Create Tunable Adhesion Even to Rough Surfaces. *Adv. Funct. Mater.* **2016**, *26*, 4687−4694.

(43) Kroner, E.; Paretkar, D. R.; McMeeking, R. M.; Arzt, E. Adhesion of Flat and Structured PDMS Samples to Spherical and Flat Probes: A Comparative Study. *J. Adhes.* **2011**, *87*, 447−465.

(44) Kruttwig, K.; Moreira Lana, G.; Moh, K.; Arzt, E.*Krafttollerante Struktur2021103895.2*.

(45) Purtov, J.; Frensemeier, M.; Kroner, E. Switchable Adhesion in Vacuum Using Bio-Inspired Dry Adhesives. *ACS Appl. Mater. Interfaces* **2015**, *7*, 24127−24135.

(46) Paretkar, D.; Kamperman, M.; Schneider, A. S.; Martina, D.; Creton, C.; Arzt, E. Bioinspired Pressure Actuated Adhesive System. *Mater. Sci. Eng., C* **2011**, *31*, 1152−1159.

(47) Wang, A.; Müser, M. H. On the Adhesion between Thin Sheets and Randomly Rough Surfaces. *Friction* **2022**, DOI: 10.1007/s40544-022-0644-3.

(48) Wang, A.; Müser, M. H. Is There More than One Stickiness Criterion? *Friction* **2022**, 4−7.

(49) Charyulu, M. K.*Theoretical Stress Distribution in an Elastic Multi-Layered Medium*; Iowa State University, 1964.

(50) Kajita, S. Green's Function Nonequilibrium Molecular Dynamics Method for Solid Surfaces and Interfaces. *Phys. Rev. E* **2016**, *94*, 1−9.

(51) Sainsot, P. Analytical Stresses in Rough Contacts. *Proc. Inst. Mech. Eng., Part C* **2011**, *225*, 274−279.

(52) Müller, C.; Müser, M. H. Analytical and Numerical Results for the Elasticity and Adhesion of Elastic Films with Arbitrary Poisson's Ratio and Confinement. *J. Adhes.* **2022**, 1−24.

(53) Carbone, G.; Lorenz, B.; Persson, B. N. J.; Wohlers, A. Contact Mechanics and Rubber Friction for Randomly Rough Surfaces with Anisotropic Statistical Properties. *Eur. Phys. J. E* **2009**, *29*, 275−284.

(54) Martina, D.; Creton, C.; Damman, P.; Jeusette, M.; Lindner, A. Adhesion of Soft Viscoelastic Adhesives on Periodic Rough Surfaces. *Soft Matter* **2012**, *8*, 5350−5357.

III Viscoelastic contact formation

Permission

Contributions of co-authors

Christian Müller: conceptualization, methodology: GFMD implementation, software, investigation: GFMD simulations, formal analysis, writing–original draft.
Martin H. Müser: conceptualization, formal analysis, supervision, writing–original draft.

The study was conceptualized by C.M. and M.H.M. as a follow-up to Publ. **IV**.

All simulations were set up, run and post-processed by C.M. under the supervision of M.H.M., including small adjustments to the GFMD source code. M.H.M. performed the derivation of the generalized Tabor parameter in the appendix. Ideas on how to evaluate and visualize results came from both authors and were then realized by C.M.

The original manuscript was prepared and revised by both authors under the lead of M.H.M. Everyone agreed on the publication of the article in the Journal of Chemical Physics and its inclusion in this thesis.

How short-range adhesion slows down crack closure and contact formation

View Online Export Citation CrossMark

C. Müller[1] [iD] and M. H. Müser[2,a)] [iD]

AFFILIATIONS

[1] INM—Leibniz Institute for New Materials, 66123 Saarbrücken, Germany

[2] Department of Materials Science and Engineering, Saarland University, 66123 Saarbrücken, Germany

Note: This paper is part of the JCP Special Topic on Adhesion and Friction.
[a)]Author to whom correspondence should be addressed: martin.mueser@mx.uni-saarland.de

ABSTRACT

While viscoelastic, adhesive contact rupture of simple indenters is well studied, contact formation has received much less attention. Here, we present simulations of the formation of contact between various power law indenters and an adhesive, viscoelastic foundation. For all investigated indenters, we find that the macroscopic relaxation time τ scales approximately with $1/\rho^{1.8}$, where ρ is the range of adhesion. The prolongation of contact formation with Tabor parameter is rationalized by the increased dissipation that short-range adhesion causes on a moving crack.

Published under an exclusive license by AIP Publishing. https://doi.org/10.1063/5.0174379

I. INTRODUCTION

The modeling of mechanical contacts between elastomers and rigid counterfaces has advanced substantially in the recent past.[1–3] In particular, the comparison between simulated contact configurations and real-laboratory images has reached new levels, mainly thanks to improved capabilities of computing and measuring detailed features in partial contacts of nominally flat surfaces.[1,4–8] However, the progress made pertains mostly to situations where either the experiment is conducted quasi-statically or multi-scale roughness is insignificant. Viscoelastic simulations with roughness on separate length scales remain scarce.[8–10] As a consequence, it remains difficult to ascertain or to predict when contact hysteresis in a given system is mostly viscoelastic in nature[11] or caused by elastic multistability[12–14] and whether their effects are deemed additive[10] or inseparable.[8] When assessing contact hysteresis, it is as important to describe contact formation as contact rupture.[15] However, despite continuous progress in the simulation of viscoelastic, adhesive contacts,[16–20] contact formation is explored rather little although it is similarly important as contact rupture. It could be one reason for the so-called Monday morning problem, which refers to the sticking of valves in production engines after resting over the weekend. Further applications, where (slow) contact formation matters, are hydraulic and pneumatic seals or adhesive gripping devices.

The difficulty of simulating adhesion-driven contact formation involving soft matter is that the short-range nature of adhesion must be accounted for, even for macroscopic objects. First, non-contact puts much greater demands on the range of adhesion than contact:[15,21] While a Tabor parameter $\mu_T \approx 5$ (μ_T is a dimensionless measure inversely proportional to the range of adhesion and introduced in detail further below) suffices to reproduce the $\mu_T \to \infty$ load–displacement curves under retraction, the energy loss would be less than 50% of the real value, due to a premature jump into contact. Unfortunately, short-range adhesion requires a modeler to use small mesh sizes to avoid discretization artifacts, most notably lattice trapping.[15] Making matters worse, the errors in energy hysteresis disappear only with the inverse cube of the linear mesh-element size.[15] Second, short-range adhesion enhances the dissipation of a moving crack or contact line,[22–26] whereby not only crack opening but also crack closure is impeded, which in turn puts large demands on the computing time.

The discussion above implies that simulating effectively viscoelastic processes using relatively coarse scales might be achievable by reinterpreting the time scales used in the viscoelastic model. This would be possible if multiplying the range of adhesion by a factor s accelerated the dynamics by a power of s. Testing for the possibility of such a mapping was the original motivation for the research reported in this work. However, the simulations can also serve as a test for theoretical predictions on contact closure and extend the

25 December 2023 02:19:53

number of geometries, for which gap closure is investigated. In this context, our focus is on indenter shapes, where the height of the indenter is a power law of the distance from the indenter's symmetry axis. This problem class offers the greatest potential for us to exploit the similarity of solutions.

The remainder of this work is organized as follows: The methods used are laid out in Sec. II, results are presented in Sec. III, and conclusions are drawn in Sec. IV. Some scaling arguments allowing the Tabor parameter to be generalized to adhesive power law indenters are given in the Appendix.

II. METHODS

We use Green's function molecular dynamics (GFMD),[27] which is a boundary-element method for the simulation of linearly (visco)elastic contact problems assuming elastic bodies to be isotropic in planes normal to their (originally flat) surface and to be periodically repeated in that plane. We focus on normal, frictionless contacts within linear elasticity. Our systems consist of various perfectly rigid indenters and a homogeneous and isotropic, linearly viscoelastic body described in the continuum limit.

The shape of the indenter is given by

$$h(r) = \frac{R}{n}\left(\frac{r}{R}\right)^n, \tag{1}$$

where R has the unit of length and corresponds to a radius of curvature for a Hertzian ($n = 2$) indenter, while r is the distance from the indenter's symmetry axis. For a conical indenter ($n = 1$), $h(r)$ could be written as $h(r) = r \tan \varphi$, in order to implement different opening angles φ. Investigated exponents are $n = 1$ for a conical indenter, $n = 2$ for a Hertzian indenter, and $n = 3$ as well as $n = 4$ as crude approximations for a flat punch. A true flat punch has no interesting contact formation dynamics, as its instantaneous contact radius is identical to the relaxed one.

Indenter and elastic body interact through a cohesive-zone model that is twice differentiable everywhere but in one isolated point, which proves to be useful for numerical or stability reasons.[15] It is given by an interaction potential density of

$$V_{int}(g) = -\gamma \times \begin{cases} 0 & \text{if } \rho \leq g, \\ \{1 + \cos(\pi g/\rho)\}/2 & \text{if } 0 < g < \rho, \\ \{1 - (\pi g/2\rho)^2\} & \text{else.} \end{cases} \tag{2}$$

Here, g refers to the gap or interfacial displacement between elastomer and indenter, γ is the energy gained per unit area when indenter and elastic body touch, while ρ is the range of adhesion. In all investigated systems, a numerical value of $\gamma = 0.01 \, E^* R$ is assigned. The numerical value of ρ was adjusted according to the individual Tabor parameters. In principle, ρ could be set to a smaller value for negative than for positive gaps to better mimic hard-wall repulsion. However, since all reported simulations addressed rather short-ranged adhesion and thus small ρ, we used the same value for ρ for attraction and repulsion.

The elastic energy of a relaxed body (under an external surface stress) is given by

$$V_{ela} = \sum_{\mathbf{q}} \frac{qE^*}{4}|\tilde{u}(\mathbf{q})|^2, \tag{3}$$

where $\mathbf{q}$ is an in-plane wave vector, or wave number for one-dimensional interfaces, q is its magnitude, while E^* is the static contact modulus and $\tilde{u}(\mathbf{q})$ the Fourier transform of the displacement field. However, as we study a viscoelastic system, E^* is made frequency dependent. Our default model consists of a single Maxwell element in parallel with a spring, yielding a frequency-dependent contact modulus of

$$E^*(\omega) = E_0 \frac{1 + s\omega^2\tau_{Mxw}^2 + i(s-1)\omega\tau_{Mxw}}{1 + \omega^2\tau_{Mxw}^2} \tag{4}$$

with $s \equiv E_\infty^*/E_0^* = 100$, where E_0^* and E_∞^* are the quasi-static and the high-frequency elastic moduli, respectively. The model is implemented as described in Ref. 8. E_0^* is used as the unit for pressure, while times are reported in units of τ_{Mxw}, unless stated otherwise. Any deviation from our default model is explicitly pointed out. For example, in one case, the surface modes are coupled to three rather than to one Maxwell element. The real and imaginary parts of $E^*(\omega)$ are shown in Fig. 1 for the three-element model and the default, one-element model. The "weights" $E_0^{(n)}$ and relaxation times $\tau_{Mxw}^{(n)}$ in the three-element models are chosen as $E_0^{n+1} = 6E_0^n$ and $\tau_{Mxw}^{(n+1)} = \tau_{Mxw}^{(n)}/6$.

While a "brute-force" Fourier method is certainly not the most effective approach to address the questions in this paper, it
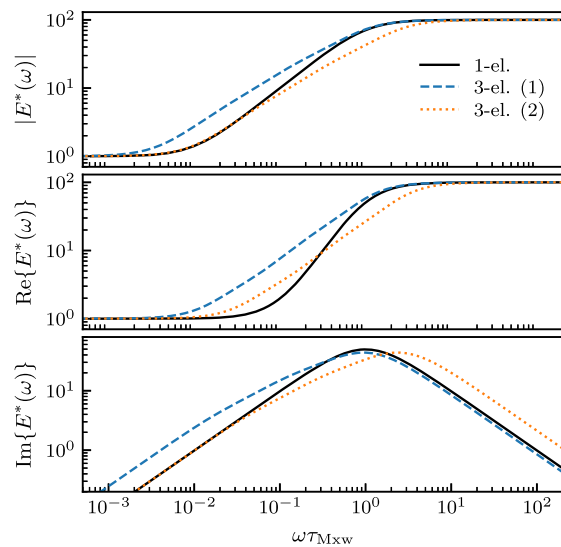
FIG. 1. Absolute value $|E^{*\prime}(\omega)|$ (top), real part $E^{*\prime}(\omega)$ (middle), and imaginary part $E^{*\prime\prime}(\omega)$ (bottom) of the contact modulus for a one-element (1-el, solid lines), standard linear-solid model and a three-element (3-el, dashed and dotted lines) model. The frequency is expressed in inverse units of τ_{Mxw} of the one-element model (blue line), while the data for the three-element are shifted one time to have a similar high-frequency (dashed, blue line) and one time to have a similar low-frequency (dotted, orange line) modulus as the one-element model.

is sufficiently efficient to obtain satisfying answers. Moreover, by addressing primarily line contacts having a formal interfacial dimension of $D = 1$, much of the computational overhead spent on not exploiting the symmetry of the problem in $D = 2$ is alleviated.

The most critical dimensionless parameter for a (force-free) adhesive contact of a Hertzian indenter is the Tabor parameter μ_T. It is inversely proportional to the range of adhesion and is designed such that $\mu_T \gg 1$ makes a (quasi-static) contact behave as in the limit for zero-range adhesion, which was first solved analytically by Johnson, Kendall, and Roberts (JKR)[28] for $n = 2$ and $D = 2$. For arbitrary n at $D = 2$, the contact problem can be solved using Sneddon's method.[29,30] Less relevant for most real purposes, but easier to tackle numerically and theoretically, is long-range adhesion. For $D = n$, adhesion effectively acts like an external load that does not depend on ρ for $\rho \to \infty$ or $\mu_T \to 0$ when γ and R are fixed, as is readily seen using the Bradley model,[31] which becomes exact in the long-range limit. Its analysis also reveals that a physically meaningful long-range-adhesion limit does not exist for $n \neq D$, because the offset load vanishes ($n > D$) or diverges ($n < D$) for a diverging ρ at fixed γ and R.

Zheng and Yu[32] generalized the Tabor parameter for arbitrary power law indenters to

$$\mu_T = \frac{R}{\rho}\left(\frac{\gamma}{RE^*}\right)^{n/(2n-1)}. \tag{5}$$

after solving the contact mechanics of adhesive power law indenters in the Dugdale approximation. In the Appendix, we identify the same expression using rather simple, dimensional analysis, which is also valid for an interfacial dimension of $D = 1$. In the following, we will usually report μ_T rather than the range of adhesion ρ. Note that the precise value for μ_T would differ if the ratio γ/σ_{max} were used instead of ρ in Eq. (5).

In this work, we study exclusively crack closure dynamics under zero external load. We focus on the time evolution of the contact radius $r_c(t)$, which we define to be the distance from the indenter's symmetry axis to the point where the tensile stress takes its maximum, specifically, the distance in a direction parallel to a main axis of the simulation cell rather than its diagonal, though the two measures are very close to each other and thus show identical scaling. A small relaxation run is done first, using "regular" rather than viscoelastic GFMD, during which the elastomer is allowed to relax to the shape that it would have under the assumption that E_∞^* rather than E_0^* was its static contact modulus. The estimates of quasi-static contact properties are obtained from similar calculations with the proper static contact modulus E_0^*. This way, initial contact radii $r_{in} \equiv r_c(t = 0)$ and quasi-static contact radii $r_{qs} \equiv r_c(t \to \infty)$ can be determined with high accuracy. Results for $r_c(t)$ are reported in terms of a relaxation function defined as

$$C(t) \equiv \frac{r_c(t) - r_{in}}{r_{qs} - r_{in}}. \tag{6}$$

While we do not yet have experimental reference data, it might be important to stress that it might be difficult to rigorously define r_{in} in real experiments, since contact with a rigid counter body cannot be simply switched on as in a computer simulation, while inertial effects would prevent an immediate contact at $t = 0^+$ with the high-frequency modulus from occurring. Thus, we expect deviations

between our idealized model and real experiments in the very early stages of contact formation to be unavoidable.

III. RESULTS

While this study focuses on contact formation for different tip geometries, we first wish to analyze how details of the viscoelastic model affect the dynamics. To this end, Fig. 2 contrasts the gap closure for the one-element model and the three-element model introduced in Sec. II. Both rheological models reveal the same generic features of the crack closure process for power law indenters: Early-time dynamics, in the specific example for $t \lesssim 10\tau_{Mxw}$, a regime where the contact radius depends approximately logarithmically on time, i.e., for times $10 \lesssim t/\tau_{Mxw} \lesssim 10^4$, and a final regime at $t \gtrsim 10^4 \tau_{Mxw}$, which has an exponential time dependence according to

$$C(t \to \infty) - C(t) \propto \exp\left(-t/\tau\right), \tag{7}$$

which defines the macroscopic or largest relaxation time τ. While the relaxation in the intermediate time curve is somewhat flattened for the three-element model compared to the one-element model, the contrast in different $r_c(t)$ curves in Fig. 2 appears somewhat less noticeable to the eye than those of the frequency-dependence of the elastic modulus shown in Fig. 1. Interestingly, though perhaps not surprisingly, the early-time (later-time) dynamics of the two models superimpose reasonably well when the relaxation times of the three-element model are scaled such that the high-frequency (low-frequency) $E''(\omega)$ or $|E(\omega)|$ exhibits similar behavior. In the following, we will merely consider the one-element model, widely known also as the standard linear solid (SLS).

Similar crack closure dynamics as those just discussed are maintained when extending the range of Tabor parameters. To this end, $C(t)$ rather than $r_c(t)/R$ is shown for different μ_T, one time for two-dimensional interfaces in Fig. 3 and one time, as before, for one-dimensional interfaces in Fig. 4. Similar behavior is revealed in both figures. A double logarithmic representation was chosen for them
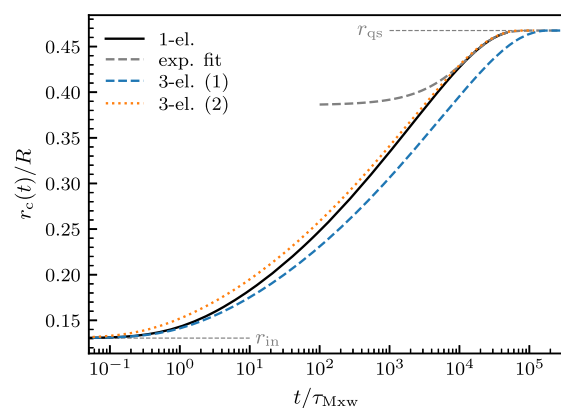
FIG. 2. Contact formation of the one-element model and the three-element model(s), whose frequency-dependent elastic modulus is shown in Fig. 1; $D = 1$, $n = 2$, $\mu_T = 7.2$. Thin gray lines indicate the instantaneous contact radius for $t \to 0$ as well as the final exponential approach (exp) to the quasi-static value r_{qs} reached at $t \to \infty$.
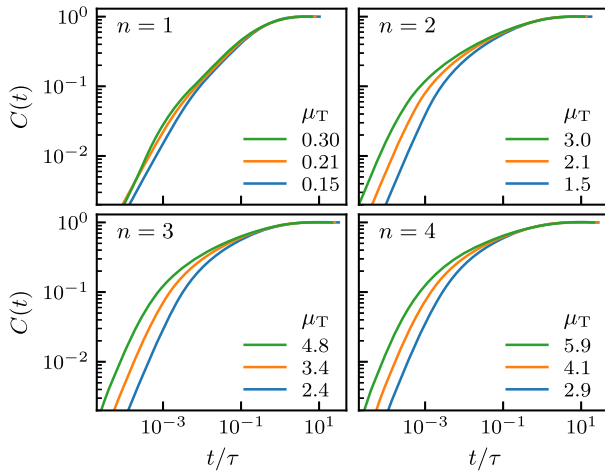
FIG. 3. Crack closure dynamics for different axisymmetric tips.
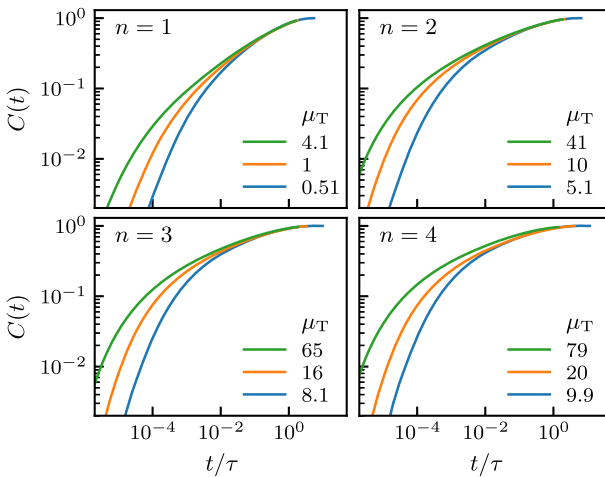
FIG. 4. Crack closure dynamics for different one-dimensional tips.

TABLE I. Quantities needed to reconstruct the full $r_c(t)$ dependence, for each investigated geometry at the largest investigated Tabor parameter μ_T. Radii are given in units of the (generalized) radius of curvature R and times in units of τ_{Mxw}. $\tau_{1/2}$ is defined implicitly by $C(\tau_{1/2}) = 1/2$.

D	n	r_{in}	r_{qs}	$\tau_{1/2}$	τ	μ_T	s
	1	0.0021	0.062	130	1060	4.1	19
1	2	0.11	0.46	23	910	41	5.9
	3	0.28	0.67	9.8	670	65	4.1
	4	0.41	0.78	6.6	750	79	3.5
	1	0.013	0.10	23	110	0.30	24
2	2	0.17	0.52	3.7	83	3.0	7.2
	3	0.35	0.71	1.6	45	4.8	4.9
	4	0.48	0.81	1.0	36	5.8	4.2

for the ultimate relaxation time τ as well as intermediate relaxation times τ_x defined by $C(\tau_x) = x$ with $x \gtrsim 0.5$. To make the different data sets appear in a rather narrow range, the Tabor parameter was scaled (multiplied) with a scaling variable s, while the relaxation time was divided by $s^{1.8}$ (Fig. 5).

It remains to be discussed to what degree our results depend on the precise form of the cohesive-zone model (CZM). To address this issue, we repeated some simulations using a Dugdale model[33] and found the same $\tau \propto \mu_T^{1.8}$ scaling law as when using Eq. (2). Prefactors of the scaling laws cannot be compared directly because the length scale used in the definition of the Tabor parameter can be either the literal range of adhesion ρ or the ratio of surface energy and maximum tensile stress. Taking the geometric mean of those two options makes the Dugdale potential relax roughly 15% more slowly than the default CZM with the same Tabor parameter. We attribute the slight increase in relaxation time and thus dissipation by the Dugdale model to the discontinuity of the CZM at the cutoff. It leads to

as to highlight differences in the functional form of $C(t)$ during the early-time dynamics. Note that the time is expressed in units of τ, which allows us to reveal that $C(t/\tau)$ is quite insensitive to μ_T at sufficiently large t. The collapse of curves when represented as $C(t/\tau)$ improves with increasingly large μ_T. Factors and related information helpful to reconstruct the full $r_c(t/\tau)$ are collected in Table I, however, each time only for the largest Tabor parameter.

The increase in relaxation time compared to the times associated with the Maxwell element can certainly be related to the increased dissipation that short-range adhesion causes in a propagating crack.[22,24,25] Initial dynamics are relatively fast, when the crack-tip radius is large and thus dissipation small[10,26] but then slows down as the crack-tip radius becomes smaller, while the slopes of the displacement field increase. For the investigated tip shapes, we find the relaxation times to scale approximately with $\mu_T^{1.8}$. This is true

FIG. 5. Scaled relaxation time as a function of a scaled Tabor parameter for different power law indenters and interfacial dimensions. Open and filled symbols refer to $D = 1$ and $D = 2$, respectively. Moreover, $n = 1$ (blue circles), $n = 2$ (orange squares), $n = 3$ (green diamonds), and $n = 4$ (red triangles). The dashed, gray line shows the power law $(s\mu_T)^{1.8}$.

a diverging second derivative, which in turn induces enhanced local surface velocity for a moving crack and thus enhanced velocity gradients in the material and increased total dissipation compared to more smoothly evolving CZMs.

IV. CONCLUSIONS

In this work, we confirmed numerically that the crack closure dynamics of indenters with power law profile in contact with an adhesive, linearly viscoelastic foundation has a universal behavior, at least at the late stages of the contact formation process when the contact radius has grown to a size that adhesion can be labeled short-ranged. Analysis of the final stages of the contact formation reveals that the relaxation times increase approximately with the inverse range of adhesion to the power of 1.8. Since Tabor parameters can be quite large in practical applications, this means that crack closure can last rather long times. To give an admittedly extreme example, assuming $E^* = 10$ MPa, $\gamma = 40$ mJ/m^2, $R = 20$ μm, and a range of adhesion typical for Lennard-Jones interactions, say $\rho = 3.5$ Å, yields $\mu_T = 195$. Thus, using the data for $D = n = 2$ in Table I, we obtain $\tau/\tau_{Mxw} \approx 83 \cdot (195/3)^{1.8} \approx 0.15 \cdot 10^6$. Making the link to real viscoelastic materials is challenging, because they have a broad distribution of relaxation times, which are quite sensitive to temperature and materials composition. This in turn makes it difficult if not impossible to state a generally valid numerical value for τ_{Mxw}. However, if a dynamical analysis is known, an upper estimate for τ_{Mxw} should be given by the equation $E''(1/\tau_{Mxw}) = E_0$ on the small-frequency branch of the loss modulus.

Unfortunately, it is not clear to what degree the scaling might be affected by small-scale roughness. In the extreme case, there will be contact line pinning due to elastic multistability, which can be caused by structural heterogeneity.[14] In this case, our estimates would only imply a crude lower bound for the contact formation time. A hint in this direction comes from previous simulations.[8] They mimicked successfully dynamical experiments on the adhesion between an elastomer and a flat punch to which (single-sinusoidal) small-scale roughness was added. In that work, we had identified a steeper dependence of relaxation times on the range of adhesion than in the present work, although our old estimate was based on an analysis, which was much less systematic than the one presented here.

AUTHOR DECLARATIONS

Conflict of Interest

The authors have no conflicts to disclose.

Author Contributions

C. Müller: Conceptualization (equal); Data curation (lead); Formal analysis (equal); Investigation (lead); Methodology (equal); Software (lead); Writing – original draft (supporting); Writing – review & editing (equal). **M. H. Müser**: Conceptualization (equal); Formal analysis (equal); Methodology (equal); Supervision (lead); Writing – original draft (lead); Writing – review & editing (equal).

DATA AVAILABILITY

The data that support the findings of this study are available from the corresponding author upon reasonable request.

APPENDIX: SCALING ANALYSIS AND GENERALIZED TABOR PARAMETER

While the contact mechanics of both short-range[30] and finite-range[32] adhesive power law indenters have been solved, it might be beneficial to have simple arguments allowing one to estimate pull-off forces, work of adhesion, and Tabor parameters in simple terms up to prefactors of order unity without having to embark on the high level of complexity pioneered by Maugis.[34] For this purpose, it is helpful to realize that the crack closure dynamics for a given $E(\omega)$ can only depend on the dimensionless numbers describing the problem, i.e., n and μ_T. In the following, we derive an expression, which, up to constants of order unity, gives the generalized Tabor parameter. To this end, we define μ_T such that $\mu_T \equiv 1$, when simple estimates for the stress-standard deviation in the limit of short-range adhesion match the maximum tension for finite-range adhesion. Our treatment also allows us to identify scaling relations for power law indenters. While similar relations can be deduced from existing literature, we believe our derivation to be original while requiring close to the least possible amount of prior background on contact mechanics and graphite, chalk, ink, or toner in order to arrive at generally valid scaling relations.

For a given shape (shp) of the displacement field, be it the zero-load (zl) or the pull-off (po) shape, the elastic energy U_{el} in areal contacts ($D = 2$) or its line density $u_{el} \equiv \Delta U_{el}/\Delta L_y$ in line contacts ($D = 1$) can only be of the form

$$U_{el} = g_{n,2}^{shp} E^* a h^2(a) \quad \text{for } D = 2, \tag{A1a}$$

$$u_{el} = g_{n,1}^{shp} E^* h^2(a) \quad \text{for } D = 1, \tag{A1b}$$

in the limit of short-range adhesion. Here, a is the contact radius, while the $g_{n,D}^{shp}$ are constants that depend on the exponent n, the interfacial dimension D, and on the shape of the displacement field. The corresponding total surface energy U_s or line density u_s gained on making contact are

$$U_s = -\pi a^2 \gamma \quad \text{for } D = 2, \tag{A2a}$$

$$u_s = -2a\gamma \quad \text{for } D = 1. \tag{A2b}$$

Eliminating $h(a)$ with the help of Eq. (1) and minimizing the total energy in the load-free case w.r.t. a yield a zero-load radii of

$$\frac{a_{zl}}{R} = \sqrt[2n-1]{\frac{c\gamma}{E^* R}} \quad \text{with } c = \begin{cases} \dfrac{2\pi n^2}{(2n+1)g_{n,2}^{zl}} & \text{for } D = 2, \\[2mm] n/g_{n,1}^{zl} & \text{for } D = 1. \end{cases} \tag{A3}$$

For the surface of a semi-infinite solid, the stress variance is nothing but $\Delta\sigma^2 = (E^*/2)^2\langle(\nabla u)^2\rangle$, where $\langle\cdots\rangle$ denotes spatial average. This relation is heavily exploited in Persson's contact mechanics theory for the contact mechanics of randomly rough contacts. However, it also turns out useful for deterministic tip shapes,

in particular power law indenters, when restricting the spatial average over the true contact. Since the mean-square height gradient $\bar{g}_c^2$ averaged over the contact satisfies

$$\bar{g}_c^2 = \left\langle (\nabla u)^2 \right\rangle_c$$
$$= \left(\frac{a}{R} \right)^{2n-2} \times \begin{cases} 1/n & \text{for } D = 2, \\ \dfrac{1}{2n-1} & \text{for } D = 1, \end{cases} \tag{A4}$$

the stress variance in the limit of short-range adhesion is roughly on par with the square of the maximum tension if

$$E^* \left(\frac{\gamma}{E^* R} \right)^{(n-1)/(2n-1)} = \frac{\gamma}{\rho}, \tag{A5}$$

where we suppressed all numerical prefactors, which are deemed to be usually of order unity. We define the Tabor parameter to be unity for the range of adhesion satisfying Eq. (A5) so that

$$\mu_T = \frac{\gamma}{E^* \rho} \left(\frac{\gamma}{E^* R} \right)^{(1-n)/(2n-1)}, \tag{A6}$$

which is identical to Eq. (5).

As a side comment, we note that our scaling analysis also allows the pull-off force F_{po} and the work of adhesion W_{po} in $D = 2$ and their corresponding line densities using lower-case letters in $D = 1$ to be estimated. To this end, we assume that the mean contact stress at pull-off scales linearly with the stress-standard deviation at zero load. Thus, $F_{po} \propto a_0^2 E^* \bar{g}_c$ for $D = 2$ while $f_{po} \propto a_0 E^* \bar{g}_c$ for $D = 1$ so that

$$F_{po} \propto E^* R^2 \left(\frac{\gamma}{E^* R} \right)^{(n+1)/(2n-1)} \quad \text{for } D = 2, \tag{A7a}$$

$$f_{po} \propto E^* R \left(\frac{\gamma}{E^* R} \right)^{n/(2n-1)} \quad \text{for } D = 1, \tag{A7b}$$

which satisfies well-known relations like $F_{po} \propto \gamma R$ for a regular Hertzian geometry ($n = 2, D = 2$) or $F_{po} \propto \sqrt{E^* \gamma R^3}$ for a regular flat punch ($n \to \infty, D = 2$). The work of adhesion of a power law indenter can only scale as the product of surface energy and (zero-load) contact area so that

$$W_{po} \propto \gamma R^2 \left(\frac{\gamma}{E^* R} \right)^{2/(2n-1)} \quad \text{for } D = 2, \tag{A8a}$$

$$w_{po} \propto \gamma R \left(\frac{\gamma}{E^* R} \right)^{1/(2n-1)} \quad \text{for } D = 1. \tag{A8b}$$

Thus, the work of adhesion for a flat punch in $D = 1$ and $D = 2$ alike is the same when conducted very slowly or very quickly, i.e., when probing it with the high- or the low-frequency modulus, but it would be large at intermediate pull-off velocities, as argued, for example, in Ref. 26.

REFERENCES

[1] M. H. Müser, W. B. Dapp, R. Bugnicourt, P. Sainsot, N. Lesaffre, T. A. Lubrecht, B. N. J. Persson, K. Harris, A. Bennett, K. Schulze, S. Rohde, P. Ifju, W. G. Sawyer, T. Angelini, H. Ashtari Esfahani, M. Kadkhodaei, S. Akbarzadeh, J.-J. Wu, G. Vorlaufer, A. Vernes, S. Solhjoo, A. I. Vakis, R. L. Jackson, Y. Xu, J. Streator, A. Rostami, D. Dini, S. Medina, G. Carbone, F. Bottiglione, L. Afferrante, J. Monti, L. Pastewka, M. O. Robbins, and J. A. Greenwood, "Meeting the contact-mechanics challenge," Tribol. Lett. **65**, 118 (2017).

[2] D. Wang, G. de Boer, A. Neville, and A. Ghanbarzadeh, "A review on modelling of viscoelastic contact problems," Lubricants **10**, 358 (2022).

[3] M. H. Müser and L. Nicola, "Modeling the surface topography dependence of friction, adhesion, and contact compliance," MRS Bull. **47**, 1221–1228 (2022).

[4] A. I. Bennett, K. L. Harris, K. D. Schulze, J. M. Urueña, A. J. McGhee, A. A. Pitenis, M. H. Müser, T. E. Angelini, and W. G. Sawyer, "Contact measurements of randomly rough surfaces," Tribol. Lett. **65**, 134 (2017).

[5] B. Weber, T. Suhina, T. Junge, L. Pastewka, A. M. Brouwer, and D. Bonn, "Molecular probes reveal deviations from amontons' law in multi-asperity frictional contacts," Nat. Commun. **9**, 888 (2018).

[6] F. Zhang, J. Liu, X. Ding, and R. Wang, "Experimental and finite element analyses of contact behaviors between non-transparent rough surfaces," J. Mech. Phys. Solids **126**, 87–100 (2019).

[7] G. Violano, A. Chateauminois, and L. Afferrante, "Rate-dependent adhesion of viscoelastic contacts. Part II: Numerical model and hysteresis dissipation," Mech. Mater. **158**, 103884 (2021).

[8] C. Müller, M. Samri, R. Hensel, E. Arzt, and M. H. Müser, "Revealing the coaction of viscous and multistability hysteresis in an adhesive, nominally flat punch: A combined numerical and experimental study," J. Mech. Phys. Solids **174**, 105260 (2023).

[9] C. Putignano and G. Carbone, "On the role of roughness in the indentation of viscoelastic solids," Tribol. Lett. **70**, 117 (2022).

[10] F. Pérez-Ràfols, J. S. Van Dokkum, and L. Nicola, "On the interplay between roughness and viscoelasticity in adhesive hysteresis," J. Mech. Phys. Solids **170**, 105079 (2023).

[11] B. Persson, "Contact mechanics for randomly rough surfaces," Surf. Sci. Rep. **61**, 201–227 (2006).

[12] S. Dalvi, A. Gujrati, S. R. Khanal, L. Pastewka, A. Dhinojwala, and T. D. B. Jacobs, "Linking energy loss in soft adhesion to surface roughness," Proc. Natl. Acad. Sci. U. S. A. **116**, 25484–25490 (2019).

[13] V. L. Popov, Q. Li, I. A. Lyashenko, and R. Pohrt, "Adhesion and friction in hard and soft contacts: Theory and experiment," Friction **9**, 1688–1706 (2021).

[14] A. Sanner and L. Pastewka, "Crack-front model for adhesion of soft elastic spheres with chemical heterogeneity," J. Mech. Phys. Solids **160**, 104781 (2022).

[15] A. Wang, Y. Zhou, and M. H. Müser, "Modeling adhesive hysteresis," Lubricants **9**, 17 (2021).

[16] M. Scaraggi and B. Persson, "Theory of viscoelastic lubrication," Tribol. Int. **72**, 118–130 (2014).

[17] M. Scaraggi and B. N. J. Persson, "Friction and universal contact area law for randomly rough viscoelastic contacts," J. Phys.: Condens. Matter **27**, 105102 (2015).

[18] J. S. van Dokkum and L. Nicola, "Green's function molecular dynamics including viscoelasticity," Modell. Simul. Mater. Sci. Eng. **27**, 075006 (2019).

[19] J. S. Van Dokkum, F. Pérez-Ràfols, L. Dorogin, and L. Nicola, "On the retraction of an adhesive cylindrical indenter from a viscoelastic substrate," Tribol. Int. **164**, 107234 (2021).

[20] L. Afferrante and G. Violano, "The adhesion of viscoelastic bodies with slightly wave surfaces," Tribol. Int. **174**, 107726 (2022).

[21] M. Ciavarella, J. Greenwood, and J. Barber, "Effect of tabor parameter on hysteresis losses during adhesive contact," J. Mech. Phys. Solids **98**, 236–244 (2017).

[22] R. A. Schapery, "A theory of crack initiation and growth in viscoelastic media," Int. J. Fract. **11**, 141–159 (1975).

[23] R. A. Schapery, "A theory of crack initiation and growth in viscoelastic media ii. approximate methods of analysis," Int. J. Fract. **11**, 369–388 (1975).

[24] P. G. de Gennes, "Soft adhesives," Langmuir **12**, 4497–4500 (1996).

[25] B. N. J. Persson and E. A. Brener, "Crack propagation in viscoelastic solids," Phys. Rev. E **71**, 036123 (2005).

[26] M. H. Müser and B. N. J. Persson, "Crack and pull-off dynamics of adhesive, viscoelastic solids," Europhys. Lett. **137**, 36004 (2022).

[27] C. Campañá and M. H. Müser, "Practical green's function approach to the simulation of elastic semi-infinite solids," Phys. Rev. B **74**, 075420 (2006).

[28] K. L. Johnson, K. Kendall, and A. D. Roberts, "Surface energy and the contact of elastic solids," Proc. R. Soc. A **324**, 301–313 (1971).

[29] I. N. Sneddon, "The relation between load and penetration in the axisymmetric Boussinesq problem for a punch of arbitrary profile," Int. J. Eng. Sci. **3**, 47–57 (1965).

[30] H. Yao and H. Gao, "Optimal shapes for adhesive binding between two elastic bodies," J. Colloid Interface Sci. **298**, 564–572 (2006).

[31] R. Bradley, "LXXIX. The cohesive force between solid surfaces and the surface energy of solids," London, Edinburgh Dublin Philos. Mag. J. Sci. **13**, 853–862 (1932).

[32] Z. Zheng and J. Yu, "Using the Dugdale approximation to match a specific interaction in the adhesive contact of elastic objects," J. Colloid Interface Sci. **310**, 27–34 (2007).

[33] D. Dugdale, "Yielding of steel sheets containing slits," J. Mech. Phys. Solids **8**, 100–104 (1960).

[34] D. Maugis, "Adhesion of spheres: The JKR-DMT transition using a Dugdale model," J. Colloid Interface Sci. **150**, 243–269 (1992).

25 December 2023 02:19:53

IV   Coaction of viscous and multistability hysteresis

Permission

Contributions of co-authors

Christian Müller: conceptualization, methodology: GFMD implementation, software, investigation: GFMD simulations, formal analysis, writing–original draft.
Manar Samri: conceptualization, methodology: experiments, investigation: experiments, writing–original draft.
René Hensel: conceptualization, supervision: experiments.
Eduard Arzt: conceptualization, writing–review & editing, funding acquisition.
Martin H. Müser: conceptualization, supervision: simulations, writing–original draft.

The study was conceptualized in the context of the MUSIGAND project led by E.A. R.H. and M.H.M. defined the system of interest, based on which M.S. and C.M. developed the experimental and numerical realization.

M.S. was responsible for the development of the experimental methodology under the supervision of R.H., including the design of the optical system for contact observation. A generalized viscoelastic material model, as well as an imitation of experimental boundary conditions and displacement control was implemented into GFMD by C.M. under the supervision of M.H.M. C.M. also developed a software to convert arbitrary digital height profiles into *stl* files.

All simulations were set up, run and post-processed by C.M. The authors acknowledge Xuan Zhang's fabrication of the wavy indenters by 3D printing. Optical and adhesion measurements were performed by M.S. and post-processed by M.S. and C.M. Ideas on how to evaluate and visualize results came from all authors and were then realized by M.S. and C.M.

The draft was prepared by C.M., M.S. and M.H.M. and then discussed and revised together with E.A. and R.H. Everyone agreed on the publication of the article in the Journal of the Mechanics and Physics of Solids and its inclusion in this thesis.

Revealing the coaction of viscous and multistability hysteresis in an adhesive, nominally flat punch: A combined numerical and experimental study

Christian Müller [a,b], Manar Samri [a], René Hensel [a], Eduard Arzt [a,b], Martin H. Müser [a,b,*]

[a] *INM - Leibniz Institute for New Materials, Germany*
[b] *Department of Materials Science, Saarland University, Germany*

A B S T R A C T

Viscoelasticity is well known to cause significant hysteresis of crack closure and opening when an elastomer is brought in and out of contact with a flat, rigid, adhesive counterface. A separate origin of adhesive hysteresis is small-scale, elastic multistability. Here, we study a system in which both mechanisms act concurrently. Specifically, we compare the simulated and experimentally measured time evolution of the interfacial force and the real contact area between a soft elastomer and a rigid, flat punch, to which small-scale, single-sinusoidal roughness is added. To this end, we further the Green's function molecular dynamics method and extend recently developed imaging techniques to elucidate the rate- and preload-dependence of the pull-off process. Our results reveal that hysteresis is much enhanced when the saddle points of the topography come into contact, which, however, is impeded by viscoelastic forces and may require sufficiently large preloads. A similar coaction of viscous- and multistability effects is expected to occur in macroscopic polymer contacts and to be relevant, e.g., for pressure-sensitive adhesives and modern adhesive gripping devices.

1. Introduction

Bringing two surfaces into contact and separating them again is generally associated with a net, rate-dependent energy loss. Several processes can cause this hysteresis to occur, in particular, physicochemical interfacial aging (Chen et al., 1991; Liu and Szlufarska, 2012), such as chain interdigitation in polymer–polymer contacts (Maeda et al., 2002), viscoelastic relaxation in the vicinity of and far from true contact (Giri et al., 2001; Shull, 2002; Lorenz et al., 2013; Tiwari et al., 2017), and the formation of capillaries (Pickering et al., 2001; Feiler et al., 2006; Israelachvili, 2011), to name a few. Over the years, elastic multistability (Prandtl, 1928; Tomlinson, 1929) has also received much attention as a potential adhesive dissipation mechanism occurring during the relative motion of nominally flat surfaces, i.e., the discontinuous jump of small-scale asperities in and out of contact (Tomlinson, 1929; Thomson et al., 1971; Gao and Rice, 1989; Zheng and Ya-Pu, 2004; Guduru, 2007; Glassmaker et al., 2007; Kesari et al., 2010; Xia et al., 2012; Carbone et al., 2015; Dalvi et al., 2019; Wang et al., 2021) during quasi-static motion, or the discontinuous motion of a contact line during approach and retraction resulting from chemical or structural surface heterogeneity (Sanner and Pastewka, 2022).

C. Müller et al.

Ascertaining what adhesion-hysteresis mechanism dominates under what circumstances is a difficult task, because analytical solutions for the rate- and/or the preload dependence of the pull-off force scarcely exist, even when only one relaxation process dominates. Moreover, it is certainly conceivable that competing mechanisms, e.g., contact aging and contact growth, lead to a similar, for example, logarithmic time dependence of the pull-off force on the waiting time. The validity of models and theories, irrespective of whether they are solved analytically or numerically, should therefore be tested against information additional to load–displacement relations and their dependence on rate, waiting time, and preload. A central quantity to be known is the time evolution of true contact, including its size and shape.

While small-scale features of adhesive experimental and *in-silico* contacts have been successfully compared in the recent past, such as in the contact-mechanics challenge (Müser et al., 2017; Bennett et al., 2017) or to demonstrate the breakdown of Amonton's law at the small scale in soft-matter contacts (Weber et al., 2018), we are not aware of similarly sophisticated studies involving time-dependent phenomena as they occur during adhesion hysteresis. Detailed comparisons between simulations and experiments are often conducted only during compression but not during retraction. This may be the case because simultaneously simulating multi-scale roughness, viscoelasticity, and adhesion has only been tackled recently (Afferrante and Violano, 2022; Pérez-Ràfols et al., 2022). Perez-Rafols et al. simulated a parabolic tip with single-wavelength roughness and found contributions of viscoelasticity and waviness to adhesion hysteresis to be nearly independent and additive as long as the viscoelasticity was confined to the edges of the wavy contact. However, despite being cutting edge, the study lacks comparison to experiments and is limited a single relaxation time and one-dimensional interfaces. Violano et al. (2021b,a) also modeled two surface dimensions with a bearing-area model and successfully compared to experiments. However, the surfaces were designed to have random asperity heights without spatial correlation, which formally corresponds to a Hurst exponent of $H = -2$. For $H \leq -1$, scaling laws deduced from rigorous simulations (Campañá et al., 2008) or Persson theory (Persson, 2008) predict spatial correlations to be absent at large distance so that one can get away with bearing-area models in this atypical situation.

The central difficulty when conducting rigorous, two-dimensional simulations lies in the short-range nature of adhesion, whose range of interaction ρ critically affects not only the viscoelastic losses caused by propagating cracks (Müser and Persson, 2022) but also the energy hysteresis induced by elastic instabilities (Ciavarella et al., 2017; Wang et al., 2021). Unfortunately, using realistically small values for ρ requires extremely fine discretization to be used so that lattice instabilities are avoided (Wang et al., 2021). The latter would lead to Coulomb friction for propagating cracks rather than to the more realistic polynomial crack-speed dependence (Schapery, 1975; Persson and Brener, 2005). As of now, it does not seem to be clear how to reproduce reliably realistic dynamics of viscoelastic adhesion theory with continuum-theory based simulations.

In this work, we study the contact between a viscoelastic film and a nominally flat, cylindrical punch to which single-wavelength, small-scale roughness is added. Depending on the relative orientation of different wavevectors $\mathbf{q}$, which all have the same magnitude q, different patterns can be produced for which the local height maxima form either a hexagonal or a triangular lattice. The questions to be addressed in this study are manifold. Can simulations reproduce experimentally observed dependencies, such as the normal force as a function of time and the concomitant contact-area evolution? How does the unit of time, or retraction velocity, have to be renormalized for a successful comparison between simulation and experiment when it is computationally unfeasible to work with realistically small values of ρ? Is it possible to clearly discriminate between dissipation due to elastic instabilities and viscoelastic crack propagation? And last but not least, can visualizing the contact area aid the prediction of imminent contact failure? The latter question can be relevant for modern adhesive gripping devices coupled with machine learning and robotics for performance prediction and automation (Tinnemann et al., 2019; Samri et al., 2022).

The remainder of this paper is organized as follows: Section 2 summarizes the ideal reference model, the computational approach, and the experimental methods. Results are presented in Section 3. A detailed discussion is given and conclusions are drawn in Section 4.

2. Models and methods

2.1. Reference model

In this work, we compare simulations and experiments mimicking an ideal (mathematical) reference model, which is sketched in Fig. 1. It consists of a flat, cylindrical, perfectly rigid punch of radius a to which single-wavelength corrugation $z(x, y)$ is added. The punch is indented into a homogeneous, isotropic, and elastomeric film with linear viscoelasticity. Inspired by the experimental realization, we will call this material PDMS, although the theoretical model does not necessarily imply a specific polymer compound. The elastomer has a finite height h, infinite in-plane dimension with a frequency-dependent Young's modulus $E(\omega)$ and a constant Poisson's ratio ν. "PDMS" and punch interact through a cohesive-zone model, which is characterized by a surface energy per unit area γ and a small but finite interaction range ρ. Punch and elastomer are frictionless and cannot interpenetrate.

Numerical values of the reference model are $a = 375$ μm, $h = 2$ mm, $E(0) = 2$ MPa, $E(\infty) = 2$ GPa, $\nu = 0.495$, and $\gamma = 50$ mJ/m^2, which are admittedly our best guesses for the values of the laboratory version of the reference model. The precise frequency dependence of $E(\omega)$ as well as the interaction range cannot be well matched between the laboratory and the *in-silico* realization of the reference model, which is why we abstain from defining reference values here. The experimental range of adhesion can certainly be classified as short-ranged, while that used in the simulations is merely as short-ranged as computationally feasible.

C. Müller et al.
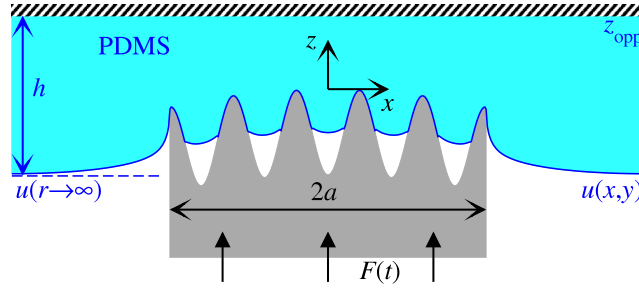
Fig. 1. Illustration of the reference system. Normal and lateral dimensions are not to scale. However, $u(x, y)$ and the indenter shape represent data obtained from the simulation during compression. The used height profile reflects deviations from the target and the true sinusoidal undulations of the flat punch.
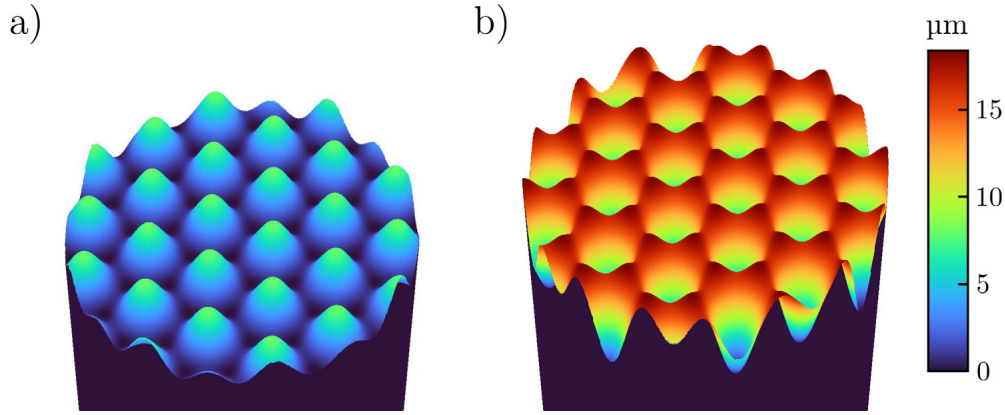
Fig. 2. Top view of the flat indenter with (a) triangular and (b) hexagonal waviness. Height and lateral dimensions are not to scale.

Two different height topographies are added to the punch, a triangular (tri) and a hexagonal (hex) one. Redefining prefactors compared to previous work (Dapp and Müser, 2015), they are given by

$$\frac{z_{\text{hex}}(x, y - \sqrt{3}\lambda/4)}{z_0(\text{hex})} = \frac{4}{9} \left\{ \frac{3}{2} + 2 \cos(qx) \cos\left(\frac{1}{\sqrt{3}} qy\right) + \cos\left(\frac{2}{\sqrt{3}} qy\right) \right\} \tag{1a}$$

$$\frac{z_{\text{tri}}(x, y)}{z_0(\text{tri})} = 2 - \frac{z_{\text{hex}}(x, y)}{z_0(\text{hex})}, \tag{1b}$$

where $q = 2\pi/\lambda$ is the wave vector and $\lambda = 150$ µm. The amplitude of the undulations—defined as half the difference between maximum and minimum—are set to $z_0(\text{hex}) = 9.2$ µm and $z_0(\text{tri}) = 4$ µm. Resulting punch profiles are shown in Fig. 2. Different amplitudes were chosen, because the jump into contact of saddle points occurs much earlier for hexagonal than for triangular corrugations (Dapp and Müser, 2015). With these choices of z_0, the radii of curvature of the asperities turned out to be $R_c \approx 150$ µm for both profiles. Moreover, the dimensionless surface energy $\tilde{\gamma} \equiv \gamma/v_{\text{ela}}^{\text{full}}$, where $v_{\text{ela}}^{\text{full}}$ is the areal elastic energy in full, static contact, $v_{\text{ela}}^{\text{full}}$, are approximately $\tilde{\gamma}(\text{tri}) \approx 0.32$ and $\tilde{\gamma}(\text{hex}) \approx 0.061$ for the respective, periodically repeated wave patterns. These values are less than 1/2, which has been identified as the (approximate) dividing line between sticky and non-sticky for many surfaces with a symmetric height distribution (Wang and Müser, 2022).

The indenter is moved from non-contact at different constant velocities v_{ext} ranging from 0.5 to 25 µm/s into the elastomer until a target force, or preload, F_{pl}, is reached, at which point the velocity is reverted quasi-instantaneously to initiate detachment. The preload is varied between 1 and 10 mN for the hexagonal and between 40 and 80 mN for the triangular surface.

A brief note on the choice of the frequency- and wavenumber-independent Poisson's ratio is in order. Real elastomers deviate from ideal incompressibility at high frequency much more than at low frequency, i.e., their Poisson's ratio falls from just below 0.5 at $\omega \to 0$ to typically around 0.3 for large ω (Caracciolo and Giovagnoni, 1996; Tschoegl et al., 2002). In the present study, we can ignore this effect, because the film thickness clearly exceeds the punch radius, which means that all relevant modes, other than the center-of-mass mode, can be treated as if the film was semi-infinite. In this case, the contact modulus, $E^*(\omega) = E(\omega)/\{1 - v^2(\omega)\}$, which is not very sensitive to the frequency dependence of the Poisson's ratio, becomes the central elastic parameter determining the viscoelastic response.

C. Müller et al.
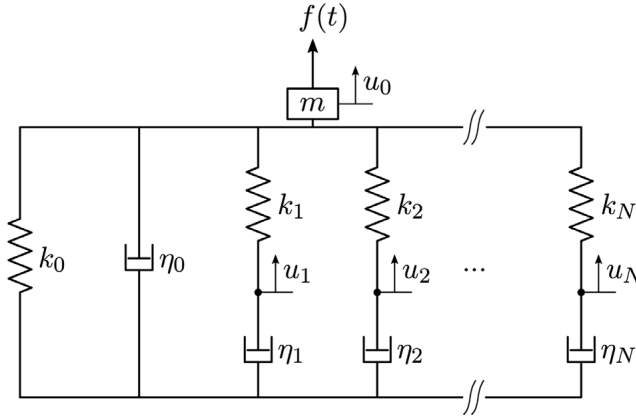
Fig. 3. Illustration of the rheological model employed, which consists of one Kelvin–Voigt element (k_0, η_0) and N Maxwell elements (k_n, η_n) in parallel plus an inertial mass m. In GFMD, each mode $\tilde{u}(\mathbf{q}) \hat{=} u_0$ is represented with such a model.

2.2. Numerical model and methods

The solution of the dynamics defined implicitly in Section 2.1 requires some idealizations to be given up, while other specifications can be perfectly realized, at least to numerical precision. The latter include linear elasticity, the topographies, velocities, loads, and any other specified number. Compromises are related to the numerical solution of the problem, which include the necessity to discretize space and time as well as the use of periodic boundary conditions for reasons of efficiency.

2.2.1. Reproducing viscoelastic properties using GFMD

The time evolution of an isotropic and linearly elastic bottom layer, being infinitely large in the plane or periodically repeated, can be cast as

$$\tilde{u}(\mathbf{q}, t) = \int_{-\infty}^{t} dt' \, \tilde{G}(q, t - t') \, \tilde{f}(\mathbf{q}, t'), \tag{2}$$

for reasons of symmetry. Here, $\tilde{u}(q, t)$ is the spatial Fourier transform of the displacement field as a function of time t, $\tilde{f}(\mathbf{q}, t)$ is the spatial Fourier transform of the external force per unit area acting on the elastomer, and $\tilde{G}(q, t - t')$ is the Green's function conveying the effect that this Fourier transform, at time $t' \leq t$ has on (the Fourier transform of) the displacement at time t. For a half space, $\tilde{G}(q, t)$ is formally given by

$$\tilde{G}(q, t) = \frac{2}{q} \int_{-\infty}^{\infty} d\omega \frac{1}{E^*(\omega)} e^{i\omega t}. \tag{3}$$

The time dependence of the Green's functions $\tilde{G}(q, t)$ or the response functions they produce can be represented via a Prony series, which in turn can be realized through rheological models, as that depicted in Fig. 3, where stiffness (k_n) and damping (η_n) terms are introduced. An appropriate choice of weights $\kappa_n = k_n/k_0$ and relaxation times $\tau_n = \eta_n/k_n$ allow the target frequency dependence $\kappa(\omega) = E(\omega)/E(0)$ to be approximated through

$$\kappa(\omega) = 1 + \sum_{n=1}^{N} \kappa_n \left\{ \frac{\omega^2 \tau_n^2}{1 + \omega^2 \tau_n^2} + i \frac{\omega \tau_n}{1 + \omega^2 \tau_n^2} \right\}. \tag{4}$$

An example of a system producing such a target dependence is shown in Fig. 4a.

An inertia m and damping η_0 were added to the rheological elements, which allowed us to implement the final rheological model into a Green's function molecular dynamics (GFMD) (Campañá and Müser, 2006) based code. The two added elements alter the frequency dependence to

$$\kappa_{\text{GFMD}}(\omega) = \kappa(\omega) - \omega^2 \frac{m}{k_0} + i\omega \frac{\eta_0}{k_0}. \tag{5}$$

By replacing k_0 with $k_0(q) = qE^*/2$ for each $\tilde{u}(\mathbf{q}, t)$, all k_n and η_n turn into $k_n(q)$ and $\eta_n(q)$, with the exception of $\eta_0(q)$, whose parametrization will be discussed separately.

The resulting equations of motion for each mode and its associated extra degrees of freedom $u_n(\mathbf{q}, t)$ read:

$$m(q)\ddot{\tilde{u}}(\mathbf{q}, t) + \eta_0(q)\dot{\tilde{u}}(\mathbf{q}, t) + k_\infty(q)\tilde{u}(\mathbf{q}, t) = \tilde{f}(\mathbf{q}, t) + \sum_{n=1}^{N} k_n(q)u_n(\mathbf{q}, t), \tag{6a}$$

$$\eta_n(q)\dot{u}_n(\mathbf{q}, t) = k_n(q)\left\{\tilde{u}(\mathbf{q}, t) - u_n(\mathbf{q}, t)\right\}, \quad n \in 1...N, \tag{6b}$$

C. Müller et al.
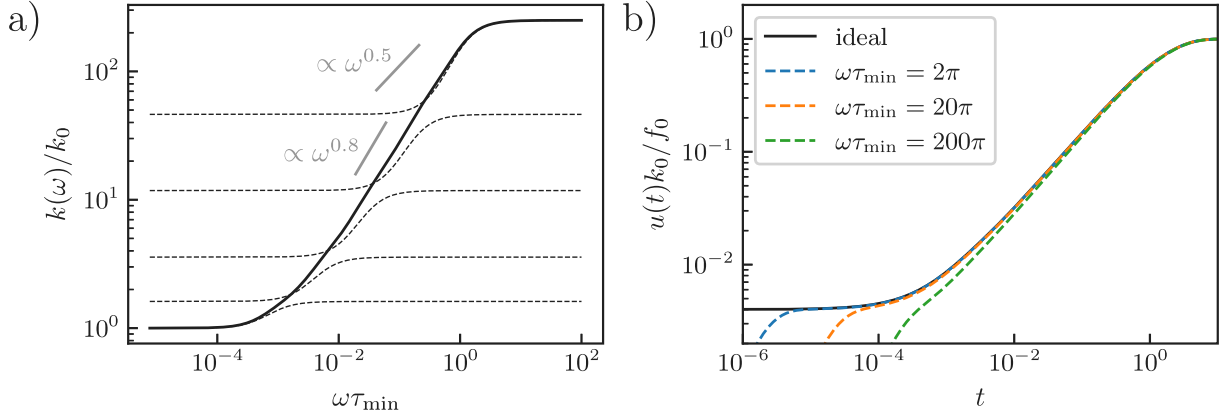
Fig. 4. (a) Frequency-dependent target stiffness $k(\omega)$ as a function of frequency ω using $k_{n+1} = 6^{0.8} k_n$, $\tau_{n+1} = \tau_n/6$, and $N = 5$. Dotted lines show the relaxation process of individual Maxwell elements and the solid, gray line a $\omega^{0.8}$ power law. A more realistic $\omega^{0.5}$ power law is shown for comparison. (b) Associated response function $u(t)$ to a point force $f(t) = f_0 \Theta(t)$ using different auxiliary masses leading to different eigenfrequencies $\omega_{\mathrm{GFMD}} = \sqrt{k_\infty/m}$. The full black line shows the ideal or target response function, while dashed colored lines reflect the implemented response function. In each case, the auxiliary damping was chosen to satisfy the condition for critical damping $\eta_0 = 2\, m\omega_{\mathrm{GFMD}}$.

with $k_\infty(q) \equiv \sum_{n=0}^{N} k_n(q)$, which is nothing but $k_\infty(q) = E(\infty)k_0(q)/E(0)$, where only one of the two "arrays" $k_0(\mathbf{q})$ and $k_\infty(\mathbf{q})$ needs to be stored in memory. Even for a single Maxwell element, the solution of the equations of motion turned out simpler and more stable (but not necessarily faster) than our previous extension to GFMD (Sukhomlinov and Müser, 2021), which was similar in spirit to that proposed by Van Dokkum and Nicola (2019) in that the first-order time derivatives of the external forces were needed. Our current approach rather resembles that pursued by Bugnicourt et al. (2017), who used Zener instead of Maxwell models and a conjugate gradient (CG) minimization method for the solution of the instantaneous or high-frequency response instead of the auxiliary masses.

Before proceeding, a few additional notes of clarification might be in order. First, tildes on the $u_n(\mathbf{q}, t)$ are omitted, as they are not subjected to an inverse Fourier transform. Second, the equations of motion solved in conventional GFMD are recuperated by setting $N = 0$, while the standard linear solid is obtained when using $N = 1$ and (infinitesimally) small values for m and η_0. Third, the presented methodology is readily extended to more general situations, even if the above treatment merely targets the specialized problem defined in Section 2. For example, if the elastic properties were anisotropic in the xy-plane, as they would be if the elastomer were prestrained in x but not in y direction, the coefficients $k_0(q)$ and thereby $k_n(q)$ and $\eta_n(q)$ would be functions of the vector $\mathbf{q}$ and not merely of its amplitude. Similarly, if the elastic properties changed with depth, as is the case when the crosslinking and thus the stiffness depends on the depth (Müser et al., 2019), but similarly when the elastomer is confined by a hard wall (Carbone and Mangialardi, 2008; Carbone et al., 2009), the term $k_0(q) = qE^*/2$ would have to be replaced or multiplied with an appropriate q-dependent function. Last but not least, using N Maxwell elements does not imply a single time step to take N times longer than a conventional GFMD time step, because the most demanding operation is the fast Fourier transform. For example, using $N = 5$ Maxwell elements per mode only increases the CPU time per time step by roughly 50%, compared to a regular GFMD time step for a discretization of 2048×2048. Relative costs on memory are clearly larger. The reason why we do not go beyond five Maxwell elements in this study is that almost four decades of relaxation times can be covered when choosing $\tau_{n+1} = \tau_n/6$, which requires the time step Δt to be chosen very small assuming τ_1 to remain fixed. Mimicking an even broader relaxation-time spectrum would impose further and eventually unfeasible demands on the used time step Δt.

While the values of $k_0(q)$ as well as $k_n(q)$ and $\eta_n(q)$ for $n \geq 1$ are predetermined by κ_n, τ_n, and E^*, the remaining parameters $m(q)$ and $\eta_0(q)$ should be chosen such that they provide a compromise between accuracy and efficiency. The goal must be to find the high-frequency elastic response as quickly as possible, albeit without making it necessary to dramatically reduce Δt. Under the made assumption that $E(\omega)$ does not depend on q, each free surface mode must have the same response function. This implies $m(q) \propto k_0(q)$, which is the choice made in so-called mass-weighted GFMD (Zhou et al., 2019). The period associated with the resulting frequency $\omega_{\mathrm{GFMD}} = \sqrt{k_\infty(q)/m(q)}$ is best chosen such that it is not much larger than $1/\tau_{\min} = 1/\tau_N = 1/\min(\tau_n)$. We found the "aggressive" choice of $\omega_{\mathrm{GFMD}}\tau_{\min} = 2\pi$ to be sufficient. If, however, the pulling velocity is so large that the time step Δt is no longer limited by $\tau_{\min}$ but by a large pulling velocity, e.g., by the ratio of a characteristic height amplitude and the pulling velocity, we recommend to set $m(q)$ such that $\omega_{\mathrm{GFMD}}\Delta t \approx \pi/10$ as to achieve a numerically stable but fast relaxation of the high-frequency response to its exact solution. After realizing that the left-hand side of Eq. (6a) represents a damped harmonic oscillator, $\eta_0(q)$ is set to satisfy the condition for critical damping, i.e., $\eta_0(q) = 2m(q)\omega_{\mathrm{GFMD}}$.

As a consequence of the just-made choices, the target viscoelastic response, for example, to an indenter exerting a force on a single (grid) point starting at time t_0, is mimicked quite accurately at times satisfying $t > t_0 + \tau_{\min}$, which can be achieved within one or two dozen time steps. The validity of this claim is demonstrated in Fig. 4b for our system with $N = 5$ Maxwell models. It can be seen that even $\omega_{\mathrm{GFMD}}\tau_{\min} = 2\pi$ leads to quite satisfactory results, although the time step, Δt was set by default to $\Delta t = \tau_{\min}/20$. The ratio k_∞/k_0 was reduced from its reference value of 1000 to 250 because this made the $\kappa(\omega)$ dependence at small ω be closer to the real PDMS (Tiwari et al., 2017) when using a single Maxwell element. When using five Maxwell elements, in addition to the k_0

C. Müller et al.

spring, we can produce a response function $E'(\omega)$ that roughly scales proportional to ω^β with $\beta \approx 0.8$ at an intermediate frequency ω_{int} defined through $E'(\omega_{\text{int}}) = \sqrt{E'(0)E'(\infty)}$, where $E'(\omega)$ is the storage modulus, i.e., the real part of the complex function $E(\omega)$. A single element yields $\beta \approx 2$, while experimental systems are often close to $\beta \lesssim 0.5$ (Tiwari et al., 2017). An exponent of $\beta = 0.8$ thus appeared a good trade-off between computational efficiency and reality.

2.2.2. Modeling adhesion

The adhesive and repulsive interaction between elastomer and indenter is modeled by the cohesive zone model (CZM) proposed in Ref. Wang et al. (2021). Assuming their two surfaces with nominal surface energy γ to have a gap $g(x, y)$, the interaction potential $\Gamma(g)$ is given by

$$\Gamma(g) = -\gamma \cdot \begin{cases} \{1 + \cos(\pi g/\rho)\}/2 & \text{for } 0 \le g < \rho \\ \{1 - (\pi g/\rho)^2/4\} & \text{for } g < 0 \\ 0 & \text{else}, \end{cases} \tag{7}$$

where ρ is the range of adhesion. Our CZM allows two surfaces to overlap marginally but penalizes the overlap with a harmonic function. Enforcing a strict non-overlap constraint might be possible, albeit only at a much enhanced numerical cost, since this would certainly require all internal modes $u_n(\mathbf{q})$ to be Fourier transformed. Moreover, the quadratic dependence of the potentials implies an upper bound for the stiffness of the equation to be solved, thereby ensuring stable integration with an appropriately chosen time step. The maximum adhesive stress $\sigma_{\text{th}} = \max(\mathrm{d}\Gamma/\mathrm{d}g)$ that can locally occur using this model is $\gamma\pi/(2\rho)$.

The range of adhesion is generally chosen such that it is as small as possible for a given discretization but not so small that lattice pinning and subsequent instabilities of the grid points at a propagating crack front would occur. This can be achieved when the maximum curvature of the potential is set to approximately $0.2q_{\text{ref}}E^*$, where $q_{\text{ref}} \equiv 2\pi n/L$, n being the number of discretization points parallel to one spatial direction and L the linear dimension of the periodically repeated simulation cell (Wang et al., 2021). Given a default choice of $L = 1.5$ mm and discretizations of the elastomer surface into grid points whose number ranged from 2048×2048 to 4096×4096, ρ turned out to lie in between 0.187 and 0.264 µm, which is not only much more than typical Lennard-Jones interaction ranges of 3 Å but also exceeds recent estimates (Thimons et al., 2021), which were obtained from experimentally measured pull-off forces between ruby and diamond, by a little more than a factor of ten.

To meaningfully compare simulations and experiments, it is necessary to assess whether the adhesive interactions used in the model are short- or long-ranged. This can be done using a (generalized) Tabor parameter, which is defined as the ratio $\mu_T = \rho_c/\rho$, where ρ_c is a characteristic interaction range at which the cross-over from short- to long-ranged adhesion takes place. Assuming that γ/E^* and a characteristic radius R_c are the only two independent length scales that can be constructed from the model, the only possible dependence of μ_T on the two length scales is

$$\mu_T = \frac{1}{\rho} R_c^\beta \left(\frac{\gamma}{E^*} \right)^{1-\beta}, \tag{8}$$

assuming either a flat punch with radius R_c or an indenter whose shape is a power law in the radius, i.e., $h(r) = R_c(r/R_c)^n/n$. It will be shown in a separate work that the exponent β turns out to be $\beta = (n-1)/(2n-1)$ so that $\beta = 1/3$ for a parabolic ($n = 2$) and $\beta = 1/2$ a flat-punch ($n \to \infty$) indenter. These two limiting cases agree with the definition of the conventional Tabor parameter for a parabolic indenter (Tabor, 1977) and for the parameter allowing one to assess if the high-velocity retraction of a flat-punch indenter fails through crack propagation or through uniform bond breaking. They correspond to the limits of $\mu_T \gg 1$ and $\mu_T \ll 1$, where the high-frequency rather than the small-frequency modulus is used in the calculation of the Tabor parameter (Persson, 2003).

The numerical Tabor parameters at the scale of local parameters turns out to be $\mu_T \approx 2$ for either profile when using the default discretization of 4096×4096 and thus $\rho = 0.187$ µm. This is because the radii of curvature associated with the peaks of the (ideal) profiles have similar values, namely $R_c = 163$ µm (triangular) and $R_c = 142$ µm (hexagonal). While $\mu_T \approx 2$ produces (quasi-static) load–displacement curves in contact similar to short-range adhesion (Müser, 2014; Wang et al., 2021), it must be considered long-ranged in non-contact (Ciavarella et al., 2017; Wang et al., 2021). This is because the jump-into contact occurs at a relatively large separation so that the adhesion hysteresis is about 50% of the true hysteresis for parabolic indenters with $\mu_T = 4$. From that point on, adhesion hysteresis converges only with the cubic root of the linear mesh size to the exact result (Wang et al., 2021). Consequently, simulations cannot be expected to reproduce experimental results with close-to-perfect precision, at least not using currently available methods and computers. If surfaces were not corrugated, the generalized Tabor parameter for the flat punch would be reasonably large, i.e., $\mu_T \approx 10$ for the 2048×2048 resolution and $\mu_T \approx 14$ for 4096×4096. It may also be of interest to calculate the Tabor parameter at a coarse scale, i.e., the one that is obtained when using the measured quasi-static pull-off force (from which an effective surface energy can be constructed) and the given range of adhesion while assuming a perfectly flat punch. For the hexagonal surface, these "effective" Tabor parameters turn out to be 0.880 and 1.24 for 2048×2048 and 4096×4096, respectively. The triangular variant shows a 40% smaller quasi-static pull-off force and hence an equally reduced effective Tabor parameter.

2.2.3. Refinements and corrections

A few adjustments were made to the numerical model in order to facilitate the comparison between simulations and experiments. Firstly, the velocity inversion was not abrupt but happened over a few but sufficiently many time steps to yield a smooth force–distance relation. Secondly, the 3D printing process introduces deviations from the ideal reference model, most notably an undesired macroscopic curvature, which was reflected in the numerical model. This curvature is a result of shrinkage induced by cross-linking during UV-curing. In selected simulations, we also accounted for the quasi-discrete height steps of $\Delta z = 0.2$ µm, which result from

C. Müller et al.
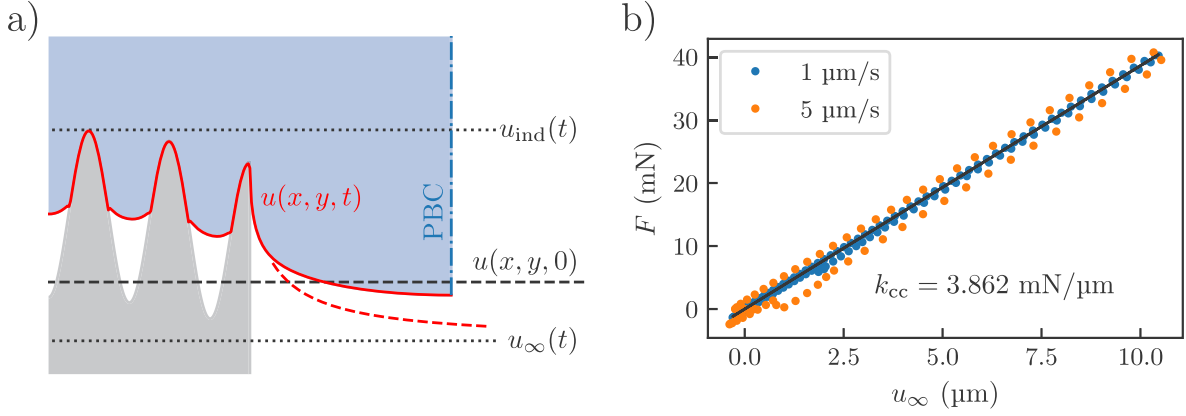
Fig. 5. (a) Illustration of the different displacements considered for compliance correction. (b) Linear fit of u_∞ for stiffness evaluation.

the layer-by-layer nature of the printing process. Final results were only marginally affected by this since Δz is of similar order of magnitude as our interaction ranges $\rho = 0.187$ to 0.264 µm and the steps in the topography are not very sharp.

A final technical aspect deserves mentioning. For reasons of computational efficiency, the buffer between the indenter and its periodic image should be made as small as possible but large enough so that the stress field on the indenter is not significantly affected. This is achieved quite well with our choice of $L = 4a$, supposedly because the displacement field of standard indenters approach the $1/r$ asymptotes quite closely at a distance from the symmetry axis being twice the contact radius. However, the center-of-mass mode of a periodically repeated surface, $\tilde{u}(q = 0)$, deviates from the real $u_\infty = u(r \gg a)$ that would be obtained in a real system without periodic boundary conditions (PBC) and with respect to which the indenter penetration is measured. An example for this difference is depicted in the form of the dashed and solid red lines in Fig. 5a. Given that $a/h = 5$ yields a contact stiffness only 20% in excess of the semi-infinite case (Hensel et al., 2019; Müller and Müser, 2022), the system can be approximately treated as semi-infinite so that the correction

$$u_\infty \approx 6u(L_x/2, L_y/2) - 5u(L_x/2, 0) \tag{9}$$

can be used, which was originally identified for sharp indenters in square simulation cells (Müser, 2014).

The described adjustment can also be thought of as a correction of an unwanted finite stiffness in the system, which does not always require a change of the experimental/numerical procedure. If the mismatch between ideal and measured indenter penetration, u_{ideal} and u_{ind}, is caused by a quasi-static elastic stiffness k_{cc}, it can be accounted for by adding the missing displacement during data post-processing with the correction $u_{ideal}(t) \approx u_{ind}(t) + \Delta u_{cc}$ with $\Delta u_{cc} = F(t)/k_{cc}$ and k_{cc} determined from $u_{ideal}(t) - u_{ind}(t) = u_\infty(t) = F(t)/k_{cc}$ as shown in Fig. 5b. Similarly, the experimental curves must be corrected for the machine compliance or machine stiffness k_M to $u_{ideal} = u_{ind}(t) - F(t)/k_M$. It turned out that the visualization of differences between experiments and simulations was best when subtracting the correction Δu_{cc} from the experiments rather than adding it to the simulations.

An issue to keep in mind regarding compliance corrections is that the occurrence of local instabilities, e.g. pull-off events, generally depends on the global system compliance. As such, the effect of k_{cc} on the load–displacement curves cannot be rigorously accounted for in post-processing (Booth and Hensel, 2021; Hensel et al., 2021). For viscoelastic systems, it may also happen that a simulation or measurement performed at constant speed $u_{ind}(t) = v_{ext}t$ implies that $\mathrm{d}u_{ideal}(t)/\mathrm{d}t$ is not exactly constant but varies over time as $(1/k_{cc})\mathrm{d}F(t)/\mathrm{d}t$ or $(-1/k_M)\mathrm{d}F(t)/\mathrm{d}t$.

2.3. Experimental methods

The development of optical observation techniques has benefited a wide range of applications, notably for assessing the true contact area between solids. Frustrated total internal reflection (FTIR) started to be applied to image the contact in the 1960s (Harrick, 1962; McCutchen, 1964). FTIR and related methods are routinely employed nowadays to measure stress distributions (Eason et al., 2015), contact area of rough surfaces (Bennett et al., 2017; McGhee et al., 2017), or to visualize the contact formation and separation of fibrillar microstructures (Tinnemann et al., 2019; Samri et al., 2021; Thiemecke and Hensel, 2020; Samri et al., 2022; Booth and Hensel, 2021). Despite the successful use of FTIR to determine multiple contact properties, obtaining high contrasts is limited to observing the contact of an opaque specimen through a transparent counter-surface. Another technique that was employed for contact measurement is the optical interference observed as Newton's rings (McCutchen, 1964; Wahl and Sawyer, 2008; Sawyer and Wahl, 2008). This technique became more and more relevant in contact mechanics and tribology after Krick et al. (2012) employed it to develop an *in-situ* optical micro tribometer, which allowed them to visualize the intimate contact between solids during loading and sliding experiments. In this work we use a new approach for contact observation based on the coaxial lighting principle, as illustrated in Fig. 6. Using light from a collimated light source (collimated LED, Thorlabs, New Jersey, USA), a parallel light beam is created for homogeneous lighting. The parallel beam is scattered at the contact points between indenter and substrate, reducing

C. Müller et al.
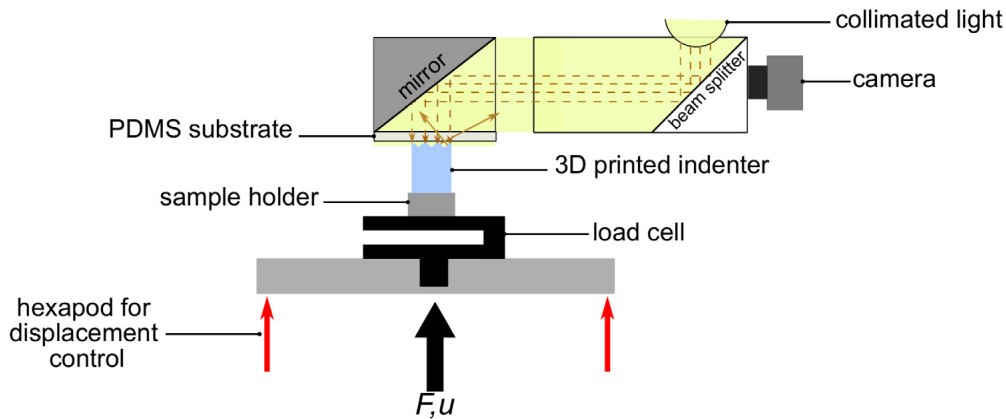
Fig. 6. Schematic representation of the experimental setup.

the intensity that is reflected back to the camera. This enhances the contrast between contact and non-contact areas compared to non-parallel or transmitted light. It also makes it easy to keep the optics in focus, because the reflecting surface remains static during the experiment.

In preparation of the 3D printing process, the computer-generated topographies shown in Fig. 2 were converted to STL file format, vertically sliced into slabs with an adaptive thickness of 0.2 to 1.0 μm and laterally hatched with a fixed width of 0.5 μm. The resulting models were then printed by a two-photon lithography direct laser writing device (Photonic Professional GT2, Nanoscribe, Karlsruhe, Germany), using a 25x objective, writing speed of 100 mm/s, and a laser power of 40 mW. The printing material was a commercial photoresist (IP-S, Nanoscribe, Karlsruhe, Germany) used in dip-in mode, with an elastic modulus of $E_{\text{IP-S}} = 1.34$ GPa. After being printed, the indenter topographies were measured using a confocal microscope (MarSurf CM expert, Mahr, Göttingen, Germany).

The substrate was fabricated from PDMS (Sylgard 184, Dow, Midland, MI, USA) by mixing the base and the curing agent in a ratio of 10 : 1. The pre-polymer was degassed using a Speed-Mixer (DAC600.2 VAC-P, Hauschild Engineering, Hamm, Germany) with 2350 rpm at 1 mbar for 3 min and then cured at 95 °C for 1 h. Fig. 6 shows the employed custom setup for tack tests with optical contact imaging. The normal displacement was controlled by a SMARPOD hexapod (SmarAct, Oldenbug Germany) and the force was measured by a 2 N load cell. The PDMS substrate was glued to the bottom of a transparent sample holder containing a mirror allowing the side-mounted optical system to see through. This holder was mounted to a modular positioning system with six degrees of freedom (SmarAct, Oldenbug Germany) for precise surface alignment using two side-view cameras. The whole mechanical setup was measured to have an effective machine stiffness of $k_{\text{M}} = 38.1$ kN/m. Videos of the contact evolution during the tack tests were recorded at 50 frames per second using a digital camera (DFK 33UX273, Imaging Source Europe GmbH, Bremen, Germany). All experiments were performed in a laboratory with regulated temperature of 21 ± 0.2 °C and relative humidity at $50 \pm 5\%$.

3. Results

3.1. 3D printing

We first analyze optical images of the experimental topographies obtained by the 3D printing process. Fig. 7a shows the difference between targeted and measured height profile exemplarily for the triangular surface. The main deviation between them is a mean curvature, which is supposedly due to shrinkage of the resin after 3D printing. This global curvature was reflected in the topographies used for the simulations. Ignoring it substantially reduces the agreement between simulations and experiment, because stresses in the flat-punch solution are largest where the correction is most noticeable. Ideal, simulated, and experimental height profiles are compared in Fig. 7b.

3.2. Tack tests for the triangular surface

Fig. 8 shows the measured and simulated load–displacement curves obtained for the triangular surface. The loading process, shown as a gray dashed line, is smooth and rather insensitive to the approach velocity. The more interesting detachment parts of the curves are highlighted in color. Experiments and simulations show similar trends: Two bulges occur at small velocity v_{ext} and small preload F_{pl}. A bulge located at slightly compressive force is related to the detachment of saddle points—as revealed in more detail further below—while the bulge at a tensile force relates to the final pull-off process. Their locations approach each other when either v_{ext} and/or F_{pl} is increased. Ultimately, they merge into a single minimum, whose value corresponds to the (negative) pull-off force. Although experimental and simulated curves agree only semi-quantitatively, the tensile pull-off force is increased from about $F_{\text{po}} = 2.5 \pm 0.5$ mN for a preload force of $F_{\text{pl}} = 40$ mN to up to $F_{\text{po}} = 14 \pm 2$ mN for $F_{\text{pl}} = 80$ mN in both cases.

C. Müller et al.
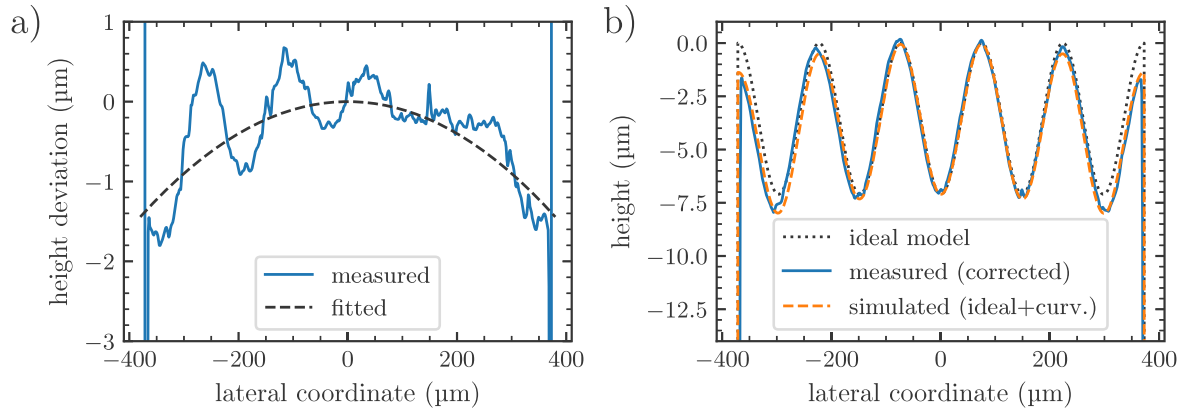
Fig. 7. (a) Deviation of an experimental line profile from the ideal model and (b) absolute heights of model, simulated and experimental indenter, shown exemplarily for the triangular pattern. The curvature correction shown in (a) proved necessary for a successful comparisons between simulations and experiments.
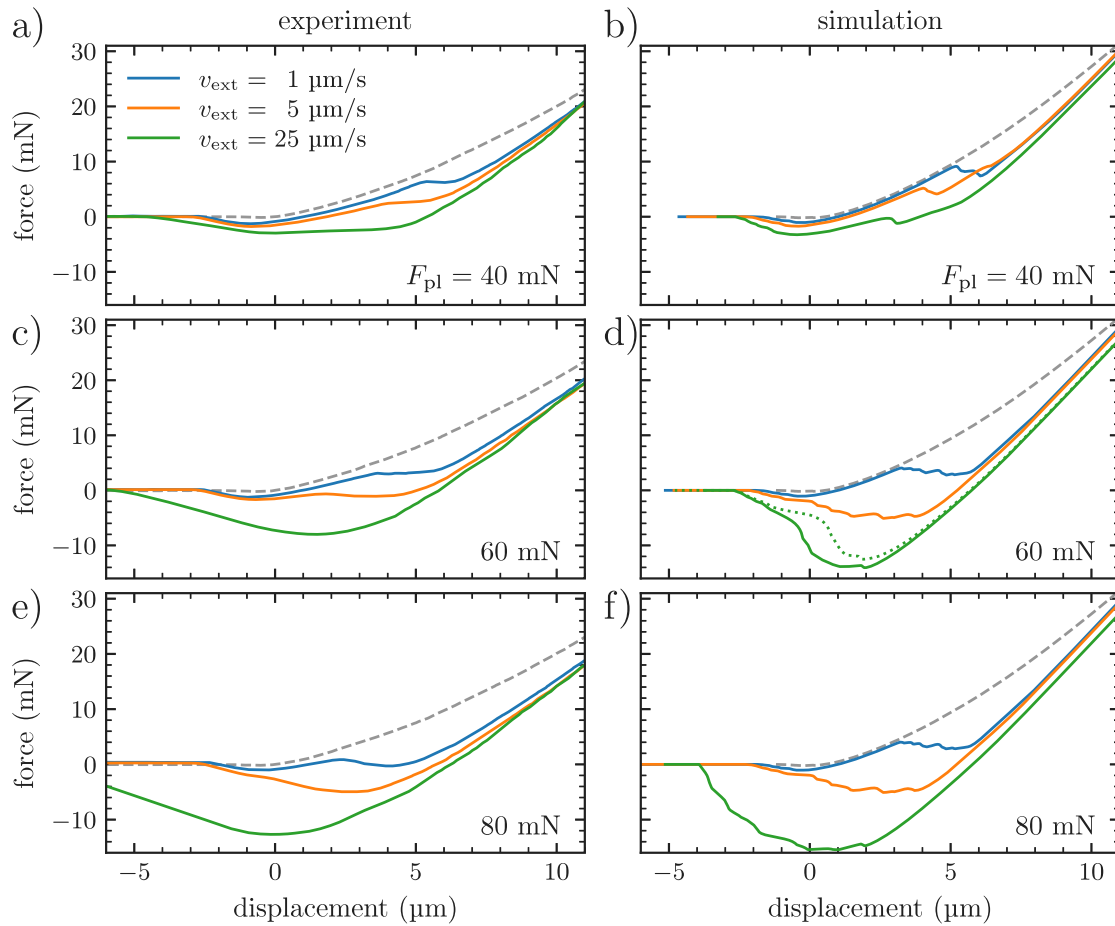
Fig. 8. Load–displacement curves recorded during the detachment of the triangular surface at different velocities. The left column always shows experimental results, while the right column shows single-relaxation time simulations. From the first to the last row, the preload is increased from 40 to 60 and then 80 mN. Semi-quantitative agreement is achieved across the board, despite a slight mismatch in macroscopic contact stiffness and the intermediate preload case.

One qualitative difference between the experimental and the simulation data is that the simulation data is more rugged. The smoother experimental data arises for three reasons: first, symmetry-related peaks in the real punch do not have the exact same height so that they depin at slightly different moments, while symmetry is perfect in simulations yielding sharper signals. Second, the real viscoelastic response function is based on a broader range of relaxation times. Third, the experimental data was low-pass filtered with a resolution of approximately 0.1 μm.

C. Müller et al.

It is quite noticeable that the comparison for $F_{pl} = 60$ mN in Fig. 8 is substantially less good than for the other two preloads. This is because a jump into full contact occurs in the simulations a little before 60 mN were reached, while valleys are a nudge short of making contact in the experiments. One effect potentially contributing to the later, experimental jump-into-full-contact instability — in addition to the single-relaxation time approximation — could be the drag forces exerted by the air that needs to be squeezed out of the thin gap between elastomer and indenter before reaching full contact. To indirectly account for, or, fake, the absence of full contact at intermediate loads, we added a dotted line from a simulation with a slightly reduced preload of $F_{pl} = 50$ mN, whereby agreement with experiments was much enhanced.

The sensitivity of the load–displacement curves w.r.t. range of adhesion and the viscoelastic model will be scrutinized after establishing that the semi-quantitative agreement between experimental and simulated load–displacement curves is not fortuitous: experimental and simulated contact topographies evolve in concert, as is revealed exemplarily in Fig. 9 for the preload of $F_{pl} = 40$ mN and the retraction velocity of $v_{ext} = 1$ μm/s. In the simulations representing two differently parametrized single-relaxation time models, dark gray means contact (negative gap), medium gray is experimentally indistinguishable from contact ($0 \leq g \lesssim 500$ nm), while light gray is non-contact and very light gray the background color. The gray shades in the real-laboratory, optical images do not allow us to determine the true interfacial separation to a high precision. Yet, very dark pixels can be assumed to indicate contact, while less dark and bright pixels certainly imply non-contact. Hence, the medium-gray color level was introduced to represent gaps smaller than the medium wavelength of visible light, which we expect to appear quite dark in the optical images. To better visualize details of the gap distribution in the *in-silico* surface, heat maps of the interfacial stresses are included in Fig. 9 and in later related figures for the hexagonal surface.

Experiments and simulations reveal similar characteristics: at the point of maximum preload, contact occurs in all peaks but only in those saddle points that are close to the outer rim, despite the slightly convex macroscopic surface curvature. The snapshots in the last two columns of Fig. 9 were taken right before and after the bulge in the force–displacement curve near a displacement of 6 μm. Hence, we can associate this bulge with the saddle-point detachment at the outer rim of the corrugated punch whenever it did occur.

Similar qualitative agreement of the contact evolution in real-laboratory and *in-silico* was found for all load–displacement curves shown in this study. Nonetheless, quantitative differences exist: for example, while the initial experimental and simulated frames at the maximum preload in the left column of Fig. 9 look astoundingly similar, given that the simulations cannot be seen as short-range adhesion on approach, the experimental contact barely changes to the next shown image. In contrast, the *in-silico* contact reveals a noticeable retardation or aftereffect from the moments of high compression during the initial decompression in that the contact keeps growing slightly. We attribute this to the necessity of large viscoelastic relaxation times for a proper reproduction of the dissipation caused by moving cracks. This makes the response to simple indentation be too sluggish so that aftereffects of the compression branch are noticeable shortly after inverting the direction of motion. Upon further decompression, the trend reverses and the contact evolves slightly more slowly in the experiments than in the simulations: the destruction of contact at the saddle points between the last two columns of Fig. 9 happens earlier in the simulations than in the experiments.

To elucidate the role of the range of adhesion on the dynamics, we contrast the contact formation obtained in two simulations based on slightly different models, which both assume a single relaxation time and the same E_∞ / E_0 ratio. The second model uses a range of adhesion that is increased by a factor of $\sqrt{2}$ w.r.t. the first model while the relaxation time was multiplied with 2.5 to achieve close agreement between the dynamics of the two models. A slightly different redefinition of the relaxation time might have lead to even better agreement. However, even with the made choice, the second and the third row of Fig. 9, representing the alternative and the default single-relaxation time model, respectively, barely allow the naked eye to distinguish the contact break-up between the two models. Only the second contact images, taken at a time $1.125\ t_{pl}$, where t_{pl} is the time elapsed between initial contact and maximum compressive load, differ slightly: in the given time of $0.125\ t_{pl}$, the contact with the smaller relaxation time has grown more than the other one.

The reason why changing the viscoelastic relaxation time can be "compensated" by a change in the range of adhesion ρ during the retraction process is an interplay between the range of adhesion and the viscoelastic properties of the elastomer (Schapery, 1975; Müser and Persson, 2022). The dissipation caused by the propagating opening cracks must be reproduced in simulations in order to yield accurate load–displacement curves. Since steeper slopes at the contact edge imply larger (relative) velocities in a moving crack and thus enhanced dissipation, a shorter range of adhesion, leading to steeper slopes, can be compensated by shorter relaxation times used in the viscoelastic model.

To elucidate the role of viscoelasticity, three different viscoelastic models were considered in addition to the purely elastic model reflecting the quasi-static limit. Their frequency-dependent contact moduli are depicted in Fig. 10a with model 1 having a single relaxation time of $\tau = 400$ μs and $E_\infty / E_0 = 250$, while model 2 and 3 contain five relaxation times—with ratios and weight chosen as described in Section 2.2 and $\tau_{min} = 40$ μs. Moreover, $E_\infty / E_0 = 8$ in model 2 and $E_\infty / E_0 = 250$ in model 3. Panels (b–d) in Fig. 10 reveal that all three viscoelastic models increase the adhesion hysteresis with respect to the quasi-static model, which shows a rather small pull-off force of 0.7 mN independent of the preload. While the effect is relatively minor for model 2 with its relatively small E_∞ / E_0 ratio, the preload sensitivity is largest for model 3 with a large E_∞ / E_0 ratio and a tail of the "excess"-$E(\omega)$ extending to small frequencies. Interestingly, the changes to the viscoelastic model in that range of frequencies seems to have a larger impact than the change associated with the high-frequency end of the spectrum. For the intermediate preload of 60 mN, the maximum tensile force occurs at slightly positive displacement and is clearly associated with the detachment of saddle-points rather than with that of asperity peaks.

C. Müller et al.
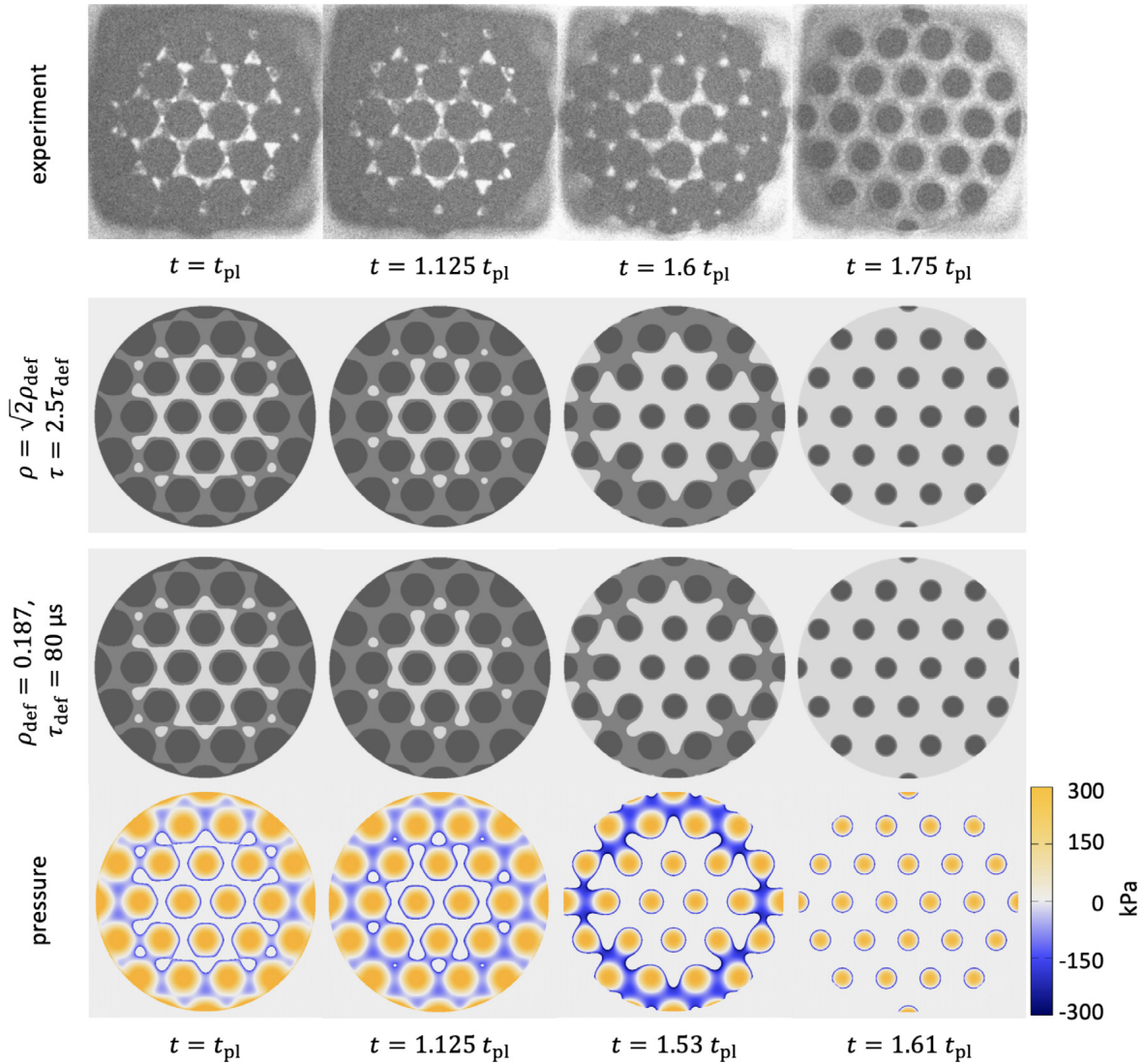
Fig. 9. Contact observation during retraction in a tack test at 1 μm/s and a maximum compressive load of F_{pl} = 40 mN. The upper row shows experimental data, while the two center rows represent simulations using different relaxation time τ and range of adhesion ρ. The darker areas represent points with interfacial separations less than 500 nm, while the lighter areas represent larger gaps. The last row shows the pressure distribution associated with the previous row. t_{pl} denotes the time between first contact and preload for the respective row. The times for the last two columns are located just before and past the bulge in the force–displacement curve on the compressive part of the unloading curve, i.e. at $u \approx 5$ μm. Similar features are observed in all cases, e.g., the loss of contacts start with the saddle points at the edges and contact exists in all asperities but in no saddle point before the maximum tensile force during detachment is reached, i.e., at a displacement near −1 μm.

3.3. Tack tests for the hexagonal surface

The tack tests on the hexagonal surface were carried out similarly as on the triangular surface, however using smaller preloads. The resulting load–displacement curves are shown in Fig. 11, this time only for two velocities but including the loading part. The $v_{ext} = 1$ μm/s contact evolution is depicted in Fig. 12 with an emphasis on the loading rather than the detachment process.

The force–displacement curves on separation contain only one minimum at all investigated velocities for the hexagonal surface. The extra bulge related to the saddle-point detachment in the triangular surface has disappeared for the hexagonal pattern, because their detachment coincided in all investigated cases with that of the asperity peaks. This is because saddle points are almost as high as the peaks in the hexagonal lattice. In fact, they are so high that contact formation of saddle points between asperities occurs shortly after (0.7 μm) contact formation at the peaks even in the quasi-static limit on approach. This, in turn, is due to the fact that the height of the contact line of a zero-load isolated asperity (in the Hertzian, i.e., parabolic approximation) almost extends down to a height where the corrugated profile crosses over from convex to concave. Due to the large dissipation of a propagating closing crack, viscoelastic saddle-point contact formation is far from being instantaneous.

C. Müller et al.
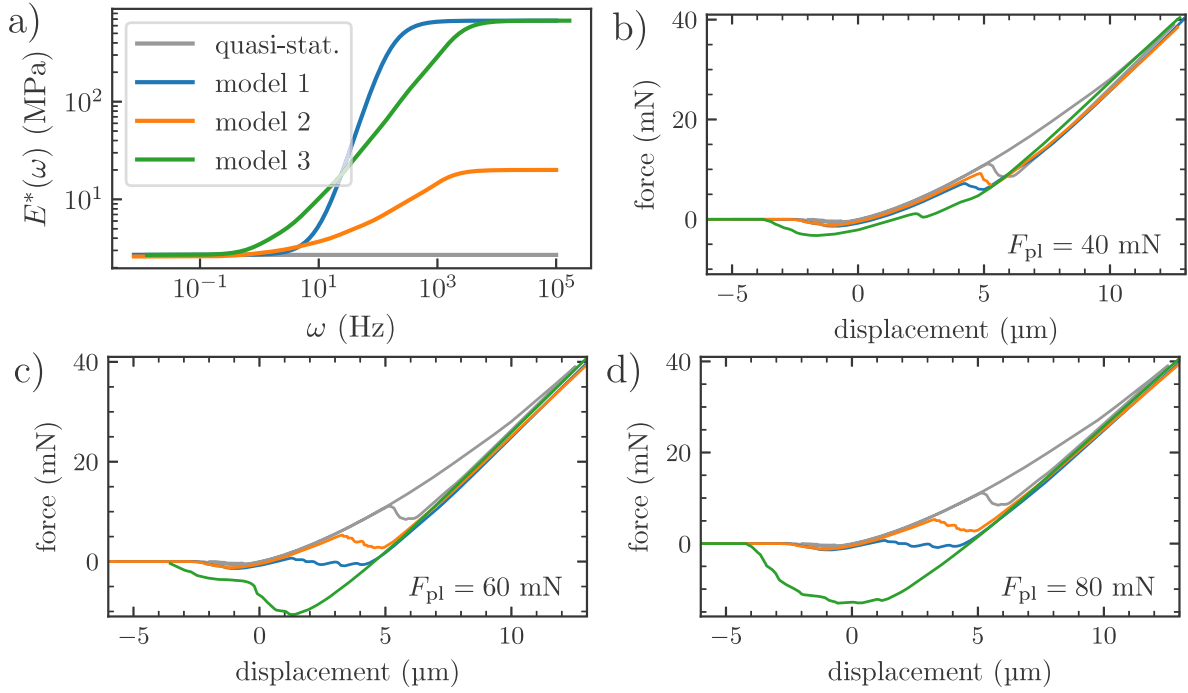
Fig. 10. Load–displacement curves obtained for the triangular surface exposed to a preload of (b) 40 mN, (c) 60 mN and (d) 80 mN using different rheological models defined in panel (a). The detachment speed is 1 μm/s in all cases. Larger stiffness at small frequencies leads to larger pull-off forces.

While the detachment curve shows fewer features for the hexagonal than for the triangular pattern, the approach curves for the operating velocities of 1 and 25 μm/s no longer superimpose within line width in Fig. 11. More interestingly, the load–displacement curves under compression start to be quasi-linear at a load of roughly 4 mN, at which point all saddle points have made contact. Upon decompression, the quasi-linear dependence applies to normal loads well below 4 mN and ends when saddle points start to jump out of contact.

Increasing the preload past the point of saddle point formation changes the load–displacement relation for the hexagonal pattern only moderately, particularly little between panels c and e of Fig. 11, corresponding to $F_{pl} = 5$ and 10 mN, respectively. This can be rationalized by the contact image obtained at the maximum tensile force in the last column of Fig. 12, where most saddle points are still in contact. Those panels also corroborate the statement made at the beginning of the results section that correcting for the "macroscopic" surface curvature induced during cooling after the printing process was needed to achieve reasonable or, depending on viewpoint, good agreement between the laboratory and *in-silico* samples: the contact area close to the rim of the punch is noticeably reduced by the "macroscopic" curvature correction.

4. Discussion and conclusions

This work addressed the interplay between viscoelastic hysteresis in contact mechanics and the hysteresis due to elastic multistability being responsible for the quasi-discontinuous snap into and out of individual contact patches observable during quasi-static driving. To elucidate the coaction of viscoelastic and multistability effects, we studied numerically and experimentally a flat punch to which small-scale corrugation—in the form of either a hexagonal or a triangular height profile—was added. The two height spectra are identical although the profiles are their mutual negatives, i.e., the phases of the height Fourier coefficients are shifted by π. This makes the saddle points, which are located between two maxima and which turn out crucial for the contact mechanics, be closer to the asperity summits in the hexagonal than in the triangular lattice.

Contact of an *ideal* flat punch forms quasi-instantaneously so that both viscoelastic losses due to closing cracks and multi-stability effects are negligible on approach. Consequently, preload effects of ideal-punch detachment are minor. However, the detachment requires a crack to propagate from the rim to the center, which leads to a viscoelasticity-enhanced work of separation at intermediate pull-off velocities (Jiang et al., 2014; Müser and Persson, 2022): the work of separation approaches $2\gamma A$ at very small and very large velocities, assuming high- and low-frequency contact moduli to be well defined.

After small-scale roughness was added to the flat punch, the wavelength of the pattern being one fifth of the punch diameter, strong preload effects occurred at intermediate operating velocities but not under quasi-static driving. Thus, preload and multi-stability effects are intertwined in the corrugated punches. The preload effects were distinctly larger for the triangular than for the hexagonal pattern. Specifically, the pull-off force for the hexagonal lattice saturated at roughly 6 (experiment) and 7 mN (simulation) once the preload had reached 5 to 10 mN at an operating velocity of 25 μm/s. These two forces were roughly twice and ten times

C. Müller et al.
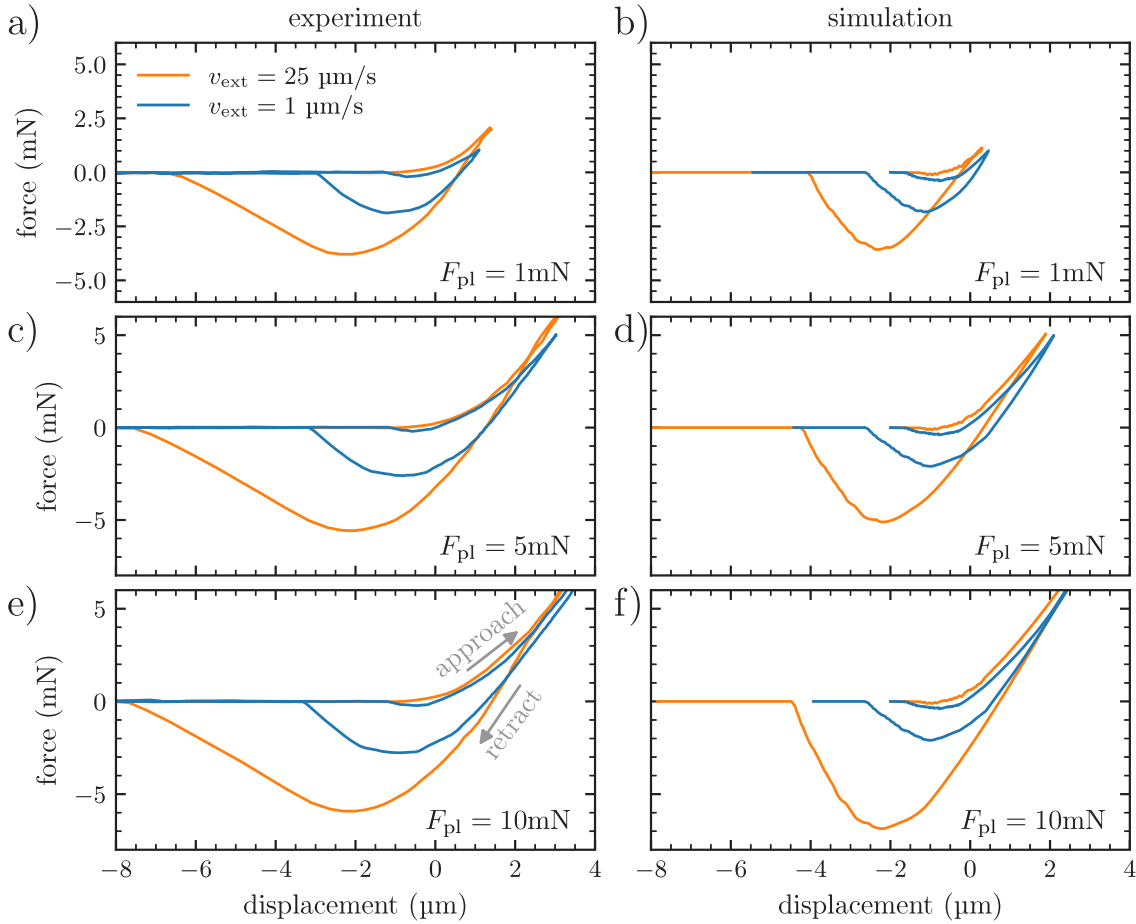
Fig. 11. Load–displacement curves obtained during detachment at different velocities for the hexagonal pattern. The left column shows experimental results, while the right column shows single-relaxation-time simulations. The preload increases from 1 to 5 and then to 10 mN from the first to the last row,. A quasi-static reference calculation with the same adhesive interaction resulted in a pull-off force of 1.2 mN and a tensile force of 0.8 mN immediately after the jump-into-contact instability. Preload effects are distinctly reduced compared to the triangular surface in experiment and simulation alike.

larger, respectively, for the triangular pattern. Despite these quantitative differences, pull-off forces saturated in both cases once the preload had been large enough to induce contact at the saddle points and retraction was fast enough so that saddle-points were still in contact at the point of maximum tensile force. Since the saddle-point heights are rather close to (far from) the height maxima in the hexagonal (triangular) lattice, preload effects saturated earlier in the hexagonal than in the triangular system, although the hexagonal amplitude was chosen more than twice that of the triangular corrugation.

A purely spectral approach to our system assuming random phases, as pursued in Persson's contact mechanics theory (Persson, 2001, 2002), would not be in a position to reproduce or predict the observed trends. In the quasi-static case, the hexagonal surface pattern even shows a substantially larger pull-off force than the triangular one, despite its 2.3 times larger height amplitude. In principle, phase-correlation effects can be included into the theory (Müser, 2008; Zhou and Müser, 2020), which might fix this shortcoming. Furthermore, Persson's rough surface contact theory only takes either viscoelasticity (Persson, 2001) *or* adhesion (Persson, 2002) into account, but not (yet) both simultaneously. Both effects have to be accounted for in a proper description of our system.

Can our results be rationalized with bearing-area models (BAMs), such as the popular approach by Fuller and Tabor (1975) for nominally flat, adhesive contacts? BAMs assume the highest asperity to come into contact first and out of contact last, the second-highest peak to come into contact second and out of contact second last, and so on and so forth. The load–displacement laws of the individual peaks, whose shapes are approximated as paraboloids, are then added up to yield a global load–displacement curve. While BAMs are commonly used to describe quasi-static contact loading, generalization to dynamics seems to be straightforward, e.g., by "feeding" the time-dependent force–displacement relation of an isolated asperity contact at the given operating velocity into the model, see also Ref. Violano et al. (2021b). For our system, the radii of curvature of the hexagonal and the triangular lattice turned out quite similar. (The minor curvature corrections w.r.t. the ideal model changes things quantitatively but not qualitatively.) Thus, the depinning force of a corrugated (ideal) punch would be expected to scale linearly with the number of maxima given fixed heights and fixed radii of curvature at a fixed operating velocity. Since the number density of maxima in the hexagonal lattice is twice that

C. Müller et al.
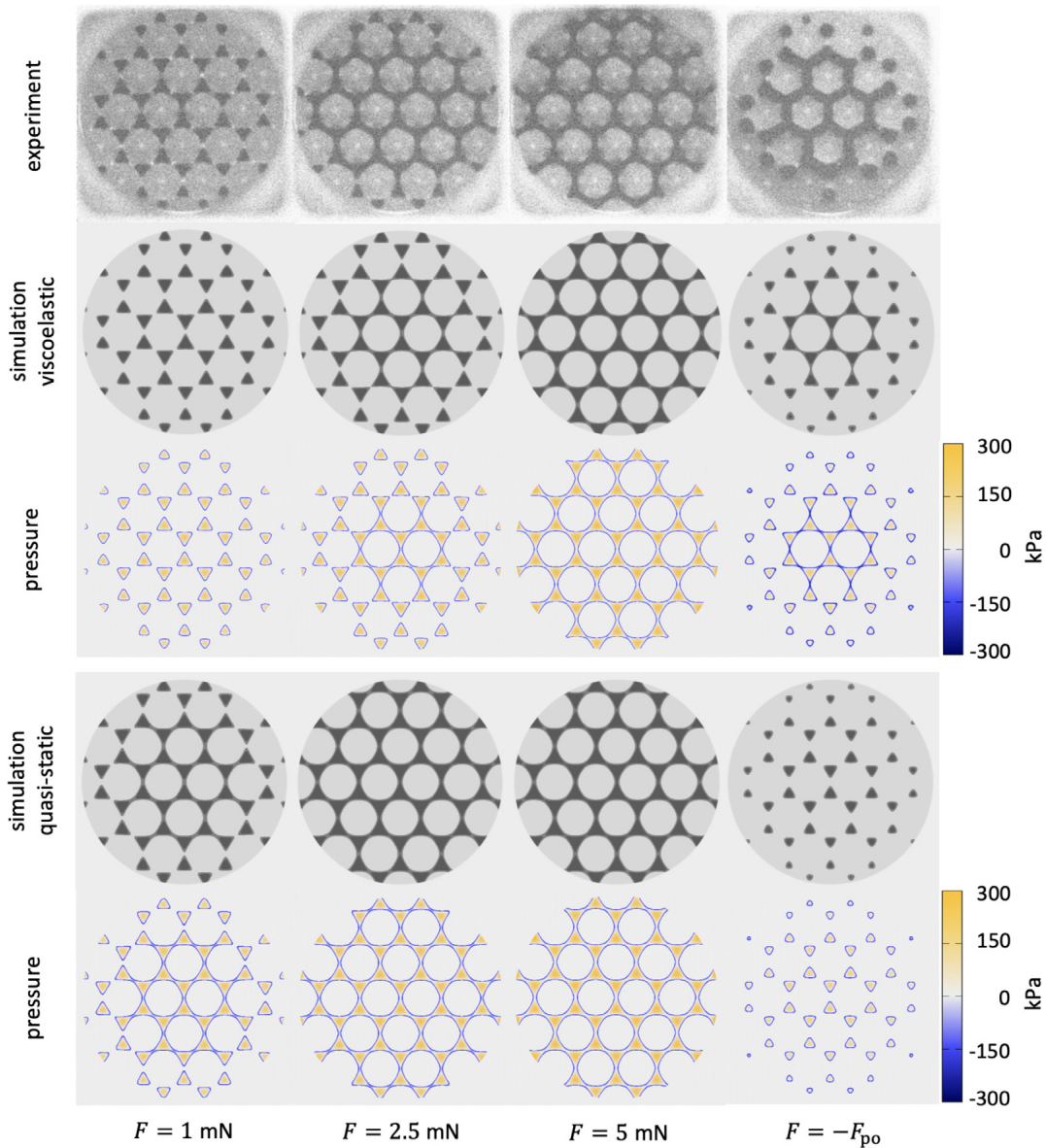
Fig. 12. Contact observation during a tack test at $1~\mu m/s$ and a maximum compressive load of 10 mN. The upper row is taken from the experiment, the center row from a simulation with a single relaxation time ($\tau = 200~\mu s$ and $\rho = 2.642~\mu m$) and the last two rows from a quasi-static simulation with the same range of adhesion ρ. Gray scales as in Fig. 9. Frames are taken from the approach part of the tack test, except for the last ones, which reflect the moment of maximum tensile force. In real-laboratory and *in-silico* contacts, all maxima are always in contact while saddle points close to the rim only come into contact with increasing load. The attachment of saddle points and asperities is clearly separated on approach, but their detachment occurs quasi-simultaneously.

of the triangular lattice, BAMs predict roughly twice the adhesion force for our hexagonal than for our triangular patterned punch, again assuming identical velocities in both cases. Finite-size effects and cut-off asperities at the rim of the punch renormalize that ratio but do not affect the trend. Unfortunately, things turn out the other way around in the viscoelastic case, i.e., the triangular surface with the fewer peaks has clearly greater (viscoelastic) pull-off forces, due to the pivotal role of saddle points. Obviously, BAMs approximating each peak as parabolic intrinsically fail to account for saddle points, which is why we are beyond skeptical on studies reporting models in the spirit of Fuller and Tabor to be quantitative for nominally flat contacts, even if agreement can be fudged during the post-diction of experimental data.

This leaves numerical approaches, such as the here-reported number-crunching exercise, as the least problematic non-experimental tool to tackle adhesive problems similar to that investigated here. Nonetheless, number-crunching is not entirely unproblematic either. We also gauged the model parameters on the experiments that were reproduced, even if the few adjustable parameters were kept constant throughout all simulations. One problem in the attempt to make quantitative predictions is the multi-scale nature of the dissipation during viscoelastic crack propagation. The range of adhesion critically affects the dissipation of moving cracks, which must be reproduced correctly to model the formation and the failure of adhesive contacts reliably (Schapery,

1975; Hui et al., 1998; Persson and Brener, 2005; Müser and Persson, 2022). This means that the vicinity of the crack must be resolved with a computationally unfeasible large resolution or the viscoelastic properties of the elastomer relaxation times must be rescaled, which, however, implies that the time-dependent response of the elastomer to a point indenter would no longer be correct. For experimental *in-situ* contact observation, one challenge was to keep the focus on a moving indenter and to obtain good contrast between contact and non-contact with a lateral resolution close to the wavelength of light. Another difficulty was to remove artifacts from the confocal-microscopy measurements of the height profiles, which would have been even more challenging if the surfaces had relevant roughness on finer length scales (Jacobs et al., 2022).

Despite all difficulties related to the numerical modeling, we would argue that the simulations matched the experiments not only qualitatively but almost quantitatively, that is, both force–distance relationships and contact images correlated quite well between simulations and experiments. This was accomplished not for fortuitous reasons but because (a) the simulations captured all the essential ingredients of real contacts, (b) imperfections in the 3D printing process were accounted for so that the adhesion at pull-off originated on the contact rim for the triangular pattern but in the center of the contact for the hexagonal pattern. It is noteworthy that this was achievable entirely within linear response theory, neglecting in-plane stresses as well as large displacement effects. For the observed system, we would expect these phenomena only change results quantitatively but not qualitatively as in other systems (Hui and Jagota, 2016; Liu et al., 2021).

Before concluding, we would like to answer the questions raised at the end of the introduction in the order of their occurrence. First, yes, simulations can reproduce the experimental dependencies, however, at this stage, only semi-quantitatively. Second, for the current system, reducing the range of adhesion by a factor of $\sqrt{2}$ required the relaxation times to be divided by approximately 2.5 to yield similar dynamics. This scaling might differ for other geometries. Third, we find that the dissipation due to elastic and viscoelastic instabilities cannot generally be discriminated, due to their coaction. And last but not least, contact visualization can certainly help to determine if a contact is about to break, e.g., loss of saddle points in the given system indicates imminent detachment at small retraction velocity. However, details may differ from system to system.

Due to the good correlation between experimental and simulation results, we are confident that any (qualitative) conclusion drawn in this work is on solid grounds. This makes us hopeful that simulations like the ones presented here will soon be in a position to address systems beyond the demonstrator model considered here, such as pressure-sensitive adhesives or hydraulic seals in contact with surfaces having complex and not only single-sinusoidal micro-scale roughness. Likewise, optically studying the time evolution of contacts, in particular their saddle points, as done in this work, bears much promise to predict if a given contact is close to detachment.

CRediT authorship contribution statement

Christian Müller: Conception and design of study, Acquisition of data, Analysis and/or interpretation of data, Writing – original draft, Writing – review & editing. **Manar Samri:** Conception and design of study, Acquisition of data,Analysis and/or interpretation of data, Writing – original draft, Writing – review & editing. **René Hensel:** Conception and design of study, Analysis and/or interpretation of data, Writing – review & editing. **Eduard Arzt:** Conception and design of study, Writing – review & editing. **Martin H. Müser:** Conception and design of study, Analysis and/or interpretation of data, Writing – original draft, Writing – review & editing.

Declaration of competing interest

The authors declare that they have no known competing financial interests or personal relationships that could have appeared to influence the work reported in this paper.

Data availability

Data will be made available on request.

Acknowledgments

C. Müller et al.

References

Afferrante, L., Violano, G., 2022. The adhesion of viscoelastic bodies with slightly wave surfaces. Tribol. Int. 174.

Bennett, A.I., Harris, K.L., Schulze, K.D., Urueña, J.M., McGhee, A.J., Pitenis, A.A., Müser, M.H., Angelini, T.E., Sawyer, W.G., 2017. Contact measurements of randomly rough surfaces. Tribol. Lett. 65.

Booth, J.A., Hensel, R., 2021. Perspective on statistical effects in the adhesion of micropatterned surfaces. Appl. Phys. Lett. 119 (23), 230502.

Bugnicourt, R., Sainsot, P., Lesaffre, N., Lubrecht, A.A., 2017. Transient frictionless contact of a rough rigid surface on a viscoelastic half-space. Tribol. Int. 113, 279–285.

Campañá, C., Müser, M.H., 2006. Practical Green's function approach to the simulation of elastic semi-infinite solids. Phys. Rev. B 74 (7), 1–15.

Campañá, C., Müser, M.H., Robbins, M.O., 2008. Elastic contact between self-affine surfaces: Comparison of numerical stress and contact correlation functions with analytic predictions. J. Phys.: Condens. Matter 20 (35).

Caracciolo, R., Giovagnoni, M., 1996. Frequency dependence of Poisson's ratio using the method of reduced variables. Mech. Mater. 24 (1), 75–85.

Carbone, G., Lorenz, B., Persson, B.N., Wohlers, A., 2009. Contact mechanics and rubber friction for randomly rough surfaces with anisotropic statistical properties. Eur. Phys. J. E 29 (3), 275–284.

Carbone, G., Mangialardi, L., 2008. Analysis of the adhesive contact of confined layers by using a Green's function approach. J. Mech. Phys. Solids 56 (2), 684–706.

Carbone, G., Pierro, E., Recchia, G., 2015. Loading-unloading hysteresis loop of randomly rough adhesive contacts. Phys. Rev. E 92.

Chen, Y.L., Helm, C.A., Israelachvili, J.N., 1991. Molecular mechanisms associated with adhesion and contact angle hysteresis of monolayer surfaces. J. Phys. Chem. 95, 10736–10747.

Ciavarella, M., Greenwood, J.A., Barber, J.R., 2017. Effect of Tabor parameter on hysteresis losses during adhesive contact. J. Mech. Phys. Solids 98 (September 2016), 236–244.

Dalvi, S., Gujrati, A., Khanal, S.R., Pastewka, L., Dhinojwala, A., Jacobs, T.D.B., 2019. Linking energy loss in soft adhesion to surface roughness. Proc. Natl. Acad. Sci. USA 116 (51), 25484–25490.

Dapp, W.B., Müser, M.H., 2015. Contact mechanics of and Reynolds flow through saddle points: On the coalescence of contact patches and the leakage rate through near-critical constrictions. Europhys. Lett. 109 (4), 44001.

Eason, E.V., Hawkes, E.W., Windheim, M., Christensen, D.L., Libby, T., Cutkosky, M.R., 2015. Stress distribution and contact area measurements of a gecko toe using a high-resolution tactile sensor. Bioinspir. Biomim. 10, 16013.

Feiler, A.A., Stiernstedt, J., Theander, K., Jenkins, P., Rutland, M.W., 2006. Effect of capillary condensation on friction force and adhesion. Langmuir 23, 517–522.

Fuller, K.N.G., Tabor, D., 1975. The effect of surface roughness on the adhesion of elastic solids. Proc. R. Soc. Lond. A. Math. Phys. Sci. 345 (1642), 327–342.

Gao, H., Rice, J.R., 1989. A first-order perturbation analysis of crack trapping by arrays of obstacles. J. Appl. Mech. Trans. ASME 56 (4), 828–836.

Giri, M., Bousfield, D.B., Unertl, W.N., 2001. Dynamic contacts on viscoelastic films:{\hspace{0.167em}} work of adhesion. Langmuir 17, 2973–2981.

Glassmaker, N.J., Jagota, A., Hui, C.Y., Noderer, W.L., Chaudhury, M.K., 2007. Biologically inspired crack trapping for enhanced adhesion. Proc. Natl. Acad. Sci. USA 104 (26), 10786–10791.

Guduru, P.R., 2007. Detachment of a rigid solid from an elastic wavy surface: Theory. J. Mech. Phys. Solids 55 (3), 445–472.

Harrick, N.J., 1962. Use of frustrated total internal reflection to measure film thickness and surface reliefs. J. Appl. Phys. 33 (9), 2774–2775.

Hensel, R., McMeeking, R.M., Kossa, A., 2019. Adhesion of a rigid punch to a confined elastic layer revisited. J. Adhes. 95 (1), 44–63.

Hensel, R., Thiemecke, J., Booth, J.A., 2021. Preventing catastrophic failure of microfibrillar adhesives in compliant systems based on statistical analysis of adhesive strength. ACS Appl. Mater. Interfaces 13 (16), 19422–19429.

Hui, C.Y., Baney, J.M., Kramer, E.J., 1998. Contact mechanics and adhesion of viscoelastic spheres. Langmuir 14 (22), 6570–6578.

Hui, C.Y., Jagota, A., 2016. Effect of surface tension on the relaxation of a viscoelastic half-space perturbed by a point load. J. Polym. Sci. Part B Polym. Phys. 54 (2), 274–280.

Israelachvili, J., 2011. Intermolecular and Surface Forces, 3rd editio ed. Elsevier Inc.

Jacobs, T.D.B., Miller, N., Müser, M.H., Pastewka, L., 2022. The surface-topography challenge: Problem definition. arXiv.

Jiang, Y., Grierson, D.S., Turner, K.T., 2014. Flat punch adhesion: Transition from fracture-based to strength-limited pull-off. J. Phys. D. Appl. Phys. 47 (32).

Kesari, H., Doll, J.C., Pruitt, B.L., Cai, W., Lew, A.J., 2010. Role of surface roughness in hysteresis during adhesive elastic contact. Phil. Mag. Lett. 90, 891–902.

Krick, B.A., Vail, J.R., Persson, B.N., Sawyer, W.G., 2012. Optical in situ micro tribometer for analysis of real contact area for contact mechanics, adhesion, and sliding experiments. Tribol. Lett. 45 (1), 185–194.

Liu, Z., Hui, C.Y., Jagota, A., 2021. Energetics of cracks and defects in soft materials: The role of surface stress. Extrem. Mech. Lett. 48.

Liu, Y., Szlufarska, I., 2012. Chemical origins of frictional aging. Phys. Rev. Lett. 109.

Lorenz, B., Krick, B.A., Mulakaluri, N., Smolyakova, M., Dieluweit, S., Sawyer, W.G., Persson, B.N.J., 2013. Adhesion: role of bulk viscoelasticity and surface roughness. J. Phys.: Condens. Matter 25, 225004.

Maeda, N., Chen, N., Tirrell, M., Israelachvili, J.N., 2002. Adhesion and friction mechanisms of polymer-on-polymer surfaces. Science 297, 379–382.

McCutchen, C.W., 1964. Optical systems for observing surface topography by frustrated total internal reflection and by interference. Rev. Sci. Instrum. 35 (10), 1340–1345.

McGhee, A.J., Pitenis, A.A., Bennett, A.I., Harris, K.L., Schulze, K.D., Urueña, J.M., Ifju, P.G., Angelini, T.E., Müser, M.H., Sawyer, W.G., 2017. Contact and deformation of randomly rough surfaces with varying root-mean-square gradient. Tribol. Lett. 65.

Müller, C., Müser, M.H., 2022. Analytical and numerical results for the elasticity and adhesion of elastic films with arbitrary Poisson's ratio and confinement. J. Adhes..

Müser, M.H., 2008. Rigorous field-theoretical approach to the contact mechanics of rough elastic solids. Phys. Rev. Lett. 100 (5), 1–4.

Müser, M.H., 2014. Single-asperity contact mechanics with positive and negative work of adhesion: Influence of finite-range interactions and a continuum description for the squeeze-out of wetting fluids. Beilstein J. Nanotechnol. 5 (1), 419–437.

Müser, M.H., Dapp, W.B., Bugnicourt, R., Sainsot, P., Lesaffre, N., Lubrecht, T.A., Persson, B.N., Harris, K., Bennett, A., Schulze, K., Rohde, S., Ifju, P., Sawyer, W.G., Angelini, T., Ashtari Esfahani, H., Kadkhodaei, M., Akbarzadeh, S., Wu, J.J., Vorlaufer, G., Vernes, A., Solhjoo, S., Vakis, A.I., Jackson, R.L., Xu, Y., Streator, J., Rostami, A., Dini, D., Medina, S., Carbone, G., Bottiglione, F., Afferrante, L., Monti, J., Pastewka, L., Robbins, M.O., Greenwood, J.A., 2017. Meeting the contact-mechanics challenge. Tribol. Lett. 65 (4).

Müser, M.H., Li, H., Bennewitz, R., 2019. Modeling the contact mechanics of hydrogels. Lubricants 7 (4), 1–21.

Müser, M.H., Persson, B.N., 2022. Crack and pull-off dynamics of adhesive, viscoelastic solids. Europhys. Lett. 137 (3).

Pérez-Ràfols, F., Van Dokkum, J.S., Nicola, L., 2022. On the interplay between roughness and viscoelasticity in adhesive hysteresis. J. Mech. Phys. Solids 105079.

Persson, B.N., 2001. Theory of rubber friction and contact mechanics. J. Chem. Phys. 115 (8), 3840–3861.

Persson, B.N., 2002. Adhesion between elastic bodies with randomly rough surfaces. Phys. Rev. Lett. 89 (24), 1–4.

Persson, B.N., 2003. Nanoadhesion. Wear 254 (9), 832–834.

Persson, B.N., 2008. On the elastic energy and stress correlation in the contact between elastic solids with randomly rough surfaces. J. Phys.: Condens. Matter 20 (31).

Persson, B.N., Brener, E.A., 2005. Crack propagation in viscoelastic solids. Phys. Rev. E 71 (3), 1–8.

C. Müller et al.

Pickering, J.P., Meer, D.W.V.D., Vancso, G.J., time, title=and surface roughness on the adhesion hysteresis of polydimethylsiloxane, 2001. J. Adhes. Sci. Technol. 15, 1429–1441.

Prandtl, L., 1928. Ein Gedankenmodell zur kinetischen Theorie der festen Körper. Z. Angew. Math. Mech. 8 (2), 85–106.

Samri, M., Kossa, A., Hensel, R., 2021. Effect of subsurface microstructures on adhesion of highly confined elastic films. J. Appl. Mech. Trans. ASME 88 (3), 1–9.

Samri, M., Thiemecke, J., Prinz, E., Dahmen, T., Hensel, R., Arzt, E., 2022. Predicting the adhesion strength of micropatterned surfaces using supervised machine learning. Mater. Today 53 (February), 41–50.

Sanner, A., Pastewka, L., 2022. Crack-front model for adhesion of soft elastic spheres with chemical heterogeneity. J. Mech. Phys. Solids 160 (August 2021), 104781.

Sawyer, W.G., Wahl, K.J., 2008. Accessing inaccessible interfaces: in situ approaches to materials tribology. MRS Bull. 33 (12), 1145–1150.

Schapery, R.A., 1975. A theory of crack initiation and growth in viscoelastic media - I. Theoretical development. Int. J. Fract. 11 (1), 141–159.

Shull, K.R., 2002. Contact mechanics and the adhesion of soft solids. Mater. Sci. Eng. R Rep. 36, 1–45.

Sukhomlinov, S., Müser, M.H., 2021. On the viscous dissipation caused by randomly rough indenters in smooth sliding motion. Appl. Surf. Sci. Adv. 6, 100182.

Tabor, D., 1977. Surface forces and surface interactions. J. Colloid Interface Sci. 58 (1), 2–13.

Thiemecke, J., Hensel, R., 2020. Contact aging enhances adhesion of micropatterned silicone adhesives to glass substrates. Adv. Funct. Mater. 30 (50).

Thimons, L.A., Gujrati, A., Sanner, A., Pastewka, L., Jacobs, T.D.B., 2021. Hard-material adhesion: Which scales of roughness matter? Exp. Mech. 61, 1109–1120.

Thomson, R., Hsieh, C., Rana, V., 1971. Lattice trapping of fracture cracks. J. Appl. Phys. 42 (8), 3154–3160.

Tinnemann, V., Hernández, L., Fischer, S.C., Arzt, E., Bennewitz, R., Hensel, R., 2019. In situ observation reveals local detachment mechanisms and suction effects in micropatterned adhesives. Adv. Funct. Mater. 29 (14).

Tiwari, A., Dorogin, L., Bennett, A.I., Schulze, K.D., Sawyer, W.G., Tahir, M., Heinrich, G., Persson, B.N., 2017. The effect of surface roughness and viscoelasticity on rubber adhesion. Soft Matter 13 (19), 3602–3621.

Tomlinson, G., 1929. Cvi. A molecular theory of friction. Lond. Edinb. Dublin Philos. Mag. J. Sci. 7 (46), 905–939.

Tschoegl, N.W., Knauss, W.G., Emri, I., 2002. Poisson's ratio in linear viscoelasticity - a critical review. Mech. Time-Depend. Mater. 6 (1), 3–51.

Van Dokkum, J.S., Nicola, L., 2019. Green's function molecular dynamics including viscoelasticity. Modelling Simul. Mater. Sci. Eng. 27 (7).

Violano, G., Chateauminois, A., Afferrante, L., 2021a. Rate-dependent adhesion of viscoelastic contacts, Part I: Contact area and contact line velocity within model randomly rough surfaces. Mech. Mater. 160.

Violano, G., Chateauminois, A., Afferrante, L., 2021b. Rate-dependent adhesion of viscoelastic contacts, part II: Numerical model and hysteresis dissipation. Mech. Mater. 158.

Wahl, K.J., Sawyer, W.G., 2008. Observing interfacial sliding processes in solid–solid contacts. MRS Bull. 33 (12), 1159–1167.

Wang, A., Müser, M.H., 2022. On the adhesion between thin sheets and randomly rough surfaces. Front. Mech. Eng. 8.

Wang, A., Zhou, Y., Müser, M.H., 2021. Modeling adhesive hysteresis. Lubricants 9 (2), 1–30.

Weber, B., Suhina, T., Junge, T., Pastewka, L., Brouwer, A.M., Bonn, D., 2018. Molecular probes reveal deviations from amontons' law in multi-asperity frictional contacts. Nature Commun. 9, 888.

Xia, S., Ponson, L., Ravichandran, G., Bhattacharya, K., 2012. Toughening and asymmetry in peeling of heterogeneous adhesives. Phys. Rev. Lett. 108 (19).

Zheng, W., Ya-Pu, Z., 2004. Adhesion elastic contact and hysteresis effect. Chin. Phys. 13, 1320–1325.

Zhou, Y., Moseler, M., Müser, M.H., 2019. Solution of boundary-element problems using the fast-inertial-relaxation-engine method. Phys. Rev. B 99 (14), 1–8.

Zhou, Y., Müser, M.H., 2020. Effect of structural parameters on the relative contact area for ideal, anisotropic, and correlated random roughness. Front. Mech. Eng. 6 (August).

V   Significance of elastic coupling and friction

Permission

Contributions of co-authors

Christian Müller: methodology: GFMD implementation, software, investigation: GFMD simulations, formal analysis, writing–original draft.
Martin H. Müser: conceptualization, formal analysis, supervision, writing–original draft.
Giuseppe Carbone: conceptualization, writing–review & editing.
Nicola Menga: conceptualization, formal analysis, supervision, writing–original draft.

The original idea for studying elastic coupling in 3D rough contacts came from N.M. and G.C., contacting M.H.M. and C.M. to collaborate on the numerical investigation including Reynolds flow calculations. M.H.M. suggested to further extend the scope of the study to the stress-tensor and single-asperity analysis.

The necessary mathematical framework for the inclusion of elastic coupling and friction in GFMD were determined by N.M. and M.H.M., where the final equations were derived by N.M. Both M.H.M and N.M. then supervised C.M.'s implementation and validation of the friction model and the 3D GFMD method in the simulation code.

All simulations were set up, run and post-processed by C.M. Ideas on how to evaluate and visualize results came from all authors and were then realized by C.M.

An early draft was prepared by C.M. and N.M., which was then rewritten under the lead of M.H.M. with the letter format in mind. The finished draft was reviewed and adjusted in multiple iterations involving all authors. Everyone agreed on the publication of the article in Physical Review Letters and its inclusion in this thesis.

PHYSICAL REVIEW LETTERS

Published week ending   13 OCTOBER 2023
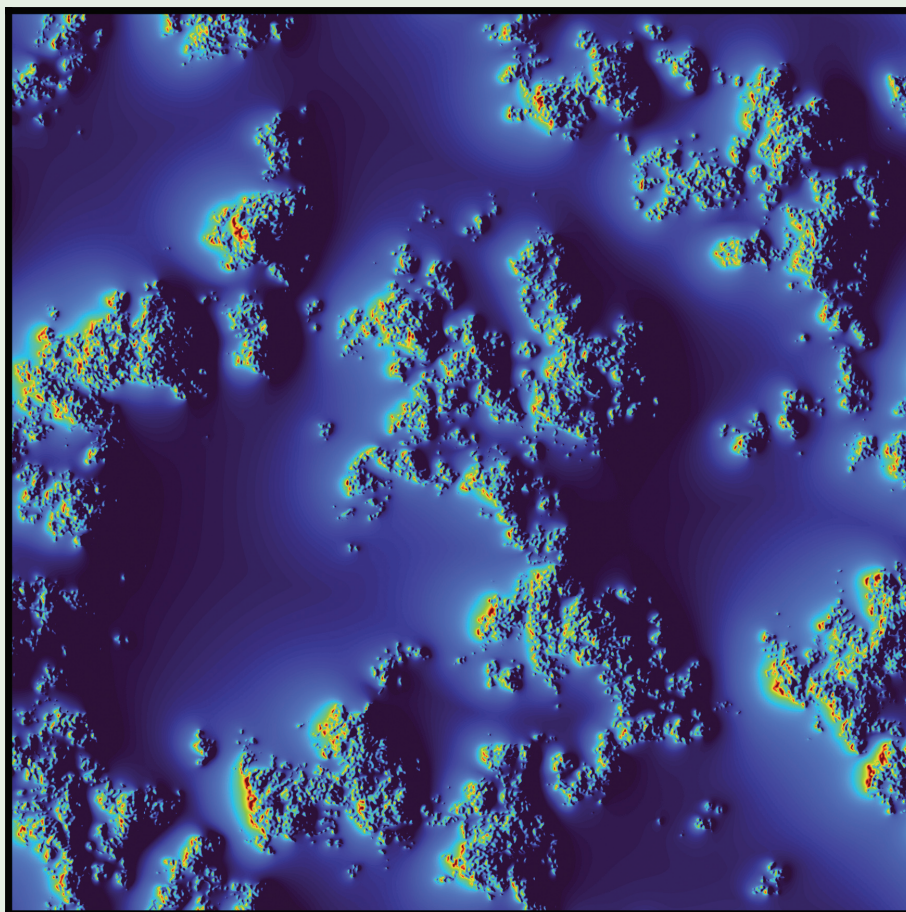
Significance of Elastic Coupling for Stresses and Leakage in Frictional Contacts

Christian Müller[ID],[1] Martin H. Müser[ID],[1,2] Giuseppe Carbone[ID],[3] and Nicola Menga[ID][3,*]

[1]*INM—Leibniz Institute for New Materials, 66123 Saarbrücken, Germany*
[2]*Department of Materials Science and Engineering, Saarland University, 66123 Saarbrücken, Germany*
[3]*Department of Mechanics, Mathematics, and Management, Politecnico di Bari, 70125 Bari, Italy*

We study how the commonly neglected coupling of normal and in-plane elastic response affects tribological properties when Hertzian or randomly rough indenters slide past an elastic body. Compressibility-induced coupling is found to substantially increase maximum tensile stresses, which cause materials to fail, and to decrease friction such that Amontons' law is violated macroscopically even when it holds microscopically. Confinement-induced coupling increases friction and enlarges domains of high tension. Moreover, both types of coupling affect the gap topography and thereby leakage. Thus, coupling can be much more than a minor perturbation of a mechanical contact.

Explaining and predicting the properties of interfaces between solid bodies requires a proper description of mechanical contacts at microscopic scales. This is because small-scale roughness, which is even present on nominally flat solids, makes true contact be smaller, often distinctly smaller than if the contacting surfaces were atomically flat [1–3]. The zones of noncontact cause interfacial electric- and heat-flow resistances [4,5] as well as extra mechanical compliances in normal and tangential directions [6,7]. Adhesion can be strongly reduced [8–10] and fluid may leak through the thin gap between a surface and a seal [11,12]. To assess structural and mechanical properties of contacts—most notably, contact area, stress, and gap distributions—in the important limiting case of linearly (visco-) elastic solids, the in-plane and out-of-plane elastic coupling, in the following simply referred to as *coupling*, is commonly neglected [13]. Yet, shear stresses acting on originally flat surfaces do induce normal displacements or stresses already in linear order, unless the solid is semi-infinite and incompressible. Without coupling, the sound of friction, be it caused by violins or squealing breaks [14], would often be different and Schallamach waves [15,16], which are kinetic-friction induced buckling instabilities of elastomers, would not be possible. Generally speaking, coupling has a destabilizing effect on sliding friction and weakens frictional cracks [17].

While a description of the just-mentioned phenomena requires approaches beyond either linear elasticity or quasi-static conditions, quite a few questions related to linear coupling have not yet found satisfactory answers even for steady-state sliding. For instance, how does friction affect size and shape of the true contact during sliding [18,19], do moving seals seal better than static seals, and, given a microscopic friction coefficient for planar surfaces, does roughness increase or decrease the macroscopically

measured friction? How do changes compare to those induced by loading configuration in soft-matter systems, which were reported to be of order $\mathcal{O}(10\%–30\%)$ and sometimes substantially more [20,21]?

In this Letter, we explore these and related questions for various rigid indenters sliding past an elastic solid with arbitrary contact modulus E^*, Poisson's ratio ν, and height h [see Fig. 1(a)], assuming steady-state conditions and Amontons' microscopic friction. Although some of the issues raised here have already been addressed in line contacts [22–24], load-area and other relations do not generalize from line to areal contacts, neither in simple indenter geometries [25] nor in randomly rough contacts [26,27], so that the effect of roughness on the friction coefficient can differ between the two cases. More importantly, the analysis of how coupling affects leakage cannot be addressed in line contacts, since they automatically seal
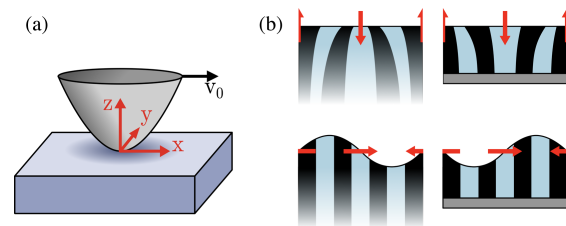
FIG. 1. (a) Contact setup: a rigid indenter sliding along the x axis at constant velocity v_0. Vector components in the x, y, and z direction are called longitudinal, transverse, and normal, respectively. (b) Cross sections of a compressible (left) and confined (right) body loaded by sinusoidal surface stresses, whose extrema are indicated by red arrows. Stripes and shapes represent coupling-induced longitudinal (top) and normal (bottom) displacements, respectively.
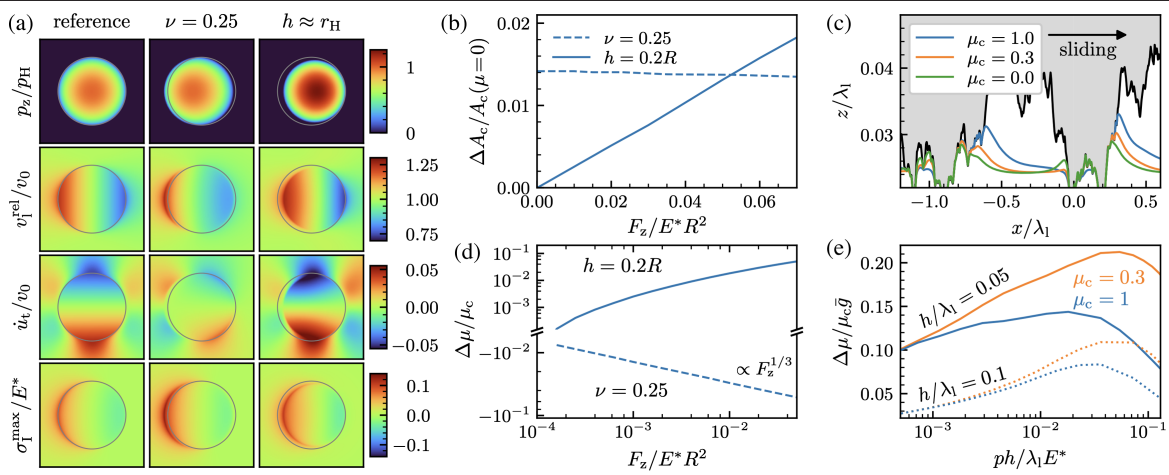
FIG. 2. Panels (a),(b),(d) and (c),(e) relate to Hertzian indenters of radius R and randomly rough indenters, respectively. (a) Contact pressure p_z (top row) normalized to the maximum regular Hertzian contact pressure p_H, relative longitudinal v_l^{rel} (second row), transverse $\dot{u}_t$ (third row) velocity, and the maximum principal surface stress σ_I^{max} (bottom row) for the reference ($\nu = 0.49$, $h \to \infty$, left column), the semi-infinite compressible (middle column), and the confined nearly incompressible (right column) elastomer. The applied normal load is $F_z = 0.01 E^* R^2$ yielding a Hertzian contact radius of $r_H \approx 0.2R$ (gray circles). Coupling-induced relative changes in (b) contact area $\Delta A_c / A_c$ and (d) friction coefficient $\Delta \mu / \mu_c$ as functions of dimensionless normal load $F_z / E^* R^2$. (c) Rough contact cross section, and (e) normalized relative change of the friction coefficient vs the dimensionless normal pressure $ph/E^* \lambda_l$ for confinement-induced coupling. Moreover, $\bar{g}$ and λ_l are the rough surface's root-mean-square gradient and long-wavelength cutoff, respectively.

in the lateral (sliding) direction, while they are open in the transverse direction. In contrast, percolation of randomly rough two-dimensional surfaces is isotropic, even if roughness and flow factors are not [28]. Moreover, still unexplored is the important effect of linear coupling on either von Mises or maximum tensile stresses in rough contacts, although they are crucial for the onset of plastic deformation and the mechanical failure of materials, respectively.

We solve the contact problem numerically using Green's function molecular dynamics (GFMD) [29], which is a Fourier-based boundary value method to calculate elastic surface displacements under periodic boundary conditions. To elucidate the effects of coupling, the continuum description of the normal displacement in Sec. 2.2.1 of Ref. [30] was generalized to compute the full three-dimensional stress tensor and displacement field for a solid with arbitrary thickness and compressibility. The needed analytical (inverse) Green's functions [23,31] are summarized in the Supplemental Material [32], along with model and methods details, including the topography generation for rigid, randomly rough indenters and the procedure for the leakage calculation [33]. The essence of coupling effects is depicted in Fig. 1(b). Codes, input files, and results are available [34].

The default value for the microscopic friction coefficient is set to $\mu_c = 1$. A Poisson's ratio of $\nu = 0.25$ is used to analyze the generic behavior of compressible materials and $\nu = 0.49$ for (nearly) incompressible ones. The first value is halfway between that of many metals with $\nu \gtrsim 0.3$ and that of many ceramics with $\nu \lesssim 0.2$.

To set the stage for this work, we first establish in Fig. 2 that coupling affects areal and line contacts in a similar fashion [23,24]. For example, for a Hertzian geometry, Fig. 2(a) reveals that coupling destroys the normal pressure symmetry also in areal contacts, which now entails non-circular contact shapes. More specifically, confinement-induced coupling skews the pressure to the leading edge so that it carries more load than the trailing edge, as in line contacts [24,35]. This effect can be deduced directly from Fig. 1(b) showing that the shear stress in the center—pointing to the right as does the shear force in Fig. 1(a)—makes the displacement field "want" to lift up near the leading edge, which, to keep the normal load constant and steady sliding conditions, the indenter must counteract with an increased constraint force, in a similar fashion as in viscoelastic contacts [36–38]. By virtue of what could be called a downhill-slope force [39], the leading edge opposes sliding more than the trailing edge pushes the indenter forward, which increases the global friction coefficient from the microscopic value μ_c to $\mu_c + \Delta \mu$. These trends reverse for compressible elastomers, for which the pressure maximum shifts to the trailing edge, resulting in smaller friction. Changes in global friction can also be related to an interplay of coupling-induced loss of (anti-) symmetry in velocity and stress fields, which alters the local heat production. This argument is presented in detail in the Supplemental Material [32] (Sec. 2b) together with a compilation of linescans for displacement, velocity, and stress fields (Fig. SI-2 of [32]).

In the case of compressibility-induced coupling, the increase of a normal constraining pressure on the trailing edge (preventing surfaces from interpenetrating) and the decrease of the compressive stress on the leading edge can only be proportional to the original normal stress. Ultimately, this is because the coupling correction, as described by the variable Φ_{13} introduced in the Supplemental Material [32], only depends on q_x/q but not explicitly on q when the elastomer is semi-infinite. Consequently, the correction to the downhill force and thus to the friction coefficient is proportional to the mean absolute slope, which, in the case of Hertzian indenters, is proportional to the contact radius r_c and thus to $F^{1/3}$, as is confirmed in Fig. 2(d). Algebraic scaling relations for the confinement-induced coupling do not arise, because the amplitudes of coupling terms have a nonalgebraic dependence on film thickness and wave number.

Simulations similar to those for Hertzian indenters were repeated for randomly rough indenters, a cross section of which is depicted in Fig. 2(c) along with an elastic, confined counterbody. The characteristics of its displacement fields resemble those of Hertzian indenters; however, Fig. 2(e) reveals that the friction coefficient now increases only initially with load before it starts to decrease at high loads. When coupling is caused by finite compressibility, the friction coefficient of a randomly rough indenter is also nonmonotonic in load, but trends are inverted again, i.e., it is always μ_c but increases after the initial decrease with load (not shown explicitly). The predominant reason for the nonmonotonicity is that the normal displacement gradients at trailing and leading edges first increase with load, as in a Hertzian geometry, but eventually become smaller with increasing contact dimension due to sinusoidal characteristics of the roughness profile, thereby reducing the downhill-slope effect.

In addition to friction, von Mises and tensile stresses are central tribological quantities, since they affect the failure of materials. Roughly speaking, ductile solids deform plastically first near defects where the von Mises stress, which is $\sqrt{3/2}$ times the standard deviation of the stress-tensor eigenvalues, is largest, while polymers and brittle materials like ceramics break near points of high tension, given by the largest stress-tensor eigenvalue. So far, analytical solutions for stress distribution below frictional Hertzian indenters have been obtained neglecting coupling [40,41], in which case the maxima of tensile and von Mises stresses are located in the surface at the trailing edge for $\mu_c > 0.3$, as depicted in Fig. SI-2, row six, second column [32]. Experiments confirm these trends for line contacts with thin elastomers [35]. For this reason, and because crack initiation is most effective in the near-surface region [42], we focus on surface stresses in the following discussion of coupling effects.

Analysis of the stress profiles—details are shown in Fig. SI-2, row 6 [32] being most relevant to this paragraph

—reveals a remarkable 30% increase in the tensile stress due to coupling for $\nu = 0.25$ and $r_H/R = 0.2$, whereas the von Mises stress is barely affected. Changes in the stress due to confinement-induced coupling are more difficult to evaluate, because confinement reduces the contact area at given normal load so that the semi-infinite, incompressible elastomer is no longer a good reference. The reduced contact area leads to a dramatic increase of σ_{vM}. In addition, the zone where the tensile stress is close to its maximum value increases substantially in size. Thus, both types of coupling can strongly enhance the likelihood of crack formation. Of course, linear elasticity can only be used to estimate the onset of plasticity and/or material failure. Once triggered, additional phenomena, which are likely dissipative in nature, occur, thereby altering friction further.

To highlight the importance of in-plane stress and deformations, we redefine the reference to which numerical results are compared. To this end, we first conduct a regular contact-mechanics calculation for a frictionless interface and then add the interfacial shear stress in postanalysis as a perturbation under the assumption that all material points at the interface have the same relative in-plane velocity v_0. The top row of Fig. 3 reveals that this procedure substantially underestimates tension. One effect missing in the pursued approach is symmetry breaking, which makes maximum tensile stresses move to the trailing edge for both couplings. Besides this qualitative effect, quantitative differences between the true tensile stress and the one obtained in postanalysis are factors easily surpassing two to four in the studied systems.

Coupling does not only alter stresses but also displacements and thereby the interfacial separation, which will be called gap g in the following. The gap determines the local resistance ρ to in-plane fluid flow in between a rigid surface and a seal. In the Reynolds thin film equation, $\rho \propto 1/g^3$ [12,43]. The bottom row of Fig. 3 shows the fluid current for our confined elastomer in four cases, i.e., for two sliding and two flow directions. Leaking matters in the sliding direction for applications like scrubbers and syringes and in the orthogonal direction for rotary seals and journal bearings. The shown images reveal that fluid flow is affected by the sliding direction and thus by coupling.

The flow patterns depicted in Fig. 3 are in line with the idea that fluid flow is impeded predominantly by a few constrictions [43,44], where current densities are high and which become critical just before they block fluid flow completely. The average effect of coupling on the fluid flow suffers from large statistical uncertainties near the percolation threshold, since the number of relevant constrictions per unit area is minuscule. Therefore, we studied an individual constriction to isolate the effect of coupling on it. For this purpose, we choose a roughness of square-lattice symmetry having the form $h(\mathbf{r}) = h_0\{\cos(qx) + \cos(qy)\}$, because its relative contact area at the percolation threshold, $a_c^* \approx 0.405$ [33], is close to that of randomly
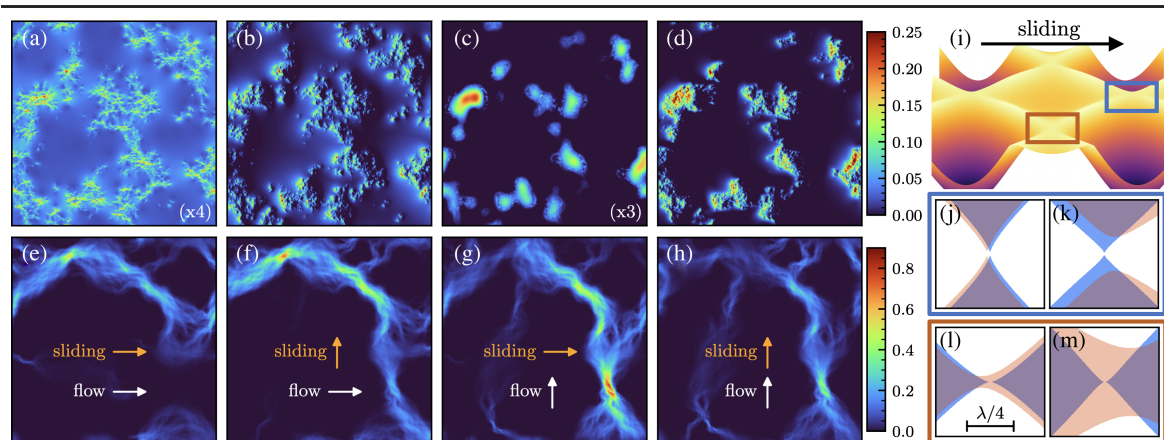
FIG. 3.   Top row: maximum tensile stress normalized to E^* for a (a),(b) compressible and (c),(d) confined elastomer. Panels (a),(c) were deduced from static simulations and lateral stress added in postprocessing, whereas (b),(d) are based on full sliding simulations. Bottom row: (e)–(h) leakage current *density* for different fluid flow and sliding directions for the confined layer at a relative contact area of approximately 19%. Each panel was produced using the same randomly rough indenter and, for (e)–(h), the same fluid-pressure difference. Results are normalized to the maximum value in frictionless conditions. (i) 3D contact around the critical constriction for the square roughness profile against either (j),(l) a semi-infinite, $\nu = 0.25$ elastomer or (k),(m) a confined, $\nu = 0.49$ elastomer. Blue color indicates the frictionless contact area, while orange marks the case with friction. The purple region is the overlap of the two. Constrictions open in sliding direction (j),(k) but close in the transverse direction (l),(m).

rough surfaces, $a_c^* \approx 0.42$ [12], while the exponent $\zeta = 69/20$ with which the total current disappears near the percolation threshold, $I \propto (a_c^* - a_c)^{\zeta}$ was found to be identical for square [33] and random roughness in the case of semi-infinite elastic bodies [45].

Using $q = 2\pi/\lambda$, where the wavelength λ coincides with the linear dimension of the periodically repeated simulation cell, and $h_0 = \lambda/(2\pi)^2$, we obtain a radius of curvature at the peaks of $R = \lambda$. The indenter is then squeezed against either a semi-infinite elastomer with $\nu = 0.25$ or a $\nu = 0.49$ elastomer slab of height $h = \lambda/10$. In the first case, a_c^* does not change in a frictionless reference, while it increases to essentially $a_c^* = 0.5$ for the confined elastomer. This "canonical percolation threshold" is the one that applies to square or random roughness if points above the mean height are (assumed to be) in contact, while those below it are not. Because of coupling, the contact area increases in both cases compared to the frictionless reference at fixed pressure, i.e., from 0.405 to 0.416 for the $\nu = 0.25$ elastomer and from 0.5 to 0.556 for the confined elastomer. In addition, flow factors are enhanced parallel to the sliding direction in an isolated constriction but blocked in the transverse direction, as depicted in Figs. 3(j)–3(m). Thus, at loads slightly smaller than those needed to reach the percolation threshold in a random surface, roughly half of the critical constrictions would start to block fluid due to friction and coupling, while some previously closed constrictions would open up.

The implications that results in isolated constrictions have for flow in randomly rough contacts cannot be easily ascertained: while the opening of channels in parallel direction facilitates fluid flow in that direction, the percolation is isotropic in the thermodynamic limit [28] so that the blocking of previously open channels in the transverse direction can prevent complete percolation. In fact, after averaging results over eight independent surface realizations using Bruggeman's self-consistent equation [12,28], we find a reduction of fluid flow in both directions in all cases. For compressibility coupling, under given normal load, it turned out to be 11% and 20% in longitudinal and transverse directions, respectively. For confined elastomers these numbers changed to 27% and 30%. All numbers apply to a relative contact area of $a_c \approx 0.2$, which is still far from the percolation threshold, i.e., relative corrections will be much enhanced as the pressure is further increased.

The simulations presented in this Letter reveal that linear coupling can strongly affect all central tribological properties by 10% and even much beyond when the materials in contact are either sufficiently thin or compressible. Specifically, we find that coupling counteracts the validity of Amontons' law and increases both contact area and in-plane tensile stresses at fixed normal load compared to the uncoupled case. Leakage is also impacted by coupling-induced changes in the gap distribution and contact stiffness, entailing an overall reduction of the fluid flow and shifting the percolation threshold to smaller nominal pressures. Thus, the common practice of neglecting coupling can indeed lead to substantial errors in the prediction of interfacial properties as foreseen by Johnson [46].

Seeking for experimental confirmation of our findings may be a challenging task, because nonlinear elasticity is likely to play a role in sliding contact tests [47]. Some

studies [35,48], however, seem to have successfully avoided nonlinear phenomena (e.g., contact shrinking), which makes us optimistic that our findings can be experimentally verified after all. However, we expect them to matter in a broad variety of systems, i.e., for any rough solid with a Poisson's ratio clearly different from 0.5 or any system of finite thickness, including coatings and confined elastomers. Particular examples would be MEMS, hard antiwear–antifriction or other protective coatings, e.g., on photovoltaic panels but also thin static seals or electric brushes used in sliding electrodes.

---

*nicola.menga@poliba.it

[1] F. P. Bowden, D. Tabor, and F. Palmer, *The Friction and Lubrication of Solids* (Clarendon Press, Oxford, 1950).

[2] B. N. Persson, Theory of rubber friction and contact mechanics, J. Chem. Phys. **115**, 3840 (2001).

[3] T. D. Jacobs and L. Pastewka, Surface topography as a material parameter, MRS Bull. **47**, 1205 (2022).

[4] J. R. Barber, Bounds on the electrical resistance between contacting elastic rough bodies, Proc. R. Soc. A **459**, 53 (2003).

[5] B. N. Persson, On the electric contact resistance, Tribol. Lett. **70**, 1 (2022).

[6] A. Baltazar, S. I. Rokhlin, and C. Pecorari, On the relationship between ultrasonic and micromechanical properties of contacting rough surfaces, J. Mech. Phys. Solids **50**, 1397 (2002).

[7] C. Campañá, B. N. Persson, and M. H. Müser, Transverse and normal interfacial stiffness of solids with randomly rough surfaces, J. Phys. Condens. Matter **23**, 085001 (2011).

[8] L. Pastewka and M. O. Robbins, Contact between rough surfaces and a criterion for macroscopic adhesion, Proc. Natl. Acad. Sci. U.S.A. **111**, 3298 (2014).

[9] B. N. Persson and M. Scaraggi, Theory of adhesion: Role of surface roughness, J. Chem. Phys. **141**, 124701 (2014).

[10] A. Wang and M. H. Müser, Is there more than one stickiness criterion?, Friction **11**, 1027 (2023).

[11] F. Bottiglione, G. Carbone, L. Mangialardi, and G. Mantriota, Leakage mechanism in flat seals, J. Appl. Phys. **106**, 104902 (2009).

[12] W. B. Dapp, A. Lücke, B. N. Persson, and M. H. Müser, Self-Affine Elastic Contacts: Percolation and Leakage, Phys. Rev. Lett. **108**, 244301 (2012).

[13] A. I. Vakis *et al.*, Modeling and simulation in tribology across scales: An overview, Tribol. Int. **125**, 169 (2018).

[14] N. M. Kinkaid, O. M. O'Reilly, and P. Papadopoulos, Automotive disc brake squeal, J. Sound Vib. **267**, 105 (2003).

[15] A. Schallamach, How does rubber slide?, Wear **17**, 301 (1971).

[16] M. Barquins, Sliding friction of rubber and schallamach waves—a review, Mater. Sci. Eng. **73**, 45 (1985).

[17] M. Aldam, Y. Bar-Sinai, I. Svetlizky, E. A. Brener, J. Fineberg, and E. Bouchbinder, Frictional Sliding Without Geometrical Reflection Symmetry, Phys. Rev. X **6**, 041023 (2016).

[18] N. Menga, G. Carbone, and D. Dini, Do uniform tangential interfacial stresses enhance adhesion?, J. Mech. Phys. Solids **112**, 145 (2018).

[19] N. Menga, G. Carbone, and D. Dini, Corrigendum to "do uniform tangential interfacial stresses enhance adhesion?" [J. Mech. Phys. Solids **112**, 145 (2018)]; J. Mech. Phys. Solids **133**, 103744 (2019).

[20] O. Ben-David and J. Fineberg, Static Friction Coefficient is Not a Material Constant, Phys. Rev. Lett. **106**, 254301 (2011).

[21] S. Maegawa, A. Suzuki, and K. Nakano, Precursors of global slip in a longitudinal line contact under non-uniform normal loading, Tribol. Lett. **38**, 313 (2010).

[22] M. K. Salehani, N. Irani, and L. Nicola, Modeling adhesive contacts under mixed-mode loading, J. Mech. Phys. Solids **130**, 320 (2019).

[23] N. Menga, Rough frictional contact of elastic thin layers: The effect of geometrical coupling, Int. J. Solids Struct. **164**, 212 (2019).

[24] N. Menga, G. Carbone, and D. Dini, Exploring the effect of geometric coupling on friction and energy dissipation in rough contacts of elastic and viscoelastic coatings, J. Mech. Phys. Solids **148**, 104273 (2021).

[25] V. L. Popov, M. Heß, and E. Willert, *Normal Contact Without Adhesion* (Springer, New York, 2019).

[26] M. K. Salehani, J. S. v. Dokkum, N. Irani, and L. Nicola, On the load-area relation in rough adhesive contacts, Tribol. Int. **144**, 106099 (2020).

[27] Y. Zhou and M. H. Müser, Effect of structural parameters on the relative contact area for ideal, anisotropic, and correlated random roughness, Front. Mech. Eng. **6**, 59 (2020).

[28] A. Wang and M. H. Müser, Percolation and reynolds flow in elastic contacts of isotropic and anisotropic, randomly rough surfaces, Tribol. Lett. **69**, 1 (2021).

[29] C. Campañá and M. H. Müser, Practical green's function approach to the simulation of elastic semi-infinite solids, Phys. Rev. B **74**, 075420 (2006).

[30] S. Sukhomlinov and M. H. Müser, On the viscous dissipation caused by randomly rough indenters in smooth sliding motion, Appl. Surface Sci. Adv. **6**, 100182 (2021).

[31] M. Scaraggi and D. Comingio, Rough contact mechanics for viscoelastic graded materials: The role of small-scale wavelengths on rubber friction, Int. J. Solids Struct. **125**, 276 (2017).

[32] See Supplemental Material at http://link.aps.org/supplemental/10.1103/PhysRevLett.131.156201 for model and methods: 3D Green's tensor implementation for GFMD

simulations; generation procedure for single-wavelength and randomly rough surface profiles; models for normal repulsion and lateral friction between the contacting bodies. Observables: calculation of the in-plane stress tensor; measurement of the resulting macroscopic friction force; numerical solution of the Reynolds equation. Details on Hertzian contact properties: comparison between multiple different values for Poisson's ratios and thickness in terms of in-plane and out-of-plane displacements, velocities, stress components and locally dissipated power.

[33] W. B. Dapp and M. H. Müser, Contact mechanics of and reynolds flow through saddle points: On the coalescence of contact patches and the leakage rate through near-critical constrictions, Europhys. Lett. **109**, 44001 (2015).

[34] Christian Müller, Data-coupling-2023-07, v1.0.1 Submitted version, https://github.com/sintharic/Data-Coupling-2023-07, Accessed: 2023-07-14.

[35] J. Scheibert, A. Prevost, G. Debrégeas, E. Katzav, and M. Adda-Bedia, Stress field at a sliding frictional contact: Experiments and calculations, J. Mech. Phys. Solids **57**, 1921 (2009).

[36] N. Menga, C. Putignano, G. Carbone, and G. P. Demelio, The sliding contact of a rigid wavy surface with a viscoelastic half-space, Proc. R. Soc. A **470**, 20140392 (2014).

[37] C. Putignano, N. Menga, L. Afferrante, and G. Carbone, Viscoelasticity induces anisotropy in contacts of rough solids, J. Mech. Phys. Solids **129**, 147 (2019).

[38] S. C. Hunter, The rolling contact of a rigid cylinder with a viscoelastic half space, J. Appl. Mech. **28**, 611 (1961).

[39] N. Menga, L. Afferrante, and G. Carbone, Effect of thickness and boundary conditions on the behavior of viscoelastic layers in sliding contact with wavy profiles, J. Mech. Phys. Solids **95**, 517 (2016).

[40] G. M. Hamilton and L. E. Goodman, The stress field created by a circular sliding contact, J. Appl. Mech., Trans. ASME **33**, 371 (1964).

[41] G. M. Hamilton, Explicit equations for the stresses beneath a sliding spherical contact, Proc. Inst. Mech. Eng. C **197**, 53 (1983).

[42] K. L. Johnson, *Contact Mechanics* (Cambridge University Press, Cambridge, England, 1985).

[43] B. N. Persson and C. Yang, Theory of the leak-rate of seals, J. Phys. Condens. Matter **20**, 315011 (2008).

[44] D. Huang, X. Yan, R. Larsson, and A. Almqvist, Leakage threshold of a saddle point, Tribol. Lett. **71**, 1 (2023).

[45] W. B. Dapp and M. H. Müser, Fluid leakage near the percolation threshold, Sci. Rep. **6**, 1 (2016).

[46] R. H. Bentall and K. L. Johnson, An elastic strip in plane rolling contact, Int. J. Mech. Sci. **10**, 637 (1968).

[47] J. Lengiewicz, M. d. Souza, M. A. Lahmar, C. Courbon, D. Dalmas, S. Stupkiewicz, and J. Scheibert, Finite deformations govern the anisotropic shear-induced area reduction of soft elastic contacts, J. Mech. Phys. Solids **143**, 104056 (2020).

[48] K. Vorvolakos and M. K. Chaudhury, Kinetic friction of silicone rubbers, Langmuir **19**, 6778 (2003).

1

Supplementary materials

Model and method

Model and method are similar to those used in many previous studies using GFMD, most notably in the original work [29], which, however, relied on atomistic Green's functions of Cu [111] surfaces rather than those valid in the continuum limit and on interfacial potentials lacking explicit interfacial dissipation. GFMD is contained in a few open source packages, however, the features needed to perform the simulations presented in our manuscript are not publically available to the best of our knowledge.

In principle, GFMD is a boundary-value method, which solves Newton's equation of motion for the Fourier coefficients of the surface displacements $\tilde{\mathbf{u}}(\mathbf{q})$. Convergence to the desired elastic deformation state can be achieved quickly by assigning inertia to surface modes with well-designed dependencies on the wave vector $\mathbf{q}$ of a given mode [27]. Calculation of stresses or forces acting on the surface mesh elements requires the elastic Green's functions and the interactions with the counterbody to be known. These aspects as well as other model and method details are described next in separate sections.

Before going into details, we alert the reader to a change of notation. In the main manuscript, a position in the interface is denoted as $\mathbf{r} = (x, y)$ and the (default) sliding direction is parallel to x. We switch to index notation $\mathbf{r} = (r_1, r_2)$ in the more technical appendix and assume the (default) sliding direction to be parallel to the unit vector $\mathbf{e}_1$, while using Einstein summation convention. Thus, the (default) sliding velocity would be denoted as $\mathbf{v}_0 = v_0 \mathbf{e}_\alpha \delta_{\alpha 1}$ in our notation. Since Cartesian indices run from 1 through 3, the index 0 in v_0 is not a Cartesian index.

Green's functions

In linear, continuum theory, the elastic properties of an isotropic medium are defined by its Young's modulus E and the Poisson's ratio ν. For a frictionless contact of a semi-infinite linear elastomer, the relevant modulus is the contact modulus $E^* = E/(1 - \nu^2)$, which is kept constant (unity) throughout this paper. For isotropic and homogeneous elastomers of thickness h, whose surface is flat in the absence of external stress, the Fourier coefficients or transforms of stress and strain are related through

$$\tilde{\sigma}_{3\alpha}(\mathbf{q}) = qE^* \Phi_{\alpha\beta}(\mathbf{q}, \nu, h, \cos\gamma)\tilde{u}_\beta(\mathbf{q}), \qquad (1)$$

where $\Phi_{\alpha\beta}(...) = \Phi_{\beta\alpha}^*(...)$ and the interface normal is parallel to $\mathbf{e}_3$. Moreover, γ is the angle formed by $\mathbf{q} = (q_1, q_2)$ and the in-plane displacement vector $\mathbf{r} = (r_1, r_2)$.

To simplify the dependencies of $\Phi_{\alpha\beta}(...)$ on the orientation between $\mathbf{q}$ and $\mathbf{u}$, it is easiest to express them in a coordinate system, in which $\mathbf{q}$ points parallel to the r_1 axis. Note that the current r_1-axis is, in general, not aligned with the sliding velocity $v_0\mathbf{e}_1$. Thus, for $\mathbf{q} = (q_1, 0)$, the coefficients become [23, 31]

$$\frac{\Phi_{11}(hq, \nu)}{(1-\nu)^2} = \frac{(3-4\nu)\sinh(2qh) - 2qh}{(3-4\nu)^2\sinh^2(qh) - (qh)^2} \qquad (2a)$$

$$\frac{\Phi_{13}(hq, \nu)}{(1-\nu)} = \frac{iq_x}{q}\frac{(3-4\nu)(1-2\nu)\sinh^2(qh) - (qh)^2}{(3-4\nu)^2\sinh^2(qh) - (qh)^2} \qquad (2b)$$

$$\frac{\Phi_{22}(hq, \nu)}{1-\nu} = \frac{1}{2\tanh(qh)} \qquad (2c)$$

$$\frac{\Phi_{33}(hq, \nu)}{(1-\nu)^2} = \frac{(3-4\nu)\sinh(2qh) + 2qh}{(3-4\nu)^2\sinh^2(qh) - (qh)^2} \qquad (2d)$$

and $\Phi_{12}(...) = \Phi_{23}(...) = 0$. Except Φ_{13}, which is purely imaginary up to isolated points where it vanishes, coefficients in Eq. (2) are real and positive. In this latter case, displacements and stresses are in phase. The purely imaginary nature of Φ_{13} implies a phase shift of $\pm\pi/2$. Their effect is represented graphically in Fig. 1 and can moreover be summarized as follows, where $\tilde{\mathbf{G}}$ is the inverse matrix of $\boldsymbol{\Phi}$:

cause	coupling effect
$u_1(x) = \hat{u}\cos(qx)$	$\Delta\sigma_3 = +\text{Im}(\Phi_{13})\hat{u}\sin(qx)$
$u_3(x) = \hat{u}\cos(qx)$	$\Delta\sigma_1 = -\text{Im}(\Phi_{13})\hat{u}\sin(qx)$
$\sigma_1(x) = \hat{\sigma}\cos(qx)$	$\Delta u_3 = -\text{Im}(\tilde{G}_{31})\hat{\sigma}\sin(qx)$
$\sigma_3(x) = \hat{\sigma}\cos(qx)$	$\Delta u_1 = +\text{Im}(\tilde{G}_{31})\hat{\sigma}\sin(qx)$
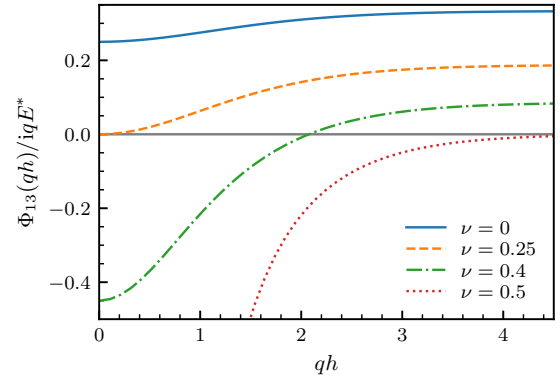
FIG. 1: Imaginary part of the (purely imaginary) coupling term Φ_{13} for different ν as a function of the product of wavevector q and height h.

Indenter geometries

The slider is assigned a height profile $h(\mathbf{r})$, which either is parabolic, consists of a square geometry or is ran-

domly rough. In the first case, $h(r) = r^2/(2R_c)$, R_c being the radius of curvature, while in the second case $h(\mathbf{r}) = h_0\{\cos(q_0 x) + \cos(q_0 y)\}/2$ with $q_0 = 2\pi/\lambda$ and $h_0 = \lambda/(2\pi)^2$, where λ is the linear dimension of the periodically repeated simulation cell.

To generate the rough surface, the squared magnitude of a height Fourier coefficient, $|\tilde{h}(\mathbf{q})|^2$, is set to the height spectrum $C(q) \propto q^{-2-2H}$ for wave vectors $\mathbf{q}$ whose magnitude satisfies $2\pi/\lambda_l \leq q \leq 2\pi\lambda_s$, while all other $\tilde{h}(\mathbf{q}) = 0$. Here $H = 0.8$ is the Hurst roughness exponent, $\lambda_l = L/2$ is the long-wavelength cutoff, while $\lambda_s = \lambda_l/128$ the short wavelength cutoff. The phase of the Fourier coefficient of the height $\tilde{h}(\mathbf{q})$ is 2π times an independent, uniform random number $U(\mathbf{q}) \in (0, 1)$ so that a height Fourier coefficient reads

$$\tilde{h}(\mathbf{q}) = \sqrt{C(q)} e^{\mathrm{i}2\pi U(\mathbf{q})}. \tag{3}$$

The proportionality factor for $C(q)$ was chosen such that the root-mean square height is $h_{RMS} = 0.01\lambda_l$, which produces a root-mean-square gradient of $\bar{g} = 0.28$. Moreover, rough surface simulations were conducted with linear mesh resolutions of $\Delta x = \Delta y = \lambda_s/8$.

Results presented on stresses pertain only to one specific surface realization. Since stresses arise mostly in response to height gradients, stress distribution self-average quite quickly so that they do not change substantially from one random realization to the next, also because the system size was twice λ_l. Specifically, standard deviations of second moments are of order 5% of stress-tensor measures. Fluctuations are more significant for flow factors deduced from leakage calculations, because leakage currents are sensitive to long-wavelength undulations, in particular near the percolation threshold. This is why results for mean flow factors were averaged over eight roughness realizations.

Interactions between elastomer and slider

To obtain the quasi-static solution of the frictional contact, we take advantage of the spatio-temporal invariance, $x(t) = x(0) + v_0 t$, which results from the employed in-plane periodic boundary conditions and the elastomer initially being flat. Thus, in our simulations, the two surfaces are not explicitly moved with respect to each other. Instead, the in-plane velocity field of the elastic body (relative to the rigid indenter) is calculated as

$$\mathbf{v}^{rel}(\mathbf{r}) = v_0 \mathbf{e}_1 - \frac{\mathrm{d}\mathbf{u}(\mathbf{r})}{\mathrm{d}t} = v_0 \mathbf{e}_1 - \frac{\partial \mathbf{u}(\mathbf{r})}{\partial x} v_0. \tag{4}$$

The Coulomb shear stress τ_C on a surface element is assumed to be antiparallel to $\mathbf{v}^{rel}$, but independent of its magnitude v^{rel}:

$$\tau_C(\mathbf{r}) = -\mu_c p_z \hat{\mathbf{v}}^{rel}(\mathbf{r}), \tag{5}$$

where μ_c is the microscopic friction coefficient, and $\hat{\mathbf{v}}^{rel}(\mathbf{r})$ is the in-plane unit vector parallel to the relative velocity.

The interaction between slider and elastomer is modeled with a potential increasing quadratically with the local overlap, i.e., the interaction potential (before discretization) reads:

$$U_{if} = \int d^2 r \frac{k_{if}}{2} \{z(\mathbf{r}) - h(\mathbf{r})\}^2 \Theta\{z(\mathbf{r}) - h(\mathbf{r})\}, \tag{6}$$

where k_{if} is set close to the normal stiffness of the stiffest elastic mode, i.e., $k_{if} = 2E^*/\Delta x$, while $\Theta(...)$ denotes the Heaviside theta function. A short- but finite-range repulsion was chosen so that forces on mesh elements could be computed directly without having to deduce constraint forces first. The repulsion was made harmonic since this allows the time step to remain essentially as large as for a free-standing surface subjected to a simple time-dependent stress, which does not need to be determined self-consistently. Normal stresses can be deduced from first order (functional) derivatives of U_{if} with respect to $z(\mathbf{r})$.

Observables

Stress tensor calculation in rough interfaces

To evaluate the stress-tensor at the interface, we use "Hooke's law"

$$\sigma_{\alpha\beta} = C_{\alpha\beta\gamma\delta}\varepsilon_{\gamma\delta},$$

with the symmetric strain tensor

$$\varepsilon_{\alpha\beta} = \frac{1}{2}\left(\frac{\partial u_\alpha}{\partial r_\beta} + \frac{\partial u_\beta}{\partial r_\alpha}\right).$$

Under the assumption of isotropy, the components of $C_{\alpha\beta\gamma\delta}$ can be expressed in dependence of only the known parameters of Young's modulus E and Poisson's ratio ν. Thus, we are provided with six equations for six known and six unknown variables. The known variables are the dispacement derivatives $\partial u_\alpha/\partial r_{\beta\neq 3}$ and the stress-tensor elements $\sigma_{\alpha 3} = \sigma_{3\alpha}$, making it possible to solve the linear system of 6 equations for the 6 unknown quantities $\sigma_{\alpha\neq 3\beta\neq 3}$ and $\partial u_\alpha/\partial r_3$.

Friction force

The kinetic friction F_k can be deduced from the dissipated power via [19]

$$P_{diss} = \mu_c \int \mathrm{d}^2 r\, p_z(\mathbf{r}) v_r(\mathbf{r}) \tag{7}$$

through $F_{\rm k} = P_{\rm diss}/v_0$. Here, $p_z(\mathbf{r})$ is the normal pressure and $v_{\rm r}(\mathbf{r})$ the absolute in-plane velocity of a point on the surface of the elastomer relative to the slider and the integral taken over the contact area. The microscopic friction coefficient equals the macroscopic one, as long as the pressure profile is symmetric and deviations of the relative velocities from the center-of-mass velocity v_0 are antisymmetric, which is the case in the absence of coupling for a Hertzian tip and steady-state sliding.

The lateral force associated with a downhill-slope force is given by [35, 38]

$$\Delta F = - \int d^2r \nabla h(\mathbf{r}) p_{\rm z}(\mathbf{r}). \tag{8}$$

We explicitly verified that our code produced the same corresponding total friction $F_{\rm k} = \mu_{\rm c} F_z + \Delta F$ via the downhill-slope argument as through a dissipation calculation.

Flow factors

The flow factors or leakage current are determined by solving the Reynolds thin-film equation, in which the local resitance to fluid flow scales with the inverse third power of the interfacial separation. To this end, we use a house-written code, which was developed for earlier work [32]. Mechanical stresses on the elastomer originating from fluid gradients are neglected.

Critical relative contact areas $a_{\rm c}^*$ were determined through nested intervals: The external pressure was it-eratively adjusted and each time a flow calculation was performed until we found the exact pressure (and corresponding contact area), at which the flow factor in a given direction drops to 0.

Details on Hertzian contact properties

Some of the discussions in the main text may benefit from line plots of data that was previously shown only as heat map. Fig. SI 2 summarizes the most important results for Hertzian contacts. Moreover, as alluded to in the main text and described in Eq. (7), changes in friction can also be rationalized by analyzing changes in the local dissipation. Without coupling, the normal stress is axisymmetric while the excess velocity field $\dot{\mathbf{u}}$ is antisymmetric with respect to a 180° rotation around the z-axis. With coupling, the only remaining plane of (anti-) symmetry is the xz plane, which is most easily visible for the transverse velocity. In principle, an asymmetry is needed in the stress field and/or a symmetric component in the excess velocity in order for coupling to affect the overall heat production. In practice, it turns out that the coupling of the symmetric preexisting normal stress to the induced symmetric excess velocity is the dominating effect, which decreases friction for compressibility coupling but increases it for confinement coupling. The coupling of the induced antisymmetric stress field with the antisymmetric preexisting velocity field has the opposite effect but is of smaller magnitude.

4
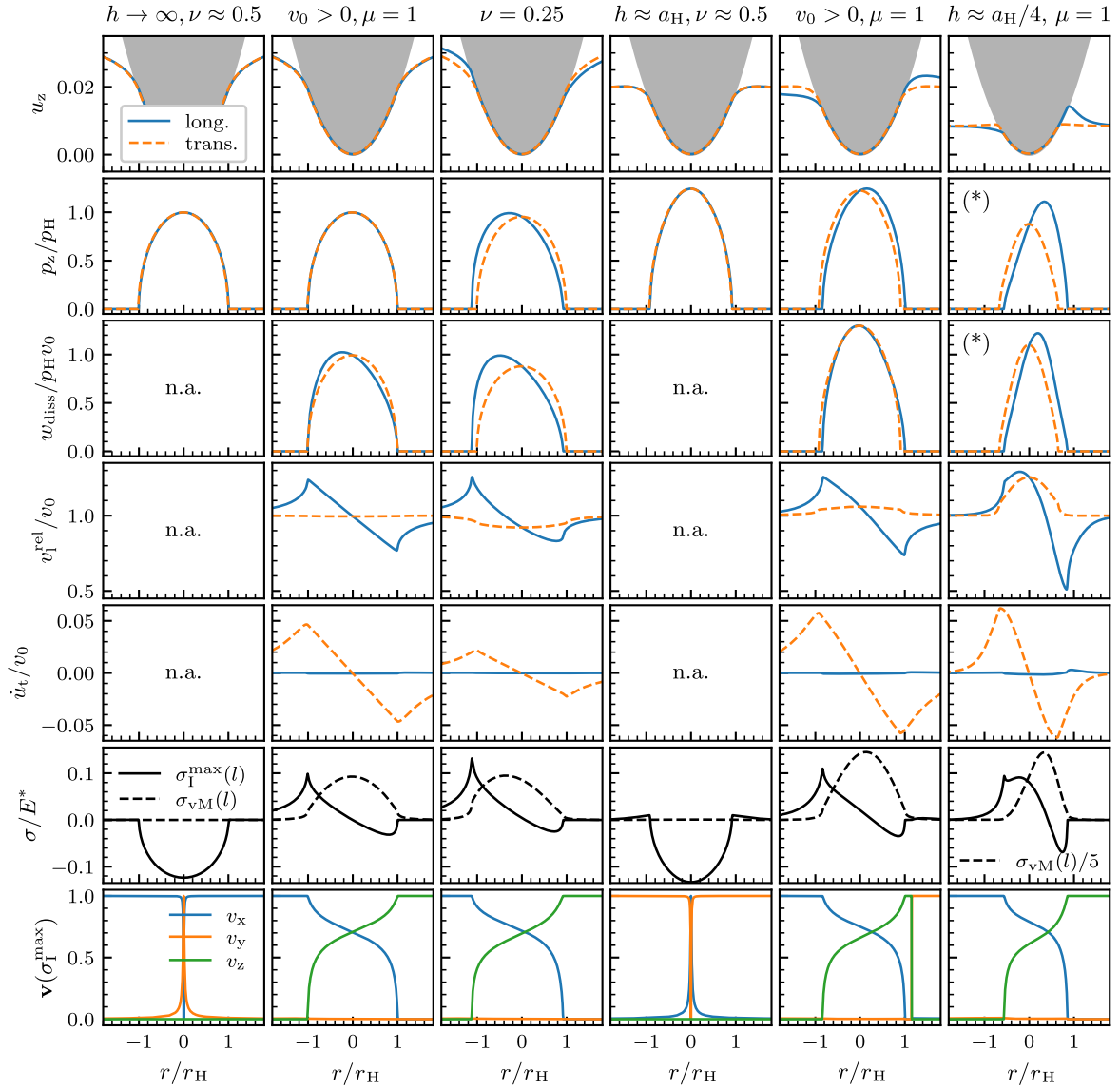
FIG. 2: Profile plots of contact properties for a rigid parabolic indenter in contact with an elastic material of varying properties. The microscopic friction coefficient was set 1, except for columns 1 and 4, which represent static cases without sliding or friction. Columns 1-3 represent semi-infinite elasomers, the first two cases being incompressible, whereas the third one has a Poisson's ratio of 0.25. Columns 4-6 show confined elastomers with finite thickness, where the last one is thinner than the first two. The seven rows represent the areal distributions of normal displacement, normal pressure, dissipated power, relative longitudinal velocity, transverse velocity, internal stresses and stress eigenvectors, respectively. Solid blue lines indicate a plot along the longitudinal (sliding) direction, dashed orange lines the transverse direction. In the last two rows, all properties are only shown in longitudinal (sliding) direction Data marked with "(*)" (last plot in the second and third row) was divided by 2.5 in order to match the scales of the other cases. Note that the plot on the far right in the sixth row also contains one rescaled data set. The last row contains the components of the normalized eigenvector belonging to the maximum eigenstress plotted in the row above. As introduced before, the indices l, t and z stand for longitudinal (parallel to sliding), transverse (perpendicular to sliding) and normal (to the surface), respectively.